Electrochemical Investigations on Functionalized 2D Graphene, Molybdenum Disulfide, and Nickel Sulfide

by

Navid Solati

A Dissertation Submitted to the
Graduate School of Sciences and Engineering
in Partial Fulfilment of the Requirements for

the Degree of

Doctor of Philosophy

in

Materials Science and Engineering

KOÇ ÜNİVERSİTESİ

June, 2022

Electrochemical Investigations on Functionalized 2D Graphene, Molybdenum Disulfide, and Nickel Sulfide

Koç University

Graduate School of Sciences and Engineering

This is to certify that I have examined this copy of a doctoral dissertation by

Navid Solati

and have found that it is complete and satisfactory in all respects,
and that any and all revisions required by the final examining
committee have been made.

Committee Members:

Assoc. Prof. Sarp Kaya (Advisor)

Assoc. Prof. Uğur Ünal

Prof. Alper Uzun

Prof. Adem Tekin

Assoc. Prof. Damla Eroğlu Pala

Date: 03.06.2022

To the soul of

all 176 innocent passengers and crews of the

Flight PS752

that lost their lives in airplane shoot-down….

ABSTRACT

Electrochemical Investigations on Functionalized 2D Graphene, Molybdenum Disulfide, and Nickel Sulfide

Navid Solati

Doctor of Philosophy in Materials Science and Engineering

June 2022

Widespread implementation of electrochemical-based energy generation and storage techniques is the indispensable strategy for addressing the issues resulting from the constant use of fossil fuels. After decades of searching for the best candidates to be used as electrodes in the electrochemical-based devices, electrochemists have started to investigate the details of electrochemical reactions, such as mechanisms, reaction site, and electrode alterations under operando conditions. Despite invaluable findings about these issues, there are still unanswered or unclearly answered significant questions.

Two dimensional (2D) materials provide unique features to design highly active electrodes and have comprehensive investigations about the details of electrochemical reactions. The distinctive structure of 2D materials delivers a high number of available sites for functionalization. This paves the way to alter the electrochemically essential properties such as surface morphologies, electronic structure, carrier concentration, charge transfer efficiency, etc. As a result, it is possible to design new electrodes with enhanced electrochemical activities.

In addition, the combination of the availability of a high number of active sites and accessibility of these sites with the surface-sensitive characterization methods provide exceptional conditions to study the electrochemical reactions in detail. This issue has gained prime importance with recent findings about the structural and compositional alterations of electrodes during electrochemical measurements.

In this thesis, the unique features of 2D graphene, MoS_2, and NiS_x derived from $Ni(OH)_2$ combined with various physical and electrochemical characterization techniques have been used to study the alterations in electrode materials during electrochemical reactions.

The initial part of the study has been focused on graphene, which is the simplest and the best-known 2D material. It has been shown that N-doping significantly enhances the

electrochemical activity of graphene toward oxygen reduction reaction (ORR). After studying the effect of different N configurations on the activity of N-doped graphene, it has been shown that pyridinic N improves the activity of bilayer N-graphene by modulating the interaction between the layers. The increased π- π interaction in pyridinic N-doped graphene, promotes the electron transfer kinetics between layers and results in an improved activity for the N-doped bilayer graphene.

In order to have a better insight into the role of different N configurations, active sites, and ORR mechanisms, bilayer pristine and N-doped graphene were investigated by the spectroelectrochemical Raman technique. It has been shown that based on the configuration of the N dopants, it is possible to have a competition between adsorption of H/OH and O_2 groups. After showing Raman fingerprints for the possible reactions between O_2 (or O_2^-) with H/OH, it has been proposed that the ORR could have multiple mechanisms with the same transferred electron numbers.

Despite enormous efforts in advancing the hydrogen evolution reaction (HER) activity of MoS_2, the presence of different phases and relatively complex structure of MoS_2 has resulted in a significant number of controversial results in the published reports so far. Unfortunately, most of the operando techniques which have been used to answer some fundamental questions, such as the active site, the mechanism on different MoS_2 structures, and the structural changes of MoS_2 during HER, have been focused on amorphous MoS_2. Here a systematic investigation has been performed to study the effect of modifying a synthesis parameter on the phase, composition, flake size, and defect density of MoS_2. It has been shown that N doping improves the HER activity of MoS_2. However, this improvement is not stable, and the strain and phase conversion induced by N dopants fade away when they abandon the MoS_2 structure.

Finally, the HER activity of different nickel sulfides phases in the alkaline electrolyte was investigated. Despite the 3D structure for NiS_x, it has been shown that it is possible to synthesize pure 2D NiS_2 using a Ni precursor, which has a layer-by-layer structure ($Ni(OH)_2$). It has been shown that the electrochemical measurements performed on these samples have better results compared to the samples with 3D structures. The non-similar dynamic behavior in linear sweep voltammetry results of the samples was investigated by performing Raman spectroscopy and XPS investigations during the course of structural transition. It has been shown that the co-presence of hydroxylated Ni and NiS_x promotes the HER activity of the electrodes.

ÖZETÇE

2 Boyutlu İşlevselleştirilmiş Grafen, Molibden Disülfit, ve Nikel Sülfit Üzerinde Elektrokimyasal Araştırmalar

Navid Solati

Malzeme Bilim ve Mühendisliği Doktora Tezi

Haziran 2022

Elektrokimyasal temelli enerji üretimi ve depolama tekniklerinin yaygın olarak uygulanması, fosil yakıtların sürekli kullanımından kaynaklanan sorunları ele almak için vazgeçilmez bir stratejidir. Elektrokimyasal temelli cihazlarda elektrot olarak kullanılacak en iyi adayları on yıllar boyunca aradıktan sonra, elektrokimyacılar, mekanizmalar, reaksiyon bölgesi ve operando koşulları altında elektrot değişiklikleri gibi elektrokimyasal reaksiyonların ayrıntılarını araştırmaya başladılar. Bu konularla ilgili paha biçilmez bulgulara rağmen, hala cevaplanmamış önemli sorular var.

2 boyutlu malzemeler, aktif elektrotlar tasarlamak için benzersiz özellikler sağlar. Bu malzemelerin özel yapısı işlevselleştirme için çok sayıda yer sunar. Bunun neticesinde, yüzey morfolojileri, elektronik yapı, taşıyıcı konsantrasyonu, yük transfer verimliliği vb. gibi elektrokimyasal olarak temel özelliklerin değiştirmesi mümkün hale gelir. Sonuç olarak, geliştirilmiş elektrokimyasal aktivitelere sahip yeni elektrotlar tasarlamak mümkündür. Bu tezde, elektrokimyasal reaksiyonlar sırasında elektrotlarda olan değişiklikleri incelemek için çeşitli fiziksel ve elektrokimyasal karakterizasyon teknikleri ile birleştirilmiş 2 boyutlu malzemelerin benzersiz özelliklerinden yararlanmıştır.

Ek olarak, çok sayıda aktif sitenin mevcudiyeti ve bu sitelerin erişilebilirliğinin yüzeye duyarlı karakterizasyon yöntemleriyle birleştirilmesi, elektrokimyasal reaksiyonların ayrıntılı olarak çalışılması için istisnai koşullar sağlar. Bu konu, elektrokimyasal ölçümler sırasında elektrotların yapısal ve bileşimsel değişiklikleri hakkındaki son bulgularla büyük önem kazanmıştır.

Bu tezde, elektrokimyasal reaksiyonlar sırasında elektrot malzemelerindeki değişiklikleri incelemek için çeşitli fiziksel ve elektrokimyasal karakterizasyon teknikleri ile birlikte 2D Grafen, MoS_2 ve NiS_x'in benzersiz özellikleri kullanılmıştır.

Çalışmanın ilk kısmı, en basit ve en iyi bilinen 2D malzeme olan grafen üzerine odaklanmıştır. N-katkılaman'ın, grafenin oksijen indirgeme reaksiyonuna (ORR) yönelik elektrokimyasal aktivitesini önemli ölçüde arttırdığı gösterilmiştir. Farklı N konfigürasyonlarının N-katkılı grafenin aktivitesi üzerindeki etkisini inceledikten sonra, piridinik N'nin, tabakalar arasındaki etkileşimi modüle ederek iki tabakalı N-grafenin aktivitesini geliştirdiği gösterilmiştir. Pirrdinik N katkılı grafen içindeki artan π- π etkileşimi, katmanlar arasındaki elektron transfer kinetiğini desteklediği ve N katkılı çift katmanlı grafen için geliştirilmiş bir aktivite ile sonuçlandığı isbat edilmiştir.

Farklı N konfigürasyonlarının, ORR esnasında rolünü daha iyi anlamak için, iki katmanlı bozulmamış ve N katkılı grafen, spektroelektrokimyasal Raman (SEC-Raman) tekniği ile araştırıldı. N katkı maddelerinin konfigürasyonuna bağlı olarak, H/OH ve O_2 gruplarının adsorpsiyonu arasında bir rekabet olmasının mümkün olduğu gösterilmiştir. O_2 (veya O_2^-) ile H/OH arasındaki olası reaksiyonlar için Raman parmak izlerini gösterdikten sonra, ORR'nin aynı aktarılan elektron sayılarına sahip birden fazla mekanizmaya sahip olabileceği önerilmiştir.

MoS_2'nin hidrojen evrim reaksiyonu (HER) aktivitesini geliştirmedeki önemli çalışmalara rağmen, farklı fazlarının varlığı ve nispeten karmaşık yapısı, şimdiye kadar yayınlanan raporlarda önemli sayıda tartışmalı sonuçlara yol açmıştır. Ne yazık ki, farklı MoS_2 yapılarındaki mekanizma ve HER sırasında yapısal değişiklikler gibi temel soruları cevaplamak için kullanılan operando tekniklerinin çoğu, amorf MoS_2'ye odaklanmıştır. Burada, bir sentez parametresini değiştirmenin MoS_2'nin fazı, bileşimi, ve kusur yoğunluğu üzerindeki etkisini incelemek için sistematik bir araştırma yapılmıştır. N katkılaman'ın MoS_2'nin HER aktivitesini geliştirdiği gösterilmiştir. Ancak, bu gelişmenin olmadığı ve N katkılamanın sonucunda ortaya gelen gerilim ve faz dönüşümünün, N atomlarının MoS_2 yapısını terk ettiklerinden sonra aradan gittiği gösterilmiştir.

Son olarak, alkali elektrolit içindeki farklı nikel sülfit fazlarının (NiS_x) HER aktivitesi araştırılmıştır. NiS_x'in 3 boyutlu yapısına rağmen, katman katman yapılı ($Ni(OH)_2$) kullanarak saf 2 boyutlu NiS_2 sentezlemenin mümkün olduğu gösterilmiştir. Bu numuneler üzerinde yapılan elektrokimyasal ölçümlerin 3 boyutlu yapılara sahip numunelere göre daha iyi sonuçlar verdiği gösterilmiştir. Numunelerin lineer süpürme voltametri sonuçlarındaki benzer olmayan dinamik davranışları yapısal geçiş sırasında Raman ve XPS incelemeleri yapılarak incelenmiştir. Hidroksillenmiş Ni ve NiS_x'in birlikte varlığının elektrotların HER aktivitesini desteklediği gösterilmiştir.

ACKNOWLEDGMENTS

First, my sincere gratitude goes to Assoc. Prof. Sarp Kaya for his support, great knowledge, and limitless energy and motivation, which helped me a lot in completing my Ph.D. and widening my scientific view from different perspectives. Starting from the first minute I joined his group until the last day, he taught me much, both scientifically and personally. It will always be an honor for me to have the title of being the first student to join his group.

I cannot thank my soulmate, Mahshid, enough for her endless support, friendship, and love. During all ups and downs of these years, she was always by my side, and she knew exactly how to guide and energize the mentally exhausted and demotivated version of me. I cannot imagine how many wrong decisions I would probably make without consulting and talking to her. Merci beaucoup my love.

My acknowledgment would be incomplete without thanking my family. I will always be thankful for what they gave and taught me throughout my life. They have patiently held my hands, supported me through every stage of my life, and motivated me to try and achieve the best.

I would like to thank my thesis progress committee members Prof. Alper Uzun, and Assoc. Prof. Uğur Ünal, for helpful scientific discussions and their valuable time and consideration that helped me improve my knowledge. I would like to thank Prof. Adem Tekin, and Assoc. Prof. Damla Eroğlu Pala for the evaluation of my thesis and for honoring me by serving on my thesis committee.

I will always cherish the wonderful atmosphere and friendship I had with my fellow lab-mates. I would like to particularly thank Dr. Timuçin Balkan, and Dr. Abdullah Kahraman for the great advice that they gave me during my studies. I appreciate the tremendous technical and scientific support of Dr. Hamaneh Zarenejhad, Saeede Tafazzoli, and Emre Usman. My appreciation also extends to all my current and former lab-mates for their support and contributions within these years.

Finally, I would like to acknowledge the generous support of all of the members in Koç University Surface Science and Technology Center (KUYTAM) and Koç University TÜPRAŞ Energy Research Center (KUTEM) for my experiments and characterizations.

TABLE OF CONTENTS

LIST OF FIGURES

LIST OF TABLES

Chapter 1
Introduction

1.1 Two Dimensional Materials; Synthesis, Properties, and Applications

The two-dimensional (2D) materials, sometimes mentioned as nanosheets or thin films, are structures with thickness in an atomic scale. Some sources define them as structures with in-plane axes to a perpendicular axis ratio greater than 100 [1]. The history of these materials can be traced back to 1824, where Thomas H. Webb thermally exfoliated vermiculite. However, the rise of research on 2D materials happened after 2004 when Novoselov and Geim reported the synthesis of graphene using the scotch tape method [2]. The 3D layered materials are known as the parent materials for the 2D structures, and they showed vast applications in the industry long before the discovery of 2D materials. For example, graphite was used as anode material in lithium-ion batteries (LIBs) because of its excellent ion insertion/extraction capability [3], and bulk MoS_2 was used as a dry lubricant originating from the weak van der Waals forces between individual MoS_2 layers [4].

As a result of quantum confinement, novel and promising properties emerge in 2D materials when the layered 3D materials are thinned to single and few layers [5]. The remarkable properties of 2D materials have attracted the attention of numerous research groups to synthesize hundreds of different types of them. Layered materials which can be exfoliated to form 2D nanosheets range from insulators (hexagonal boron nitride (hBN) [6], HfS_2, etc.) to semiconductors (MoS_2, $MoSe_2$, WS_2, WSe_2, TaS_2, $RhTe_2$, $PdTe_2$) [7] to semimetals ($TiSe_2$, WTe_2, $NiTe_2$, VSe_2) [8] and to superconductors (NbS_2, $NbSe_2$, $NbTe_2$, $TaSe_2$) [9]. This variation in electrical properties allows materials with similar high mechanical properties and thermal conductivity but significantly different electrical properties. For instance, compared to graphene with metallic conductivity, hBN displays similar mechanical and thermal properties while having a 5.1 eV bandgap [10]. Recently, new mono-element 2D structures beyond graphene have evolved, these include Group 13 borophene [11], [12], Group 14 silicene, germanene, and stanene [13], and Group 15 phosphorene [14], arsenene [15], antimonene [16], and bismuthene [17]. There are also a growing number of graphene derivatives, including graphene oxide [18], heteroatom-doped graphene [19], graphdiyne [20], graphane [21]. Another developing main class of

2D materials is chalcogenides including transition metal dichalcogenides (TMDs) with MX_2 stoichiometry (M = Groups 4–10 metals, X = S, Se and Te) [22], metal tri-chalcogenides (Bi_2Te_3, Sb_2Se_3, $NbSe_3$, $TaSe_3$) [23], III-VI (GaSe, InSe) [24], and IV-VI (SnS_2, SnS) chalcogenides [25]. Graphitic carbon nitride (g-C_3N_4) is another type of 2D material that consists of sp^2 hybridized C and N with lots of pyrrolic N defects [26]. Other classes of 2D materials include transition metal halides such as PbI_2 and $MgBr_2$ [27], transition metal oxides (MnO_2, MoO_3) [28], perovskites such as $LaVO_3$, $LaMnO_3$ [29], and $Ni(OH)_2$ [30], layered double hydroxides (LDHs) [31], and MXenes [32]. Finally, in addition to inorganic 2D compounds, organic and organometallic porous 2D nanosheets are also a focus of interest, encompassing 2D covalent organic frameworks (COFs) [33], 2D metal-organic frameworks (MOFs) [34]. The availability and flexibility of this range of 2D materials enable the development of new layered hybrid materials and heterostructures. Since most exfoliated nanosheets possess distinct surface charges, van der Waals heterostructures of graphene, h- BN, and TMDs, have already been synthesized and showed unique properties. This characteristic property is the main key in using 2D materials as building blocks to form electrostatically-driven hybrid structures [35], [36].

The remarkable intrinsic properties of 2D materials, such as thermal and electrical conductivity, the tunability of these properties, and the synthesis of numerous types of them have provided a chance to use them in a broad range of applications. The feasibility of using 2D materials in biomedical applications [37]–[41], gas storage systems [42], [43], sensors [44]–[46], chemical separators [47], [48], variety of energy storage and conversion applications [49]–[53], and electronics and optoelectronics [54], [55] have been studied, and they have shown promising performances in most of these applications. Due to some specific properties of 2D materials, the extent of investigation on using them for catalysis, energy conversion, and energy storage technologies has been far more than the other applications. These suitable properties are [56]–[60]:

(1) Improved electronic and optical properties such as higher electron mobility and carrier concentrations as well as tunable band gap compared to the bulk structures,

(2) High specific surface area improves mass transport and solar harvesting (photocatalysis), provides plentiful active sites for cation storage and redox reactions, reduces electrical transport and ion diffusion path length, and facilitates high power density of batteries and supercapacitors [61].

(3) Availability of unsaturated edges and dangling bonds which are commonly active sites for catalytic reactions.

(4) The feasibility of modifying the electronic structure and catalytic activity by mechanical strain, applied electric fields, doping, heterostructure forming, chemical functionalization, and alloying provides new catalysis and energy applications opportunities [62]–[64].

(5) Unique atom-thick structure presents an ideal platform for revealing the catalytic mechanism and active sites to researchers [65].

(6) The large specific area makes 2D materials a versatile scaffold for preparing various hybrids to provide multifunctional catalysis.

The research paradigm on 2D materials has recently shifted from discovery and property characterization toward materials engineering and property tuning. This is due to some limitations of 2D structures caused by their intrinsic properties and certain processing-related structural disadvantages [66]. For example, many 2D materials provide planar diffusion channels for charge-carrying ions between their layers, making them potential electrode materials for electrochemical energy storage devices [56]. However, their practical performance is primarily restrained by the intrinsic interlayer distance, which results in limited ion accessibility and structural instability [67]. Another example is the different catalytic activity between the basal plane and the edges of 2D materials. In most of the 2D materials, the catalytic activity originates from scarce edge sites, [68] while the basal plane with a large areal portion is inactive.

Various synthesis approaches have been used to prepare and grow 2D materials. These methods can be classified into two main groups of top-down and bottom-up techniques. A simple top-down method to synthesize 2D nanosheets is to peel off single layers from bulk layered compounds using Scotch tape. The nanosheets obtained with this technique are usually of high quality since no chemicals and chemical reactions are involved in the process. After the first report for graphene, [2] this technique has been widely applied for synthesis of 2D nanosheets of TMDs (MoS_2, $MoSe_2$, WS_2, WSe_2, TaS_2, $TaSe_2$, $NbSe_2$, PtS_2, $PtSe_2$, etc.),[69] metal phosphorous trichalcogenides, [70] antimonene, [71] and h-BN [72]. Additionally, sonication on bulk layered compounds in a proper solvent can induce an effective exfoliation [73]. A good match of the surface energy between layered compound and solvent is crucial for efficient exfoliation. Using this technique, high yield

and large-scale production are possible. Another top-down method is the ion intercalation and subsequent hydroxylation under mild sonication processes [74]. This process involves the intercalation of small-sized cations into the interlayer space of layered compounds. Since the control over cation intercalation is very difficult, either insufficient intercalation or over intercalation frequently occurs. In comparison with chemical routes, electrochemical routes can provide a more efficient way for the intercalation and exfoliation of layered materials. During the electrochemical ion exchange method, interlayer spacing is expanded by replacing existing small ions with relatively bulky ions, which weakens the interaction between adjacent layers, resulting in the facile exfoliation of layered material into individual nanosheets with the aid of mechanical shaking or sonication [75], [76].

The bottom-up methods can be categorized into two classes based on the reaction medium: wet-chemistry-based synthesis and chemical vapor deposition (CVD) [69]. A well-known wet-chemistry-based synthesis is hydrothermal or solvothermal reaction, extensively used to synthesize many 2D nanosheets [77]. Moisture-sensitive 2D inorganic nanosheets can be prepared by solvothermal reaction using organic solvents [78]. In these methods, high pressure is generated to promote the reaction and increase the crystallinity of the nanosheets. The concentration of precursors, reaction temperature, and solvent system are the controlling factors for hydrothermal/solvothermal methods. High yield and facile operation make the wet-chemical approaches quite attractive. However, they suffer from high energy consumption and high production costs, limiting their use in scalable industrial production [79], [80].

On the other hand, CVD involves the reaction and/or decomposition of vapor phase precursors on preselected substrates at high temperatures. The structural and physicochemical properties of the CVD-grown nanosheets can finely be tuned by controlling growth parameters such as precursor, reaction temperature substrate properties, and atmosphere [81]. 2D films with scalable size and quantity, controllable thickness, high purity and crystallinity, and lower defects can be obtained using this method [82]–[85]. However, the need for a suitable substrate, high temperature, and inert atmosphere impedes its wide-scale use to produce 2D nanosheets.

1.2 Electrochemical Energy Conversion

Widespread implementation of renewable energy has been the indispensable strategy for

addressing the issues resulting from the constant use of fossil fuels, such as global climate change, energy security, and sustainability. Solar and wind are probably the amplest and most readily accessible renewable energy sources, which have been considered essential components of the future global energy portfolio [86]. However, due to wind and the sun's random and intermittent nature, efficient and economical energy storage and conversion technologies are required to produce and utilize inexpensive renewable energy. Among these technologies, electrochemical-based energy generation and storage techniques such as fuel cells and metal-air batteries can provide a temporary medium to store and release electricity when and where needed. Electrochemistry which deals with chemical reactions at the electrode and the electrolyte interface and studies conversions between the electrical energy and chemical changes [86], could be one solution to the sustainable energy supply and to achieve the transition from the current "hydrocarbon economy" to a "hydrogen economy" [87]. The electricity produced by renewable energy is mainly for end-users, while the surplus electricity can be used in water electrolysis to generate hydrogen and oxygen. Part of the hydrogen can be transported to serve industry, traffic, and household. Moreover, the other part can be used to power up fuel cells to generate electricity.

1.2.1 Oxygen Reduction Reaction (ORR)

Fuel cells, rechargeable metal-air batteries, and dye-sensitized solar cells are next-generation energy devices for clean power production [88]. A fuel cell is an electrochemical device designed to convert the energy of a chemical reaction directly to electrical power. The employment of gaseous and liquid precursors in fuel cells is one of the differences between this technology and the primary and secondary batteries run by metals and metal oxides. Hence, the continuous supply of the reactants provided and uninterrupted elimination of the reaction products to keep a long operation time is relatively easy [89], [90]. The most significant advantage of fuel cells is that the pollution-free electrical energy comes directly from the devices. There are no combustion reactions in fuel cells to produce environmentally unfriendly products, such as CO_2, SO_2, and nitrogen oxides. In addition, fuel cells also feature good energy efficiency, light weight, silent operation, and vibration-free operation.

A fuel cell is composed of three main parts, a cathode electrode, an anode electrode, and an electrolyte. The reaction in the cathode part of fuel cells and rechargeable metal-air batteries is ORR, where electrons reduce O_2 molecules. The electrochemical cleavage of

the strong O=O bond, which has bonding energy of 498 kJ.mol^{-1}, is very challenging [91]. As a result, the ORR is more than six orders slower than hydrogen oxidation at the anode part of the fuel cells [92]. Hence, to lower the overall energy barrier for ORR, active electrocatalyst materials are vital to enhance the kinetics of this reaction.

There are two possible pathways for ORR in aqueous electrolytes; a one-step four-electron (4e-) pathway (Equation 1-1) or a two-step two-electron pathway (2e-). While the direct 4e- the pathway is recognized as the faster and more efficient root in fuel cells, the selective 2e- ORR is useful for industrial H_2O_2 production [93]. The overall 4e- ORR pathway in the alkaline electrolytes is as follows:

$$O_2 + 2H_2O + 4e^- \rightarrow 4OH^- \quad (0.401 \text{ V vs. SHE}) \qquad \text{Equation 1-1}$$

Where, SHE stands for standard hydrogen electrode.

For the indirect two-steps two-electron pathway, after the consumption of the first two electrons (Equation 1-2), either a further two-electron reduction of H_2O_2 (Equation 1-3) or the chemical disproportionation of H_2O_2 (Equation 1-4) happens:

$$O_2 + H_2O + 2e^- \rightarrow OH^- + HO_2^- \quad (-0.076 \text{ V vs. SHE}) \qquad \text{Equation 1-2}$$

$$HO_2^- + H_2O + 2e^- \rightarrow 3OH^- \quad (0.878 \text{ V vs. SHE}) \qquad \text{Equation 1-3}$$

$$2HO_2^- \rightarrow 2OH^- + O_2 \qquad \text{Equation 1-4}$$

Nørskov and co-workers were the first group to study the reaction free energy (ΔG) of different reaction intermediates during the electrochemical processes of ORR [94]. To achieve the optimum condition, reactants, products, and intermediates should bind neither too weakly nor too strongly on a given catalyst surface. Within this framework, they proposed two possible ORR mechanisms: associative and dissociation mechanisms. Although the elementary steps and the intermediates in ORR depend on the electrode and electrolyte [95], a possible associative mechanism in the alkaline electrode can be stated as follows:

$$O_2 + * \rightarrow O_2^* \qquad \text{Equation 1-5}$$

$$O_2^* + H_2O + e^- \rightarrow OOH^* + OH^- \qquad \text{Equation 1-6}$$

$$OOH^* + e^- \rightarrow O^* + OH^- \qquad \text{Equation 1-7}$$

$$O^* + H_2O + e^- \rightarrow OH^* + OH^- \quad \text{Equation 1-8}$$

$$OH^* + e^- \rightarrow OH^- + * \quad \text{Equation 1-9}$$

The dissociative mechanism starts with the following elementary reaction:

$$O_2 + * + * \rightarrow O^* + O^* \quad \text{Equation 1-10}$$

Followed by Equation 1-8 and Equation 1-9.

After investigating the detailed mechanism of ORR, the rate-limiting step can be recognized by finding the elementary reaction with minimum reaction Gibs free energy. This elementary step determines the overpotential of ORR, which is described as the difference between applied and standard potentials.

Pt-based materials are the most active ORR catalysts and are commercially available [96]. However, high cost, limited availability, and poor stability impede the large-scale implementation of these materials [93], [97]. Therefore, finding inexpensive, earth-abundant, highly active, and stable ORR electrocatalysts is of paramount importance. Numerous candidate materials have been investigated to achieve these criteria. For instance, replacing precious metals with transition metals is an effective method to reduce costs and improve performance in ORR catalysts. Hence, the electrochemical properties of transition metal oxides, such as manganese oxides [98] and cobalt oxides [99], towards ORR have been extensively studied. In order to overcome the poor conductivity drawback of metal oxides, researchers have focused on supporting them on conductive substrates to enhance catalytic performance [100], [101]. The employment of support carbon-based materials can significantly reduce the amount of transition metals needed in corresponding catalysts [102].

Additionally, the presence of different valence states in the mixed-metal oxides has attracted the attention of researchers to study their electrochemical properties. Transition metal nitrides such as TiN [103], Mn_4N [104], and MoN [105] are also ORR electrocatalyst candidates. The significant electronegativity difference between metals and N can allow for charge delocalization in nitrides, creating basic or acidic sites with good catalytic activity.

Aside from these examples, researchers have also reported that metal-free carbon materials have promising ORR activity in alkaline electrolytes owing to their large

surface area, good conductivity, tunable morphology, facile preparation, and economic viability [106]. The report published by Dai et al. [107] is known as the pioneering work in this field. Following this report, various heteroatom-doped carbon materials were investigated, such as B-doped CNTs or graphene [108], [109], sulfur-doped graphene [110], [111], phosphorus-doped graphite layers [112], and edge-halogenated (Cl, Br or I) graphene nanoplatelets [113]. Moreover, different co-heteroatoms doped carbon materials were synthesized and investigated, such as B, N co-doped CNTs or graphene [114], [115], N, S-doped graphene [116], N, P-doped graphene [117], N, B, P-doped carbon [118]. While initial studies were pointing out at delocalization of spin and charge density and introduction of damages to the integrity of π conjugation [88], [119], [120] as the main mechanisms in the electrocatalytic activity improvement of heteroatom doped carbon-bases materials, recently new finding have opened the window for further debates regarding the exact explanation of this enhancement.

1.2.2 Hydrogen Evolution Reaction (HER)

Hydrogen is a versatile energy carrier that can help tackle various critical energy challenges. From the global electricity consumption point of view, the idea of using electrolysis of water to generate hydrogen to store excess electricity or to replace fossil-based electrical power generation plants, which typically have an efficiency of 34%, with a renewable source are the main driving forces to investigate on generation and utilization of hydrogen. Hydrogen can also play a vital role in global transportation challenges either directly (e.g., fuel cell vehicles) or indirectly as a feedstock chemical for hydrocarbon synthesis or upgrading of, for example, biomass via hydrogenation. This simple but precious molecule can be produced by three main technologies: water electrolysis, coal gasification, and methane reforming [121]. While coal gasification and methane reforming generate most of the hydrogen, water electrolysis took only 4% of hydrogen production share by 2019 [122]. The strong dependency of current hydrogen production on fossil fuels, with significant associated CO_2 emissions, brings inevitable air pollution and global warming. Therefore, among these three technologies for hydrogen production, electrochemical water splitting provides tremendous prospects for driving the HER.

The global water electrolysis reaction can be shown by Equation 1-11:

$$H_2O \rightarrow H_2 + 1/2O_2 \qquad \text{Equation 1-11}$$

The energy required for the water electrolysis is ΔG = 237.2 kJ/mol at the standard

condition, corresponding to voltage at 1.23 V. Under practical operation conditions, excess potential should be applied to overcome the resistance of the electrolyzer and drive the sluggish kinetics of this reaction. The operation potential can be arrived at as follows:

$$E = 1.23V + \eta_{anode} + \eta_{cathode} + iR \quad \text{Equation 1-12}$$

Where *iR* is the electrolyte resistance during electrocatalysis, and η is the voltage applied to drive the electrode catalytic oxidation or reduction reaction [123]. One of the main hurdles to increasing water electrolysis penetration in the H_2 production share is the low efficiency of this process and the absence of cheap and earth-abundant catalysts for the cathodic (HER) and anodic (OER) reactions.

1.2.2.1 HER in Acidic Media

The overall HER and OER reactions in acidic media can be seen in Equation 1-13 and Equation 1-14:

$$\text{HER:} \quad 2H^+ + 2e^- \rightarrow H_2 \quad \text{Equation 1-13}$$

$$\text{OER:} \quad H_2O \rightarrow 2H^+ + 2e^- + \frac{1}{2}O_2 \quad \text{Equation 1-14}$$

HER undergoes a multistep reaction process, which can be divided into two mechanisms with three possible reaction steps [124]. The first step of these mechanisms is common, and it is the reduction of a proton on an active site of the catalyst surface (Volmer step, Equation 1-15). An intermediate state of an adsorbed hydrogen atom (H*) forms during this step. Then the HER can proceed by the evolution of molecular H_2, either through a second proton/electron transfer (Heyrovsky step, Equation 1-16) or through the recombination of two adsorbed protons (Tafel step, Equation 1-17) [125].

$$\text{Volmer:} \quad H_3O^+ + e^- + * \rightarrow H^* + H_2O \quad \text{Equation 1-15}$$

$$\text{Heyrovsky:} \quad H^* + H_3O^+ + e^- \rightarrow H_2 + H_2O \quad \text{Equation 1-16}$$

$$\text{Tafel:} \quad 2H^* \rightarrow H_2 \quad \text{Equation 1-17}$$

The Tafel slope (*b*), which is dependent on the rate-determining step (RDS), can be applied as a semi-quantitative indicator to determine the reaction mechanism. While the Volmer step has a Tafel slope of about 118 mV.dec^{-1}, the Tafel and Heyrovsky reactions have characteristic Tafel slope of ~30 mV dec^{-1} and ~40 mV dec^{-1}, respectively [125]. Previous studies have revealed the dependency of the HER mechanism on the catalyst,

electrolyte pH, and H^* coverage on the catalyst [123]. It has also shown that different facets of Pt enable different HER mechanisms [126].

With the growing research attention to finding the best catalyst candidates for HER, it was needed to define a descriptor to evaluate and compare the activity of different materials. Trasatti compared the exchange current density of the HER on various metals with their work function [127]. An ideal HER catalyst should have an intermediate hydrogen bonding energy. In other words, a perfect catalyst for the HER should bind hydrogen strong enough to adsorb protons from the electrolyte (Volmer step). However, if the binding is too strong, it slows down the desorption of H^* necessary to generate H_2, thus limiting the HER kinetics. In light of this ideology and inspired by previous experiments, Nørskov et al. computed the free energy of the formation of the H^* intermediate (ΔG_{H^*}) on several metallic surfaces and obtained a volcano shape plot for ΔG_{H^*} versus the exchange current density, suggesting that Hydrogen Binding Energy (HBE) can be used as the descriptor for the HER activity of electrodes, and the Sabatier principle can apply to the HER [128]. The early studies using HBE theory suffered from the fact that the work function of the metals under the operation conditions was different from their pure form due to the presence of electrolyte and adsorbed species. Recently, Zeradjanin et al. reinvestigated the HER catalysts' work function, including the role of adsorbed water, and reported a more precise volcano plot [129]. This plot was obtained by plotting the exchange current density versus the difference in work functions between hydrogenated and non-hydrogenated metals in the presence of an interfacial water layer. Despite this modification, some recent findings have raised concerns about the reliability of the HBE theory [130]. For instance, the reversibility of the H^+/H_2 couple on the Pt surface,[131] and the fact that all HER and HOR intermediates are identical,[132] suggest that the HBE should control the HER and the HOR in a similar fashion. However, for some materials with relatively good HER activity and a small HBE value, such as MoS_2 [133], it is observed that HOR is catalyzed poorly. Hence, the absence of reversibility on a low-HBE material suggests that the energy and the nature of the intermediates for the HOR and HER reactions are not identical. This may originate from changes of some material properties or the double-layer structure/composition as a function of the applied potential, thus preventing the use of HBE as a sole descriptor of the HER kinetics. While the HBE was initially seen as a good candidate, this theory cannot predict how the electrode-electrolyte interfacial structure impacts the performances of a given surface.

These recent findings have attracted researchers towards investigating the exact mechanisms and key parameters affecting HER activity and have made these topics the edge of the research focus these days.

1.2.2.2 HER in Alkaline Media

Unlike acidic media, the proton concentration is drastically diminished for HER in alkaline electrolytes. As a result, the dissociation of water provides a proton for the Volmer and Heyrovsky steps [134], as shown below:

$$\text{Volmer:} \quad H_2O + e^- + * \rightarrow H^* + OH^- \qquad \text{Equation 1-18}$$

$$\text{Heyrovsky:} \quad H_2O + e^- + H^* \rightarrow H_2 + OH^- \qquad \text{Equation 1-19}$$

The dissociation process limits the HER activity by adding an extra energy barrier for hydrogen adsorption [134]. The Tafel slope measured for Pt electrodes in alkaline solutions is around 120 $mV.dec^{-1}$, indicating that the Volmer or the Heyrovsky step is the rate-determining step [135].

Sheng et al. have investigated the HER activity of several metallic surfaces in 0.1 M KOH using the computed HBE [136]. The results revealed a volcano trend similar to the one found by Nørskov in acidic media [128]. Further investigations showed that, despite the similarity between the two volcano plots, there is a significant difference between the electrochemically calculated HBE values and those measured under the UHV condition. This realization led to the conclusion that the orientation of adsorbed water should be taken into account [137]. Additionally, it was observed that the HER kinetics of Pt(111) under alkaline conditions is considerably improved by the presence of exophilic groups [138], which could be explained as originating from an easier H_2O dissociation. Thus, the HER activity difference between acidic and alkaline electrolytes is due to the cleavage of water O-H bond and the transport of OH^- from the catalyst surface to the bulk of the electrolyte [139], [140]. Inspired by these studies, researchers investigated the effect of cationic species (such as Li^+ and K^+) on the HER activity of different catalysts under alkaline conditions. They showed that the presence of these species facilitates water dissociation by modifying the bond length between the catalyst and oxygen of water, resulting in an improvement in HER activity [141], [142].

In light of these observations, many reports are regularly published to introduce the best HER catalyst. Since regardless of the mechanism, the H* participates in every step of

HER, the Gibbs free energy for hydrogen adsorption (ΔG_{H^*}) is still regarded as the primary descriptor. In addition, some electrochemical parameters such as low over potentials (η), low Tafel slopes, and high exchange current densities are desired in water splitting. Finally, some other concepts are also being used to evaluate the hydrogen evolution catalysts. These include stability, faradaic efficiency (the ratio between the practical and the theoretical amount of produced H_2), and turnover frequency (considered as the number of reagents converted to a targeted product at a single catalytic site per unit of time).

Recently, the research paradigm in HER activity under alkaline conditions has shifted towards studying the role of water orientation and the nature of double-layer on the interactions between electrode and electrolyte [141], [143]. Also, researchers are trying to find convincing explanations for fundamental questions such as; what is the rate-determining step for the HER under alkaline conditions? Which is the proton donor? What is the role of the spectator species? How is the catalyst surface modified during HER?

1.3 Aim of Study

Historically, scientific investigations on electrochemical applications can be divided into two phases. In the first phase, the majority of published articles were focused on finding the best electrode candidates for various electrochemical reactions. The new phase, which has started in the last decade, is focused on the pathways of these reactions and the mechanisms by which different electrode materials contribute to the overall electrochemical process. Despite invaluable findings about these pathways and mechanisms, there are still unanswered or unclearly answered significant questions, especially about the state of the electrode material under the operando conditions.

This study aims to employ the unique features of 2D materials and combine them with various physical and electrochemical characterization techniques to study the alterations in electrode materials during electrochemical reactions. After introducing experimental and characterization techniques used in this study in chapter 2, the ORR activity of nitrogen-doped (N-doped) graphene will be discussed in chapter 3. The role of different N configurations on the overall performance of N-doped graphene will be investigated. Chapter 4 will focus on studying the ORR mechanisms and electrochemical active sites of N-doped graphene using the Spectroelectrochemical Raman (SEC-Raman) technique. In chapter 5, it will be shown how it is possible to tailor the structure of MoS_2 and its

activity towards HER in acidic media by modifying a synthesis parameter and applying post-synthesis plasma treatment. The SEC-Raman will then be used to study the state of MoS_2 under operando conditions. Finally, the stability of different compositions of Ni sulfide and the actual active site for the HER in alkaline media will be discussed in chapter 6.

Chapter 2
Experimental and Characterization Methods

2.1 Synthesis Methods

2.1.1 Chemical Vapor Deposition (CVD)

2.1.1.1 The CVD System

The vapor-based thin film synthesis methods where a substrate is placed in an atmosphere of atoms and/or molecules of the precursors are classified as either physical vapor deposition (PVD) or chemical vapor deposition. Despite PVD, which is driven by physical impacts, chemical reactions between precursors, precursor fragments, and substrate are the primary mechanism behind CVD.

The atmosphere often consists of diluted precursor molecules in a carrier gas that makes up the major gas volume in the process. In the case of growing large areas and high-quality graphene on metal substrates, CVD is a promising technique [144].

The CVD systems used in this project are composed of three primary stages [145]. The first stage is called the "gas delivery system," where the dilute atmosphere containing precursors and carrier gas is provided. The required amount of each gas is precisely controlled by mass flow controllers and regulated in terms of "standard cubic centimeter per minute" (sccm). These three gases are mixed adequately before being fed into the reacting system (quartz tube).

Next is the "reacting system" or "growth chamber," where quartz tube is mainly used due to its high stability at high temperatures. The melting point of the quartz tube is as high as 1670 °C (β tridymite) and 1717 °C (β cristobalite), which makes it a suitable material of choice for sustaining at high temperatures. The quartz tube is mounted onto the CVD furnace, and care is ensured that it is precisely at the center point of the furnace to provide a homogeneously distributed temperature on both sides.

The last stage is the "gas removal system," which involves a vacuum pump connected to one end of the quartz. This pump provides the desired pressure level by sucking out the necessary amount of air or gas from the tube. The optimum pressure is determined based

on the substrate and the characteristics of the required 2D material, such as the number of layers, flake size, and uniformity. A schematic representation of a CVD system is shown in Figure 2-1.

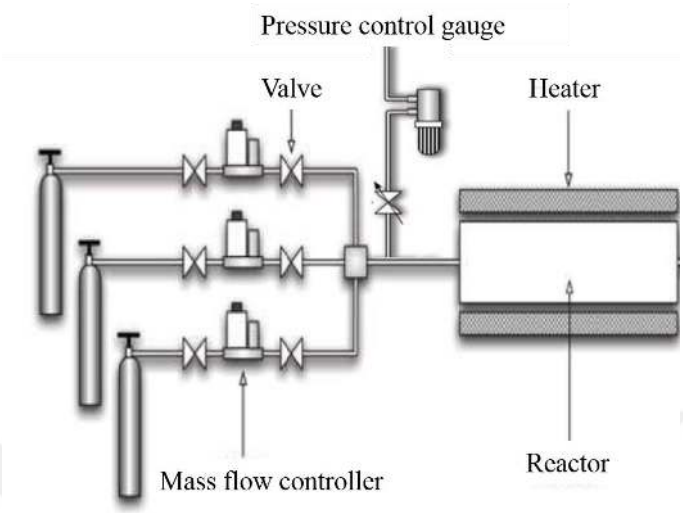

Figure 2-1 Schematic representation of the CVD system

2.1.1.1 Theory of CVD Technique

In order to grow a film by CVD, a series of surface and gas-phase chemical reactions, such as pyrolysis, reduction, oxidation, and co-deposition, happen (Figure 2-2). These reactions are schematically summarized in Figure 2. A boundary layer develops on top of the substrate surface when flowing a gas mixture above it. This layer has a vital role in CVD because the velocity and concentration of species are significantly different from those in the main gas stream. Due to these unique properties, almost all chemistry of importance to the CVD process takes place in this layer and on the substrate surface.

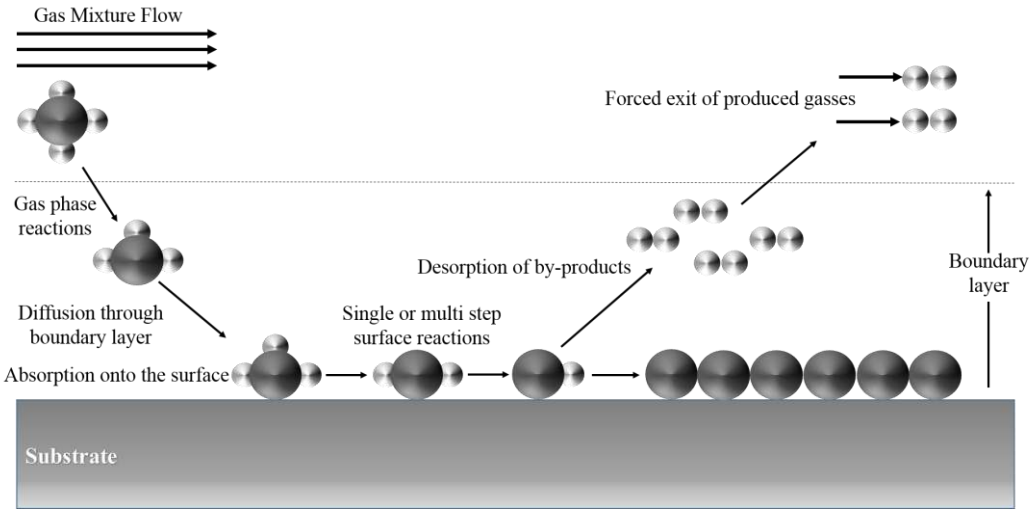

Figure 2-2 The most important chemical reactions involved in the CVD technique

Most of the CVD processes happen at low pressures and high temperatures. There is a significant lifetime for the reactive species formed due to the gas phase chemical reactions under these circumstances. However, in some CVD approaches, this gas-phase chemical reaction can result in particles' formation, interfering with the desired film deposition. In contrast, it is necessary to convert systems with relatively unreactive reactant molecules to reactive species through gas-phase reactions. As a result, the temperature and pressure of the system have to be optimized based on the selected precursors and desired film.

The precursor molecules or the more reactive fragments of the precursor molecules are transported via gas diffusion through the boundary layer to the substrate surface. All types of precursor molecules can be expected to be weakly physisorbed, at least for a short time, on the substrate, followed by desorption. Sufficient chemical complementarity between precursor or reactive fragment and substrate surface results in stronger chemisorption, leading to longer lifetimes of the adsorbate. Adsorbate molecules or elements may be mobile on the surface and may sample a variety of surface sites via diffusion, which may lead to reactions. In the end, the portion of the precursor molecule that does not constitute the target material desorb from the film surface as by-products.

From a kinetics point of view, the whole CVD process can be divided into two main steps, the mass transport step and the surface reactions. The temperature determines the rate-limiting step. At lower temperatures, the deposition rate is generally surface reaction limited. The rate of these reactions increases with the temperature resulting in a mass transport limited deposition at high temperatures [145].

2.1.2 Plasma

A mixture of positively and negatively charged ionized gas particles generated by supplying energy to a neutral gas is called Plasma [146]. Plasmas can be divided into two broad categories: natural and artificial. Interestingly, according to some estimations, most of the material in the visible universe, as much as 99% is in the plasma state. This includes the Sun, most stars, and a significant fraction of the interstellar medium [147].

One of the conventional methods for plasma generation is heating gas to such a high temperature that the random kinetic energy of the molecules exceeds the ionization energy. Since the temperature at which some electrons are ejected from the atoms, forming a mixture of electrons and atoms, is relatively well-defined, plasma is often referred to as the "fourth" state of matter. Other possible methods to generate plasma include exposing an ordinary gas to ultraviolet light or X-rays [147], adiabatic compression of the gas, or shining beams of neutral particles to a gas reservoir [148].

From the technological point of view, it is of crucial importance to generate plasma at low temperatures. Since any volume of a neutral gas always contains a few electrons and ions formed, for example, due to the interaction of cosmic rays or radioactive radiation with the gas, applying an electric field to a neutral gas can generate plasma at low temperatures. Upon application of the electric field, free charge carriers will be accelerated, and new charged particles may be created when these charge carriers collide with atoms and molecules in the gas or with the surfaces of the electrodes. This leads to an avalanche of charged particles that is eventually balanced by charge carrier losses so that a steady-state plasma develops. There should be a balance between ionization and recombination in order to maintain the steady-state plasma. This can be achieved by either making the ionization source stronger or diluting the plasma, which helps to decrease the recombination rate.

According to the definition of the plasma, there should not be any loss mechanism during ionization since all ionization processes produce an equal amount of positive and negative charges. As a result, only minor deviations from local charge neutrality can be found in plasma. Large electric fields will be produced immediately when the charge imbalances develop to restore charge neutrality. As a result, the systems that display large deviations from charge neutrality, such as vacuum tubes and various electronic devices, cannot be classified as plasmas, even though some aspects of their physics are similar.

In the plasma, particles must be in an unbound gaseous state. That to say, the random kinetic energy must be much greater than the average electrostatic energy. As a result, in a plasma, long-range electrical forces are much more important than short-range forces, leading to many complex effects that do not occur in an ordinary gas.

The most fundamental parameters relevant to the description of essentially all plasma phenomena are Number density, Temperature, Debye length, Plasma frequency, Cyclotron frequency, Collision frequency, and Number of electrons per Debye cube.

A detailed explanation of these parameters is out of this thesis's scope and can be found in different reference books.

From the metal nitriding to improve surfaces' hardness, wear, and corrosion resistance to the treatment of organic polymer surfaces to change the wettability and promote adhesion, nitrogen plasma has numerous industrial applications [149]. Furthermore, there are many applications of nitrogen plasmas in thin film deposition [150].

Identifying the constituent particles and estimating the gas temperature are the most critical factors in characterizing any plasma environment. The temperature of a nitrogen plasma can be estimated from the profile shape of the UV-visible emission spectra [151]. In the case of constituent particles, since the dissociation of molecular nitrogen requires considerable energy, at least 10 eV, the first positive system ($N_2(B^3\Pi_g\text{-}A^3\Sigma u^*)$ and the second positive system ($N_2(C^3\Pi_u\text{-}B^3\Sigma_g)$ are the most dominant particles of nitrogen plasma [151]. However, a non-negligible fraction of the high-energy electrons, atomic nitrogen, and N^+ ions exist in the environment of nitrogen plasma as well.

2.2 Physical Characterization Methods

2.2.1 Raman Spectroscopy

When a material is exposed to monochromatic photons, the majority of the photons are elastically scattered (only the direction of light changes with no change in photon energy), known as Rayleigh scattering. However, some of the photons are scattered inelastically through a process known as Raman scattering. Raman spectroscopy is based on identifying wavelength distributions of these scattered photons. Most of the textbooks classify Raman spectroscopy as a vibration spectroscopy method. The initial state of most of the molecules of a sample at room temperature is the ground state. So, the scattered photon will have lower energy (longer wavelength) than the incident photon. This

phenomenon causes a Raman shift which is known as the Stokes shift. On the other hand, a small fraction of the molecules are in vibrationally excited states. Raman scattering from these molecules leaves the molecule in the ground state and the scattered photon appears at higher energy. This process is anti-Stokes-shift, and due to the lower population of excited states, it is always weaker than the Stokes-shifted spectrum, but at room temperature, it is strong enough to be useful for vibrational frequencies less than about 1500 cm^{-1}[152].

Understanding the effect of electromagnetic fields on the matter would help to explain a sample's Raman spectrum precisely. The dipole moment, P, induced in a molecule by an external electric field, E, is proportional to the field

$$P = \alpha E \qquad \text{Equation 2-1}$$

The proportionality constant α is the polarizability of the molecule. When studying the Raman effect, the electrical field is caused by electromagnetic radiation. Indeed, light can be considered as an oscillating electrical field. The α is dependent on the shape and dimensions of the chemical bond. The variation of the polarizability induced by a molecular vibration is the origin of Raman scattering. This variation can be described by the polarizability derivative, dα/dQ, where Q is the normal coordinate of the vibration. As a result, the selection rule for a Raman-active vibration can be shown as

$$\frac{d\alpha}{dQ} \neq 0 \qquad \text{Equation 2-2}$$

In other words, during the considered normal vibration, a change in polarizability should happen.

As a consequence of the harmonic oscillation approximation, the vibrational frequency can be expressed as:

$$\nu_\nu = \frac{1}{2\pi}\sqrt{\frac{\kappa}{\mu}} \qquad \text{Equation 2-3}$$

Where κ is the force constant of the bond and μ is the reduced mass. This equation shows that these two factors determine the Raman band position. Since κ and μ are relatively stable for a specific type of bond or a particular functional group, so-called group frequencies can be determined for a series of functional groups. These characteristic

wavenumbers indicate the region where a specific Raman band can be expected, but don't say whether this band is present or not, as this depends on the selection rules [153].

Both sample-related and experiment-related parameters influence the intensity of the Raman band. These include the radiation intensity, analyzed volume, and instrument-dependent factors. Although there is a linear relationship between the observed Raman band intensity and the number of molecules in the sample, the probability of degeneration (the fact that two different vibrations may correspond to the same energy level) must be considered while performing quantitative analysis on Raman results. Additionally, the light absorption by the analyte molecules or the matrix is probable, directly affecting the recorded band intensity. Finally, time-dependent factors may enhance the intensity of the Raman scattered light. One of the most important time-dependent effects is the resonance-enhanced Raman effect, where the excited state of a vibrating molecule coincides with a stable electronic state [154].

The local molecular neighborhood is the most critical cause of band broadening for most materials. The chemical environment influences the force constant of the chemical bond, which affects the Raman band position. If each of the bonds present in the measured volume of the sample does not have the same chemical environment, there may be a range of slightly different force constants, which consequently causes band broadening. Apart from this theoretical aspect, instrumental parameters impact the Raman bandwidth. The line density of the spectrometer grating, the size of the entrance slit, the pixel size of the CCD detector, and the distance between grating and detector determine the spectral resolution of the spectrometer [152].

Depending on the number of scattering events involved in the Raman process, its order is determined. In the first-order Stokes Raman scattering process, the photon energy excitation creates one phonon in the crystal with a minimal momentum ($Q \approx 0$). The restriction for $Q \approx 0$ is relaxed in the second-, third-, or higher-order Raman processes.

2.2.2 X-ray Photoelectron Spectroscopy (XPS)

The surface is the boundary between a material and the outside world and thus governs the interaction between this material and its surrounding. The surface layer of a sample can be chemically or structurally different from the bulk of that sample. As a result, in order to modify the properties of thin films and the surface layer of bulk materials to improve their performance, it is of great scientific and technological importance to

characterize the composition and speciation of this layer.

Photoelectron spectroscopy is based on the photoelectric effect, in which an electron initially bound to an atom/ion is ejected by a photon in a single-step process. Since photons have zero rest mass and are chargeless energy packages, the interactions between these photons and electrons occur without any energy loss. If the initial energy is sufficient, it will result in the emission of the electron from the atom/ion. The detectors measure the kinetic energy (E_k) of the emitted electron. The fact that this energy is unique for any specific electronic level and is a function of the electron binding energy (E_b) makes photoelectron spectroscopy extremely useful for studying thin films and surfaces [155]. The number of these photoelectrons (and hence the observed peak intensities) depend on the light intensity and the electrons' energy.

Even though almost seven decades have passed since Siegbahn and his coworkers recorded the first XPS spectrum, the importance and popularity of this method in surface characterization has grown enormously in the last decade. To identify a technique as "surface-sensitive," the radiation or particles to be detected should travel no more than a few atomic distances through the solid. According to the diagram shown in Figure 12, the mean free path, λ, of electrons in solids varies by the kinetic energy, but it never exceeds 2 nm for kinetic energies in the range 15 to 1000 eV [156]. The electrons with kinetic energies in the range of 50 to 250 eV, which can travel not far than ~ 0.5 nm inside the samples, provide optimum surface sensitivity since almost half of these photoelectrons come from the outermost layer. For an element located in the top 10 nm of a sample to be identified with XPS, the atomic percentage should be higher than 0.05 % [155].

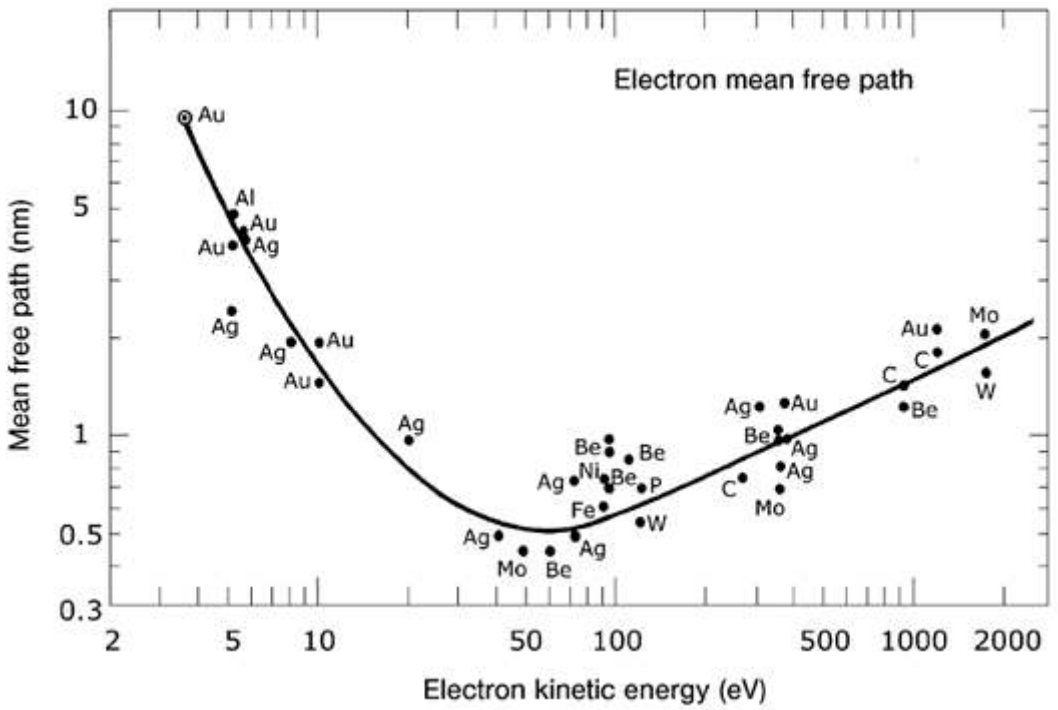

Figure 2-3 The mean free path of an electron depends on its kinetic energy and determines how much surface information it carries. Optimum surface sensitivity is obtained with electrons in the 25 to 200 eV range. (Adapted from [156])

As mentioned above, the kinetic energy of the ejected electron is the quantity that the detector of XPS records. This information is used to obtain the binding energy of the electron. The relation between kinetic and binding energies can be expressed as:

$$E_k = h\nu - E_b - \varphi \qquad \text{Equation 2-4}$$

Where:

E_k is the kinetic energy of the photoelectron;

h is the Planck's constant;

ν is the frequency of the exciting radiation;

E_b is the binding energy of the photoelectron with respect to the Fermi level of the sample;

Φ is the work function difference between the sample and the spectrometer

The most common X-ray sources used in XPS are Mg Kα (hν=1253.6 eV) and Al Kα (hν=1486.3 eV). It is noteworthy that the value obtained from XPS is different from the exact binding energy in the ground state atom; because the obtained values are calculated

while a photoemission induced core hole is generated, and this core hole alters binding energy slightly. This effect is known as the final state effect and can be divided into "core-hole induced polarization" and "core-hole induced rearrangement." An instantaneous polarization occurs as a result of removing a spinning charge (the photoelectron). This core hole-induced polarization engenders both electrostatic and magnetic fields and consequently can affect the recorded binding energy in a number of different ways. The lifetime of core-hole generated during the photoelectron emission process is in the scale of femtoseconds. The dissipation of this core-hole is associated with an energy transfer that yields rearrangement effects. In addition to affecting binding energies calculated by the detectors, the similar timescale of these rearrangements and photoelectron emission gives rise to new rearrangement-specific spectral features like satellite peaks, photoelectron peaks asymmetry, plasmon loss peaks, and Auger electron peaks.

For the elements with three or more electrons, there is always a probability that a two-electron-involved process follows the photoelectron emission. First, an electron in an electronic level with lesser binding energy decays and fills the core-hole generated by photoelectron emission. Then the energy released by this transition is taken up by another electron, which leaves the sample with element-specific kinetic energy. This electron is called the Auger electron, and the probability of its generation is a function of Z. While Auger peaks have valuable information about the surface of the sample, in the analysis of XPS data, it is crucial to distinguish them from the peaks induced by photoelectrons.

Two main factors are determining the sensitivity of XPS, the photoelectron cross-section, and the spectral background level. The former is the yield of electrons produced by the impacting photon energy. The primary source of the spectral background in XPS is the inelastic scattering of electrons. This scattering engenders a non-discrete energy loss to the surrounding electrons and produces a broad background to the lower kinetic energy side of the peak of interest. In addition, the vacuum under which the analysis is carried out can also affect the experiment's sensitivity. The low vacuum level is the sign of the high density of the molecules in the gas phase, which decreases the flight path of the photoelectrons.

The XPS results were deconvoluted using Shirley's background for quantitative analysis of the samples investigated in this study. The area under the peak of desired elements (I_i) was normalized by dividing their values to the associated sensitivity factor (S_i). The

sensitivity factors were provided by the "ThermoFisher co." and were driven by multiplying the photoelectron cross-section and inelastic mean free path of each element with parameters related to the quantitative detection of a signal by the system. The equivalent homogenous atomic fraction of each element (X_i) was then calculated by:

$$X_i = \frac{I_i/S_i}{\sum_j (I_j/S_j)} \qquad \text{Equation 2-5}$$

The atomic composition of the samples investigated in this study was characterized by a Thermo K-alpha X-ray photoelectron spectroscopy system equipped with a monochromatized Al K-alpha X-ray source.

2.2.3 X-ray Absorption/Emission Spectroscopy (XAS/XES)

When X-ray passes through a material, the intensity is attenuated. According to Beer's law, this attenuation can be characterized by the absorption coefficient according to:

$$I_t = I_0 e^{-\mu(E)t} \qquad \text{Equation 2-6}$$

Where I_0 is the incident X-ray intensity, I_t is the transmitted X-ray intensity, t is the sample thickness, and $\mu(E)$ is the absorption coefficient dependent on the photon energy [157]. XAS measures the energy-dependent fine structure of the X-ray absorption coefficient [158]. At the heart of the photon absorption process, there is the transition of a core electron up to some level where a photoelectron can propagate or, at least, occupy a free orbital. This means that the phenomenon is local and centered around an absorbing atom and depends on its close surrounding. Hence, in principle, the corresponding spectroscopy is applicable to any sample, ordered or not ordered, in gas, liquid, or solid phases.

For the X-ray energies lower than the electron's binding energy in the element's orbital, the excitation to the highest unoccupied state or the vacuum does not occur. The lack of effective X-ray and electron interaction leads to the flat region shown in Figure 2-4; however, some unfavored transitions such as 1s to 3d in transition metals will appear as a pre-edge peak [159]. Once the X-ray energies are high enough to excite core electrons to the unoccupied state, X-ray is strongly absorbed, leading to a significant jump in the spectrum called edge. Each edge has a typical energy, mainly depending on the atomic number of the absorbing atom. The study of the spectra recorded in the 50 eV vicinity of the edge is called X-ray Absorption Near Edge Structure (XANES) or NEXAFS (Near Edge X-Ray Absorption Fine Structure). The NEXAFS data contains information about

the symmetry and geometry around the absorbing atom and its electronic and magnetic structures [160]. With the further increase in X-ray energies, the core electrons excited to continuum state form the outgoing and scattering wave interference with neighboring atoms. The constructive or deconstructive interferences of the scattering waves form the wiggles in the Extended X-ray Absorption Fine Structure (EXAFS) region, which reflects local atomic structures such as bond distance and coordination number [161].

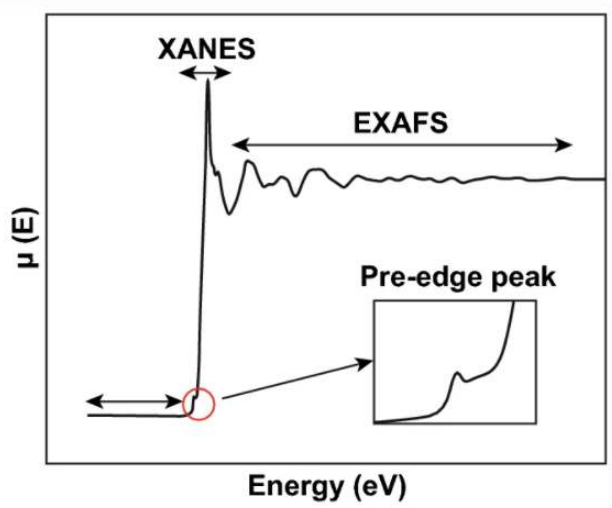

Figure 2-4 Schematic of XAS including the pre-edge, XANES, and EXAFS regions

There are three basic modes for XAS signal collections: transmission, fluorescence, and electron yield modes. The concentrated and homogenous samples are recommended for the transmission mode, where the difference between the intensity of the incident and directly transmitted X-ray is measured [160]. In contrast, fluorescence mode, suitable for the dilute and non-homogenous samples, measures the emitted X-rays from the elements. The intensity of this fluorescence is proportional to the absorption caused by the investigated element but could also be affected by the self-absorption effect [160]. Instead of measuring the emitted fluorescence, we can also measure the emitted photoelectrons. This mode is surface sensitive because of photoelectrons' relatively short mean free path [157], while the two other modes are bulk sensitive.

X-Ray Emission Spectroscopy (XES) is inverse to XAS, i.e., it measures the emission of a photon from the sample due to deexcitation from a conduction band to a valence band. This technique measures valence bands' occupied projected density of states (DOS). Another prominent feature of XES is that in contrast to XAS, it is calculated using the initial state Hamiltonian, i.e., without a core hole [162].

XAS and XES require synchrotron sources that can tune the X-ray energy easily. When magnetic fields force electrons or other charged particles to move at relativistic speeds to follow curved trajectories, they emit electromagnetic radiation in the direction of their motion, known as synchrotron radiation. Such radiation is exceptionally intense and extends over a broad energy range from the infrared through the visible and ultraviolet, into the soft and hard x-ray regions of the electromagnetic spectrum [163]. Recent progress of x-ray undulators at third-generation synchrotron light sources enables delivery of unprecedented high photon flux as well as high flux density. In order to have a more precise investigation on the samples prepared in this project, an XAS device fed by X-ray coming from the synchrotron radiation was also used.

2.2.4 X-ray Diffraction (XRD)

Elastic scattering of X-ray photons by atoms in a crystalline material is X-ray diffraction. The scattered monochromatic rays undergo constructive interference and create the resulting XRD pattern. Diffraction of X-rays by crystal planes allows finding the lattice spacing using Bragg's law [164]:

$$2d \sin\theta = n\lambda \qquad \text{Equation 2-7}$$

Where n is the reflection order, λ is the wavelength of incident X-rays, d is the lattice spacing between planes, and θ is the angle between the incident X-ray and the normal to the reflecting plane. To identify the unknown materials, diffraction patterns recorded with a diffractometer and d values and relative intensities of the diffracted lines are compared with the standard patterns available for different compounds in the Powder Diffraction File (PDF) database.

Crystallite size can be calculated from the Scherrer equation [164]:

$$D = n\lambda\beta \cos\theta \qquad \text{Equation 2-8}$$

Where D is the crystallite size, λ is the X-ray wavelength, β is the peak width at half maximum (FWHM), and θ is the angle between the beam and normal of the reflection plane. Finally, k is constant and is taken as a unity.

The quantitative analysis of XRD results is done by the Reference Intensity Ratio (RIR) method [165]. The RIR method is based upon scaling all diffraction data to the diffraction of standard reference materials. By convention, Corundum is used as the international

reference, and the scale factor is defined by I/I_c, where I is the intensity of an analyte and I_c is the intensity of Corundum. In PDF, I/I_c has been experimentally calculated for more than 170,000 materials. The intensity of reflection i of an α phase is determined by:

$$I_{i\alpha} = \frac{K_{i\alpha} X_\alpha}{\rho_\alpha \mu} \qquad \text{Equation 2-9}$$

Where X_α is the weight fraction of phase α, ρ_α is the density of phase α, μ is the linear attenuation coefficient, and $K_{i\alpha}$ contains structure factor, multiplicity, Lorentz-polarization factor, temperature factor, and scale factor for reflection I of phase α. Based on the fraction of each phase in a multi-phase sample can be determined as follows:

$$\frac{I_\alpha}{\sum_j I_j} = \frac{(I/I_c)_\alpha X_\alpha}{\sum_j (I/I_c)_j X_j} \qquad \text{Equation 2-10}$$

XRD patterns of the samples investigated in this study were collected using Bruker D8 and D2 Advance X-Ray Diffractometer.

2.2.5 Atomic Force Microscopy (AFM)

AFM, first proposed by G. Binnig and C. F. Quate in 1986 [166], is a microscope studying the interaction between a sharp tip, usually made of silicon or silicon nitride and a sample. It is mounted on a cantilever which is the bridge between the tip and the oscillator. During the scanning of the surface of a sample by the movement generated with the piezo oscillator, some interactions (Van der Waals or electrostatic if the tip is coated with cobalt, etc.) will be created. Consequently, the tip will be pulled towards the surface and will be deflected. This deflection causes the laser beam, which hits the backside of the cantilever and in a no-interaction situation, goes directly to the center of a quadrant photodiode, to shift. As a result, it will no longer be hitting the center of the photodiode and different signals will be produced in each of the four parts of the detector. The calibration of this signal variation helps to detect the position of the tip and the amount of deflection, which is a sign of the above-mentioned interaction's strength [167]. The typical length of the cantilever is about 100 µm and the radius of the tip usually is less than 10 nm.

Due to the potential of AFM to study a wide range of surfaces, different modes have been developed to modify the device in a suitable way for these samples and characterize various properties. All these modes can be classified into three main categories, which are shown in Figure 2-5. These categories are contact mode, intermittent contact mode,

and non-contact mode. During contact mode, the tip touches the surface, and their interaction is repulsive. Comprehensive information about the topography of the surface with high resolutions can be obtained using this mode. However, the main drawback of this method is that the number of runs that the tip can perform is limited and after some time it gets blunt. The non-contact mode is an alternative method to overcome the limited durability of the tip in the contact mode. Here the tip approaches the surface but does not touch it, and instead of analyzing the sample by scanning its surface, the change in the frequency of piezo is used to represent surface morphology changes. In the non-contact mode, whenever the tip feels the surface, the cantilever will delay coming back to its initial position due to the interaction of the tip with the surface. The resultant phase shift in the detector is used to generate the final image. The lack of a direct connection between the tip and the sample restrains the information obtained from the measurement.

Another alternative method to the problem of having high lateral forces between the cantilever and surface, while maintaining very high lateral resolution, is to have the tip touch the surface only for a short time. The Intermittent contact mode, also known as tapping mode, starts at the attractive region of the force-distance curve. When the probe approaches the sample, it experiences an attractive force and is pulled toward the surface until contact is made. From that point on, the repulsive interaction forces dominate the response [168]. As a result, the measured quantity would be only an average response of many interactions through the lock-in amplifier. Another drawback of this mode is the complexity of the oscillating system. The forces can vary some order of magnitude while scanning rough surfaces. This results in an amplitude error which can lead to tip damage. A well-tuned feedback loop for the soft part of the sample can cause feedback oscillation for the hard part of the sample, rendering optimizing the parameters for every part of the sample very difficult. To overcome these problems, a modified version of tapping mode has recently been introduced as "PeakForce tapping." This method operates similarly to tapping mode in that it avoids lateral forces by intermittently contacting the sample. However, it is very different from tapping mode because it works in a non-resonant mode. In the PeakForce tapping, an oscillating system combines the benefits of contact and tapping mode imaging: direct force control and avoidance of damaging lateral forces.

Recently new operation modes such as force modulation and lift mode have developed. Also, applying different coatings on the tip enables AFM to study specific types of interactions.

A "Bruker Dimension Icon" AFM system has been used in the investigations of this study. The system was equipped with a "Bruker ScanAssyst-Air" tip made from silicon nitride. The images were obtained by the "ScanAssyst-Air" mode defined to the system, which is a PeakForce tapping mode specialized for the Bruker microscopes.

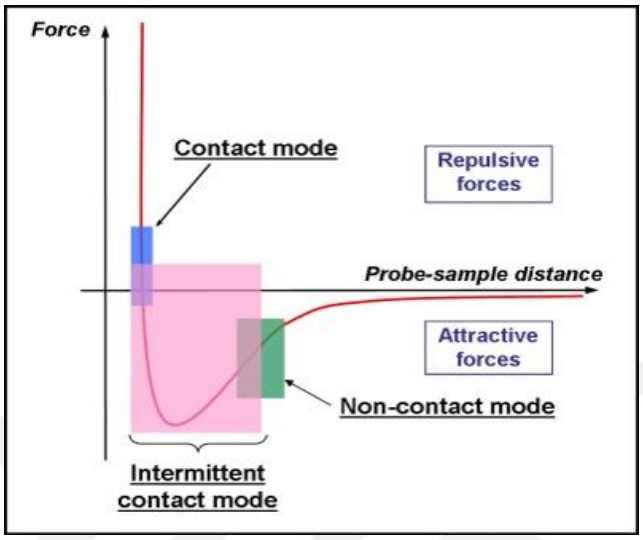

Figure 2-5 Force-distance for a tip reaching to the surface. The three main modes of AFM are shown as contact mode, intermittent contact mode, and non-contact mode.

2.2.6 Scanning Electron Microscopy (SEM)

The modern commercial SEM emerged from extensive development in the 1950s and 1960s by Prof. Sir Charles Oatley at the University of Cambridge [169]. The SEM runs via a finely focused beam of energetic electrons emitted from an electron source. The energy of the electrons in this beam, E_0, typically varies from E_0= 0.1 to 30 keV. After emission from the source and acceleration to high energy, the electron beam is modified by apertures, magnetic and/or electrostatic lenses, and electromagnetic coils, which act to reduce the beam diameter successively and to scan the focused beam in a raster (x-y) pattern to place it sequentially at a series of closely spaced but discrete locations on the specimen. The interaction of the electron beam with the sample produces two outgoing electron products; backscattered electrons (BSEs) and secondary electrons (SEs). BSEs are beam electrons emerging from the specimen with an insignificant energy loss after experiencing scattering and deflection by the electric fields of the atoms in the sample. The SEs are electrons that escape the specimen surface after beam electrons have ejected them from atoms in the sample. Even though the beam electrons are typically at high energy, these secondary electrons experience low kinetic energy transfer and subsequently escape the specimen surface with very low kinetic energies, in the range 0–

50 eV, with the majority below 5 eV in energy. The typical electron detectors used in SEM are Everhart-Thornley's "secondary electron" detector (which is sensitive to both SEs and BSEs) and a "dedicated backscattered electron detector" that is insensitive to SEs. The electron-optical column and the specimen chamber of SEM systems conventionally operate under high vacuum conditions ($<10^{-4}$ Pa) to minimize the unwanted scattering that beam electrons, as well as the BSEs and SEs, would suffer by encountering atoms and molecules of atmospheric gasses. Insulating specimens that would develop surface electrical charge because of the impact of the beam electrons must be coated with a conductive material to provide an electrical discharge path.

Field emission electron microscopy (FESEM) is a method for obtaining topographical and elemental information from the samples at magnifications of 10x to 300000x. In contrast to SEM, FESEM uses an electron beam produced by a field emission source, providing images with better clarity and less distortion with 3 to 6 times better resolution [170].

The Zeiss Evo LS15 system is employed for obtaining the SEM images in this study. The FESEM images are taken via the Zeiss Ultra Plus instrument.

2.3 Electrochemical Characterization Methods

2.3.1 Linear Sweep Voltammetry (LSV)

Any method that measures current-potential behavior is called voltammetry. Linear sweep voltammetry (LSV) is a basic voltametric method that measures the current response at the working electrode to the linear sweep of potential in a fixed range between the working electrode and a reference electrode (Ag/AgCl). Oxidation or reduction of the species can be detected as a peak in current at the oxidation or reduction potential. Figure 2-2 shows the potential sweep (E-t) and resulting LSV (i-E) diagram. In addition to the applied potential, the main parameter affecting the current is the scan rate, defined as the rate of the change in potential over time. There is a linear relationship between the scan rate and obtained current. Since there is no contribution of convective mass transfer to the rate of reaction in LSV measurement, the effect of the electrical double layer can be minimized by modifying the scan rate.

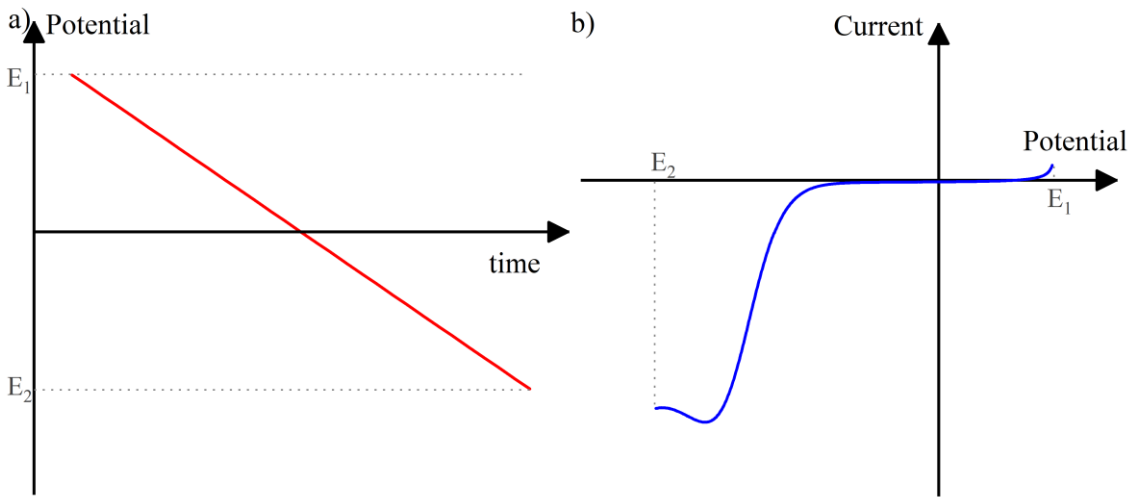

Figure 2-6 a) Linear potential sweep, and b) current-potential curve resulting from linear potential sweep

2.3.2 Cyclic Voltammetry (CV)

Cyclic voltammetry (CV) is an electrochemical technique that ramps the working electrode's potential linearly in cyclical phases versus time and measures the produced current at the working electrode (Figure 2-7a). The potential is measured between the working electrode and the reference electrode, while the current is measured between the working electrode and the counter electrode. As shown in Figure 2-7b, a typical CV plot is drawn by plotting the working electrode's current versus potential. The number of repeating cycles can be increased as many times as required for the analysis. CV technique can be used to study the redox processes and the stability of the electrodes or catalysts and the redox changes in the electrode or electrolyte, determine the presence of intermediates in the reactions, reversibility of the reactions, and kinetics of electron transfer [171].

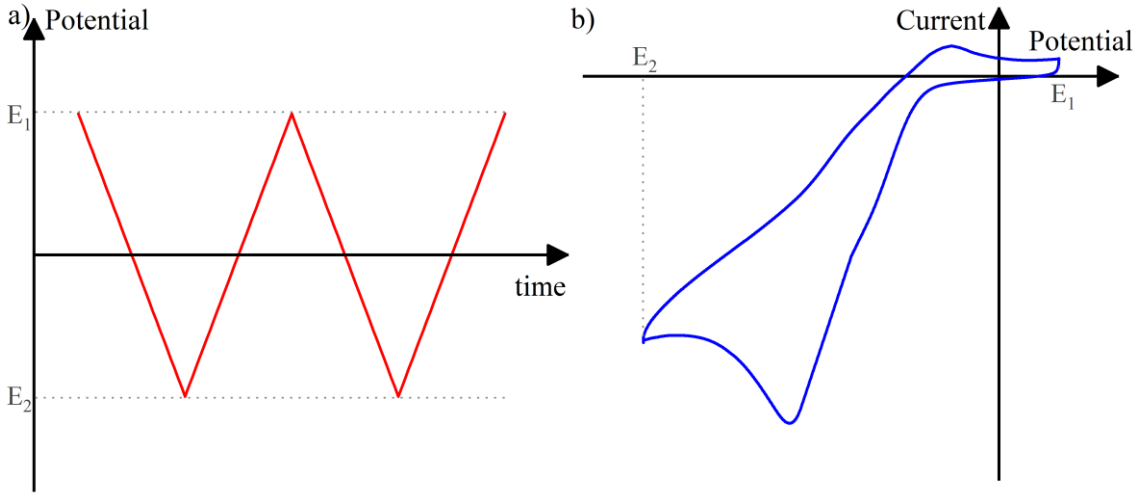

Figure 2-7 a) Potential profile as a function of time, and b) current profile as a function of potential in CV

It is possible to determine the number of electrons transferred during the electrochemical reactions by obtaining CV at different scan rates. The Randles-Sevcik equation [171] (Equation 2-11) shows the relation between the maximum current obtained and the scan rate as:

$$i_p = (2.69 \times 10^5) n^{3/2} A D^{1/2} v^{1/2} C \qquad \text{Equation 2-11}$$

Where i_p (A) is the current maximum, n is the number of electrons transferred in the redox event, A (cm^2) is the area of the electrode, D (cm^2.s) is the diffusion coefficient, ν (V.s) is the scan rate, and C ($mol.cm^{-3}$) is the concentration.

2.3.3 Rotating Disk Electrode Method (RDE)

Rotating disc electrode (RDE) is a hydrodynamic method to measure the current-potential diagram involving forced convection in addition to diffusion and migration to the mass transport where convection term dominates the others. The technique is quite helpful since it eliminates the electrical double layer, which limits the reactions. Also, the reaction rate becomes faster since the convective mass transfer is more efficient than diffusive mass transfer. The set-up contains a disc electrode attached to a rod covered with insulating material such as Teflon. The rod directly connects to the rotor, which controls the angular velocity.

The rotation of the disc generates a rotation in the electrolyte layer near the electrode's surface due to the shear stress. Therefore, as a result of this motion, the hydrodynamic layer, which is a stagnant layer, forms. Convection is the dominant mass transfer term from the bulk until the hydrodynamic layer. After reaching the hydrodynamic layer, as getting close to the electrode surface, the diffusive mass transfer term becomes dominant. The thin layer inside the immobile hydrodynamic layer and near the electrode surface where no convection exists, and mass transfer occurs only via diffusion is called the diffusion layer. The thickness of this layer depends on the rotation speed and the kinematic viscosity of the fluid [171].

2.3.4 Chronoamperometry (CA)

Chronoamperometry is a technique for measuring the current response of the working electrode by applying a stepped potential as a function of time. This technique generates a high charging current with exponential decay as a function of time. Due to the longer time intervals over which the current is integrated, a better signal-to-noise ratio is

obtained in CA than other amperometry techniques [171]. Figure 2-8 shows the step potential versus time and the resulting current versus time in chronoamperometry.

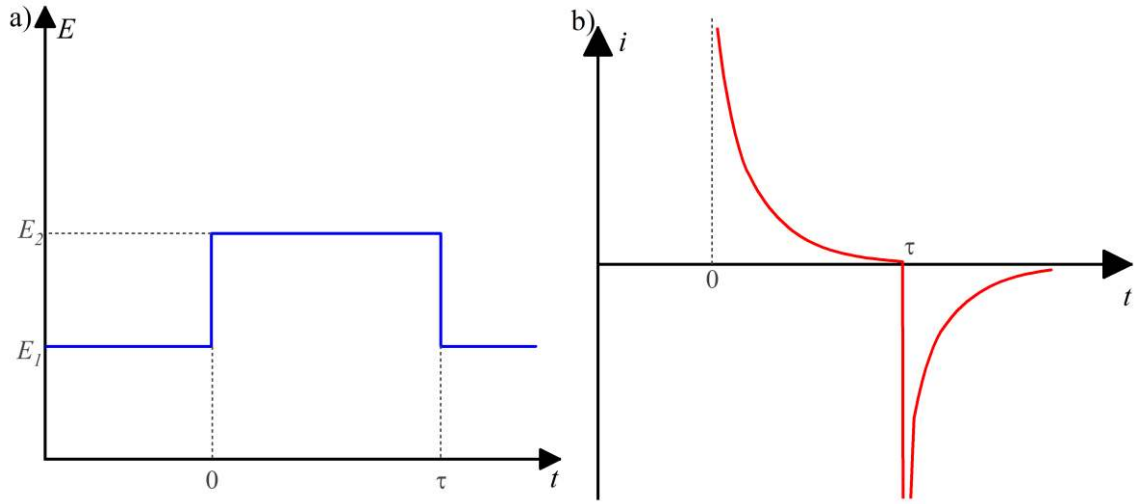

Figure 2-8 a) The potential profile as a function of time, and b) current response as a function of time during CA

2.3.5 Electrochemical Analysis

2.3.5.1 Koutkey-Levich Equation

RDE system is based on the simultaneous calculations of convective and diffusive equations. Therefore, the first critical equation derived from the current as a surface flux is the Levich equation given as:

$$i_{l,c} = 0.62nFAD_O^{2/3}\omega^{1/2}\nu^{-1/6}C_O \qquad \text{Equation 2-12}$$

Here $i_{l,c}$ is the limiting cathodic current (A), n is the number of electrons transferred, F is the faraday's constant (96485 C.mol^{-1}), A is the electrode area (cm^2), D_O is the diffusion coefficient (cm^2.s^{-1}), ω is the angular rotation rate of the electrode (rad.s^{-1}), ν is the kinematic viscosity (cm^2.s^{-1}), and C_O is the analyte concentration (mol.cm^{-3}). Equation 2-12 presents a linear relationship between the limiting current and the square root of rotational speed. The number of electrons transferred during the redox reaction can be calculated using this linear relationship. In order to do this calculation in the present study, a rearranged version of the Levich equation is used:

$$B = 0.62nFD_O^{2/3}\nu^{-1/6}C_O \qquad \text{Equation 2-13}$$

Where B is the Levich constant and is equal to the reciprocal of the slope of the j^{-1} vs. ω$^{-1/2}$ plot when j is in the unit of cm^2.A^{-1} and ω is in the unit of rad.s^{-1} [172].

The Levich equation brings a bias with a deviation near kinetic limitation conditions (Figure 2-9). Therefore, after rearranging the Levich equation by including the kinetics effect without the mass transfer effects, the Koutecky-Levich equation is obtained:

$$\frac{1}{i} = \frac{1}{i_K} + \frac{1}{i_{l,c}} = \frac{1}{i_K} + \frac{1}{0.62nFAD_0^{2/3}\omega^{1/2}\nu^{-1/6}C_0} \qquad \text{Equation 2-14}$$

Here, i_K represents the current in the absence of any mass-transfer effects, that is, the current that would flow under the kinetic limitation if the mass transfer were efficient enough to keep the concentration at the electrode surface equal to the bulk value, regardless of the electrode reaction.

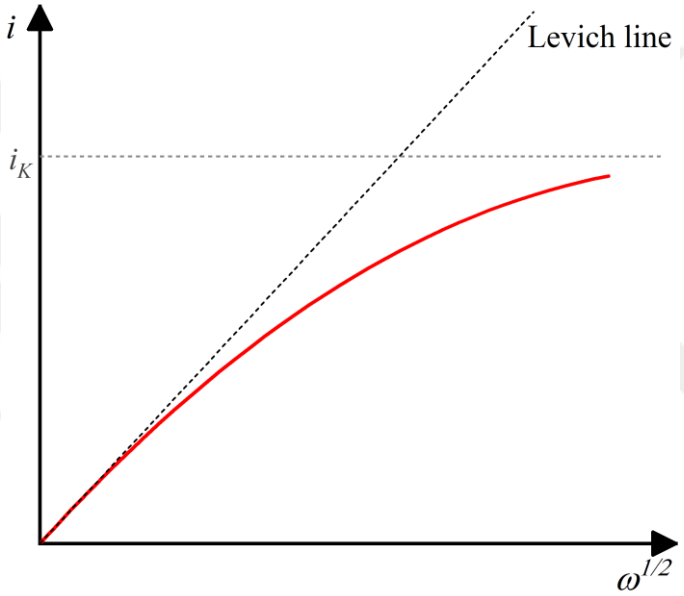

Figure 2-9 The variation of current versus square root of rotation speed at an RDE for a reaction with slow kinetics

2.3.5.2 Electrochemical Active Surface Area (ECSA)

The determination of electrochemically active surface area is a critical factor in investigating the electrochemical activity of electrodes. Thus, it should be specified since the electrode area doesn't show the actual active area where reactions take place.

One common approach to determining the ECSA is the double layer capacitance (C_{DL}) electrochemical measurement. To measure double-layer charging via CV, a potential range in which no apparent Faradaic processes occur must be determined from static CV. All measured current in this non-Faradaic potential region is assumed to be due to double-layer charging [173]. The double-layer charging current is equal to the product of the scan rate, ν, and the C_{DL}:

$$i_c = \nu C_{DL} \quad \text{Equation 2-15}$$

Thus, a plot of i_c as a function of ν yields a straight line with a slope equal to C_{DL}.

After recording CVs in the non-faradaic region as a function of various scan rates, the C_{DL} can be assessed from the linear regression slope between the current density differences $(\Delta j/2 = (j_a - j_c)/2)$ in the middle of the potential window of CV curves. This information is used to determine the ECSA by the following equation:

$$ECSA = \frac{C_{DL}}{C_s} \quad \text{Equation 2-16}$$

Where C_s is the specific capacitance of the sample or the capacitance of an atomically smooth planar surface of the material per unit area under identical electrolyte conditions. While Barton and Infield [174] have introduced a procedure for the sample preparation and calculation of a standardized value for the C_s in alkaline and acidic solution, it is not practical to prepare a standard sample for each electrode. As a result, most of the researchers use previously reported standard values for the C_s. However, it has been shown that minor variations in electrode material and experimental conditions would result in the C_s alterations up to 100% [173], [175], [176]. Consequently, comparable ECSA values could only be reached if potential and pH values are the same for the measured capacitance and the C_s. Due to these difficulties, in the present study, instead of calculating the absolute ECSA values, the obtained C_{DL} numbers for different samples were used to qualitatively compare the ECSA of different samples.

2.3.5.3 Tafel Analysis

According to the mathematical relationship between current and potential in electrochemical measurement, two factors limit the recorded current values. These factors can be classified as kinetic terms and mass transfer terms. Mass transport is the material transferred between the bulk and the electrode surface. Mass transport in the electrochemical cell occurs in three different ways such as diffusion, migration and convection. At small overpotentials, charge transfer kinetics dominate the mass transport while mass transport limits the reaction at large overpotentials. At the low potential region where there is no mass transport limitation, and also the back reaction contribution in current is less than 1%, there is a logarithmic relation between the overpotential and the current, known as the Tafel equation:

$$\eta = a + b \log i$$ Equation 2-17

Where $a = \frac{2.3RT}{\alpha F} \log i_0$, $b = \frac{-2.3RT}{\alpha F}$, η is the overpotential, α is the transfer coefficient, i_0 is the exchange current, F is the Faraday's constant, T is the temperature, and R is the gas constant. In order words, the Tafel equation provides electrochemical kinetic inferences about the reaction rate and overpotential.

A plot of $\log i$ vs. η, known as a Tafel plot (shown in Figure 2-10), is a valuable device for evaluating kinetic parameters. In general, there is an anodic branch and a cathodic branch with different slopes. As shown in Figure 3.4.4, both linear segments extrapolate to an intercept of $\log i_0$. The plots deviate sharply from linear behavior as η approaches zero because the back reactions can no longer be negligible. The transfer coefficient, α, and the exchange current, i_0, are readily accessible from this presentation.

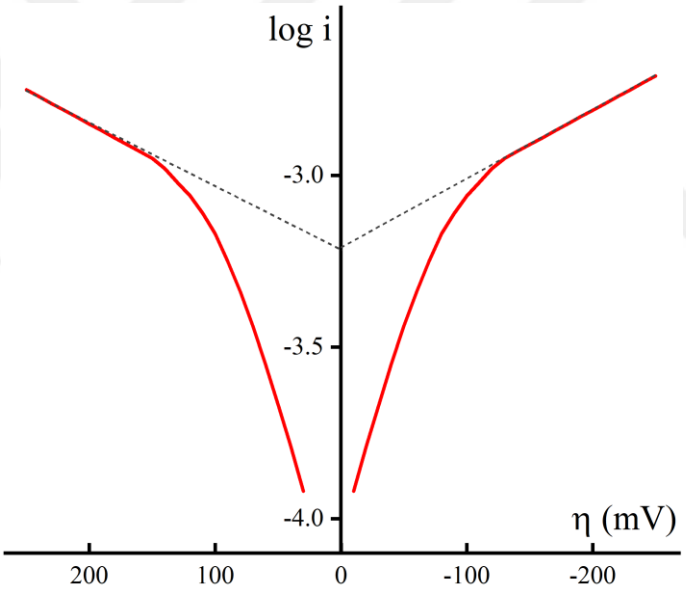

Figure 2-10 Tafel plot for anodic and cathodic branches of the current-overpotential curve

2.4 Spectroelectrochemistry (SEC)

2.4.1 Introduction to Spectroelectrochemistry

Electrochemistry is an influential area of great interest and practicability for diverse related research on chemistry, physics, energy conversion and storage, and biology with applications in fuel cells, corrosion science, self-powered devices, self-assembled coatings [177]. Various spectroscopic techniques have played a key role in expanding the understanding of different research areas for the past decades and are continually

developing and improving. The integration of electrochemistry, supplying the kinetic and thermodynamic processes, and spectroscopy, supplying the molecular vibrational process, results in a new technique, spectroelectrochemistry (SEC), which is generally defined as the application of spectroscopic methods to assay the changes initiated by an electrochemical system in an electrochemical cell [177]–[185]. By combining electrochemistry with a spectroscopic technique, more qualitative and quantitative information about the processes occurring at the electrodes can be obtained.

Since the very first SEC work by Kuwana et al. [186], it has developed into an active interdisciplinary field. Some of the examples of recently developing SEC techniques are infrared SEC (IR-SEC), ultraviolet-visible SEC (UV-Vis-SEC), Raman SEC (Raman-SEC), X-ray absorption SEC (XAS-SEC), and nuclear magnetic resonance SEC (NMR-SEC).

2.4.2 Raman-SEC

In Raman-SEC, a Raman instrument is coupled to an electrochemical cell. Since Raman is a scattering technique, it is not limited to transparent electrodes, as with transmission IR-SEC. Measurements usually take place at the electrode surface, so the laser is most often used in a configuration where it is focused on the electrode. The optical window of the cell can be made out of standard materials since a visible light source can be used. The thin-layer configuration is unnecessary, as water does not have strong absorptions in typical wavelengths used for Raman spectroscopy. The straightforward design of SEC-Raman has made it possible to use this technique in research on various materials from carbon-based materials such as nanotubes [187], and graphene [188], [189] to conductive polymers [190], organic molecules [191], proteins [192] and metal electrodes [193].

Chapter 3:
Graphene: Electrochemical Activity Enhancement

3.1. Introduction

3.1.1. Graphene and N-doped Graphene

Graphene is the simplest example of the two-dimensional sheet of sp^2-hybridized atoms. It can be considered as the building block for the other carbon-based nanostructures. The stacked layers of graphene result 3D structure of graphite, the rolled form of single and multi-layered graphene is known as 1D single wall, and multi wall nanotubes, and wrapping graphene produces a 0D structure known as fullerenes. While historically, graphene is known as the single layer of carbon atoms, different types of it can be defined based on the number of layers; single-layer graphene (SLG), bilayer graphene (BLG), and multilayer graphene (MLG) (3 to 10 layers of two-dimensional carbon sheets) [3]. A unit cell of SLG is composed of two carbon atoms, each forming a triangular in-plane network (Figure 3-1a). The 0.142 nm carbon-carbon bond length results in a 0.246 nm lattice constant for this structure. MLG can be formed by stacking SLG layers in the out-of-plane direction with an interlayer distance of 0.334 nm. There are two different possible layer sequences for the formation of BLG; hexagonal or AA stacking and Bernal or AB stacking. While AA stacking is referred to the placement of adjacent graphene layers on top of each other with the exact same position of atoms along the out-of-plane direction, in the more common and stable AB stacking, there is a 60º rotation between the layers (Figure 3-1b). As a result of this rotation, the vacant centers of the hexagons on one layer are occupied by the carbon atoms at hexagonal corner sites on the adjacent layers from the top view [194].

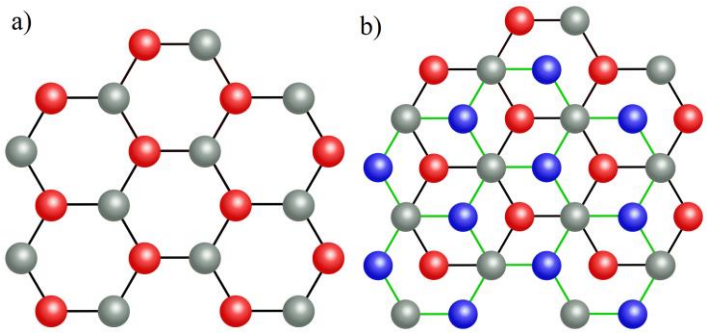

Figure 3-1 Schematic representation of a) SLG and b) AB stacked BLG

Since the first report by Geim and co-workers in 2004 [2], where they synthesized graphene by micro-mechanical cleavage of graphite, the unique properties of this 2D structure have fascinated the scientific community and has made it one of the major research topics in the last two decades. Due to the sp^2 hybridization, there are three in-plane σ bonds and one π orbital perpendicular to the graphene plane for each carbon atom. While the strong σ bond works as the rigid backbone of the hexagonal structure and is the origin of the extraordinary mechanical properties such as high Young's modulus (~1.1 TPa) and fracture strength (125 GPa), the out-of-plane π bonds control the interaction between different graphene layers [5] and are responsible for its remarkable electronic properties, including high carrier mobilities at room temperature (>200,000 $cm^2.V^{-1}.s^{-1}$) and robust ambipolar electric field effect [195], [196]. The exceptionally high thermal conductivity (3000-5000 $W.m^{-1}.K^{-1}$), high optical transmittance (97.7%), high surface area (2630 $m^2.g^{-1}$) [197], [198], tunable bandgap, and having quantum Hall effect at room temperature [6], create opportunities to use graphene in various types of applications. The anisotropy of graphene properties is another unique aspect arising from the difference between in-plane and out-of-plane bonds nature. This exceptional property leads to out-of-plane electrical and thermal conductivities 103 times lower than those of their in-plane analogs [1].

All these critical features and the potential of graphene in making dramatic changes in daily human life attracted the attention of many research groups, and hence scalable synthesis methods have been developed to achieve higher yield and larger sizes in the production of graphene. These synthesis methods can be divided into two main groups, including "top-down" and "bottom-up" routes [199]. The most representative "top-down" method to synthesize graphene is Hummer's method, which is based on oxidizing/exfoliating graphite flakes using H_2SO_4 and $KMnO_4$ and reducing the exfoliated graphite oxide into reduced graphene oxide (rGO) sheets [200]. On the other

hand, the CVD method can be mentioned as the representative "bottom-up" route for graphene synthesis, where in general, hydrocarbons are passed over a catalyst substrate at high temperatures [19].

Despite the distinctive intrinsic properties of graphene, the low chemical reactivity of pristine graphene, as well as tunability of its properties, has made its modification an appealing research topic during the last decade. Heteroatom functionalization is one of the most effective methods in tuning graphene's chemical and physical properties. This allows graphene to be used in various applications [201]. The doping effects of H, B, N, O, S, P, and F in graphene's electronic, magnetic and geometric properties have widely been investigated [202]–[204]. The doping creates sites with asymmetric spin density and unique atomic charge density [205], [206], makes graphene an excellent material for applications in the THz region [207] and in chemical sensing [208]. A particular emphasis has been put on N doping due to its inherent electrochemical activity [209]–[211]. N-doped graphene is considered to be a very active metal-free material that could replace platinum in hydrogen fuel cell applications [212]. Theoretical and experimental studies have shown that doping can tune the electrochemical activity of graphene via tailoring the HOMO-LUMO gap [205]. In this aspect, different C-N bonding configurations, as well as the distribution of N dopants in the graphene network, are shown as crucial factors in applications of N-doped graphene as a fuel cell cathode material for oxygen reduction reaction (ORR). The main N configurations in N-doped graphene are pyridinic/pyridinium-like (N_{pydn}), nitrilic-like (N_{nitr}), pyrrolic (N_{pyro}), and graphitic (N_{grap}) (see Figure 3-2) [213].

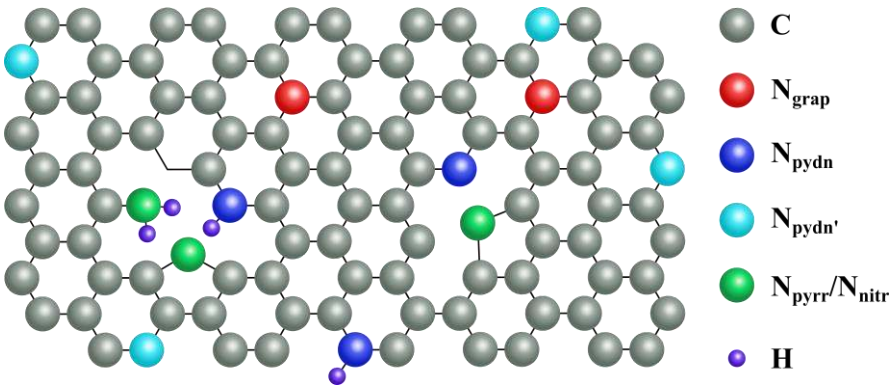

Figure 3-2 Schematic representation of different configurations for N-doped graphene

3.1.2. ORR Activity of N-doped Graphene

The history of designing noble metal-free electrocatalysts for oxygen reduction reaction (ORR) goes back to 1964 [214]; there has however been an ongoing debate on the best electrocatalyst candidates for this reaction to date. Pt nanoparticles supported on high surface area carbon composites have long been ideal for catalyzing the sluggish ORR kinetics at the cathodes of fuel cells, their vulnerability to CO poisoning [215] and scarcity of Pt hinders widespread use and commercialization. Alternatives are not limited to noble metal-free electrocatalysts, a wide range of materials including transition metal chalcogenides [216], N-doped carbon nanomaterials [107], [217], and N-containing polymer/metal chelates [218] have been investigated for the ORR. Among different N-doped carbon nanomaterials such as nanotubes [107], nanofibers [219], spheres [220], etc., graphene has attracted much more attention due to its unique two-dimensional (2D) structure, which facilitates electron transfer and hence increases its activity compared to other carbon-based nanomaterials.

It has been almost a decade since Qu et al. demonstrated enhanced electrochemical activity of N-doped graphene towards the ORR for the first time [210]. Since then, the detailed mechanisms of electrochemical conversion on N-doped graphene have been subjected to intense investigation. Controversies exist about the roles of different N species in electrochemical conversion have not been understood well. It has been shown by several groups that N_{grap} atoms generate the most active configurations for the ORR [221], [222]. In addition to local N configurations, their positions on graphene lattice have an impact on the activity. Ouyang et al. [223] have classified N_{grap} into two groups; atoms inside the graphene sheets and the atoms near the edges. They showed experimentally that N_{grap} in the edges plays a more active role in the ORR. Theoretical investigations have provided further support; it has been calculated that N_{grap} in the edges exhibits the lowest barrier for the first electron transfer and highest selectivity towards the four-electron transfer pathway [224]–[226]. The N_{grap} atoms, which give graphene n-type character, tend to reduce the electron density on the adjacent C nuclei due to their higher electronegativity. This local modification in electron density helps electrons transfer from C to N atoms, followed by a back donation from N to adjacent C 2pz orbitals. The donation and back donation processes facilitate O2 coordination on the adjacent C atoms and help to form a strong chemical bonding between O and C [223].

N_{pydn}, on the other hand, has been shown to enhance the ORR activity of N-doped graphene since p-type donor nature provides graphene matrix a superior electron donor property [227]–[229]. The most active configuration of N in graphene structure has been proposed to be N_{pydn} [210], [223], [227], [230]–[233]. Xing et al. [234] have investigated the active site for ORR in three-layer thick N-doped graphene by correlating the amount of adsorbed OH on the electrodes after ORR with their ORR performance. They suggest that N_{pydn} on the edges is more electrocatalytically active than the same N atoms in the center of the graphene sheet.

Lai et al. [209] and Zhang et al. [235] have shown that both N_{pydn} and N_{grap} configurations help to improve the catalytic activity of N-doped graphene but with different roles. While N_{grap} species' presence is crucial to increasing the limiting current density, N_{pydn} helps the process by converting the ORR reaction mechanism from the two-electron-transfer pathway to four. The impact of the total amount of N in the graphene network is another controversial subject. The increased amount of N exhibiting minor effect in ORR kinetics has been justified by density functional theory (DFT) calculations since structural defects, such as vacancies and Stone-Wales defects, form upon N-doping [236]. Defects play a role in the structural stability; the N_{pydn} becomes energetically more favorable than N_{grap} in the presence of vacancies [237]. However, the formation energy gradually drops with the increased amount on N_{grap} and N_{pydn}.

One of the main reasons for these conflicting results is that N-doped carbon materials are prepared by following various synthesis methodologies, most of which yield N in mixed configurations and different coverages. Using a model graphitic surface, it has been possible to synthesize N-doped graphene with unique N_{grap} and N_{pydn} configurations and Lewis basicity introduced by N_{pydn} has been attributed to the superior ORR activities [238]. It has been shown that mild post-heat treatment can alter the N coordination in graphene without changing the total amount of N atoms [19]. It has also been found that it is possible to distinguish N_{pydn} at the edges from the same N species in the center of graphene sheets by combining high-resolution XPS and Raman spectroscopy. In ORR, the rate-determining step is the first electron transfer to the adsorbed O_2 to form O_2^- [239]. Hence, the position of the Fermi level with respect to the electrochemical reduction potential of O_2 is critical for overpotential required [240]. Consequently, the N configuration and O_2 interaction/activity relation can be better established after revealing the electronic structures of the N-doped graphene in an atom-specific manner. X-ray

spectroscopy (absorption, emission) provides such information [241], [241], dipole transitions between the atomic (C, N) states enable us to identify the occupied and unoccupied energy densities localized on specific atoms. By using X-ray emission spectroscopy (XES) and X-ray absorption spectroscopy (XAS) at both C and N K-edges, it is possible to determine the changes in the level of doping of graphene upon chemical functionalization [242], [243].

3.1.3. Aims of Study

Herein, we report that the ORR activity of N-doped graphene grown by the chemical vapor deposition (CVD) method is maximized by increasing N_{pydn} at the edges. XES and XAS investigations and density functional theory (DFT) calculations reveal that N_{pydn} primarily gives rise to increased density of states (DOS) near the Fermi level due to interlayer bond formation and turns graphene n-type. Electrochemical characterizations justify the findings of X-ray spectroscopy.

3.2. Experimental

3.2.1. Synthesis and Transfer of Graphene

The synthesis procedure was performed in a NANOVAK Plasma Enhanced Chemical Vapor Deposition (PECVD) system. A 25μm thick copper foil (Sigma-Aldrich, 99.8% purity) was used as the substrate. This foil was placed inside the PECVD chamber with the support of a quartz sample holder. After dropping the total pressure of the system to 0.375 mTorr, the temperature was raised with a heating rate of 5 ºC/min up to 950 ºC in the presence of Ar and hydrogen (both set to 100 sccm). The substrate was then kept at this temperature and atmosphere for 180 minutes to make the copper surface smooth and clean (we call this step "hydrogen treatment"). Following the hydrogen treatment step, the flow rate of H_2 was dropped to 50 sccm and the graphene growth process was started by introducing 50 sccm of methane. The duration of the growth step was set to be 5 min. At the end of this duration, the methane flow was stopped, and the system was let to cool down to room temperature in the presence of Ar and hydrogen. The presence of relatively large amounts of argon gas, compared to hydrogen and methane, helps to displace any oxygen or water vapor present in the chamber, allowing for a cleaner growth process.

The effects of different parameters such as heating rate of copper substrate, time and temperature of hydrogen treatment step, duration and temperature of growth step, and

also flow rate of each three used gases (argon, hydrogen, and methane) during different steps as well as total pressure of the system have investigated in our previous studies.

Transferring graphene onto substrates such as SiO_2/Si and Fluorine-doped Tin oxide glass (FTO) helps to improve its characterization and increases the processability of graphene in wafer-scale devices. Due to the wet chemical nature of most transfer methods proposed so far, the formation of some defects and damages in graphene structure during the transfer process is inevitable. As a result, the most suitable transfer method is the one that lowers the amount of these damages and defects.

The transfer process employed in this project was started with coating the samples with poly(methyl methacrylate) (PMMA) 2% by spin coating PMMA onto Cu/graphene films for 30 seconds with 4000 rpm. The wafers were then dried at room temperature for four h, followed by floating them on a 0.12 M Ammonium persulfate solution for 48 h to etch the copper substrate. The concentration of the etchant solution and the duration of keeping the films floating on this solution are critical factors in obtaining Cu-free graphene with low defect density. At the end of the etching process, the films were washed and floated on DI water for 15-20 minutes. They were then transferred onto arbitrary substrates, which were either SiO_2/Si or FTO glass. Prior to this transfer, the SiO_2/Si wafers were cleaned by the modified RCA (Radio Cooperation of America) method [244], and the FTO glass substrates were washed three times with ethanol (99.0%), DI water, and acetone (96.5%), respectively. The transferred films were kept at 40 ºC with a 45° angle for five h to evacuate possible water molecules between graphene and the substrates. Finally, PMMA was cleaned from the top of graphene by soaking the films in absolute acetone.

3.2.2. Doping Graphene with Nitrogen

The PECVD system was used to prepare N-doped graphene. The N plasma was generated by flowing 1.9 sccm of N_2 gas while the chamber pressure was set to ~ 9.0 mTorr. The configuration and concentration of N species were manipulated by adjusting the duration of plasma exposure and plasma power (W). After exposing the samples to N plasma at room temperature, the system was switched off, and the flow rate of N_2 was increased to 50 sccm. The samples were kept under this atmosphere for 30 minutes to ensure that their surface has stabilized.

3.2.3. Physical Characterizations

XAS and XES measurements at N and C K-edges were performed at beamline 10−1 at Stanford Synchrotron Radiation Light source (SSRL) of SLAC National Accelerator Laboratory. A novel energy dispersive X-ray spectrometer based on transition-edge sensor (TES) technology was utilized [245], [246]. RIXS (resonant inelastic X-ray scattering) maps, a special case of XES, were collected over the entire N K-edge. XPS measurements were performed in a laboratory system (Thermo K-alpha) equipped with a monochromatized Al K-alpha X-ray source. The XPS binding energies were referenced to the Fermi edges of the copper substrates. The concentration of N in graphene structure was determined by the quantitative analysis of N 1s and C 1s XPS spectra. Sensitivity factors (1 for C 1s and 1.676 for N 1s) that took photoionization cross-section and kinetic energy dependent inelastic mean free path of electrons into account were used in the quantification. Raman spectroscopy (Renishaw INVIA) investigations were performed by setting the laser excitation wavelength at 532 nm and laser power to 2.83 mW.

3.2.4. Electrochemical Characterizations

All electrochemical measurements (except electrochemical impedance spectroscopy (EIS)) were carried out using a Pine Research WaveDriver 40 DC Biopotentiostat/Galvanostat with modulated speed rotator (MSR) in a standard three-electrode cell at room temperature. The three-electrode cell configuration consisted of a platinum coil as a counter electrode, an Ag/AgCl in 4 M KCl as a reference electrode, and N-doped graphene on a glassy carbon electrode with 5 mm in diameter as a working electrode. To prepare the working electrode, 2 layers of N-doped graphene were transferred in a layer-by-layer fashion on a glassy carbon electrode through a wet chemistry-based transfer method [19]. The cyclic voltammetry (CV) and rotating disc electrode (RDE) measurements were performed in N_2 and O_2 saturated 0.1 M KOH electrolyte solution at room temperature from 0.2 to -1.2 V vs. Ag/AgCl with a scan rate of 10 mV/s. All potentials reported here are vs. Ag/AgCl. The rotating speed in RDE measurements was varied from 400 to 2000 rpm. The double-layer capacitances (C_{DL}) were estimated by plotting anodic and cathodic current density differences (j_a-j_c) against the potential scan rate. The slopes of such plots were assumed to be twice of C_{DL} and used to represent the electrochemical surface area (ECSA) of the N-doped graphene. Tafel analysis was performed to determine the kinetic parameters of the ORR. (b) in the Tafel equation ($\eta = a + b \log(j)$) determined from the slopes of the overpotential (η) vs. log(j)

plots in the kinetic region of RDE measurements was used to compare the ORR kinetics of N-doped graphene electrocatalysts with dominant N_{grap} and N_{pydn} configurations. The EIS measurements were carried out after transferring the samples onto FTO substrates. All other components of the experiment, such as the electrolyte, reference electrode, and counter electrode were the same as other electrochemical measurements. The frequency was adjusted to change from 0.1 Hz to 100 kHz at an amplitude of 10 mV.

3.2.5. Computational Details

The computational investigations have been performed by our collaborators from Istanbul Technical University. DFT calculations were performed using Vienna Ab-initio Simulation Package (VASP) [247], [248] with projector augmented wave method [249], and the Perdew, Burke, and Ernzerhof (PBE) [250] functional within the generalized gradient approximation, was used to describe exchange−correlation effects. The cutoff energy was set to 500 eV and the energy and force convergence criteria were set to 5×10^{-6} and 5×10^{-2} eV, respectively. The corrections for van der Waals (vdW) interactions were addressed by Grimme's D3 [251]. The Brillouin-zone integrations were performed on 2 × 2 × 2 k-point grids. The interlayer binding energies (E_{bind}) of pristine graphene bilayer and N-doped graphene (NG) were calculated by $E_{bind} = (E_0 - 2 \times E_0')/N$, where E_0 and E_0' are the total energies of the bilayer and monolayer and N is the total number of atoms in the unit cell.

Bilayer graphene has been constructed using two 7 × 7 supercell of graphene sheets with unit cell parameters of a = 17.25 Å, b = 14.93 Å and c = 15.00 Å. Periodic bilayer images were separated with at least a vacuum region of 16 Å to minimize any interaction between bilayers. Both AA- and AB-stacked graphene bilayers with different doping ratios (up to 19%) of graphitic (N_{grap}), pyridinic (N_{pydn}), and a mix N (one graphene layer doped with graphitic and the other with pyridinic N, $N_{grap/pydn}$) have been considered to calculate the binding energies and interlayer distances. Both random and symmetric N doping positions have been realized in three types of N-doped graphene bilayers and the resulting structures were called DP-NG-n, where DP, NG, and n refer to stacking type, N doping type, and N doping concentration, respectively. n=0 indicates a pristine bilayer and in the case of N_{pydn} and $N_{grap/pydn}$ graphene bilayers, several carbon vacancies were created on the graphene layers. Figure 3-3 shows some of the considered AA- and AB- stacked N_{grap}, N_{pydn}, and $N_{grap/pydn}$ structures which do not contain any dangling bonds.

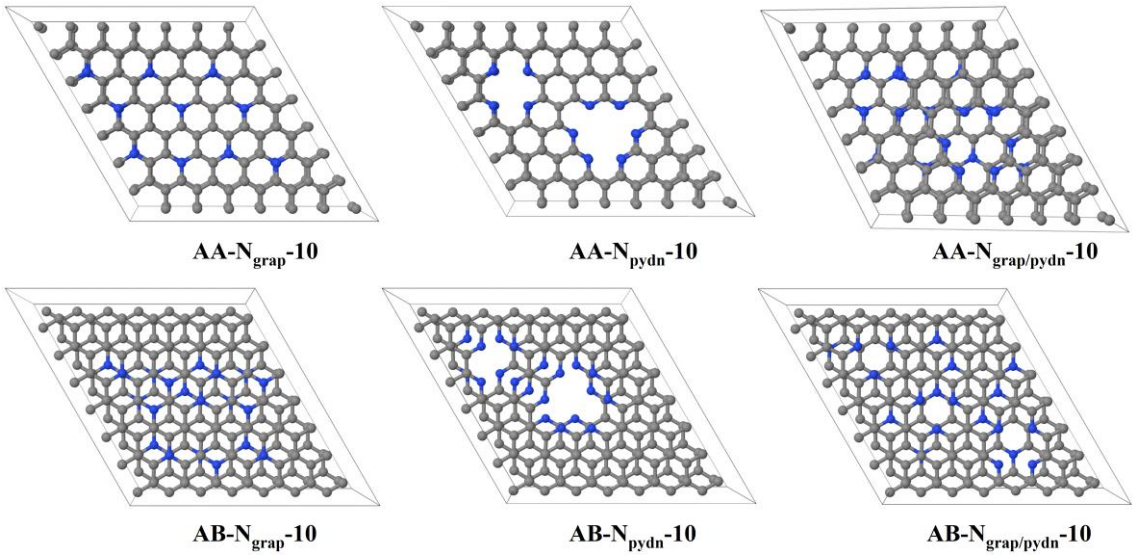

Figure 3-3 Model structures used in the computations, including 10% N doping.

It should also be mentioned that the existence of dangling bonds in the model structures of AA-N_{pydn} with N doping levels of 0, 1, and 2% leads to the clipping of graphene monolayers as shown in Figure 3-4. Such covalent bond formations between the dangling carbon atoms were already noticed in the literature [252], [253]. While there is only one covalent bond formation in both AA-N_{pydn}-0 and AA-N_{pydn}-2 with C-C distances of 1.39 and 1.40 Å, respectively, two bonds with a distance of 1.44 Å are formed in AA-N_{pydn}-1. Apart from these clipped junction points, the interlayer separations shown in Figure 2 are close to the other bilayers, which do not have any clipping.

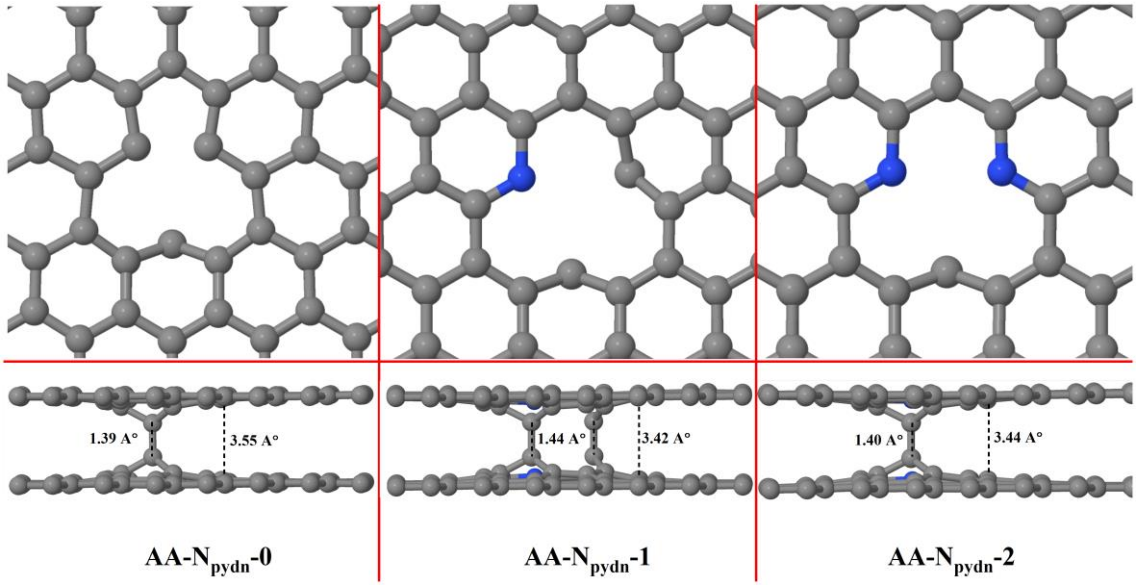

Figure 3-4 Top and side views of the clipped bilayers of AA-N_{pydn}-0, AA-N_{pydn}-1, and AA-N_{pydn}-2.

3.1. Improving Electrochemical Activity of N-doped Graphene Towards ORR

The types of the N configurations in the graphene network formed upon N_2 plasma exposures for various durations can be identified by analyzing N 1s XPS spectra. The progressive change of N 1s XPS spectra shown in Figure 3-5a indicates that the plasma exposure strongly affects both amount and configurations of N in the graphene network. The N_{grap} configuration assigned to the red peak appearing at ~399.5 eV, is the dominant N configuration in the sample with the shortest plasma exposure duration (NG60). The nitrilic (N_{nitr}), amino (N_{amin}), and pyrrolic (N_{pyro}) groups, appearing around 398.5 eV (depicted in green color in Figure 3-5a), are usually indistinguishable in the XPS spectrum, and their formation would depend on the preparation methodologies [254], [255]. N_{amin} species are considered to get converted to N_{pyro}/N_{nitr} upon high-temperature treatments, and they are labeled as N_{nitr}/N_{pyro} henceforth. It is more accurate to consider N_{pydn} under two separate configurations, on the basal planes, and at the edges, while deconvoluting XPS spectra [19]. The component at ~397.8 eV is attributed to N_{pydn} atoms on the basal planes, which are not in contact with the underlying Cu substrate. The second group is the nitrogen atoms at the edges of graphene sheets which prefer to pin to Cu substrate. This group of N atoms ($N_{pydn'}$) can be identified by the peak at ~397.2 eV. The quantitative analysis of the spectra in Figure 3-5a shows that the N_{grap} content decreases sharply when the graphene is doped with N for longer than 60 seconds (Figure 3-5c). In contrast, N_{pydn} and $N_{pydn'}$ exhibit a growing trend by increasing doping duration. Total N concentration reaches a maximum value of 16% for the samples which is exposed to N_2 plasma for 240 seconds (NG240). Further exposures lead to a rapid drop in N amount due to partial removal of graphene. The orange peak located at 396.5 eV for NG180, NG240, and NG300, which can be assigned to a copper nitride-like phase (CuN_x), points out the graphene network getting defected by increasing the plasma exposure duration.

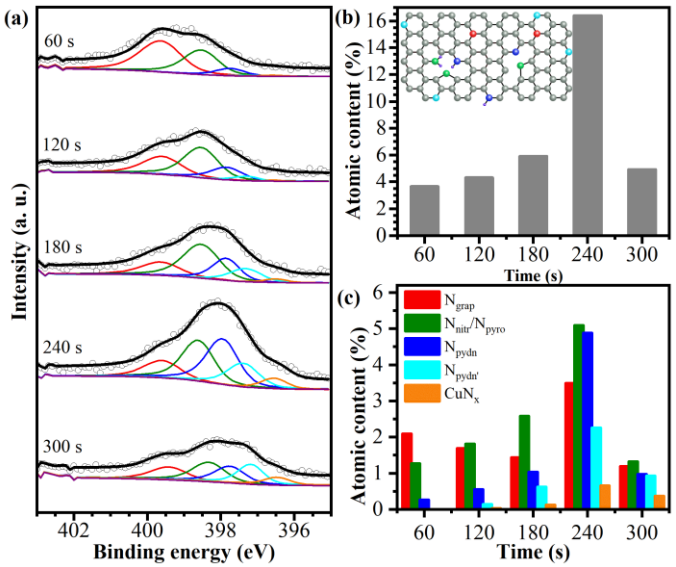

Figure 3-5 (a) Deconvoluted N 1s XPS spectra for graphene with different plasma exposure durations varying from 60 s to 300 s. Red, green, blue, cyan, and orange peaks are assigned to N_{grap}, N_{nitr}/N_{pyro}, N_{pydn}, $N_{pydn'}$, and CuN_x, respectively. (b) Total N content for each of the samples. (c) The content of each N configuration for different samples. Each bar represents the phase percentage shown with the same color at part (a).

C 1s XPS spectra of the same sample set presented in Figure 3-6 agree well with the N 1s spectra. While pristine graphene is characterized by a single peak at 284.3 eV, which is attributed to sp^2 hybridized C, N doping leads to the formation of new features in the high binding energy side. Higher electronegativity of N and O change local electronic structure; thus, C atoms coordinated to those give rise to higher binding energy components in C 1s XPS spectra. The peak at 284.9 eV (C1) and 285.7 eV (C2) are generally attributed to N-sp^2 C and N-sp^3 C, respectively. The peak at 288.0 eV (C3) is assigned to oxygenated C atoms (C-O, C-OH, and COOH) [256].

These results show that it is possible to manipulate the configuration of N atoms in graphene structure by adjusting plasma exposure duration. Similar preferential formation of N_{pydn} has previously been observed. By increasing their power and bombardment duration, N ions have been shown to form N_{pydn} rather than N_{grap} and N_{pyro}/N_{nitr} [257]. It is likely that incorporation mechanisms vary depending on the N-doped graphene synthesis strategies and growth temperatures. The extended post-plasma treatment in the absence of hydrogen seems to yield N_{pydn} and vacancies. The NG60 and NG240, which contained mainly N_{grap} and $N_{pydn}/N_{pydn'}$, respectively, were further analyzed to investigate the effect of different nitrogen configurations on the electrochemical activity of N-doped graphene towards ORR.

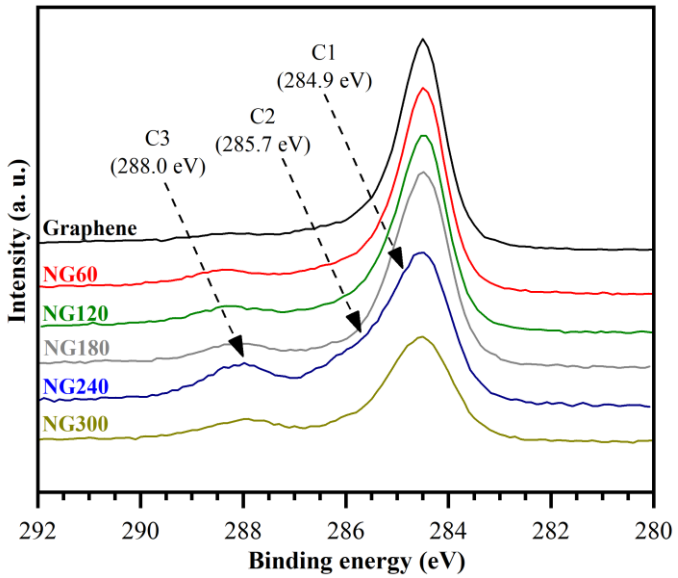

Figure 3-6 C 1s XPS spectra for graphene with different N_2 plasma exposure durations varying from 60 s to 300 s.

Figure 3-7 compares Raman spectra taken from pristine graphene, NG60, and NG240. The intensity ratio of 2D peak (located at ~2700 cm^{-1}) to G peak (located at ~1580 cm^{-1}) as well as the absence of D peak (located at ~1350 cm^{-1}) for pristine graphene, reveals that it is a bilayer film with very low defect density and large grain size [258]. The creation of defects in a honeycomb-like structure of graphene after doping with N decreases the probability of 2D scattering and results in a large D peak for Raman spectra of N-doped samples [259]. The main difference in Raman spectra of NG60 and NG 240 is the higher intensity ratio of D´ peak (located at ~1620 cm^{-1}) to G peak ($I_{D'}/I_G$) in NG240 compared to NG60. The spectra with $I_{D'}/I_G$ larger than 0.8 and I_D/I_G larger than two can be attributed to graphene samples highly doped with $N_{pydn'}$ [19], which is in good agreement with XPS findings presented in Figure 3-5.

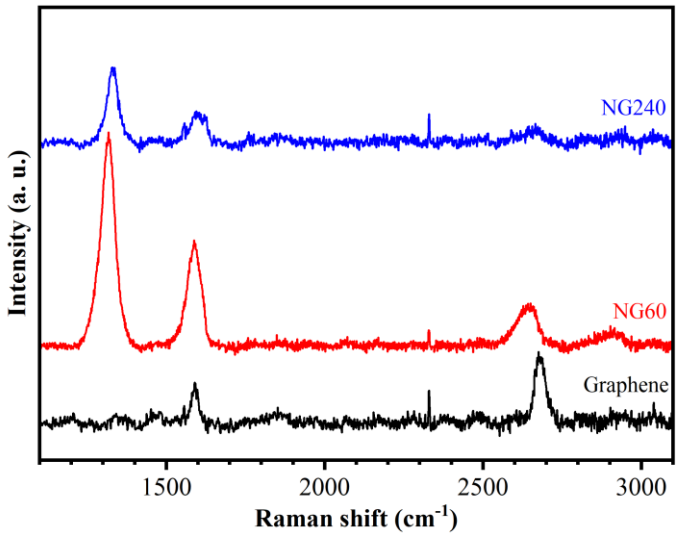

Figure 3-7 Raman spectra of pristine graphene (black), NG60 (red), and NG240 (blue).

Owing to its element specificity, the characterization of N_{grap}- and N_{pydn}-rich graphene electrocatalyst with XES and XAS provides the opportunity to probe the occupied and unoccupied partial DOS [241], [260], respectively (Figure 3-8a). The inelastic event in RIXS, a special case in XES, corresponds to the energy loss needed to excite valence electrons to unoccupied states. However, in contrast with XES, where emission is independent of excitation energy, the energy of emission in RIXS varies by changing the energy of incident X-ray while preserving the same energy separation from the elastic peak. This constant energy separation is characteristic of the net transition and provides information about the partial DOS [241].

Figure 3-8 shows N K-edge XAS spectra (Figure 3-8b) and N K-edge RIXS data obtained from N_{grap}-rich and N_{pydn}-rich graphene (Figure 3-8c and Figure 3-8d) with increasing incident X-ray energies. In N K-edge XAS spectra, π* resonance with N 2p and C 2p-hybrid states in the conduction band is composed of three peaks located at ~400.9 eV, 399.8 eV, and 398.8 eV. These peaks are assigned to N_{grap} (red), N_{nitr}/N_{pyro} (green), and N_{pydn}+$N_{pydn'}$ (blue) groups, respectively, which are in excellent agreement with previous data [261]–[264]. Increased N_{pydn} component at the low energy side and decreased N_{grap} component further confirm that extended N_2 plasma exposure enriches N_{pydn} species. The intensity of the entire π* resonance spanning between 398 and 402 eV increases in NG240 due to higher overall N content. The absence of any feature below 398 eV rules out the formation of nitride species. DFT calculations have shown that N_{grap} increases metallicity upon the donation of an electron into π* states of the conduction band (n-type), and the Fermi level is shifted to higher energies [261]. This phenomenon is also observed in our

DFT calculations: while the Fermi level is at -1.33 eV in AA-N_{grap}-0, it reaches to -0.72 eV and -0.29 eV in AA-N_{grap}-3 and AA-N_{grap}-10, respectively. An adverse effect in the Fermi level position is introduced by N_{pydn}. In particular, the Fermi energy is lowered from -1.45 eV (AA-N_{pyrid}-0) to -2.07 eV (AA-N_{pyrid}-10). However, the change of the Fermi energy in $N_{grap/pydn}$ is similar to that of N_{grap}. The charge redistribution included by N_{nitr}/N_{pyro} is, however, not straightforward. It has been reported that N_{pyro} species bonding with sp^3 hybridized C to form five-membered rings do not contribute to the doping level of graphene [243], [261]. Even though the DFT calculations have revealed the impact of N in the desired configuration on the electronic properties of graphene, it should be considered that most of these calculations are performed for low N content. The complication arises as the overall N content is high and N in various configurations is present in the structure. Thus, the N K-edge XAS spectrum of N_{pydn}-rich graphene in the present study cannot singlehandedly be interpreted in accordance with the calculated electronic structures. Nevertheless, a very large graphene sheet including 7x7 supercell was considered in the DFT calculations to get a better agreement with the experimental results. Not only the multiple types of N incorporated into graphene, but overall structural changes in graphene should be considered.

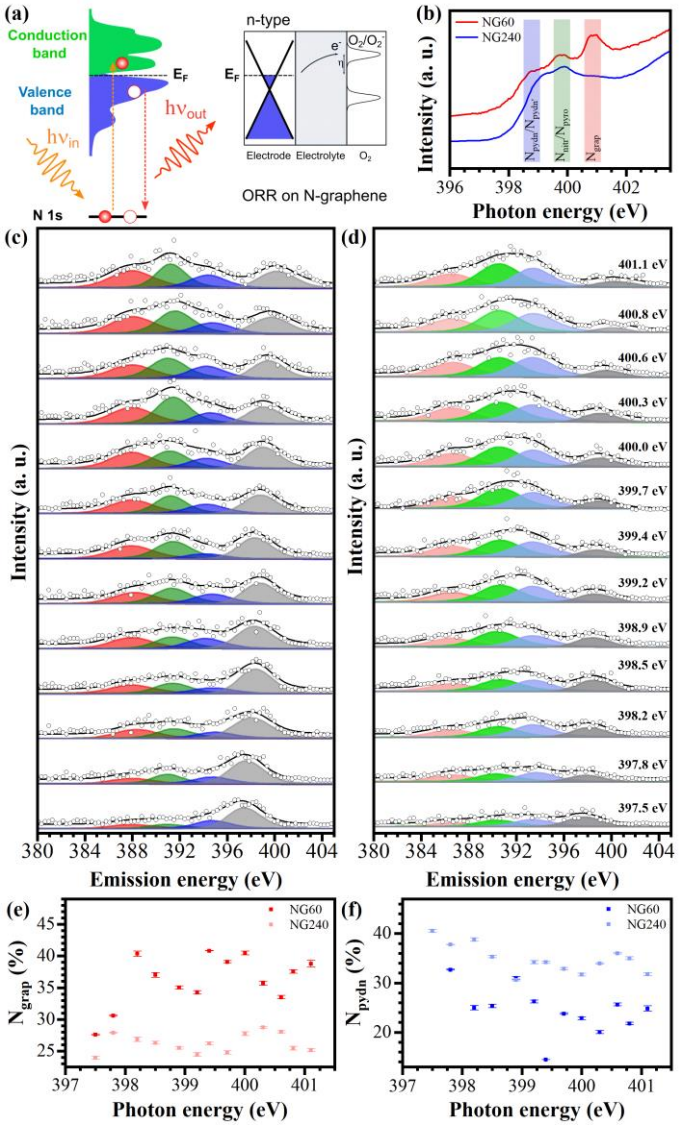

Figure 3-8 (a) Schematic drawing of X-ray absorption and emission processes. (b) N K-edge XAS data for N_{grap}-rich (red) and N_{pydn}-rich (blue) samples. N K-edge RIXS data for (c) N_{grap}-rich and (d) N_{pydn}-rich N-doped graphene samples. The fraction of (d) N_{grap}, and (e) N_{pydn} for the samples is shown in parts (c) and (d). The calculation has been done based on the area under the curve values of RIXS measurements.

Figure 3-9 shows the partial density of states (PDOS) and DOS of AA-N_{grap}, AA-N_{pydn} and AA-$N_{grap/pydn}$. In the pristine AA-N_{grap}-0 and AA-N_{pydn}-0 and AA-$N_{grap/pydn}$-0 (Figure 6 a, c, and e), the small DOS near the Fermi level indicates a very low interlayer π-π interaction. However, as described later, there is a huge binding energy gain for AA-N_{pydn}-0 compared to others and this is mainly due to the vacancy-mediated clipping of graphene monolayers. Upon the N doping, at least %3, there is a notable accumulation of DOS around the Fermi level, which indicates the possibility of the interlayer π-π interaction. As shown in Figure 3-9, the increase in the N content also increases the electronic states in the Fermi level. While the conduction band is pulled down the Fermi

level in AA-N_{grap}-3 and AA-$N_{grap/pydn}$-3, valence and conduction bands are slightly separated in AA-N_{pydn}-3 and AA-N_{pydn}-10. As a result, the interlayer π-π interaction is less in N_{pydn} compared to both N_{grap} and $N_{grap/pydn}$. Furthermore, atomic charges and electron transfer (∇q (e)) in graphene bilayers are analyzed with Bader charge analysis approach [265]. It has been found that while there are no negligible charge transfers between monolayers of N_{grap} and N_{pydn}, a significant electron transfer occurs in both AA-$N_{grap/pydn}$ and AB-$N_{grap/pydn}$. In particular, 0.18, 0.89 and 1.50 electrons have been transferred from the graphitic to the pyridinic layers respectively in AA-$N_{grap/pydn}$-0, AA-$N_{grap/pydn}$-3 and AA-$N_{grap/pydn}$-10. In addition, the amount of transferred electrons is reduced to 0.04, 0.63 and 1.20 in the case of AB-$N_{grap/pydn}$-0, AB-$N_{grap/pydn}$-3 and AB-$N_{grap/pydn}$-10. The high amount of electron transfer between the layers also indicates the existence of strong vdW interactions in $N_{grap/pydn}$ systems.

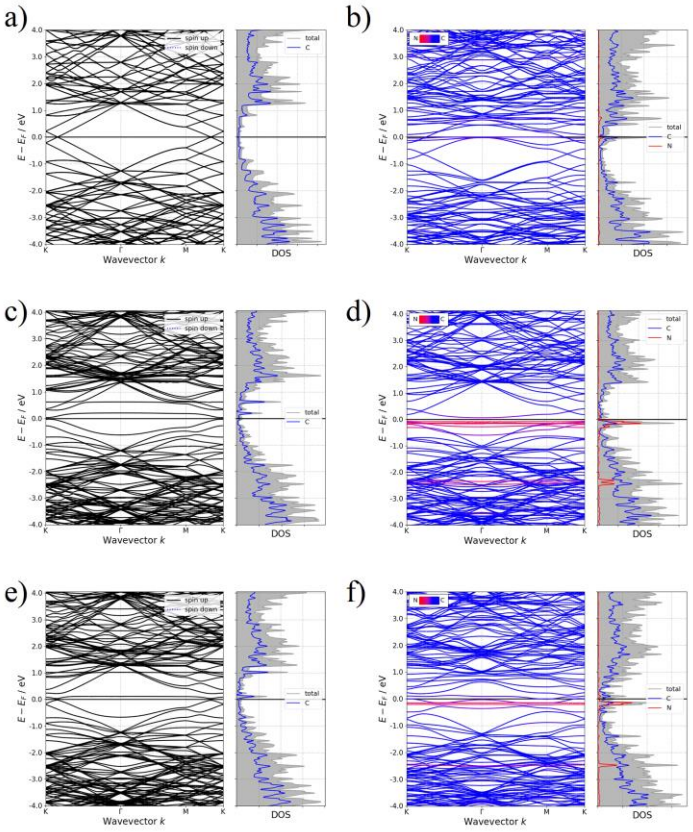

Figure 3-9 Partial density of states and density of states of (a) AA-N_{grap}-0, (b) AA-N_{grap}-3, (c) AA-N_{pydn}-0, (d) AA-N_{pydn}-3, (e) AA-$N_{grap/pydn}$-0, and (f) AA-$N_{grap/pydn}$-3.

The RIXS spectra that are deconvoluted to show N_{grap} (red), N_{nitr}/N_{pyro} (green), and N_{pydn}+$N_{pydn'}$ (blue) contributions are in a good qualitative agreement with N K-edge XAS spectra. The gray peak located at high emission energy is attributed to the elastic peak and shifts to higher emission energies with increasing the incident X-ray energy. In the

RIXS process, the momentum is not fully conserved due to electron-phonon scattering to the final state; thus, the coherence is partially destroyed. Nevertheless, resonant enhancements could be observed at the incident X-ray energies near the absorption threshold. The spectral changes as a function of the incident X-ray energy from 400 to 380 eV relate partially to the band dispersion of N-doped graphene since there is a strong hybridization between C 2sp and N 2sp states. Increasing energy leads to exciting more electrons from N_{grap} atoms, hence sharpening the red peak for both samples. However, as can be seen in Figure 3-8e and Figure 3-8f, the area under peak covered with N_{grap} component is lower for the N_{pydn}-rich sample compared to N_{grap}-rich, for all excitation energies. All these observations combined do not indicate any specific band opening upon N incorporation. As discussed in detail below, changes in the van der Waals interactions between the graphene layers induced by N in the lattice could have a more significant impact on the electronic properties of graphene, and corresponding interpretations would be required to describe ORR activities dependent on N-type and amount.

DFT calculations were performed to evaluate the structural changes and the corresponding vdW interactions in N doped graphene bilayers. As shown in Figure 3-10a, while the separation between layers for the AB-stacked structures changes slightly with increasing doping level, the AA-stacked structures show significant diversity as a function of doping concentration. Such a trend is also observed for the binding energies as seen in Figure 3-10b. At zero N doping, the binding energies and interlayer distances are computed to be -20.15, -23.52, -20.25 and -23.94 meV and 3.61, 3.43, 3.58 and 3.38 Å, respectively for AA-N_{grap}-0, AB-N_{grap}-0, AA-$N_{grap/pydn}$-0 and AB-$N_{grap/pydn}$-0. While AB-stacked graphene bilayers have stronger binding energies at low N doping concentrations, above 4% N doping especially AA-N_{grap} and AA-$N_{grap/pydn}$ become energetically more favorable. In particular, they reach a maximum binding energy (per atom) of -38.11 and -37.53 meV and the shortest corresponding interlayer distances of 2.92 Å (between N-C) and 2.94 Å (between N-N), respectively at 10% N doping level. It should also be mentioned that among the AB-stacked configurations AB-$N_{grap/pydn}$ shows a similar trend as AA-N_{grap} and AA-$N_{grap/pydn}$ upon the increasing N content.

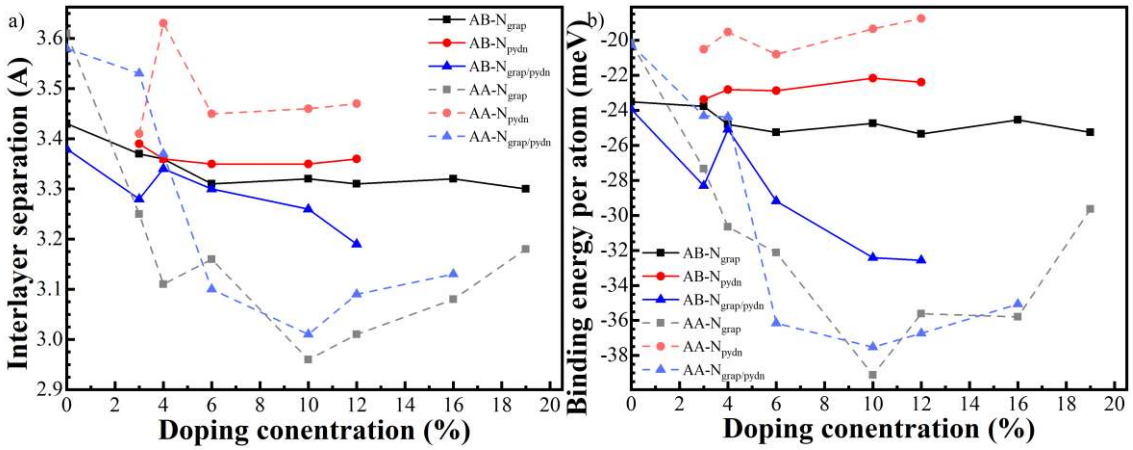

Figure 3-10 The computed (a) interlayer separations and (b) binding energies (per atom) as a function of N doping in both AA- and AB-stacked graphene bilayers.

RDE and CV measurements in O_2 and N_2 saturated 0.1 M KOH electrolyte solution were further employed to investigate the ORR kinetics of the samples. None of the CV curves in Figure 3-11a exhibits any significant reduction peak in N_2 saturated electrolyte, confirming the electrochemical stability of graphene and N-doped graphene films in the studied potential region and also the absence of any Cu contaminations [266]. The significant ORR current of N-doped graphene in comparison with the pristine graphene is an indication that the addition of N to the graphene structure creates active sites for this reaction. The CV curve from the pristine graphene had a broad peak at around -0.50 V (vs Ag/AgCl), which is attributed to the two-electron reduction reaction of converting O_2 to HO_2^- [267]. Both NG60 and NG240 samples have this peak at ~ -0.37 and ~ -0.35 V. There is also a small peak at more negative potentials (~ -0.90 V) for N-doped samples, which can be attributed to the reduction of HO_2^- to OH^- [267]. The addition of almost 2 at.% N_{grap} to graphene structure (NG60) facilitates two-electron reduction pathway, without perturbing conductivity of the film significantly, by lowering the onset potential from ~ -0.24 V to ~ -0.2 V compared to pristine graphene. On the other hand, the higher N_{pydn} content in NG240 helps to lower the overpotential in ORR further, a substantial shift of the onset potential to ~ -0.17 V is observed. Figure 3-11b shows the results obtained from RDE measurement with the rotation rate of 1600 rpm in N_2 and O_2 saturated electrolyte solution. The electrochemical features observed in CV curves can be seen here as well. Polarization curves confirm that the increased number of N and dominant N_{pydn} groups lower the onset potential significantly and make NG240 the best ORR electrocatalyst.

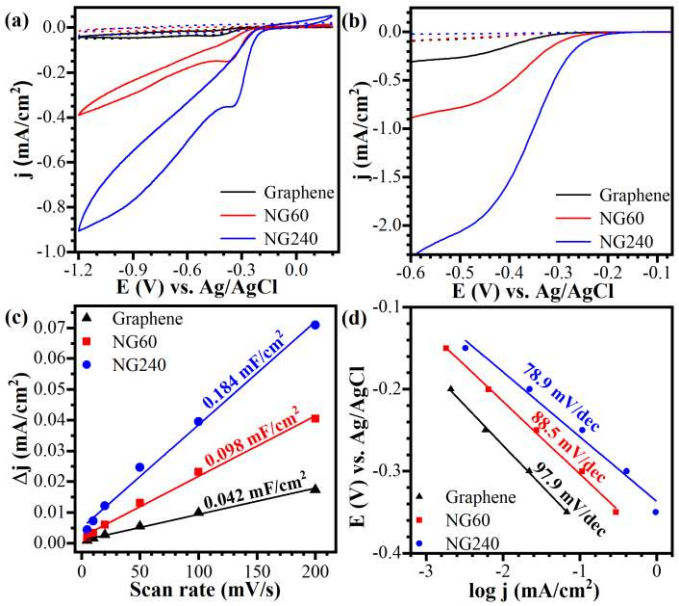

Figure 3-11 (a) CV curves of pristine graphene (black), NG60 (red), and NG240 (blue) in O_2 (solid) and N_2 (dashed) saturated 0.1 M KOH electrolyte solution. (b) Polarization curves of the electrocatalysts obtained from RDE measurements at 1600 rpm in O_2 (solid) and N_2 (dashed) saturated electrolyte solution. (c) ECSAs are determined by estimating C_{DL}. Potential scan rate dependent double layer charging was measured at 5, 10, 20, 50, 100, 150, and 200 mV/s scan rates within the -0.1 V - 0.1 V potential range. (d) Tafel plots for the ORR.

ECSAs of the electrodes are typically proportional to the C_{DL}, which can be derived from the CV curves in a non-faradaic region [175]. To investigate N dependent C_{DL} changes, CV curves for pristine graphene, NG60, and NG240 were recorded with scan rates of 5, 10, 20, 50, and 100 mV/s in -0.1 V to 0.1 V potential range (Figure 3-12). The plots for the difference between cathodic and anodic current densities versus potential scan rates at 0.0 V exhibit a linear behavior with slopes of 0.042 mF/cm^2, 0.098 mF/cm^2, and 0.184 mF/cm^2 for pristine graphene, NG60, and NG240, respectively (Figure 3-11c). Such an enormous improvement in ECSA can be attributed to having almost 8 at.% N_{pydn} and $N_{pydn'}$ in graphene structure for NG240.

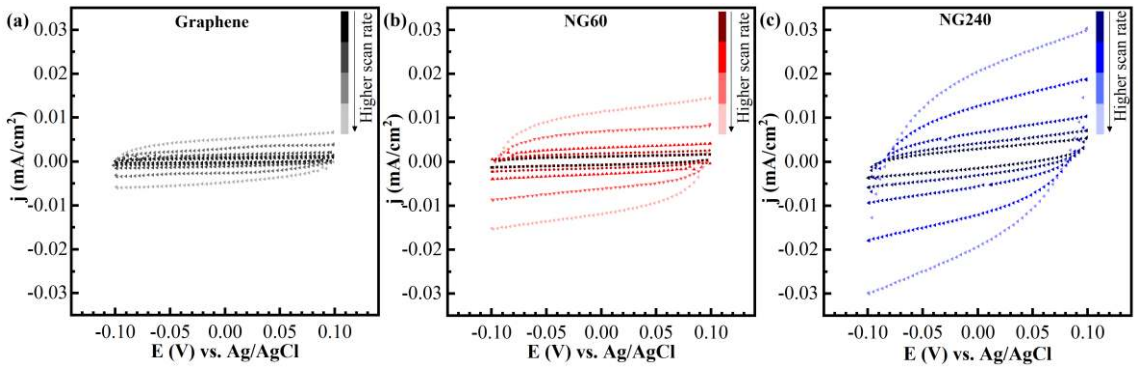

Figure 3-12 CV curves taken at various scan rates (5, 10, 20, 50, and 100 mV.s-1) from (a) pristine graphene, (b) NG60, and (c) NG240. The lighter colors in each graph represent higher scan rates.

The polarization curves with different rotation rates and the corresponding Koutecky-Levich (K-L) plots at -0.4 V and -1.0 V are shown in Figure 3-13. Due to the linear relationship between j^{-1} and $\omega^{-1/2}$ in K-L plots, the electron transferred number (n) for the ORR can be derived by Equation 2-13, where F is Faraday constant (96485 C/mol), D is the diffusion coefficient of O_2 in 0.1 M KOH electrolyte (1.93×10^{-5} cm^2/s), ν is the kinematic viscosity of the electrolyte (1.09×10^{-2} cm^2/s), C_o is the saturation concentration of O_2 in 0.1 M KOH at 1 atm O_2 pressure (1.26×10^{-6} mol/cm^3) and B is the Levich constant and is equal to the reciprocal of the slope of the j^{-1} vs. $\omega^{-1/2}$ plot when j is in the unit of cm^2/A and ω is in the unit of rad/s [172]. The K-L plots for a two-electron and a four-electron reduction reaction have been calculated and shown in Figure 3-13c. Comparing the obtained results for NG60 and NG240 with these reference curves clearly shows that both samples follow the same reduction mechanism, which starts with the two-electron pathway. The number of transferred electrons becomes four by reaching the diffusion-limited potential region. Tafel analysis was also performed to provide further insight into the mechanistic pathway of the ORR and Tafel slopes of pristine graphene, NG60, and NG240, are shown in Figure 3-11d. NG240 with dominant N_{pydn} has a lower Tafel slope (78.9 mV/dec) and runs the ORR much more effectively as compared to NG60 (Tafel slope: 88.5 mV/dec)).

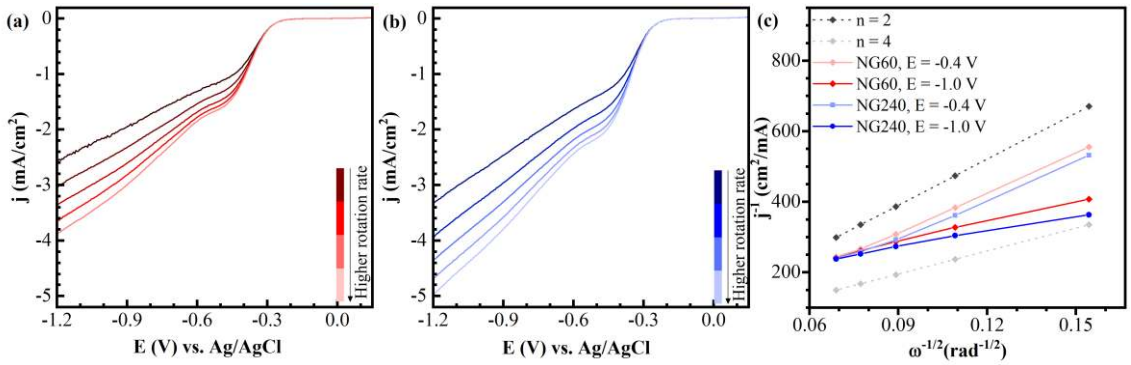

Figure 3-13 RDE polarization curves for NG240 with different rotation rates. The rotation changes from 400 rpm to 2000 rpm as the color of the curve gets lighter. (c) The K-L plots for NG60 (red curves) and NG240 (blue curves) at -0.4 V (lighter curves) and -1.0 V (darker curves). The calculated K-L plots for a two-electron and a four-electron reduction reaction are shown in dashed lines.

To reveal the unique roles of N_{grap} and N_{pydn} in the electrochemical activity of N-doped graphene, one strategy would be to minimize the effect of other N configurations and total N content. Optimizing the plasma exposure time and power provides the opportunity to prepare N-doped graphene matching these criteria. Figure 3-14a-b shows C 1s and N 1s XPS spectra of two samples with similar N_{nitr}/N_{pyro} but different N_{grap}, $N_{pydn,}$ and $N_{pydn'}$ contents. The at.% of each N configuration, as well as total N content, are reported in Table 3-1. Comparable C 1s peak areas reveal that both samples have the same number of layers of graphene; however, the N_{pydn}-rich sample has a higher total N content. ORR kinetic analysis has so far indicated that N_{pydn}-rich graphene could have more active sites owing to its largest ECSA. The lowest overpotential and the smallest Tafel slope both point out more facile oxygen reduction occurring on those active sites. However, the expectation that N_{pydn}-rich graphene would inherently be p-type is not justified by XAS and XES. The present atom-specific spectra representing local DOS even indicate metallicity with increased DOS at the Fermi level. At this point, we anticipate that an increased number of N_{pydn} leads to altered interlayer separations. Raman spectral changes are not only sensitive to the number of graphene layers but also provide information about interlayer interactions, staking type (AA, AB), etc. Previous studies have shown that the intensity ratio of 2D to G band (I_{2D}/I_G) in the Raman spectrum of graphene can be used to investigate the interlayer interactions [268]–[270]. The I_{2D}/I_G value for the pristine graphene (Figure 3-14c, black spectrum), which was used to prepare N_{grap}- and N_{pydn}-rich samples, is ~1.5, confirming the bilayer structure [271]. This ratio decreases to ~0.8 and ~0.2 for the N_{grap}-rich and N_{pydn}-rich graphene, respectively. The lower I_{2D}/I_G is a

signature of higher interlayer interactions for the N_{pydn}-rich graphene. Theoretical calculations have shown that in order to increase the interlayer interaction by N_{grap}, more than 10 at.% N should be present in an AA stacked graphene sample [272]. However, our results show that, for the randomly stacked graphene synthesized by CVD, it is possible to enhance the interlayer interaction by only ~2 at.% of N_{pydn}.

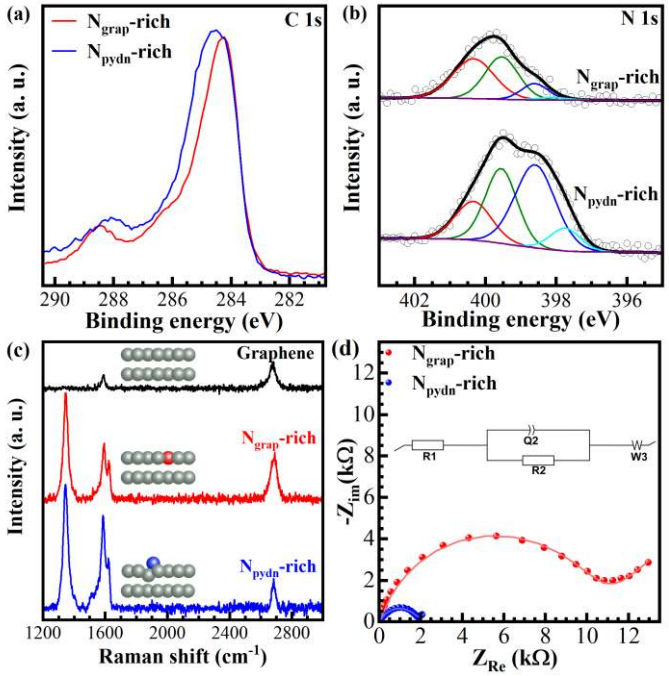

Figure 3-14 (a) C 1s XPS spectra for N_{grap}-rich and N_{pydn}-rich graphene samples prepared by exposing pristine graphene to N_2 plasma at 10 W and 20 W for 30 s, respectively. (b) Deconvoluted N 1s XPS spectra obtained from N_{grap}-rich and N_{pydn}-rich graphene on FTO substrates. Red, green, blue, and cyan peaks are assigned to N_{grap}, N_{nitr}/N_{pyro}, N_{pydn} and, $N_{pydn'}$ respectively. (c) Raman spectra for the pristine (black), N_{grap}-rich and (red), and N_{pydn}-rich graphene (blue). (d) EIS measurements on N_{grap}-rich (red) and N_{pydn}-rich graphene (blue).

Table 3-1 The atomic percentages of total N and each configuration for the N_{grap}-rich and N_{pydn}-rich graphene obtained from quantitative XPS analysis.

Sample	Total N (at.%)	N_{grap} (at.%)	N_{nitr}/N_{pyro} (at.%)	N_{pydn} (at.%)	$N_{pydn'}$ (at.%)
N_{grap}-rich	2.41	1.19	0.92	0.25	0.05
N_{pydn}-rich	4.01	0.71	1.03	1.92	0.35

Interlayer π-π interaction induced by heteroatom doping of bilayer and multilayer graphene can alter its electrochemical activity [273]. While the addition of graphene layers promotes its electrochemical activity and electron transfer kinetics in general [273], [274], no enhancement has been observed in the electrochemical activity of non-AB stacked bilayer graphene compared to a single layer [273]. This is attributed to the weak

electronic coupling between the graphene layers in the absence of AB stacking [275]–[277]. Hence, it can be concluded that in addition to all previously discussed possible mechanisms, N_{pydn} can also contribute to improving the ORR activity of N-doped graphene by increasing the extent of interlayer interaction which facilitates the electron mobility of the electrode and increases the conductivity. This is also in agreement with the results obtained by XAS (Figure 3-8) and XES (Figure 3-15). N and C K-edge spectroscopy do not exhibit spectral features that can be attributed to the band opening of graphene upon N doping. An increased band gap is expected in high N amounts, which could negatively affect electrochemical activities in general owing to increased electrode resistances. Valence band maximum approximated by linear extrapolation of the band edge of non-resonant XES spectra at the C K-edge (Figure 3-15) indicates that NG240 with high N_{pydn} maintains metal-like properties since there is an increased intensity at the valence band edge and spectra indicate charge delocalization. The Nyquist plots for the EIS measurements are shown in Figure 3-14d. Randle's model is used to describe an equivalent circuit for the Nyquist plots. Circuit elements from the fitting represent ohmic resistance of the electrolyte (R1), charge transfer resistance at electrode/electrolyte interface (R2), constant phase element (Q), and Warburg element for semi-infinite diffusion (W). The results confirm the five times improvement in conductivity of the N_{pydn}-rich graphene (~1.78 kΩ) compared to the N_{grap}-rich one (~10.2 kΩ).

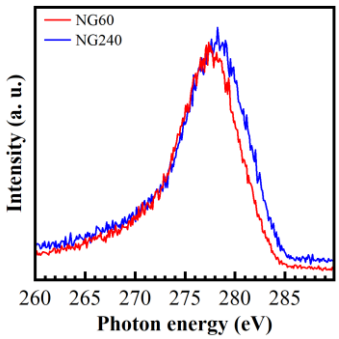

Figure 3-15 C K-edge XES data for graphitic N_{grap}-rich (red) and N_{pydn}-rich (blue) samples. Excitation energy was 440 eV.

N_{pydn}-rich graphene has certainly more catalytically active sites toward ORR. DFT calculations show that C atoms neighboring N have high positive spin densities and serve as active sites [238], [278]. Electrostatic arguments are also made to justify C as an adsorption and reaction site; C turned to more positive by N coordination attracts lone pair electrons of O_2. The elementary steps of the ORR are therefore N dependent. Moreover, the first electron transfer process depends on whether O_2 is in the inner

Helmholtz layer coordinating to the adsorption site on the surface. Outer layer electron transfer is also plausible [279]. Increased DOS near the Fermi level seen in C and N K-edge XES spectra enhances the orbital interaction and electron transfer between N-doped graphene and adsorbed O_2. Present results indicate that, in addition to interlayer bond formation between graphene bilayers, N_{pydn} is also critical in such an electron transfer process.

Although present results clearly show different roles of N_{pydn} in improving the electrochemical activity of N-doped graphene, it is essential to consider more possibilities for this complex 2D system, i.e., the effect of different configurations on the electrochemical activity. It is probable that $N_{pydn'}$ and edge defects significantly contribute to the metallicity. N_{pydn} in basal planes and at the edges of graphene flakes ($N_{pydn'}$) could modify the doping level of graphene differently. π^* resonance of N_{pydn} appearing at 398.8 eV agrees well with the previously published data and its energy position shows dependence on the associated vacancy created [236], [264]. Mono- and di-vacancies, as well as Stone-Wales defect centers alter the π^* energy positions differently. The extent of the peak widths could be attributed to the delocalization, N_{nitr}/N_{pyro} groups that also coexist with those vacancies, as well as N_{pydn}, present broader π^* resonance [264]. Also, the different intensity ratios of D peak to G peak (I_D/I_G) in Raman spectra of N_{pydn}-rich and N_{grap}-rich samples can be taken into account as a sign of different surface roughness among these samples, which can impact the electrochemical activity of N-doped graphene [273].

3.2. Conclusion

In summary, we have investigated the role of N dopant configuration on the electrochemical activity of N-doped graphene towards the ORR. The content and configuration of N in CVD grown graphene structure that can be controlled by adjusting N_2 plasma exposure time and power enable us to perform systematic investigations by combining X-ray spectroscopy and Raman spectroscopy with electrochemical activity tests. N_{grap} species are dominant at low N content however, N_{pydn} becomes the majority species as N content increases by prolonged plasma exposure. N and C K-edge XES and Raman spectroscopy investigations reveal that N_{pydn} and edge N_{pydn} species ($N_{pydn'}$) induce stronger interlayer interactions via an increased π-π orbital overlap. Corresponding enhancement in the metallicity improves the ORR activity by promoting electron transfer

kinetics between layers. Moreover, the formation of N_{pydn} and $N_{pydn'}$ leads to a significant increase in the active sites. Overall, N_{pydn}-rich bilayer graphene exhibits electrochemical activities toward ORR superior to N_{grap}-rich graphene with lower onset potential, higher electrochemical current density, and lower Tafel slope.

Chapter 4:
Graphene: Spectral and Spectroelectrochemical Investigations

4.1 Introduction

4.1.1 SEC-Raman of N-doped Graphene

Despite the fascinating and unique properties of graphene, pristine graphene is relatively inert from a chemical point of view. This hinders the feasibility of using pristine graphene in electrochemical applications. However, it is possible to tune both the chemical and physical properties of graphene by heteroatom doping. Among different heteroatoms, N-doped graphene has been found to exhibit high performance as the electrochemical interface, especially as the cathode of fuel cells [222], [280]–[282] [210].

Despite numerous reports regarding the ORR activity of N-doped graphene, the detailed mechanism behind the ORR is still not fully understood. The main reason for this uncertainty is the unique structure of N-doped graphene, which is simple to imagine as a free-standing model but a complex electrochemical system since it provides suitable sites for the simultaneous progress of different electrochemical reactions. Most of the proposed ORR mechanisms on N-doped graphene in alkaline media have suggested elementary steps similar to the associative oxygen adsorption pathways on metal surfaces [283]. This mechanism can be described as follows:

$$O_2 + * \rightarrow O_{2(ads)} \qquad \text{Equation 4-1}$$

$$O_{2(ads)} + H_2O + e^- \rightarrow OOH_{(ads)} + OH^- \qquad \text{Equation 4-2}$$

$$OOH_{(ads)} + e^- \rightarrow O_{(ads)} + OH^- \qquad \text{Equation 4-3}$$

$$O_{(ads)} + H_2O + e^- \rightarrow OH_{(ads)} + OH^- \qquad \text{Equation 4-4}$$

$$OH_{(ads)} + e^- \rightarrow OH^- + * \qquad \text{Equation 4-5}$$

Alternatively, instead of Equation 4-3, $OOH_{(ads)}$ may undergo the following mechanism [283]:

$$OOH_{(ads)} + e^- \rightarrow OOH^-_{(ads)}$$ Equation 4-6

$$OOH^-_{(ads)} + H_2O \rightarrow H_2O_{2(ads)} + OH^-$$ Equation 4-7

$$H_2O_{2(ads)} \rightarrow H_2O_2 + *$$ Equation 4-8

While the former mechanism is known as the one-step $4e^-$ pathway, the latter involves two electrons and hence is known as the two-step $2e^-$ pathway. The main unresolved issue about these mechanisms is the site(s) of N-doped graphene on which the adsorption and following steps take place. The discussion regarding this issue arose first by attempts to identify the role of a different possible configuration of N in the activity of N-doped graphene. Up to date, there are controversially experimental and theoretical results about the role of these N configurations. However, most of the studies suggested the C atoms adjacent to the N impurity being the active site for the ORR [231], [284]–[286]. This attribution is mainly based on the theoretical calculations of electron spin density and atomic charge distribution. Tao et al, [287] were one of the pioneer groups who reported improved activity of dopant-free graphene by increasing its edge concentration. Following this finding, theoretical calculations showed that the hydrogenation of the N atom in the edge sites plays a key role in the activity of N-doped graphene. It was also revealed that O_2 molecules have different affinities to adsorb on the armchair and zigzag edges of N-doped graphene [238]. Recently, Kim et al, have investigated the possibility of having an outer-sphere electron transfer mechanism in N-doped reduced graphene oxide samples [288]. Their results showed that the availability of electron density at the Fermi energy determines whether a couple proton-electron transfer (CPET) or a non-CPET process takes place as the initial step of ORR. They also identified that the most reactive sites on N-doped graphene towards ORR are correlated to the local increase in spin density and hence those are the boundaries of the sp^2-sp^3 carbon region or C adjacent to N-dopants. However, their results showed that these sites will be covered with OH^- species in alkaline electrolyte and under applied potential. Consequently, the sp^2 carbon sites located next to the oxide region were introduced as the active site for ORR.

Raman spectroscopy is a fast and non-destructive technique which gives information about both the structural and electronic properties of graphene. The similarity of Raman spectra of carbon-based materials and their simplicity combined with the considerable amount of information that can be obtained from these spectra had made the data interpretation of Raman challenging. In practice, the Raman spectra of graphene show

some main features regardless of its structural and electrical properties. Numerous researches have been shown that the shape, intensity, and position of these peaks can be used to study doping effect [19], strain [289], oxidation and sample quality [289]–[292], molecular functionalization [293], and the number of layers [294]. In Spectroelectrochemical Raman (SEC-Raman) measurement, electrical and spectroscopic measurements are performed simultaneously, which provides a great potential for determining the adsorbates and intermediates during electrochemical reactions. This can be used to have a better understanding of reaction mechanisms and to improve the performance of the electrodes. SEC-Raman has already fulfilled this purpose for ORR on metal surfaces [193]. Kim et al., have prepared few-layered mild reduced graphene oxide (f-mrGO) coated P50 on carbon paper electrodes and have investigated the ORR activity of these electrodes towards ORR using SEC-Raman. Their results revealed that either epoxy groups on the basal plane or ring ether groups located at the edges could enhance the electrochemical activity for two-step $2e^-$ pathway [295]. In another work, the evolution of the G peak upon redox reaction of RuHex, FcMeOH and $Fe(CN)_6$ on CVD synthesized graphene was used to distinguish the outer-sphere electron transfer from the inner-sphere process. The results also showed that the conductivity of graphene is influenced by the adsorbed species during electrochemical measurement leading to the complication in the analysis of the cyclic voltammograms of these samples [189].

4.1.2 Aims of Study

Here we report detailed SEC-Raman characterization of N-doped and pristine graphene samples. In order to have a better insight into the role of different nitrogen configurations, active sites, and ORR mechanism, samples with different N dopants were prepared. This report aims to propose a detailed ORR mechanism and introduce electrochemical active sites on N-doped graphene using a comprehensive investigation about Raman peaks associated with surface groups of N-doped graphene inside alkaline electrolyte.

4.2 Experimental

4.1.3 Synthesis of N-doped Graphene

The N-doped graphene films were synthesized by CVD on Cu foils (25 µm thick) at 950 °C using the parameters which we reported in detail in our previous work [19]. The samples were then subjected to N_2 plasma to dope graphene with nitrogen. The doping concentration and configuration were adjusted using the previously modified plasma duration and plasma power parameters. The samples were finally transferred on FTO

coated glass substrates through a wet chemistry-based transfer method [19] to characterize physically and spectroelectrochemically.

4.1.4 Physical Characterizations

X-ray photoelectron spectroscopy (XPS) measurements were performed using a laboratory system (Thermo K-alpha) equipped with a monochromatized Al K-alpha X-ray source.

4.1.5 SEC-Raman Characterizations

SEC-Raman measurements were carried out using a homemade electrochemical cell setup attached to a Renishaw INVIA Raman spectrometer while setting the laser excitation wavelength at 532 nm and laser power to 4.1 mW. The electrochemical home-made cell setup, which was attached to a Biologic SP-150 potentiostat, had a three-electrode configuration consisting of a platinum coil as a counter electrode, an Ag/AgCl in 4 M KCl as a reference electrode, and N-doped graphene on FTO substrate as a working electrode. The chronoamperometry (CA) was measured by setting potentials with 0.03 V intervals from -0.15 V to -1.20 V (vs. Ag/AgCl) for 3 minutes. After keeping the sample at a constant potential for 1 minute, the corresponding Raman spectrum was recorded. The experiments were performed in N_2 and O_2 saturated 0.1 M KOH electrolyte solution at room temperature. All potentials reported here are vs. Ag/AgCl. The results were deconvoluted using the Gaussian function. The error bars are calculated based on the coefficient of determination (COD or R-square) value obtained from Origin-Pro after fitting the SEC-Raman results.

4.1.6 Raman Spectra of pristine and N-doped Graphene

Graphene has become a benchmark material for Raman spectroscopy investigations owing to its well-defined and well-understood spectral features. Raman spectrum of single-layer graphene without defects contains only G and 2D peaks. The D and D´ peaks are both defect-activated modes (Figure 4-1). G peak at ~1585 cm^{-1} arises from doubly degenerate Raman-active optical vibration in which the carbon atoms move in the graphene plane [296]. The D peak at ~1345 cm^{-1} is attributed to longitudinal optical phonons around the Dirac point and activated by double resonance which connects K and K′ points in the first Brillouin zone of graphene [297]. D´ peak at ~1620 cm^{-1} originates from an intravalley double-resonant scattering process that activates phonons with a small q [298] and 2D peak (second order of the D peak) at ~2680 cm^{-1}. Additional features in the vicinity of D, G, D´, and 2D peaks could also exist, and the frequency positions and

intensities of those peaks, as well as the fundamental ones, require in-depth analysis to develop a clear insight into the involvement of graphene in the ORR.

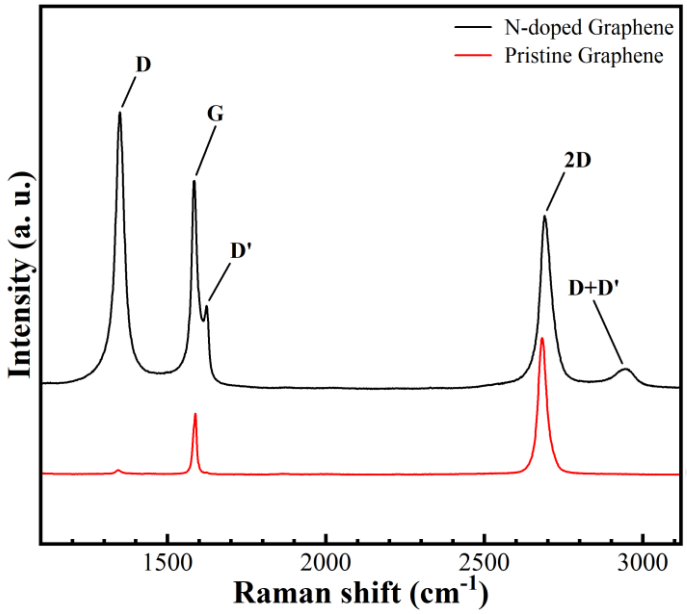

Figure 4-1 Raman spectra of a pristine defect-free graphene (red spectrum) and N-doped graphene (black spectrum)

4.3 Operando Characterization of N-doped Graphene

Our results presented in Figure 4-2 clearly show that there are two additional peaks in the lower (D_1) and higher (D_2) frequency sides of the D peak. D_1 and D_2 appear between 1315-1325 and 1362-1372 cm^{-1}, respectively. By Lazar et al., D_2 has been assigned to the modes arising from C atoms bonded to the pyridinic (N_{pydn}) and pyrrolic (N_{pyrr}) nitrogen groups [299]. While in general, both D and D´ peaks are known to be defect-activated modes, recent studies have distinguished these two by correlating the D peak with the sp^3 disorders [295]. As a result, it is expected to see the splitting of the D peak and formation of D_2 upon the creation of N_{pydn} and N_{pyrr}. The origin of D_1 will be discussed in the next sections. In the G region, three distinct peaks between 1500 and 1585 cm^{-1} can be seen. The calculations of Vecera et al. predicted the presence of two peaks in this region for hydrogenated/hydroxylated graphene [300]. According to their results, the functionalization of graphene with H/OH groups causes an alteration in the angle of C-C-C bonding and lifts the hydrogenated/hydroxylated C. As a result of this modification, there will be a range of frequencies for the E_{2g} mode vibration of the graphene structure. This is the origin of the creation of the G´´´, G´´ and G´ peaks in deconvoluted Raman spectra presented in Figure 4-2. Also, it can be expected that the coexistence of hydrogen and hydroxyl groups on the graphene will lead to a situation more complex than what

they have considered by combining calculated Raman spectra of hydrogenated graphene with hydroxylated graphene. As a result, we can see additional peaks in this region. While in almost all of the studies performed on the Raman spectrum of graphene, the D´ peak has introduced as the closest peak to G peak in its higher frequency side, our results show that an additional peak, which in this article is mentioned as G*, is present between 1601 and 1611 cm^{-1}. Previous calculations have predicted the presence of a peak at ~1647 cm^{-1} due to the Stone-Wales defects [290]. A peak (assigned as D´´) can be seen in the same frequency in Figure 4-2. Finally, the splitting of the 2D band region of graphene can have multiple basis. The variation of the number of components of 2D peak with the number of layers [294] and evolution of a single component 2D peak of graphite to a three and then two-component peak upon heat treatment [301] are just some examples of these different sources. However, considering the intensity of the shoulders shown in Figure 4-2, the strain-induced asymmetry of the Brillouin zone is the main reason for the splitting of 2D band to $2D_1$, 2D and $2D_2$ peaks. There are two possible scattering processes responsible for 2D peak of a graphene. These processes, which are usually referred as inner and outer processes based on the momentum transfer path length, are attributed to the scattering involving three *K´* points surrounding a given *K* point. For an unstrained single-layer graphene sheet, the *K´* points are totally equivalent, resulting in a single 2D peak. However, due to the distortion of graphene lattice under strain, the distance of these points with regards to the *K* point changes. As a result, the corresponding phonon energies would be different, reflecting as the splitting of 2D peak [302]. The intensity and position of the $2D_1$ and $2D_2$ peaks would change upon any alteration in the strain level, which is caused by the functionalization of the graphene.

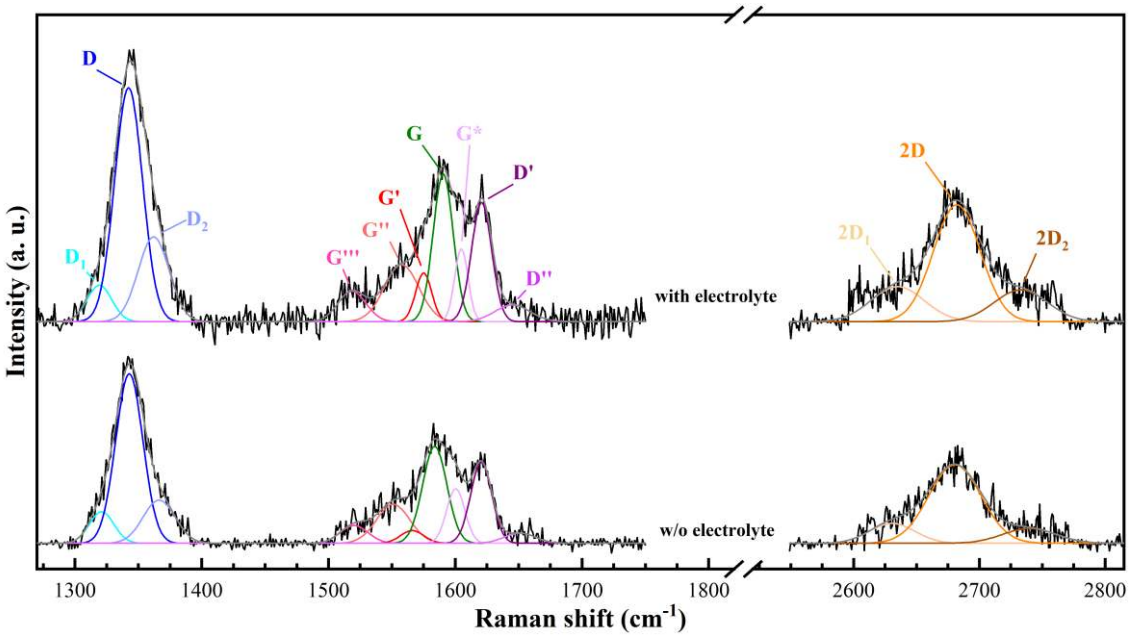

Figure 4-2 Raman spectra of PNG before immersing inside the O_2 saturated 0.1 M KOH electrolyte (lower panel) and after immersing inside the electrolyte (upper panel)

The analysis of the Raman peak intensity ratios with and without electrolyte (presented in Figure 4-2) shows that its I_D/I_G and $I_{D'}/I_G$ are 2.1 and 0.8, respectively, suggesting that graphene is doped with pyridinic N (PNG henceforth) [19]. Also, as it can be seen in Figure 4-3, before applying any potential, the I_{D_2}/I_G ratio is almost two times bigger than the value of this ratio in the sample where the majority of N dopants in the spot illuminated by Raman laser have graphitic configuration (GNG henceforth) and pristine graphene. Hence, it can be concluded that PNG sample is mainly doped with N_{pydn}.

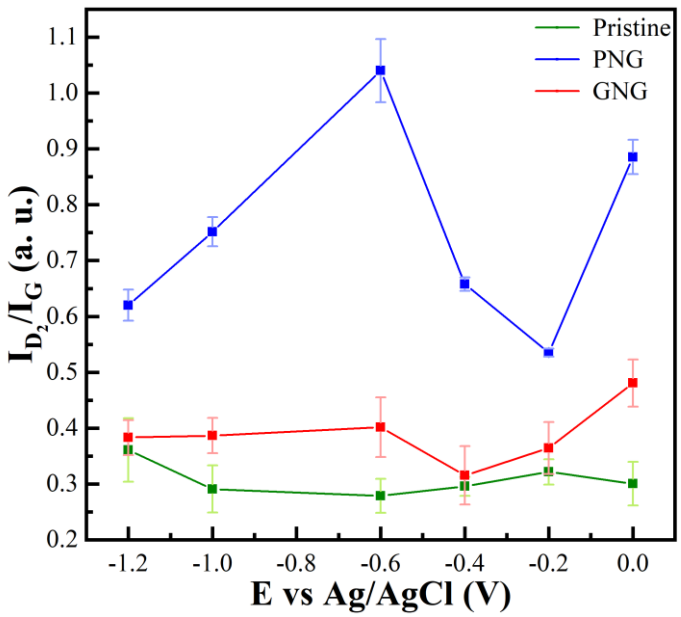

Figure 4-3 I_{D_2}/I_G ratio change for Pristine (green), PNG (blue), and GNG (red) samples without applying any bias (shown at E = 0.0 V) and under different cathodic potentials.

The results of XPS characterizations, which are shown in Figure 4-4, revealed that the conclusion made about the N configuration of PNG based on Raman results was correct. The N 1s spectrum of PNG has two main peaks at ~397.8 eV and ~399.1 eV, which are attributed to the pyridinic N attached to the Cu substrate ($N_{pydn'}$) and pyridinic N that are not attached to the Cu substrate (N_{pydn}), respectively [19]. On the contrary, graphitic N (N_{grap}) is not the dominant N configuration in the GNG sample and only 30% of the total N are N_{grap}. This inconsistency between the Raman results and XPS spectrum of GNG arises from the larger spot size of the XPS, which is almost 20 times bigger than the spot size of Raman. Hence, it can be concluded that while GNG has N_{pydn}, N_{pyrr} and N_{grap}, the spot of the sample analyzed in the SEC-Raman investigation was mainly doped with N_{grap}. Finally, the N 1s and C 1s spectra of the pristine sample confirm that while this sample does not contain any N dopants, it does not have a perfect structure and has some defects which result in the formation of the peak at ~288.0 eV of the C 1s spectrum.

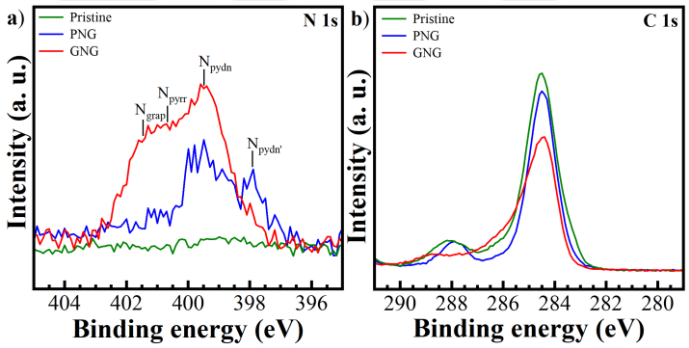

Figure 4-4 a) N 1s and b) C 1s spectra of pristine, PNG and GNG samples.

Figure 4-5 shows the differences in Raman peak intensity ratios for the PNG before and after placing it inside the O_2 and N_2 saturated electrolyte. The increase of all of the peak intensity ratios (except I_{G*}/I_G) in O_2 saturated electrolyte indicates that the G peak intensity has been dropped. This could be due to the adsorption of species on the electrode which introduces perturbation to the C-C bond stretching vibration mode. The same situation is also valid for PNG in N_2 saturated electrolyte, with the exception of I_{G*}/I_G, $I_{D'}/I_G$ and I_{2D}/I_G. Despite the general increasing trend in the intensity ratios after immersing inside both electrolytes, the highest amount of increase is observed in the $2D_1$, $2D_2$ and the peaks related to the vibration modes of hydrogenated/hydroxylated C (G´´´, G´´, and G´). While the decrease in the G peak intensity is the main reason for the intensity ratio increase upon immersing the sample inside the electrolyte, the intensities of G´´´,

G´´, and G´ also increase due to adsorption of H and/or OH species. The strain induced by this adsorption results in the increase of the intensity of $2D_1$ and $2D_2$ peaks as well.

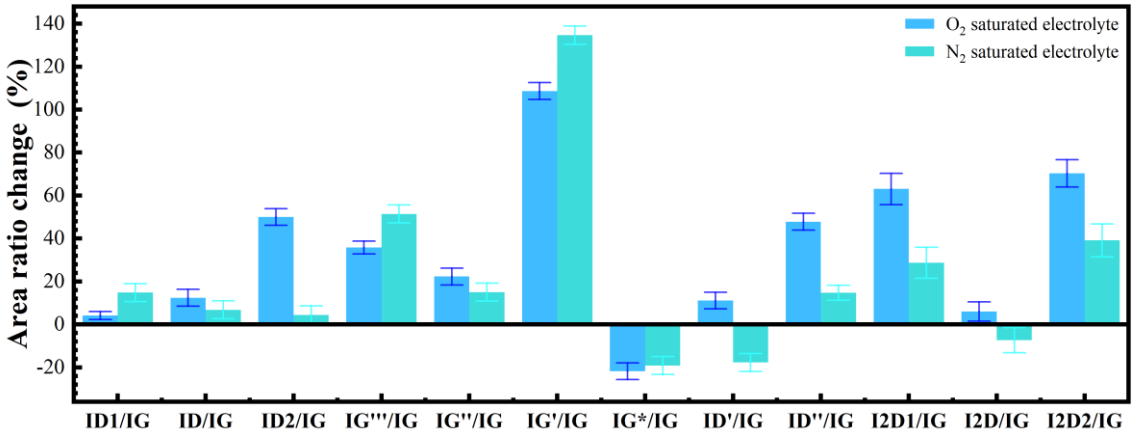

Figure 4-5 Raman intensity ratio change in percentage for PNG before and after immersing inside N_2 and O_2 saturated electrolyte.

The fact that G^* peak intensity shows more drop compared to G peak in both electrolytes, can be a sign to attribute this peak to the vibration of C atoms away from defected regions. The ascription of D´ band to the vibrations of oxidized carbon atoms in sp^2 basal plane has already been shown in some previous reports [295], [303]. On the other hand, the calculations by Lazar et al., for the chemisorbed N atoms and epoxy O on the basal plane of graphene have shown that upon formation of bridge-like structure between a heteroatom and graphene basal plane, a peak at ~1610 cm^{-1} appears. [299]. This is the same vicinity where we observe G^* in our results. Hence, it can be concluded that both G^* and D´ peaks are attributed to the vibration of defected C atoms in the basal plane. Since D´ is related to an intravalley double-resonant scattering process, the alteration in the heteroatom adsorbed on the basal plane, which affects the frequency of the vibration, can cause the splitting of this peak. Our findings show that while D´ is related to the vibration of basal C atoms connected to N atoms, the G^* peak is due to the vibration of similar C atoms which are covered by weakly adsorbed hydroxyl groups. Since the extent of variation of I_{2D}/I_G shown in Figure 4-5 for both N_2 and O_2 electrolyte experiments are comparable with their error bar, it is not possible to judge about the intensity change of 2D peak upon immersion inside the electrolyte.

When we study the percentage of changes in the peak intensity ratios for the N_2 experiment of pristine graphene and the GNG sample with and without electrolyte (Figure 4-6), it can be seen that the GNG sample has a similar trend as PNG with most of the peak ratios increasing due to the decrease in the G peak intensity, which is induced by the

adsorption of H/OH groups. However, with the absence of N groups in the pristine graphene sample, a lower amount of H and OH groups are adsorbed on the sample and hence we have a random change in the intensity ratios.

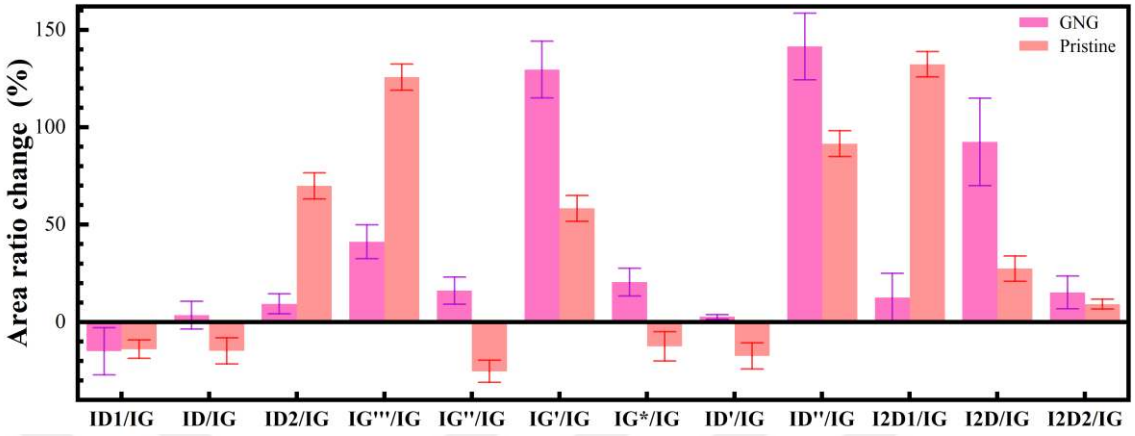

Figure 4-6 The change in the Raman spectrum intensity of pristine (orange) and GNG (pink) samples before and after immersing inside N_2 saturated electrolyte.

The significant role of N groups in the adsorption of H/OH groups is further approved by comparing the I_{Gtot}/I_G (G_{tot} is defined as the overall area under the curve for the hydrogenated/hydroxylated C atom motion-related peaks, i.e. G´´´, G´´ and G´) values in N_2 saturated electrolyte experiment of pristine graphene with PNG and GNG, shown in Figure 4-7. The results shown with arrow have been obtained from the samples in the absence of any cathodic bias and just after immersing the electrode inside the electrolyte. The lower I_{Gtot}/I_G of pristine graphene confirms that N impurities play a crucial role in creating adsorption sites for O and OH groups

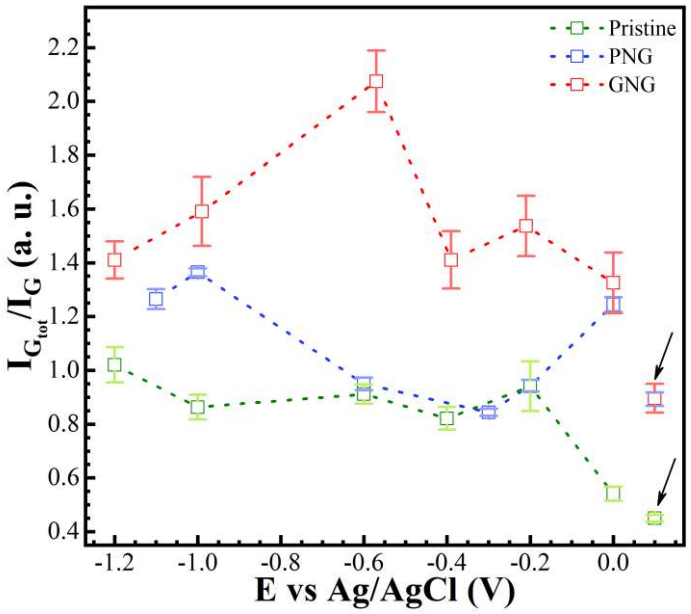

Figure 4-7 The evolution of I_{Gtot}/I_G values for pristine graphene (green), PNG (blue), and GNG (red) in N_2

saturated electrolyte

Previous calculations have shown that a sample with N_{pydn} is a suitable platform for simultaneous adsorption of OH and H groups. While the C atom adjacent to N_{pydn} (which is shown as C_A in Figure 4-8a) is a favorable site for strong adsorption of H [304], [305], The C atoms in the armchair edges (which are shown as C_B and C_C in Figure 4-8a) bond with OH strongly [306]. As a result, the PNG sample provides a suitable surface for water dissociation. This can be seen by comparing the G_{tot} to G peak intensity ratio for the PNG sample before and after immersing inside O_2 saturated 0.1 M KOH electrolyte with the GNG and pristine graphene (Figure 4-8b).

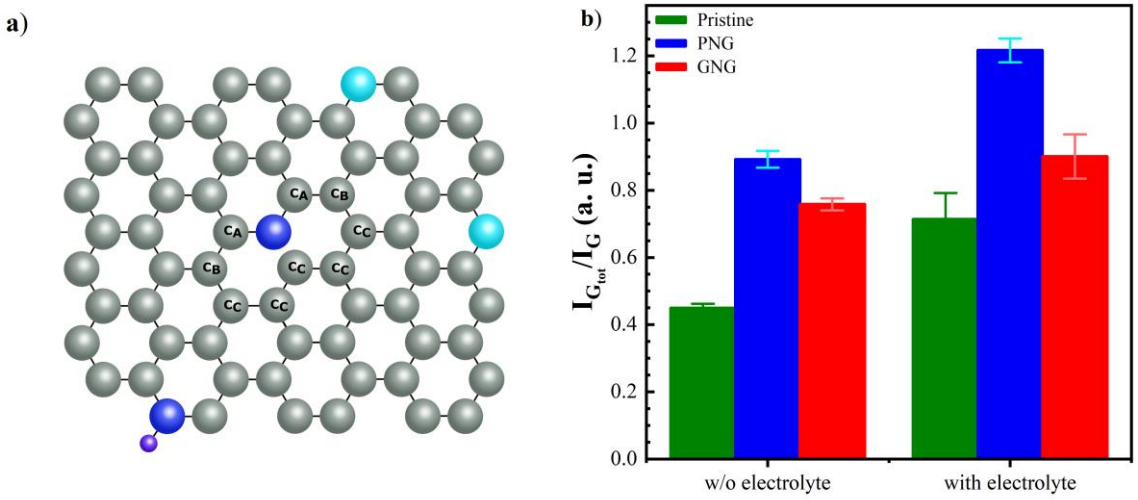

Figure 4-8 a) Schematic representation PNG structure and b) Intensity ratio of G_{tot} to G peak for PNG, GNG and pristine graphene before and after immersing inside the O_2 saturated 0.1M KOH electrolyte

Most of the previous reports regarding the activity of N-doped graphene towards ORR have introduced C_A as the active site for this reaction. In this case, H_{ads} will block the O_2 adsorption site. This is a similar result to the conclusion made by Kim et al. [288]. On the other hand, it has been shown that the presence of OH_{ads} groups promotes the outer sphere electron transfer [307]. So, it is likely for PNG sample to follow this path. In order for the ORR process to start, the O_2^- molecule, which is formed during outer sphere electron transfer process has to be adsorbed on the N-doped graphene. The active site for this adsorption is either basal C atoms (similar to the proposed mechanism in ref [288]) or C atoms at the edges, which are covered by OH and/or H groups. Our results suggest that O_2^- molecules attack the H_{ads} on the C_A and desorb as OOH^-. This is the reason for observing $I_{G'''}/I_G$, $I_{G''}/I_G$, and $I_{G'}/I_G$ become almost half between 0 and -0.2 V (Figure 4-9a-c). After this desorption, there will be a competition between H_2O and O_2 (or O_2^-) to adsorb on the C_A. However, since $OH_{(ads)}$ is already strongly adsorbed on C_B , it is not

favorable for H_2O to dissociate and O_2 (or O_2^-) will be adsorbed. Following this adsorption either two-step $2e^-$ or one-step $4e^-$ ORR mechanism will happen on this site. The proceeding ORR results in an increase in the amount of OH and OOH adsorbed on the sample, which leads to the increase in hydrogenated/hydroxylated C related peaks of PNG sample. We can see this trend between -0.20 V and -0.60 V in Figure 4-9a-c. The C_A site of PNG is not an ideal site for the HER reaction, due to the strong bonding between H and C_A. Consequently, at the HER onset potential (~ -1.00 V), this process proceeds by adsorption of water molecules on the N_{pydn} atoms, where H_2 can desorb easier. Because of this adsorption and HER process, the $I_{G'''}/I_G$, $I_{G''}/I_G$, and $I_{G'}/I_G$ exceed their initial value in 0.00 V. The adsorption of water on N_{pydn} results a decrease in the intensity of peaks related to N_{pydn}, which can be seen around -1.00 V for the I_{D_2}/I_G in Figure 4-9d. At higher potentials, there will be enough overpotential to desorb the OH bounded to the C_B and C_C and to initiate the HER via H adsorbed on C_A. This results in the decrease of the $I_{G'''}/I_G$, $I_{G''}/I_G$, and $I_{G'}/I_G$ at -1.20 V. Meanwhile, since we don't have extreme negative values for adsorption free energy of OH in the zigzag edges, negligible water dissociation will happen on those sites and consequently they won't have a strong effect on the $I_{G'''}/I_G$, $I_{G''}/I_G$, and $I_{G'}/I_G$ trend.

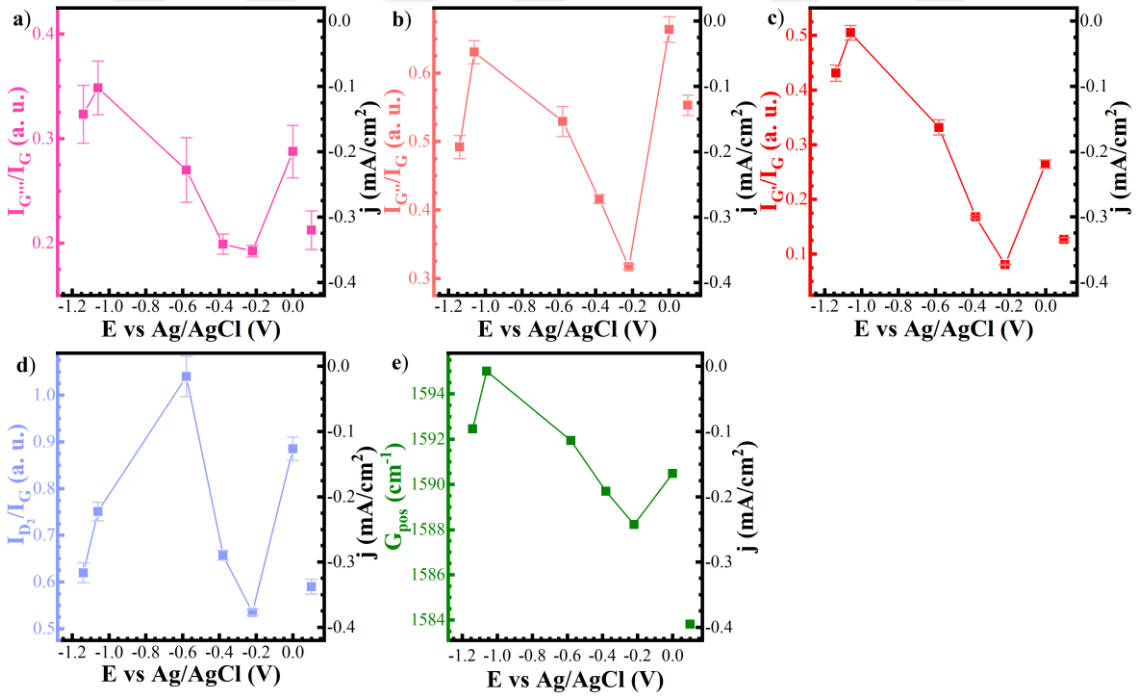

Figure 4-9 Raman peak intensities and position versus the applied potential for the PNG sample in O_2 saturated electrolyte. The single points disconnected from the spectra have been obtained without applying any potential.

The analysis of intensity ratio changes between 0.00 V and -0.20 V for all of the peaks of

PNG (shown in Figure 4-10) reveals that there is no increase in any peak ratio in both N_2 and O_2 saturated electrolytes (Except $I_{D'}/I_G$ in N_2 saturated electrolyte). This is due to the desorption of weakly adsorbed hydroxyl groups from the surface, which results in the increase of G peak intensity. However, when we compare the changes in intensity ratios in N_2 and O_2 saturated electrolytes, they are more pronounced in the O_2 saturated experiment with $I_{G'''}/I_G$, $I_{G''}/I_G$, $I_{G'}/I_G$, I_{2D_1}/I_G, and I_{2D_2}/I_G having the deepest drop. The overall higher drop percentage in the O_2 saturated experiment shows that in addition to the desorption of weakly adsorbed OH groups, there is another desorption happening on the N-doped graphene in this potential range. This additional change can be the desorption of H groups by O_2^- species. Observing the highest value of decrease for H/OH and strain sensitive peaks is in well agreement with this hypothesis.

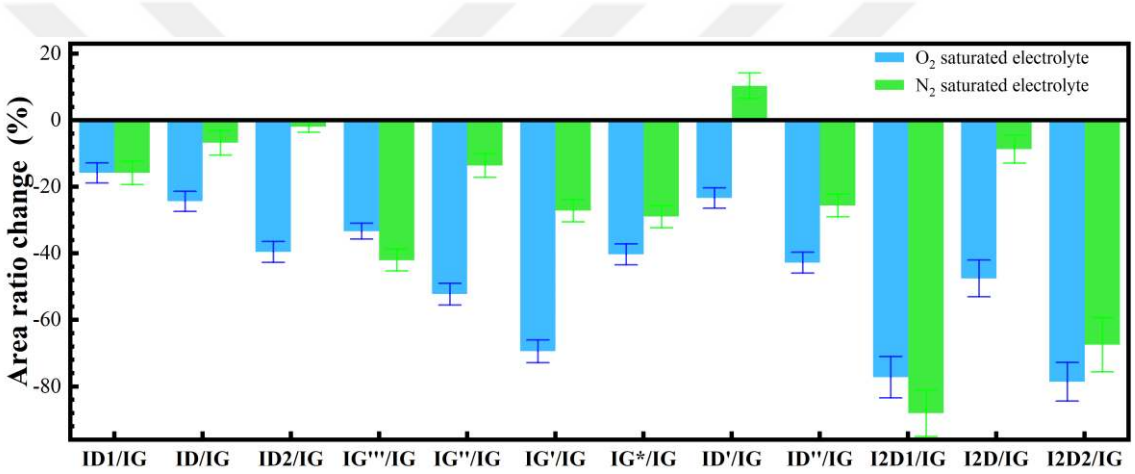

Figure 4-10 Raman intensity ratio change in percentage for PNG between 0.00 NS -0.20 V inside N_2 (green) and O_2 (blue) saturated electrolyte

The alteration in the adsorbed species on the samples, the applied potential, proceeding reactions and hence the changes in the concentration of the molecules in the Helmholtz layer, can affect the position of the peaks in the Raman spectra of graphene. Previous studies have shown that the G peak has a blue shift upon applying a negative voltage to the graphene [308]. This is due to the suppression of Kohn anomaly by charge carriers [154], [309]. When we study the position of the G peak (G_{pos}) for PNG in the O_2 saturated electrolyte experiment, it has a general blue shift trend with two redshifts (Figure 4-9e). Both of these redshifts coincide with the potentials at which there is desorption of the negatively charged species from the sample. First, it happens between 0.00 and -0.20 V, where we have desorption of OOH^-. Here the applied potential is low, so the G_{pos} is sensitive to the desorption of OOH^-. In the rest of the procedure, we don't see any redshift despite continuous desorption of OH^- produced via ORR. This is due to the fact that the

effect of applied potential is dominant. At the potential region between -1.00 and -1.20 V, again there is redshift. Despite the high negative applied potential, the number of strongly adsorbed OH^- is high enough so that their desorption affects the G_{pos}. The significant blue shift of the G_{pos} in both N_2 (Figure 4-11d) and O_2 (Figure 4-9e) saturated electrolyte when comparing the results before and after immersing the sample inside the electrolyte, further approves the sensitivity of G_{pos} to the negatively charged species at the absence of any applied potential. Also, this shows that the amount of OH^- adsorbed on the surface is higher than H, which is expected based on the fact that there are more sites for the adsorption of OH^- in the armchair edges of N_{pydn} doped graphene than the sites for H adsorption and also the concentration of available OH^- species is higher than H species due to the pH of the electrolyte. Despite the absence of recombination between O_2^- with H_{ads} in the N_2 saturated electrolyte experiment, there is still a slight red shift in the G_{pos} between 0.00 and -0.20 V (Figure 4-11d), which is due to the desorption of weakly adsorbed OH^- groups. The effect of the desorption of these groups can also be seen in the $I_{G'''}/I_G$, $I_{G''}/I_G$, and $I_{G'}/I_G$ plots in Figure 4-11a-c, where the ratios decrease but not as much as they do for O_2 saturated experiment. Finally, at the potential range of -1.00 and -1.20 V, there is a red shift in G_{pos} in N_2 saturated electrolyte which has the same origin as in O_2 saturated electrolyte and is related to the desorption of strongly adsorbed OH^- species.

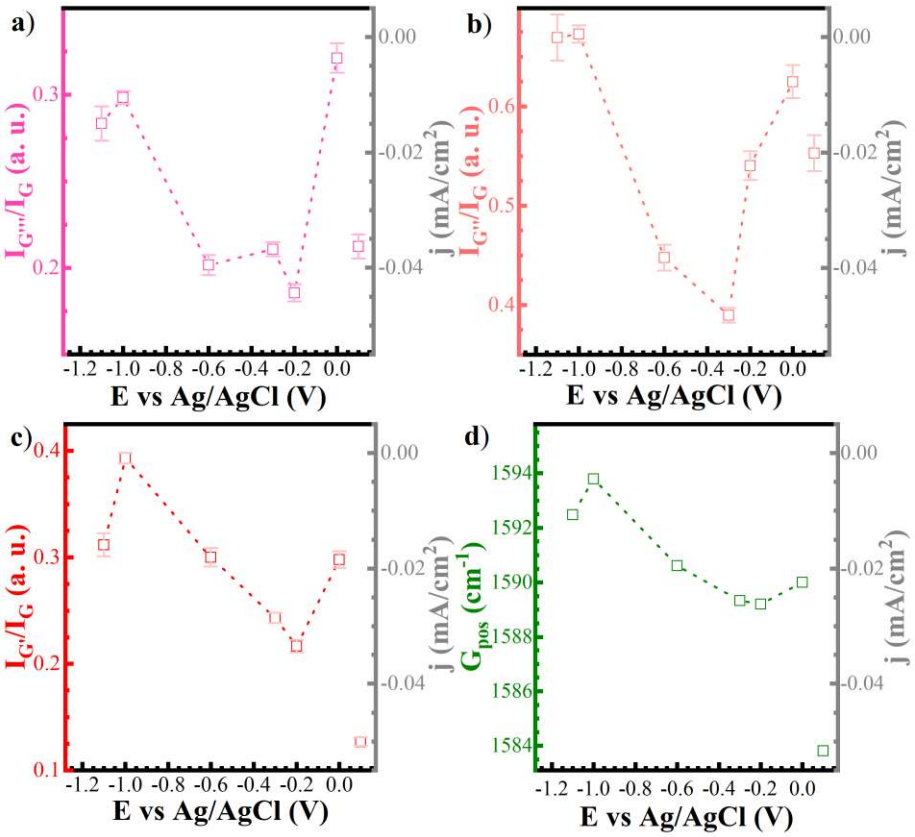

Figure 4-11 a) $I_{G''}/I_G$, b) $I_{G'}/I_G$, c) $I_{G'}/I_G$ and d) G_{pos} versus applied potential in N_2 saturated electrolyte for the PNG sample. The single points disconnected from the spectra have obtained without applying any potential.

For the GNG sample, the adsorption of O_2/O_2^- species and desorption of OOH^- produced by recombination of H_{ads} with O_2-, are not consecutive reactions. This is based on the previously performed theoretical adsorption Gibbs free energy calculations which introduce C_A and C_C shown in Figure 4-12, as the most favorable sites for the H and OH adsorption. Meanwhile, O_2 prefers to adsorb on either C_A or C_B [310]. As a result, there are available sites for O_2/O_2^- adsorption (C_B) while having H and OH on the surface.

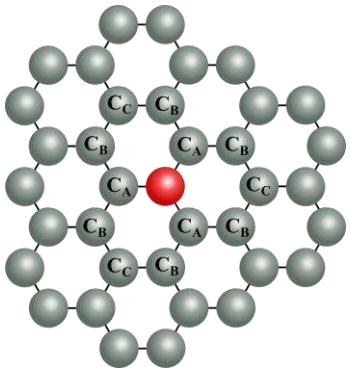

Figure 4-12 Schematic representation of GNG structure. The red atom is N_{grap} and the neighboring C atoms are labeled based on their connection and distance from the N_{grap}.

As a result, not only there is no red shift for G_{pos} of GNG in the O_2 saturated electrolyte

experiment between 0.00 and -0.20 V, but also the combination of a) applied negative potential, b) adsorption of O_2 or O_2^- (and initiation of ORR), c) reaction of H_{ads} with O_2^- (and desorption as OOH^-), and d) desorption of weakly adsorbed OH^- groups result in blueshift for G_{pos} (Figure 4-13d). However, in the N_2 saturated electrolyte, the component (b) and (c) of above-stated parameters are not present. Hence, we have a redshift similar to the N_2 experiment of the PNG sample. When we study the changes in -1.0 V to -1.20 V potential region of the GNG sample, no redshift is observed for neither N_2 nor O_2 experiment, which is in contrast with the trend seen for the PNG sample. This can be attributed to the stronger interaction of remaining OH adsorbates.

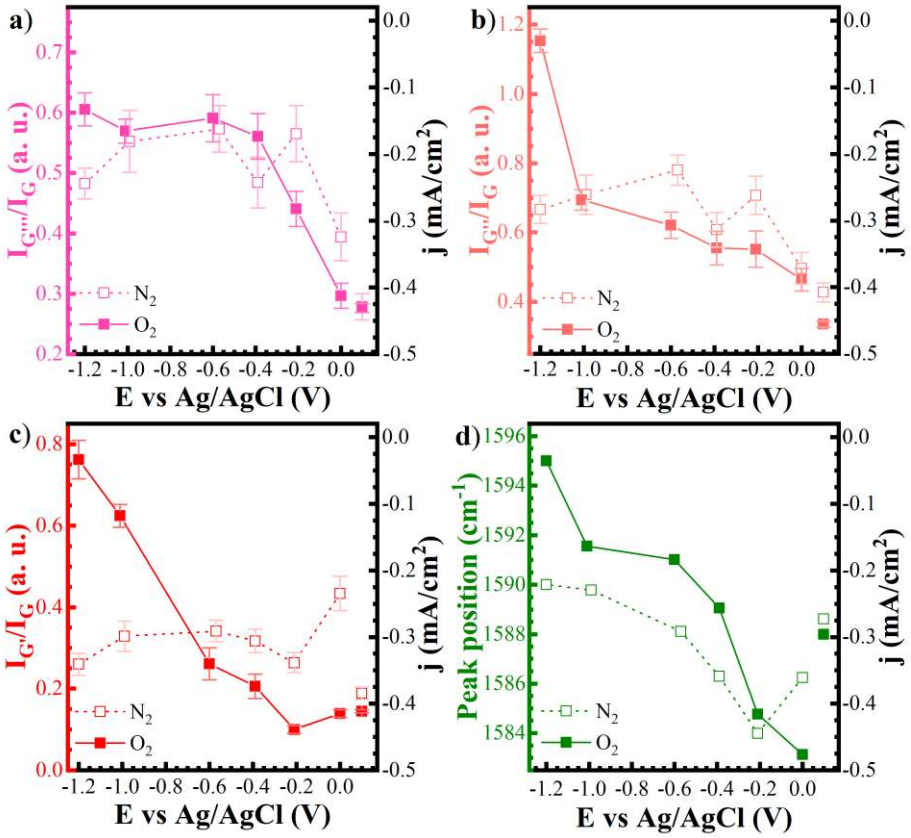

Figure 4-13 a) $I_{G''}/I_G$, b) $I_{G''}/I_G$, c) $I_{G'}/I_G$ and d) G_{pos} versus applied potential in O_2 (solid line) and N_2 (dashed line) saturated electrolyte for the GNG sample. The single points disconnected from the spectra have obtained without applying any potential.

This is further approved when we compare the I_{Gtot}/I_G ratio of GNG with the same ratio of PNG. Figure 4-14, shows that while we have a higher value of I_{Gtot}/I_G before placing the sample inside the electrolyte and at 0.00 V for PNG, which is due to the presence of more suitable adjacent sites for H and OH adsorption and hence higher water dissociation rate, the GNG sample has higher values at -1.2 V. This reveals that OH groups are bonded to graphene more strongly and the applied potential is not high enough to disrobe them.

Comparing the $I_{G'''}/I_G$, $I_{G''}/I_G$, and $I_{G'}/I_G$ plots and G_{pos} of GNG at higher potential range (Figure 4-13), we can see that H/OH related peak intensities drop in N_2 experiment, but they increase in O_2 experiment. Meanwhile, G_{pos} continues its blue shift in O_2, but it becomes constant for the N_2 experiment. These changes show that the required energy for the desorption of OH alters when the electrolyte is changed. This can be attributed to the presence of O_2^- species in the inner Helmholtz layer of O_2 saturated electrolyte experiment.

Comparing the alterations in the $I_{G'''}/I_G$. $I_{G''}/I_G$ and $I_{G'}/I_G$ between 0.00 and -0.20 V in O_2 saturated electrolyte for GNG (Figure 4-13a-c) with the same peak intensity ratio changes in PNG (Figure 4-9a-c), it can be seen that there is an opposite trend. This can be attributed to the possibility of the adsorption of O_2/O_2^- on C_B while C_A and C_C sites are covered with H and OH in GNG. Further progress of ORR on the C_B site results in an increase in the $I_{G'''}/I_G$, $I_{G''}/I_G$ and $I_{G'}/I_G$ values.

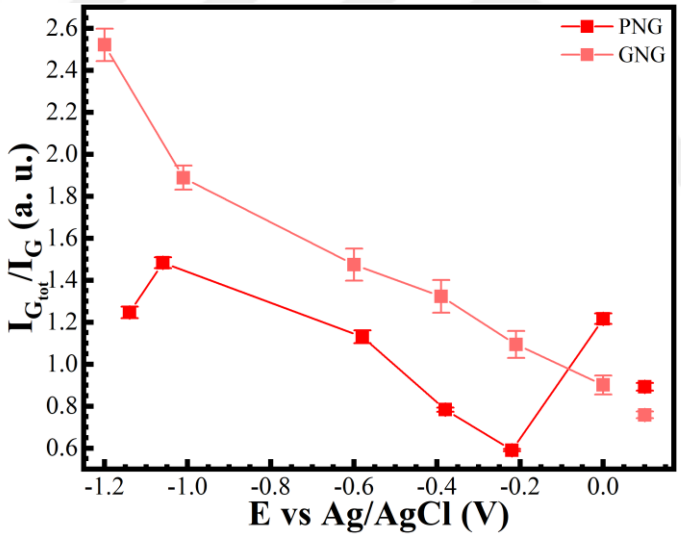

Figure 4-14 I_{Gtot}/I_G versus applied potential for the PNG and the GNG samples. The single points disconnected from the spectra have obtained without applying any potential.

In light of the above-mentioned analysis, it can be seen that the active site for ORR in N_{pydn} and N_{grap} doped graphene samples are not identical. However, there are some similarities between the two systems. The proposed site for the adsorption of O_2^- is adjacent to a C bonded to OH molecule. As a result, there is a possibility that instead of well-known two-step $2e^-$ or one-step $4e^-$ pathways, O_2^- interacts with OH and follows the pathway shown with Equation 4-9 to Equation 4-14. The adsorption and reaction sites which are mentioned inside the parentheses are attributed to the GNG sample. As a result of the interaction of O_2^- with the adjacent OH, a single O will be produced on the C_B and

C_C for N_{pydn} and N_{grap} doped graphene, respectively. This single atom is shown by O´ in Equation 4-11. Due to the strong bonding between OH groups and C atoms on which the O´ is formed, we believe it would transform to OH via Equation 4-14 and will remain on this site until the next ORR reaction takes place. During this proposed pathway $4e^-$ get consumed producing 4 OH^-. So, from the transferred number of electrons and number of generated OH^- point of view, it is not possible to distinguish this process from the pathway shown in equation 1 to equation 5. As a result, while SEC-Raman measurement does not provide direct evidence about the ORR pathway, it delivers a clear image about the alterations on the surface of graphene under bias, which can be used as a guideline to consider new pathways for the ORR.

$$O_2 + e^- \rightarrow O_2^- \qquad \text{Equation 4-9}$$

$$O_2^- + C_A(C_B) \rightarrow O^-_{2(ads,C_A(C_B))} \qquad \text{Equation 4-10}$$

$$O^-_{2(ads,C_A(C_B))} + OH_{(ads,C_B(C_C))} \rightarrow OH^- + O_{(ads,C_A(C_B))} + O'_{(ads,C_B(C_C))} \qquad \text{Equation 4-11}$$

$$O_{(ads,C_A(C_B))} + H_2O + e^- \rightarrow OH^- + OH_{(ads,C_A(C_B))} \qquad \text{Equation 4-12}$$

$$OH_{(ads,C_A(C_B))} + e^- \rightarrow C_A(C_B) + OH^- \qquad \text{Equation 4-13}$$

$$O'_{(ads,C_B(C_C))} + H_2O + e^- \rightarrow OH^- + OH_{(ads,C_B(C_C))} \qquad \text{Equation 4-14}$$

4.2 Conclusion

In conclusion, detailed investigation about the evolution of the Raman spectra of N_{grap} and N_{pydn} doped graphene revealed that prior to the ORR process, H/OH groups adsorb on different sites of N-doped graphene. These groups have a significant effect on the mechanism by which ORR proceeds and the reaction sites of ORR. While in N_{pydn} doped graphene, the occupation of C atoms adjacent to N_{pydn} and the presence of OH groups promote the outer sphere electron transfer mechanism, the reaction site on N_{grap} is different. Hence, Raman spectra of N_{grap} and N_{pydn} doped graphene show different trends under cathodic potentials. Finally, our results revealed that in addition to the widely accepted ORR pathways suggested for the N-doped graphene, which are inspired by the finding about metallic electrodes, another 4e- pathway is also possible. The neighboring O_2(or O_2^-) and OH groups adsorbed on the N-doped graphene play the main role in this

mechanism.

Chapter 5:
Effect of Structural Modifications on HER Activity of MoS_2

5.1 Introduction

5.1.1 Structure, Properties, and Applications of MoS_2

TMDs are materials with similar dimensionality to graphene. One of the main differences between TMDs and graphene is the presence of ~1-2 eV bandgap in TMDs, while pristine graphene does not have any bandgap [201].

The structure of TMDs can be described by the formula MX_2, where M and X are the transition metal and chalcogen, respectively. The layers of MX_2 are hexagonal, with Mo and S atoms alternately located at hexagon corners. A monolayer of MX_2 generally consists of a plane of M atoms sandwiched between two planes of X atoms. While inside the layers, there is covalent bonding between M atoms and the nearest X atoms, generally forming a metal-centered triangular prism or octahedral configuration [311], the interaction between the layers is mainly governed by Van der Waals interactions [312]. The structural type of the TMDs is classified based on the intralayer configuration and the interlayer distance is determined by interlayer interaction [201]. There are three main structural polytypes of MX_2 layered structure: 2H (hexagonal symmetry, trigonal prismatic coordination, two layers in each repeat unit), 3R (rhombohedral symmetry, trigonal prismatic coordination, three layers in each repeat unit), and 1T (tetragonal symmetry, octahedral coordination, one layer in each repeat unit) [313]. These polytypes are shown in Figure 5-1.

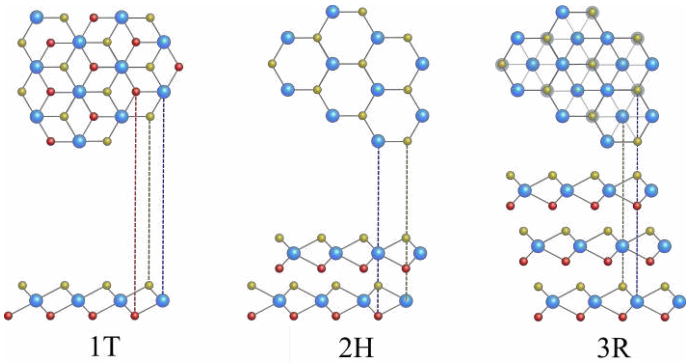

Figure 5-1 Schematic representation of MX_2 TMDs polytypes structure. The upper row shows the top view, and the bottom row shows the side view.

One of the unique properties of MX_2 is that their bulk form has an indirect bandgap, which can be dramatically tuned to a direct bandgap, when scaled down to monolayer. For instance, the maximum of the valence band of bulk MoS_2, which locates at the Γ point, shifts downward to the K point of the Brillouin zone as it scales down to monolayer, leading to unique semiconductor properties [314]–[316].

Although the 2H is the most stable phase of TMDs at room temperature, it has been shown that this phase can be transformed to the metastable metallic 1T phase through chemical and electrochemical intercalation of alkaline ions [317]. Due to its metallic nature, 1T MoS_2 has a very high electrical conductivity (10–100 $S.cm^{-1}$) [5]. Additionally, hydrophilicity, large interlayer spacing upon restacking, large anionic polarizability, and negatively charged surface of 1T MoS_2 have made it an excellent candidate for numerous applications such as electrochemical and photoelectrochemical catalysis, supercapacitors, batteries, and etc. [5]. However, due to its thermodynamical metastability, it gradually converts back to the 2H at room temperature [318]. The type and number of layers, edge morphologies, and degree of crystallinity are crucial factors that affect these materials' performance in various applications, including spintronic devices, thermal catalysis and electrochemical catalysis [319]. The determination of the nature of the different phases in MoS_2 compounds is generally based on the filling of Mo d orbitals because the p orbitals of sulfur are at much lower energy than the Fermi level. The structure of MoS_2 directly influences the filling of Mo d orbitals. Complete filling of orbitals gives rise to semiconducting behavior (2H), while partial filling results in metallic behavior (1T) [320].

Among the TMDs, group VIB metal dichalcogenides (i.e., molybdenum and tungsten disulfides (MoS_2 and WS_2) are the most studied candidates due to their moderate band

gaps of 1-2 eV, which are close to those of the conventional semiconductors such as Si and GaAs [321], [322]. The single and few-layered MoS_2 has shown promising performance in many applications such as catalysis [323], [324], electronics [325], [326], solid lubricants [327], batteries [328], biological systems [329], [330] and so on. MoS_2 is composed of S-Mo-S trilayer stacks, with weakly coupled layers and an interlayer space of approximately 3 Å. In addition to the four main crystal structures of MoS_2 (1H, 1T, 2H, and 3R) [331], intermediate distorted phases (such as 1T', 1T'', 1T''') can also be formed during the transformation of the main phases (Figure 5-2) [332].

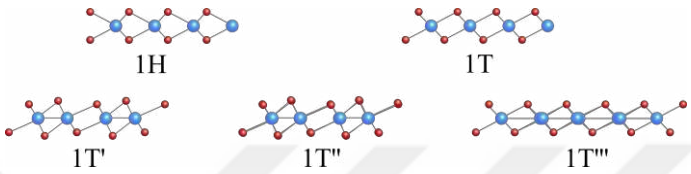

Figure 5-2 Schematic representation of main and intermediate distorted MoS_2 structures (side view)

Many efforts have been devoted to developing single-layer MoS_2 due to these appealing properties and potentials in various applications. The first investigations for obtaining 2D MoS_2 were conducted based on the mechanical exfoliation method [333], [334]. Despite the feasibility of producing high-quality 2D MoS_2 sheets, the low throughput limits this method in practical applications [27]. The liquid exfoliation [336]–[338] and electrochemical Li-intercalation [339] techniques have been used to synthesize large quantities of 2D MoS_2. These liquid phase-based strategies can exfoliate MoS_2 and stabilize the nanosheets due to their effect on the surface energy. However, inhomogeneous layer numbers, non-uniform size, and complex surface textures hinder the possibility of performing fundamental research on these sheets.

In addition to these top-down methods, some bottom-up techniques have also been employed to prepare 2D MoS_2. Wet chemistry-based synthesis methods such as hydrothermal and solvothermal reactions are the primary examples of these techniques. Previous studies have shown that the variation in the Mo and S precursors and the reaction parameters (such as temperature, time, and precursor concentration) affects the final product quality prepared by these methods. The samples synthesized by these methods are commonly low-quality MoS_2 flakes with abundant active sites for electrocatalysis applications [340]–[343].

Compared with chemical exfoliation, the CVD method is more efficient in growing high-quality monolayer MoS_2 films on different substrates with controllable thickness [344]–

[346]. Numerous CVD approaches have been tried to prepare monolayer and few-layered MoS_2 by modifying the precursors for Mo and S, growth substrate, temperature, duration, and pressure. In most of these studies, the Mo precursor (mostly MoO_3 powder) is placed inside the CVD chamber alongside S powder. The simultaneous or sequential vaporization of these powders and the reaction between MoO_3 and S result in the synthesis of 2D MoS_2 [50], [51], [54], [55]–[58]. In addition to this reaction, it is also feasible to trigger a reaction between pre-deposited Mo films and S vapor. For this purpose, it is possible to coat the desired substrate using PVD coating of metallic Mo [351] or transition metal oxide [353] or dip-coating of ammonium thiomolybdates [46]. However, the kinetics of growth and limitations in the deposition of thin continuous layers of Mo are major challenges for this strategy.

5.1.2 HER on MoS_2

In determining the best HER catalyst, the candidate material that is simultaneously efficient, durable, and cost-effective would be an ideal choice. MoS_2, is highly stable in many strong acids. However, the first HER activity studies of MoS_2 showed modest activity [355]. This observation was contrary to the activity prediction made by Nørskov based on the Gibbs free energy of hydrogen binding [94]. Later, the computational results from Hinnemann et al. revealed that S atoms on the Mo edges of the MoS_2 planes should be highly active for HER [356]. Following this finding, the race was on to improve the HER performance of MoS_2. Multiple factors such as the low concentration of exposed catalytic sites and the semiconducting behavior can be the reason for the poor catalytic performance of pristine MoS_2. Hence, it is essential to enhance the conductivity, elevate the intrinsic catalytic activity, and construct more active sites on MoS_2 to improve its HER activity.

Loading MoS_2 films on different substrates such as carbon cloth [357], carbon nanofiber [358], carbon nanotube [359], graphene [360], Au [361], Ti [362], and Si/SiO_2 [363] has been shown as an effective strategy to modulate its conductivity. The enhanced HER activity for the MoS_2 films on these substrates is mainly due to the improved electron transfer rate during the electrochemical reaction [360]–[362].

The edge sites, vacancies, and the atoms in the phase boundaries are MoS_2's intrinsic HER catalytic sites [123]. Historically, the S atoms at the edges were the first sites for which the high HER activity was revealed and different roots were developed to engineer their density to achieve high performance in the intrinsic activity of MoS_2 [356], [364]. Vertical

alignment of MoS_2 films on the substrate [363], creating defects on the films via post-synthesis hydrogen annealing or oxygen plasma treatment [62], and optimizing synthesis parameters to prepare smaller MoS_2 flakes [365], have been shown to be effective methods in increasing number of available edge sites. The S vacancies in the MoS_2 structure are acknowledged to improve the catalytic activity effectively. Hence, different methods, such as electrochemical reduction, [366] H_2, [62] or H_2O vapor etching [367], He plasma, [368] laser ablation, [369] and UV/ozone treatment [370] have been used to introduce these vacancies. The results obtained by Tsai et al. have shown that 12.5-15.62% S vacancy containing MoS_2 has the highest HER performance [366]. D. Voiry et al. have also studied the relationship between the amount of S vacancies and HER performance by heat-treating 2H-MoS_2 sample [371]. Their results showed rapid improvement in the HER performance of the S vacancy-containing samples until the S/Mo atomic ratio decreased to 1.7. After passing this threshold, the undercoordinated Mo sites become exposed to the electrolyte. Further increase in the treatment temperature, which results in the S stripping from the basal plane, showed much less effect in HER activity enhancement.

Phase and structural engineering are effective strategies to enhance catalytic performance through different mechanisms. The metallic 1T phase shows the highest HER performance among the 1T, 2H, and 3R phases, due to the faster charge transfer kinetics, improved H adsorption and activated S atoms in the basal plane [361], [372], [373]. Experimental results have revealed a significantly reduced Tafel slope from 110 $mV.dec^{-1}$ for 2H-MoS_2 to 43 $mV.dec^{-1}$ for 1T-MoS_2 approaching that of Pt at 30 $mV.dec^{-1}$ [317]. Thermodynamically the metallic 1T phase is unstable and gradually converts to the semiconducting 2H phase spontaneously [123]. As a result, besides multiple methods which have been used to synthesize 1T phase containing MoS_2, several strategies, including making heterojunctions on the basal plane [374]–[376], synthesis under a high magnetic field [377], intercalation, etc., have been applied to stabilize the metallic 1T phase. The phase conversion of the MoS_2 monolayer from 2H to 1T has been successfully traced by Suenaga et al. [306]. It has been shown that metastable distorted phases such as 1T', 1T'', and 1T''' can be formed during phase conversion due to the atomic gliding [332]. They also suggested that these metastable distorted phases could be the actual catalytic sites during the HER reaction [306]. Some studies further confirmed this, where the 1T' phase was founded to be more active than the 1T phase, and 1T' would convert from the

1T phase during electrocatalysis to work as the actual active catalytic phase [378]. Multiple studies made by Jiang et al. have shown that the H adsorption on 1T-MoS_2 promoted structural transformation to the 1T' phase [379]. Also, they found that after a crossover H coverage of 25%, the 1T phase becomes more stable than the 2H phase [372]. The closest ΔG_{H^*} value to zero was achieved around 12.5% ~ 25% H coverage. Their mechanistic investigations revealed the Volmer-Heyrovsky pathway to be the energetically favorable HER root on 1T-MoS_2, with Heyrovsky being the rate-determining step.

Most of the CVD synthesized MoS_2 films contain a mixture of 1T and 2H (or 1H) phases. In contrast to the rather complicated 2H-2H (1H-1H) phase boundary where there is a possibility for the presence of different ring arrays (such as 4-6, 6-8, 5-7, and 4-4 rings) [380], the 1T-2H phase boundary is simply a region where the S atoms slide. This boundary can be either in zigzag or armchair form [381]. Investigating the HER activity of the interface between the phases is essential for revealing the intrinsic activity of CVD-grown MoS_2. Zhu et al. fabricated the 2H-2H domain and 2H-1T domain in monolayer MoS_2 and compared the HER activities of these two domains [324]. Their theoretical results showed that the 2H-1T domain has superior activity with $\Delta G_{H^*} = -0.13$ eV at the 2H-1T boundary. This issue was further investigated in the computational study by Jiang and coworkers [381]. They showed that the HER mechanism in the basal plane of 1T-MoS_2 follows the Volmer-Heyrovsky route. However, in the "zigzag" and "armchair" 1T-2H boundaries the Volmer-Tafel reaction on S atoms was energetically favorable which was partially in contrast with the results obtained in a previous study where the Volmer-Heyrovsky route on S atoms was shown to be the favorable mechanism in 1T'-2H boundaries [382].

Doping has been extensively applied to activate MoS_2, through various effects, including generating new catalytic sites, enhancing conductivity, and elevating reaction kinetics. While Re, Tc, and Mn dopants help to improve the catalytic activity of MoS_2 by stabilizing the 1T phase [383], Zn dopants modulate the energy level and induce more active sites [384]. Moreover, doping 2H-MoS_2 with metallic SWNTs improves the catalytic activity by enhancing its conductivity [287]. The incorporation of dopants in the MoS_2 structure can enlarge the interlayer spacing, thus altering the d-band electronic structure and reducing the hydrogen adsorption free energy, facilitating the HER process. Doping MoS_2 with Se has shown to be effective in modulating the bandgap and, hence,

improving the catalyst's conductivity for HER [385]. Previous studies have shown that doping MoS_2 with nonmetal heteroatoms such as nitrogen, boron, or phosphorus has a dual function; it activates the S edges by modulating the electronic structure and elevating the kinetics of HER, and promotes rapid charge transfer. Xiao et al. studied the effect of the N dopants on edges and basal plane of MoS_2 and found that N-doped MoS_2 with ~8% N content have an excellent HER activity with exhibiting an overpotential of 121 mV (100 mA cm^{-2}) and 41 mV dec^{-1} for the Tafel slope [386]. Another study shows that the P dopant activates the basal plane and reduces the valence charge on Mo atoms; therefore, S-edge sites become optimized at the same time [386]. Finally, P and O co-doped catalyst exhibited an onset overpotential of 130 mV with a 49 mV dec^{-1} Tafel slope [387].

Strain engineering can be mentioned as the last primary strategy to enhance the HER activity of MoS_2. Due to the atomic thickness, strain can be introduced to achieve the lattice deformation of MoS_2. The d-band electronic structure would be modulated and optimized to get closer to the Fermi level, thus prompting the electron-transfer rate in hydrogen adsorption and desorption. It has been shown that direct growth of MoS_2 on a curved surface of gold could introduce the external strain into a continuous single-layer MoS_2 film [388]. As a result, the S–Mo–S bonding angles change, thus causing a local semiconductor-to-metal transition in monolayer MoS_2. Zheng et al. showed that the introduction of strain into the S vacancies of the monolayer 2H-MoS_2 would result in the transition of valence bands created by the presence of S toward the Fermi level [389]. By implementing this strategy, they made the bandgap narrower and produced richer bandgap states near the Fermi level of MoS_2.

5.1.3 Aims of study

Despite enormous efforts in advancing the HER activity of MoS_2, there are still significant controversial results in the published reports. Additionally, some fundamental questions such as the exact active site and mechanism on different MoS_2 structures are still far from being experimentally answered despite theoretical calculations. Moreover, the structural and chemical changes of crystallized monolayer MoS_2 during HER are unclear. Recently, a series of operando techniques have been employed to investigate the intrinsic electrochemical behaviors of electrocatalysts [390]–[392]. Unfortunately, almost all of these studies have chosen amorphous MoS_2 due to the presence of significantly more catalytic sites, which makes the operando investigation more feasible. However, the amorphous MoS_2 has poor stability and it would spontaneously crystallize to form 2H-

MoS_2 [393]. This study aims to provide a deeper insight into the factors affecting the structural and electrochemical properties of MoS_2. First, a systematic investigation was performed to reveal the possibility of manipulating the MoS_2 phases and intrinsic properties during CVD synthesis. Then, the effect of N_2 plasma on different phases of single-layer MoS_2 and their HER activity is studied. Finally, the evolution of various structures under operando conditions was investigated.

5.2 Experimental

5.2.1 Synthesis and Transfer of MoS_2

CVD of MoS_2 was performed inside a multitemperature-zone tubular furnace on 25μm thick Au foil as the substrate. Sulfur powder, placed outside the hot zone, was mildly sublimated at ~120 ºC with heating belts and carried by Ar gas (50 sccm) to the downstream growth zone. MoO_3 powders (Sigma Aldrich, ACS reagent) and Au foils were successively placed on the downstream region of the quartz tube. After setting the total pressure to 0.8 mbar, the MoO_3 powder was heated from room temperature to 530 ºC with a heating rate of ~17 ºC/min. The growth time and temperature were set to 60 min and 530 ºC, respectively. To study the effect of the precursor's distance on the structure of MoS_2, the Au substrates were placed on a quartz sample holder with different distances from the MoO_3 powder.

Due to the HER activity of Au foil, it is necessary to transfer the MoS_2 films onto arbitrary substrates such as FTO glass to ensure the reliability of the electrochemical results obtained while using Au as the substrate. The first step of the transfer process was to spin coat the samples with PMMA 2%. The coating time and speed were set to 30 seconds and 2000 rpm, respectively. The wafers were then baked at 170 ºC for 10 min, followed by floating them on an etchant solution at 40 ºC for 12 h, while stirring very gently. The etchant solution was prepared by a mixture of KI : I_2 : DI water = 10 g : 2.5 g : 150 ml. Finally, the films were rinsed and floated on DI water three times. FTO substrates were used to fish out the PMMA-capped MoS_2 films, followed by heating at 170 ºC for four h at a 45° angle. This heating step is crucial to enhance the sticking of the films to the substrate. Finally, PMMA was cleaned from the top of MoS_2 by soaking the films in absolute acetone.

5.2.2 Doping MoS_2 with Nitrogen

The PECVD system was used to prepare N-doped MoS_2. The N plasma was generated by

flowing 1.9 sccm of N_2 gas while the chamber pressure was set to ~ 9.0 mTorr. The films were exposed to N_2 plasma with 10 W power for 40 s. After the treatment at room temperature, the system was switched off, and the flow rate of N_2 was increased to 50 sccm. The samples were kept under this atmosphere for 30 minutes to ensure that their surface has stabilized.

5.2.3 Physical Characterization

XPS measurements were performed in a laboratory system (Thermo K-alpha) equipped with a monochromatized Al K-alpha X-ray source. The XPS binding energies were referenced to the Au 4f peak. The phase composition of the films and the concentration of N in N-doped samples were determined by the quantitative analysis of Mo 3d, S 2p, and N 1s XPS spectra. Sensitivity factors (1.676 for N 1s, 6.51 for Mo 3d, and 1.881 for S 2p) that took photoionization cross-section and kinetic energy dependent inelastic mean free path of electrons into account were used in the quantification. Raman spectroscopy (Renishaw INVIA) investigations were performed by setting the laser excitation wavelength at 532 nm and 252 μW.

5.2.4 Electrochemical Characterization

All the electrochemical measurements were carried out using a Biologic SP-200 potentiostat in a standard three-electrode cell at room temperature. The three-electrode cell configuration consisted of a Pt spiral wire as a counter electrode, an Ag/AgCl in 4 M KCl as a reference electrode, and MoS_2 samples on Au foil or FTO substrate as the working electrode. The cyclic voltammetry (CV) measurements were performed in 0.5 M H_2SO_4 electrolyte solution at room temperature from 0.15 to -0.32 V vs. RHE with a scan rate of 20 mV/s. All potentials reported here are vs. RHE. To have a standard parameter in comparing the onset potential for the different samples, the required potential to reach -10 $mA.cm^{-2}$ (η_{10}) was calculated. The double-layer capacitances (C_{DL}) were estimated by plotting anodic and cathodic current density differences (Δj) against the potential scan rate. The slopes of such plots were assumed to be twice of C_{DL} and used to represent the samples' electrochemical surface area (ECSA). Tafel analysis was performed to determine the kinetic parameters of the HER. The “b” parameter in the Tafel equation ($\eta = a + b \log(j)$) was specified at the potential range before and after onset potential.

5.2.5 SEC-Raman Characterization

SEC-Raman measurements were carried out using a homemade electrochemical cell setup attached to a Renishaw INVIA Raman spectrometer while setting the laser

excitation wavelength at 532 nm. The electrochemical cell setup, attached to a Biologic SP-150 potentiostat, had a three-electrode configuration similar to the one used in electrochemical measurements. The chronoamperometry (CA) was measured by setting potentials with 0.05 V intervals from 0.15 V to -0.25 V (vs. RHE) for 3 minutes. The corresponding Raman spectrum was recorded after keeping the sample at a constant potential for 1 minute.

5.3 Enhanced HER Activity of MoS_2 through Structural Modifications

Raman spectroscopy can be used to identify the number of layers [394] and different phases of MoS_2 [319]. Theoretical calculations predicted four first-order Raman active modes for crystalline trigonal bulk MoS_2 [395]. These modes include E^2_{2g} (at ~32 cm^{-1}), E_{1g} (at ~286 cm^{-1}), E^1_{2g} (at ~383 cm^{-1}), and A_{1g} (at ~408 cm^{-1}). The E^2_{2g} mode arises from the vibration of an S–Mo–S layer against adjacent layers. Due to the presence of this peak in the vicinity of Rayleigh scattering, it is difficult to observe it with conventional Raman spectrometers. The other three Raman active modes are mainly induced by the intralayer atomic vibrations. The E_{1g} is attributed to the in-plane vibration modes and is forbidden in the back-scattering experiment on a basal plane. The in-plane E^1_{2g} mode results from the breathing mode vibration of two S atoms with respect to the Mo atom, while the A_{1g} mode is associated with the out-of-plane vibration of only S atoms in opposite directions [394] (Figure 5-3).

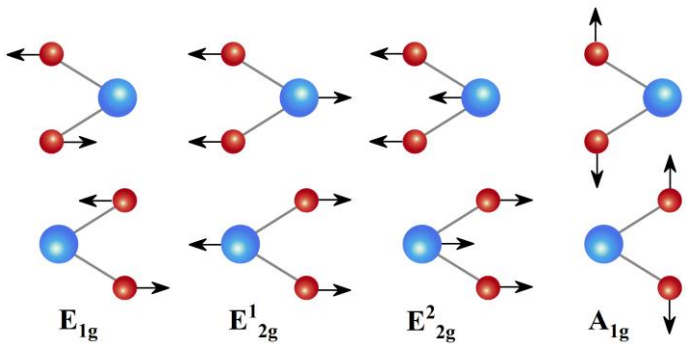

Figure 5-3 Schematic representation of the four first-order Raman active vibration modes for MoS_2

In addition to these modes, some second-order peaks promoted by strong electron-phonon couplings can be observed too. The most prominent second-order mode is around 460 cm^{-1} and is due to a process involving the longitudinal acoustic phonons at the M point (LA(M)) [394]. The frequency, intensity, and width of the peaks of E^1_{2g} and A_{1g} modes are strongly dependent on the number of layers [348]. Among these variations, the most consistent and observable change is the frequency alteration with respect to the number

of layers. The interlayer van der Waals (vdW) interactions, which suppress atomic vibrations, vanish as the layer number decreases. This results in a redshift in out-of-plane A_{1g} mode frequency induced by lower force constants [394]. On the contrary, the in-plane E^1_{2g} mode shows a blueshift as MoS_2 becomes thinner. This is attributed to stacking-induced changes or a decrease in long-range Coulombic interlayer interactions affecting the atomic vibrations [397], [398]. In addition to E^1_{2g} and A_{1g} modes, the symmetry differences in 1T-MoS_2 result in several additional Raman vibrational modes. These modes are assigned as J_1 (~160 cm^{-1}, attributed to the in-plane shear mode vibration), J_2 (~225 cm^{-1}, attributed to the slip of the S atoms layer relative to the Mo atoms), and J_3 (~330 cm^{-1}, related to the elongation of the one side of the zigzag chains relative to the other side) [270], [351], [352]. The presence of these peaks can be correlated to the existence of a superlattice. Due to the wave-vector conservation, Raman spectra typically contain peaks corresponding to zone-center modes only. However, upon formation of a superlattice, the Brillouin zone is reduced, and zone-boundary points of the original system can be combined with Γ' of the additional zone. Raman scattering events may then involve zone-edge phonons without violating wave-vector conservation [318]. So, Raman spectroscopy can be used to determine the structural phase of MoS_2. However, it is not easy to obtain an accurate quantitative analysis of the phase composition from the Raman spectra alone due to the weak Raman response of these modes and variation in scattering cross-section.

In order to study the structure of the MoS_2 samples synthesized at different distances (8, 10, 12, 14, 16, 18, 20, 22, and 24 cm) from the MoO_3 precursor, the samples were characterized by Raman spectroscopy. Henceforth, these samples will be mentioned as Mo-X (X: distance of the substrate from the Mo precursor in cm). The presence of J_2, E^1_{2g}, and A_{1g} modes for the MoS_2 samples on Au foil can be seen in Figure 5-4a. The peak at ~190 cm^{-1} corresponds to the interference of A_{1g} and longitudinal acoustic (LA) vibrations at M point [401]. Despite difficulties in quantitative analysis of MoS_2 Raman spectra, the results can be compared qualitatively. Due to the identical structural parameters between 1H-MoS_2 and 2H-MoS_2 [352], the 1H phase is generally overlooked in the literature. However, some studies have shown that there is a significant difference in the frequency of A_{1g} modes in 2H-MoS_2 (~410 cm^{-1}) and 1H-MoS_2 (~403 cm^{-1}) [353]. Although both phases show semiconducting behavior, there is an increase in bandgap and transition from indirect to direct bandgap when transforming 2H-MoS_2 to 1H-MoS_2. The

results obtained in our study revealed the A_{1g} modes at ~403 cm^{-1} (Figure 5-4a), confirming the presence of the 1H-MoS_2 phase. Due to the alteration in Mo-Mo bonds strength and length when converting 1H-MoS_2 to 1T-MoS_2, the in-plane vibrations related to the E^1_{2g} peak would be sensitive to the phase composition of MoS_2. Hence, the intensity of the A_{1g} mode is taken as the reference point, and intensity ratio analysis has been performed based on the intensity ratio of the J_2 and E^1_{2g} peak to the A_{1g} mode. The blue curve in Figure 5-4b shows the disappearance of J_2 to A_{1g} intensity ratio ($I_{J_2}/I_{A_{1g}}$) by increasing the distance of Au substrate from MoO_3 powder. Meanwhile, the intensity ratio of E^1_{2g} to A_{1g} ($I_{E^1_{2g}}/I_{A_{1g}}$) shows an inverse trend with increasing distance. These two trends reveal the distance dependent phase transformation in MoS_2 structure. While the Mo-8 sample has 1T@1H-MoS_2 structure, the samples become pure 1H at the distances above 16 cm. Another important trend for the Raman spectra showed in Figure 5-4a is the decline in the total intensity of the peaks with increasing distance. Our analysis about the distance between the E^1_{2g} and A_{1g} peak positions (showed in Figure 5-4c) revealed that it varies between ~19 and 20 cm^{-1} with changing the samples position. This range is in agreement with previously reported values for monolayer MoS_2 films on Au substrate [298], [354]. As a result, the thickness of the films does not change with modifying their synthesis position. Hence, the decline in overall Raman intensity can be correlated with the synthesis of smaller flakes of MoS_2 at distances far from the Mo precursor. In addition, there is a slight redshift in the position of E^1_{2g} and A_{1g} modes at distances higher than 16 cm. This can be due to the softening of the Mo-S bond promoted by the formation of in-plane S vacancies [355].

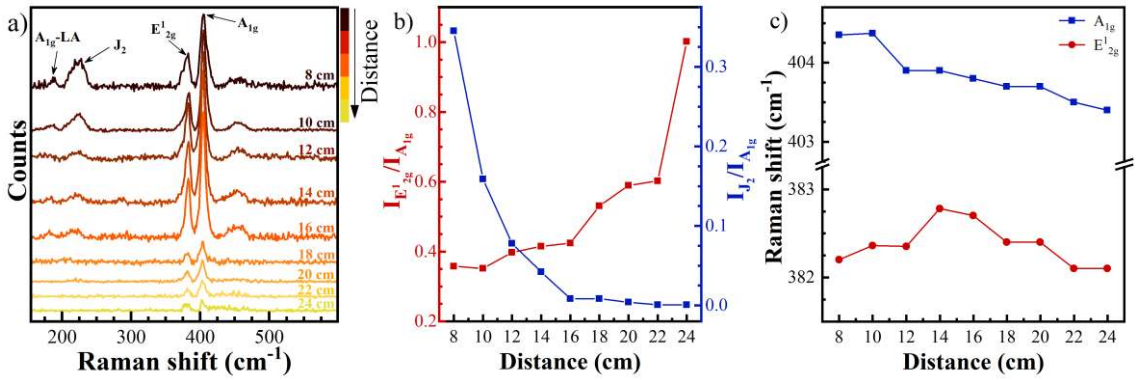

Figure 5-4 a) Raman spectra of samples synthesized on the Au substrate placed at different distances from the Mo precursor, b) the J_2 to A_{1g} intensity ratio (blue curve) and E^1_{2g} to A_{1g} intensity ratio (red curve) with respect to the synthesis distance, and c) the alteration in E^1_{2g} and A_{1g} peak positions versus the distance of the sample from Mo precursor.

A more detailed investigation about the phase transformation is possible through XPS

analysis. XPS scan from Mo 3d region of pure 2H-MoS_2 usually reveals two peaks around 230.0 and 232.5 eV, corresponding to photoelectrons from the Mo^{4+} $3d_{5/2}$ and Mo^{4+} $3d_{3/2}$ states, respectively [271], [357], [358]. These two peaks can be seen at ~229.0 and ~232.2 eV for 1H-MoS_2 in Figure 5-5a (red peaks). The XPS scans were taken while the samples were on the Au foil substrate. The combination of the contradictory effects of the metallic substrate with the wider bandgap in 1H-MoS_2, compared to 2H-MoS_2, results in a slight shift towards lower binding energies. Another doublet (shown with blue in Figure 5-5a) at ~227.8 and 231.4 eV can be seen for the Mo-8, Mo-10, Mo-12, and Mo-14 samples. These peaks are assigned to Mo^{4+} $3d_{5/2}$ and Mo^{4+} $3d_{3/2}$ states of 1T-MoS_2 [374]. The lower binding energy of 1T related peaks compared to 1H related ones indicate higher electron density around Mo atoms in the 1T phase [357]. As a result, the same observation for the phase transformation with the distance change discussed above can be seen here. The green peak at ~226.5 eV is attributed to the S 2s electrons [357]. To further investigate these observations, the S 2p spectra of the samples were analyzed (Figure 5-5b). The red peaks at ~162.1 and 163.3 eV indicate S^{2-} state in 1H-MoS_2 (S $2p_{3/2}$ and S $2p_{1/2}$, respectively). Meanwhile, the blue peaks at ~160.2 and 161.4 are assigned to the same state in 1T-MoS_2 [359]. The 1T-MoS_2 phase-related peaks in S 2p spectra vanish simultaneously with the Mo 3d peaks correlated to this phase. The peak at ~166.1 eV can be assigned to the $[SO_3]^{2-}$ groups [408], which can be due to the oxidation of the unsaturated S atoms in the boundaries under ambient conditions. The disappearance of this peak for the Mo-18 and Mo-20 samples can be due to the greater extent of 1H phase purity, which results in the lower amount of phase boundaries. Also, it can be seen that the overall signal count for both Mo 3d and S 2p regions decreases with increasing the distance. This is in agreement with the Raman peak intensities reduction observed in Figure 5-4a. As a result, XPS analysis confirms the transformation of 1T phase to 1H followed by a shrinkage in the size of the synthesized MoS_2 flakes as the synthesis distance increases.

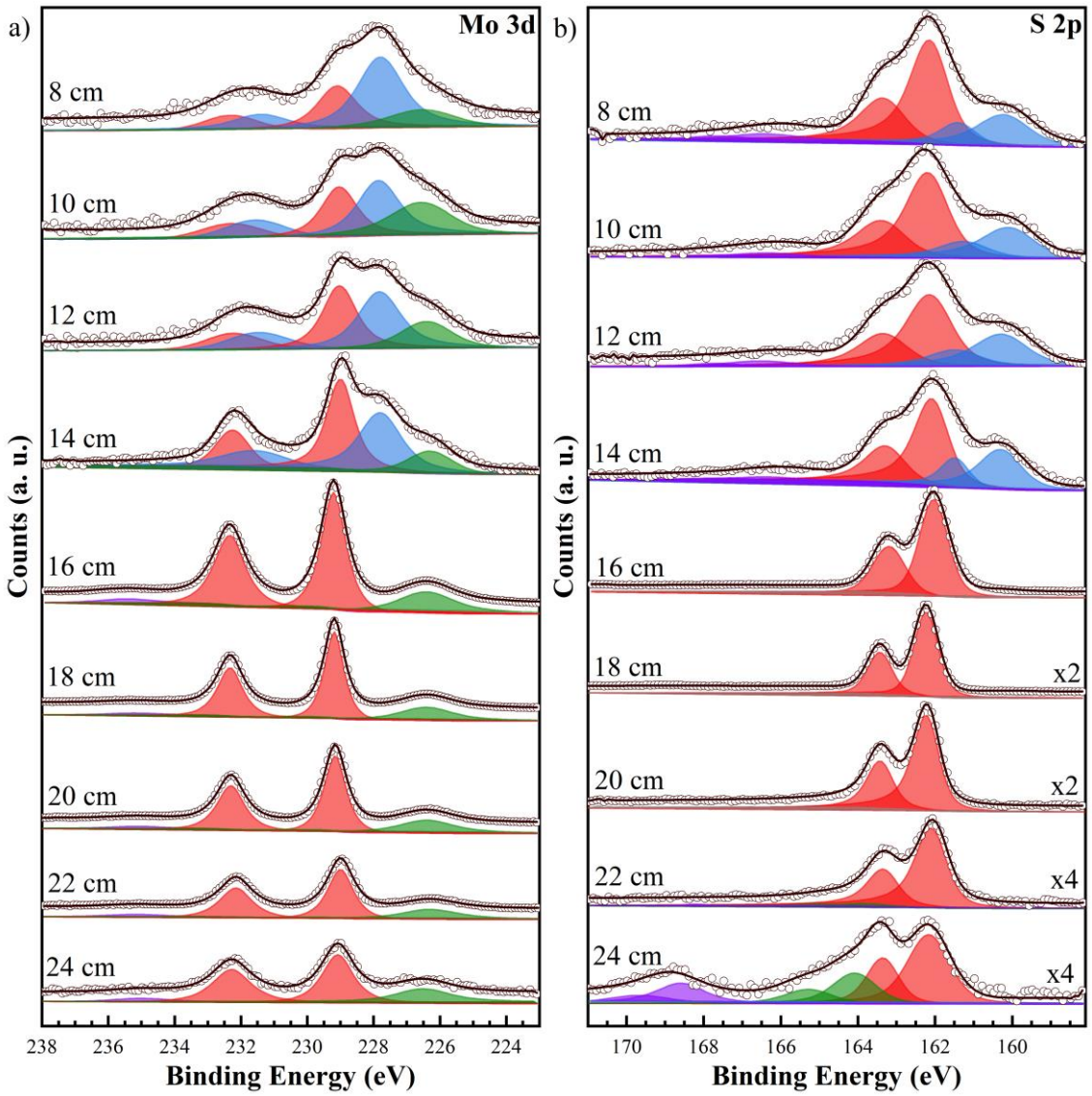

Figure 5-5 Deconvoluted high-resolution XPS spectra of a) Mo 3d region and b) S 2p region for the samples synthesized at different distances from the Mo precursor.

For the samples at higher distances, a small peak attributed to the Mo^{6+} evolves at ~235.0 eV (Figure 5-5a). This can represent the partial oxidation of Mo atoms due to the presence of S vacancies. On the other hand, in the S 2p spectrum of the Mo-24 sample, a new peak at ~168.8 emerges. This peak is correlated to the $[SO_4]^{2-}$ groups [408]. The appearance of this peak coincides with the emergence of a doublet at ~164.1 and 165.3 eV (shown with green in Figure 5-5b), which can be ascribed by the S^{2-} neighboring oxidized S species [409]. Similar observations can be made by studying the O 1s spectra of the samples shown in Figure 5-6c. Unfortunately, due to the significant overlap, it is not possible to clearly distinguish the contribution of oxidized S and Mo atoms on O 1s spectra. However, it can be clearly seen that the overall intensity of O 1s first drops by increasing the distance (and hence decreasing the density of phase boundaries) and reaches to

minimum for Mo-16. Then it starts to increase, and the total O content gets maximized for the Mo-24 sample. These observations indicate that while the flakes synthesized at higher distances are smaller than the closer ones, they are also different from the other samples in having S vacancies and oxidized S groups. Quantitative analysis on Mo 3d peaks of 1H and 1T phases revealed that the composition of the Mo-8 sample contained ~65 at. % 1T phase (Figure 5-6a). This value drops to 50 at. % for the Mo-14 and becomes almost zero for the rest of the samples. While according to XPS results, the samples synthesized at distances higher than 16 cm do not contain 1T phase, the atomic percentage of the 1H-MoS_2 never reaches beyond 97%. This is due to presence of Mo-O groups, with maximum amount of 5.78% for the Mo-24 sample. Using Mo 3d and S 2p peaks, the S/Mo ratio has been calculated and the results for different samples are shown in Figure 5-6b. It can be clearly seen that the S/Mo ratio is almost equal to the stochiometric value of MoS_2 up to the 16 cm. However, at higher distances, this ratio falls rapidly, reaching to a minimum of S/Mo:1.15 for the Mo-24 sample. This decrease in the S/Mo ratio is in agreement with the prediction of the presence of S vacancies based on Figure 5-5b. It can also be stated that while Mo-18 and Mo-20 samples contain mainly single S vacancies, for the Mo-22 and Mo-24 samples, the undercoordinated Mo atoms become exposed to the ambient conditions and electrolyte and hence get oxidized. In a recent study, the S/Mo: 1.7 was introduced as the threshold for the exposure of undercoordinated Mo atoms to atmospheric oxygen [371].

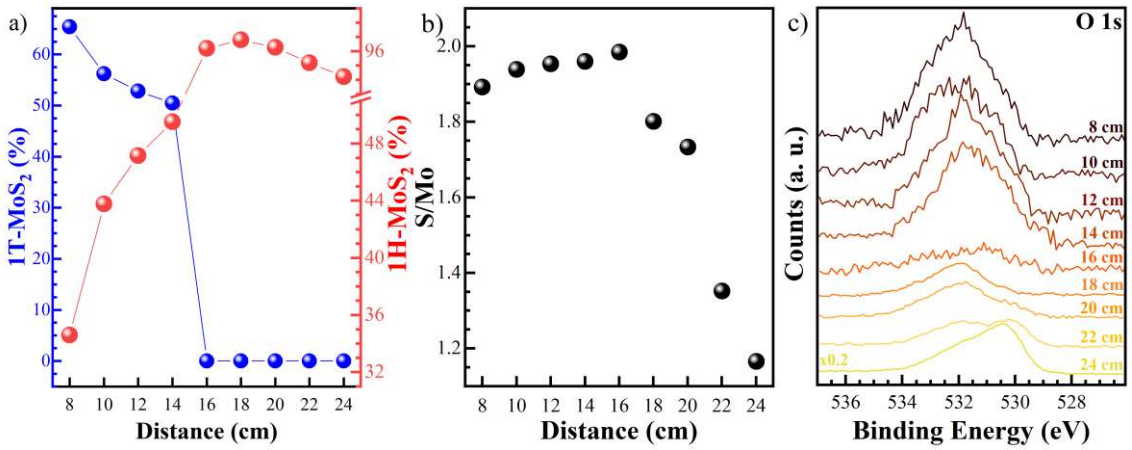

Figure 5-6 a) Phase composition evolution of the samples based on XPS Mo 3d region versus the synthesis distance and, b) The variation in the S/Mo atomic ratio with respect to the synthesis distance, and c) O 1s spectra of the samples synthesized at different distances.

The HER activity of the samples was investigated by studying CV scans obtained from them (Figure 5-7a). According to the previous characterization results and the overall

trend in CV scans, the samples can be divided into three main group. The red group (with low synthesis distance) contains the samples with 1T phase component in their structure. Due to the presence of this phase, it is expected to have a partially active basal plane for this group [374], [382]. The CV results and η_{10} values (shown in Figure 5-7b) are in agreement with this expectation. The overpotential and current density of the samples in this group worsen as the 1T phase concentration decreases by increasing the distance. The blue group, which includes Mo-16, Mo-18, and Mo-20 samples, shows the weakest HER activity among all other samples. Due to the absence of the 1T-MoS_2 phase and defects, the number of available active sites is minimum among this group, resulting in higher overpotential and lower current density. Finally, the green group is attributed to the samples synthesized at the most extended distances from the Mo precursor (Mo-22 and Mo24). The smaller flake size and the presence of vacancies in the samples of this group results in a higher number of available active edge sites. This can be confirmed by comparing the CVs and η_{10} values of this group with the blue and red groups. The only sample with similar activity to the green group is the Mo-8 sample, which contains more than 60% metallic 1T phase. A decrease in the activity was observed during recording consecutive CV cycles for all of the samples. The alteration in the η_{10} values of Mo-8, Mo-22, and Mo-24, is presented in Figure 5-7c. While the η_{10} values for all samples increase by increasing the number of the CV cycles, it follows a faster trend for the Mo-8. The quicker reduction in the activity of Mo-8 can be due to the transformation of 1T-MoS_2 to 1H-MoS_2.

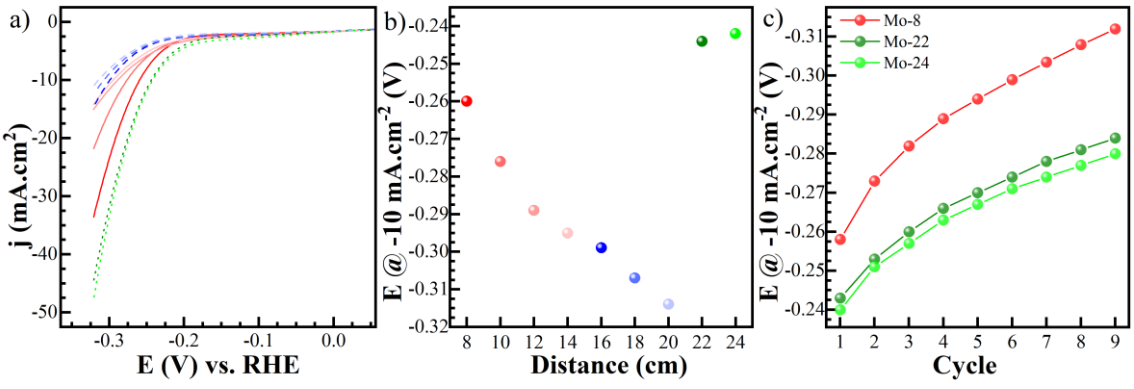

Figure 5-7 a) CV scans taken from the samples synthesized at different distances, b) the variation of the η_{10} values with the synthesis distance and, c) the change in the overpotential value of Mo-8, Mo-22, and Mo-24 samples by increasing the number of the CV scans.

To study the change in HER kinetics with varying synthesis distances, the Tafel slope for all samples was calculated, and the plots are shown in Figure 5-8a. Depending on the overpotential range in which the Tafel slope is determined, its value can show significant

variation. In order to rule out the possibility of reporting misleading values for the Tafel slope, it is calculated at two overpotential regions. These regions were chosen at the vicinity of the onset overpotential; one was before the onset potential (shown with the half-filled circles in Figure 5-8b), and the other was after the onset potential (indicated with the filled squares in Figure 5-8b). A volcano shape plot can be revealed for both regions, where the Mo-8, Mo-10, Mo-22, and Mo-24 have the lowest Tafel slopes. This indicates lower kinetic barriers for these samples compared to the others, confirming earlier discussed electrochemical results. Experimentally, the Tafel slope is viewed as an intrinsic property of electrocatalysts, which is determined by the rate-limiting step and allows for the distinction of possible mechanisms for HER. The HER kinetic models suggest a Tafel slope of about 120, 40, or 30 $mV.dec^{-1}$ for the Volmer, Heyrovsky, and Tafel steps being the rate-determining reaction, respectively [410]. Based on the results shown in Figure 5-8b, the Volmer-Heyrovsky mechanism with the Heyrovsky reaction as the rate-determining step can be introduced as the HER pathway for the samples in the peak of the volcano plot. However, depending on the chosen potential region for the Tafel slope calculation, the prediction about HER mechanisms of the samples in the downhill of the volcano plot can vary. The presence of various HER active sites with different proposed HER mechanisms on a single sample, makes it impossible to have a definite judgment about the HER mechanisms of these samples based on their Tafel slope values.

As it has mentioned in chapter two, the ECSA of the samples can be qualitatively compared based on the double layer capacitance (C_{DL}) value. Figure 5-8c and Figure 5-8d show how this quantity changes among the samples. For the 1T@1H-MoS_2 films (the red group), the main electrocatalytically active sites are the basal plane of the 1T phase and the 1T-1H phase boundaries [324]. The decline of the ECSA among the red group proves that the number of both sites decreases by increasing the distance. After obtaining the minimum C_{DL} value for Mo-16, there is an enhancement in ECSA for the other samples of the blue group. This trend aligns with the trend in the S/Mo ratio seen in Figure 5-6c, clearly confirming the role of S vacancies in the improvement of the HER activity of these samples. Despite the better electrochemical activity of the Mo-22 and Mo-24, they pose low ECSA. This can be due to the significantly lower MoS_2 flake coverage on the Au foil and hence lower geometric surface area for these samples.

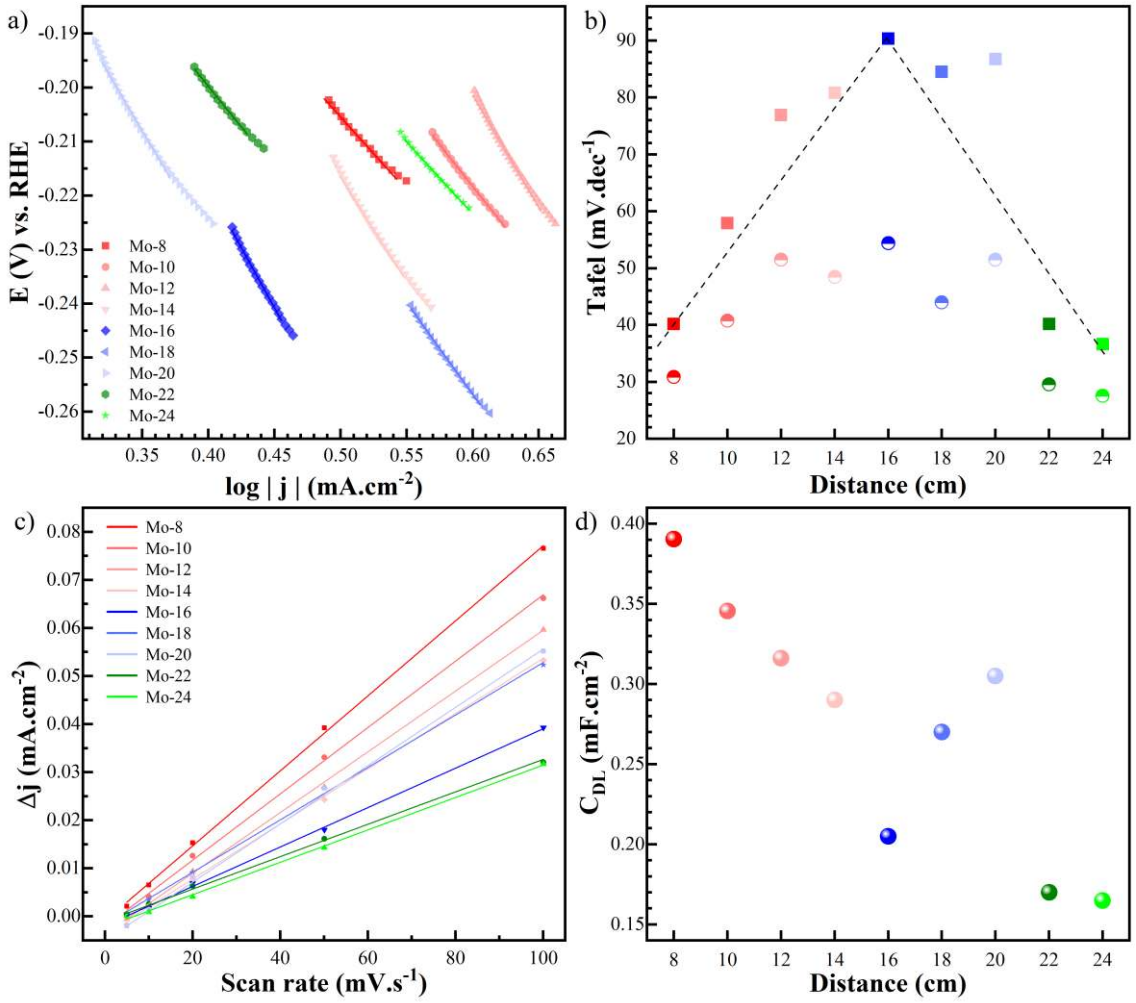

Figure 5-8 a) Tafel plot, b) variation of Tafel slope versus synthesis distance, c) the variation in the difference between cathodic and anodic current versus scan rate, and d) the C_{DL} value alteration with respect to the synthesis distance, obtained from calculating the slope in part (c).

The high current density obtained from Mo-22 and Mo-24 contrasts with the low geometric area and small flake size confirmed by Raman and XPS and low ECSA values of these samples. Since underlying Au foil has HER activity, it is necessary to evaluate the electrocatalytic activity of the samples on FTO to ensure about the effect of Au on the results reported in Figure 5-7 and Figure 5-8. Figure 5-9 shows the CV scans obtained from the same set after transferring onto FTO substrate. As it can be seen, the general trend is similar to the trend observed when performing the same experiment on the Au foil. However, due to the significantly lower electron coupling between the samples and FTO compared to Au foil, both current density and overpotential worsened [346]. Hence, the electrochemical measurements performed on Au foil are also reliable and can be used to compare the activity of the samples.

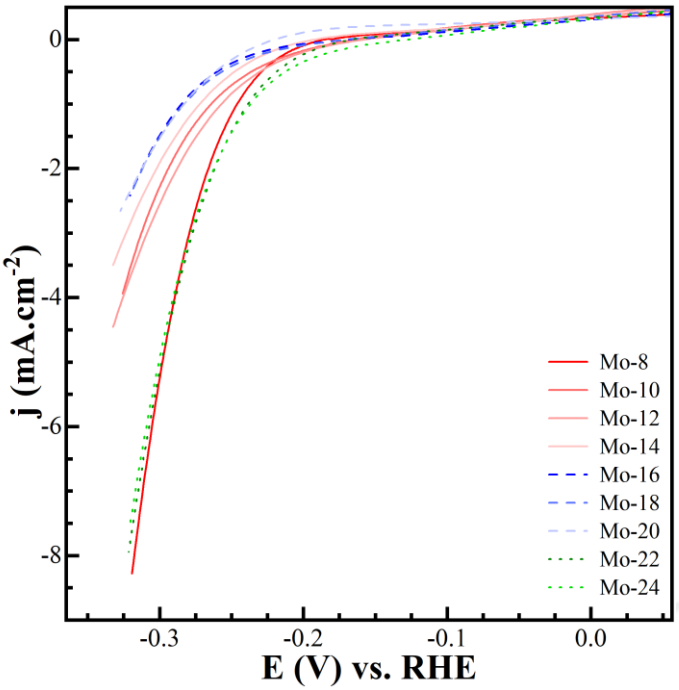

Figure 5-9 CV scans taken from the samples synthesized at different distances on FTO substrate

As mentioned earlier, one of the main strategies for enhancing the HER activity of MoS_2 is to dope nonmetal heteroatoms such as N into its structure. The main techniques to prepare N-doped MoS_2 are hydrothermal methods, calcination, and N_2 plasma. To the best of our knowledge, most of the hydrothermally prepared N-doped MoS_2 samples reported in the literature suffer from low N concentrations. On the other hand, the employment of high temperatures in the calcination, results in the transformation of 1T phase to 1H/2H [411]. Hence, N_2 plasma has been used in this study to prepare N-doped MoS_2 from Mo-8 and Mo-24, which will be called Mo-8-N and Mo-24-N, respectively. The structural alterations of MoS_2 after N doping were studied by obtaining Raman map from an area of 400 μm^2 with 0.5 µm step size on the Mo-8 and Mo-24 samples before and after N doping.

The majority of the studied area for both Mo-24 (Figure 5-10a) and Mo-24-N (Figure 5-10b) samples had an A_{1g} to E^1_{2g} peak distance between 19.7 and 21.4 cm^{-1}. The similarity in the peak distance for the two samples reveals that the exposure of N_2 plasma did not severely affect the thickness of the samples. In addition to the information obtained from analyzing the distance between the peaks, the peak position changes can provide useful information about the alterations in the bond stiffness. In order to study the peak position changes of the samples, the spot with similar A_{1g} to E^1_{2g} peak distances have to be compared. For this purpose, the spots with a A_{1g} to E^1_{2g} peak distance between

20.6 and 21.0 cm^{-1} were selected. Figure 5-10c and Figure 5-10d show the peak position of the E^1_{2g} and A_{1g} modes, respectively. It can be seen that there is ~1.5 cm^{-1} blueshift in both peak positions for most of the spots after N-doping. The blueshift of the E^1_{2g} mode suggests that a compressive strain is generated in the Mo-24-N structure due to the presence of Mo−N bonding [412]. In addition to the effect of compressive strain, charge doping effects are likely to contribute to the measured Raman signal [411], [413]. This effect is observed as the blueshift in the A_{1g} peak position, consistent with the p-type doping of MoS_2 given by substitutional N.

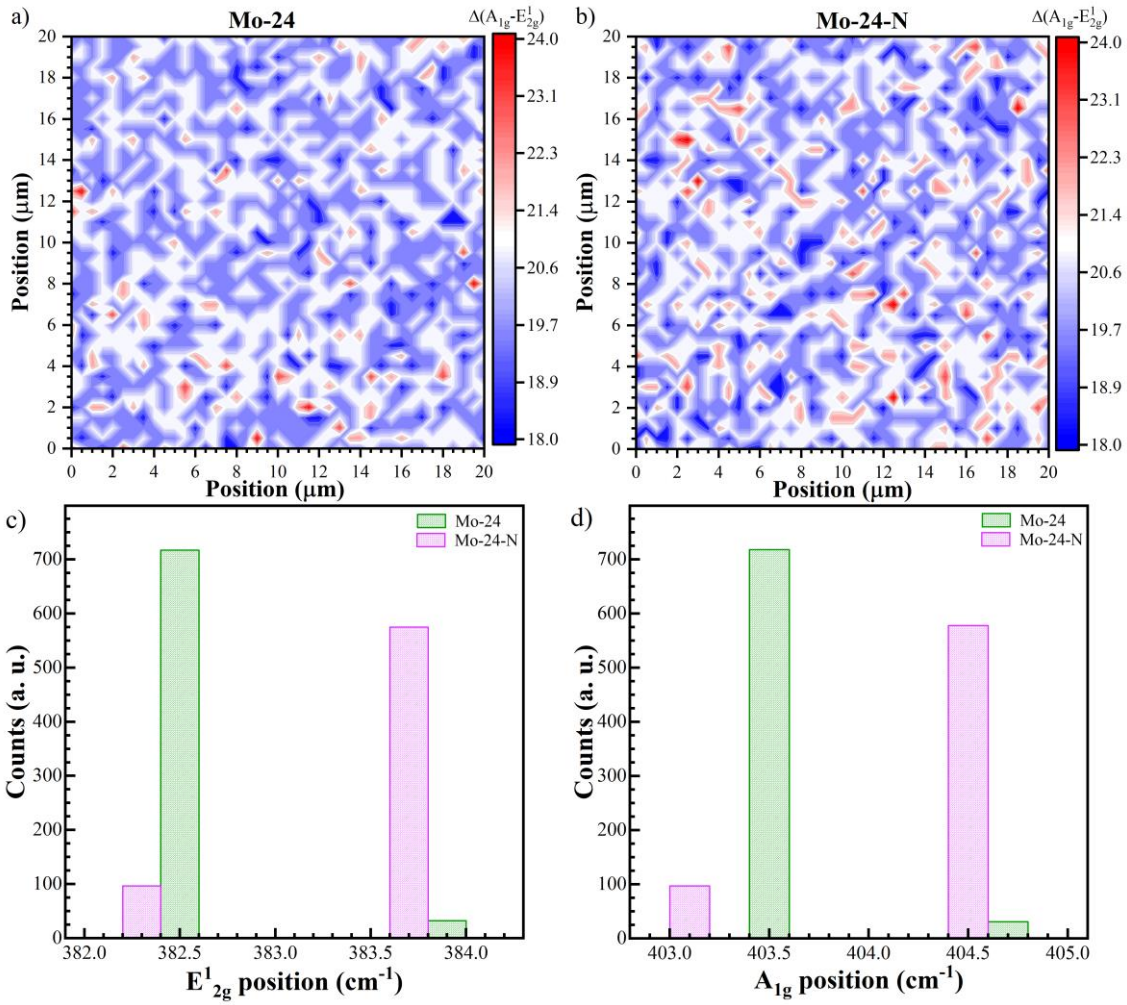

Figure 5-10 Raman maps for the peak position distance between A_{1g} and E^1_{2g} peak of a) Mo-24 and b) Mo-24-N obtained from a 400 μm^2 area. Histogram for the distribution of c) E^1_{2g} and d) A_{1g} peak positions in Mo-24 (green bars) and Mo-24-N (purple bars) at the spots with similar A_{1g} to E^1_{2g} peak position distance.

According to the previous studies, N doping does not promote 1H/2H to 1T phase transition. To evaluate this issue, the Raman maps for the $I_{J_2}/I_{A_{1g}}$ ratio of Mo-8 and Mo-24 samples were recorded. Figure 5-11a and Figure 5-11b show this ratio for the Mo-8 and Mo-8-N, respectively. As it can be seen in these maps and their corresponding

histograms shown in Figure 5-11c and Figure 5-11d, N doping had a dual effect of both increasing the area covered with red or white-colored spots ($I_{J_2}/I_{A_{1g}}$ higher than ~0.35) and also making most of the red spots darker (i.e. increasing number of the points with $I_{J_2}/I_{A_{1g}}$ higher than ~0.6). However, it is worth mentioning that while almost all of the red covered region has become darker upon N doping, the total number of the red spots increased only by 15% compared to the Mo-8 sample. As a result, the strain induced in the structure by N doping seems to promote the distortion, resulting in the conversion of 1H-MoS_2 to the 1T phase. However, doping is more effective in distorting the 1T-MoS_2. This increase in the $I_{J_2}/I_{A_{1g}}$ ratio upon N doping is in agreement with a recent report where the ratio changes from ~0.5 to higher than 1 by increasing N plasma duration [414].

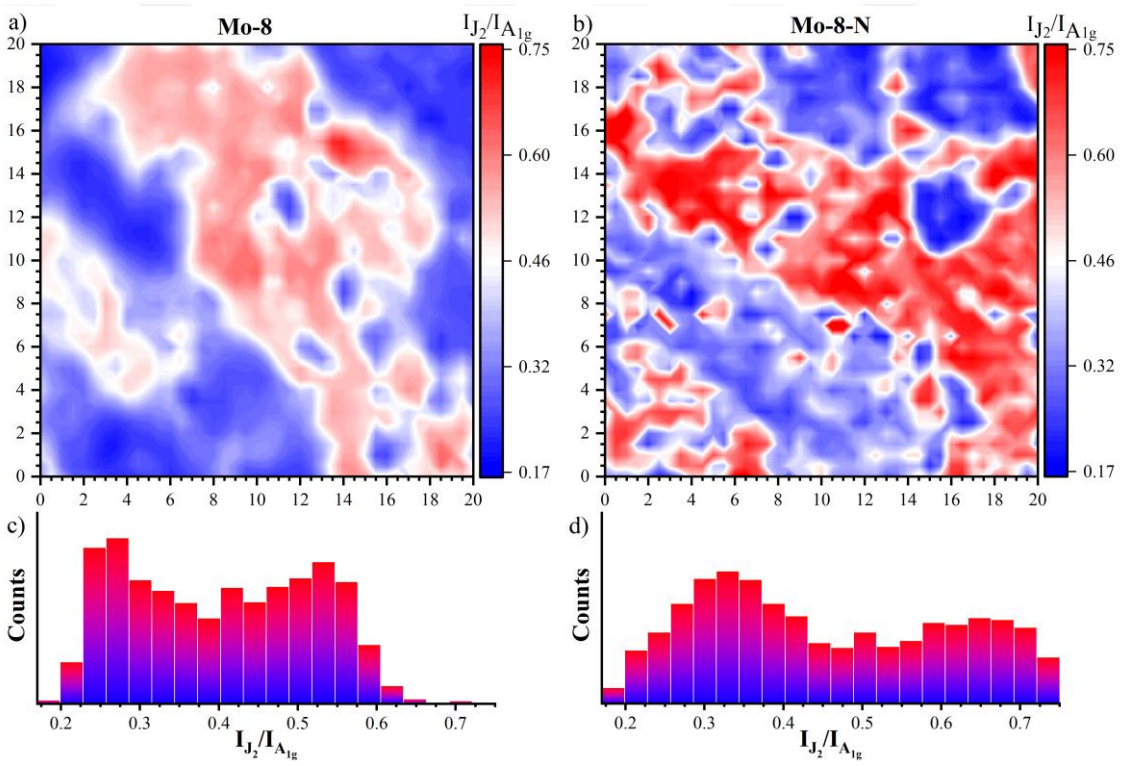

Figure 5-11 Raman maps for the I_{J2}/I_{A1g} ratio of a) Mo-8 and b) Mo-8-N samples and (c-d) their corresponding histograms.

The same analysis was performed on the Mo-24 and Mo-24-N samples. The $I_{J_2}/I_{A_{1g}}$ Raman map of Mo-24, shown in Figure 5-12a, agrees with our previous results, where no 1T phase was observed. However, in contrast to Mo-8, there is no significant increase in the intensity of the J_2 peak in the Mo-24 samples after doping with N (Figure 5-12b). It is noteworthy that due to the smaller flake size, the total intensity of the A_{1g} band for the Mo-24 and Mo-24-N samples is almost twenty times smaller than the intensity of this peak for Mo-8 and Mo-8-N. As a result, it is possible that at some spots, the intensity of

the noise in the J_2 frequency region results in a $I_{J_2}/I_{A_{1g}}$ ratio as high as 0.1. This effect becomes more pronounced on the N-doped samples, where the overall Raman intensities drop. The histograms of Mo-24 (Figure 5-12c) and Mo24-N (Figure 5-12d) show that the majority of the spots had negligible $I_{J_2}/I_{A_{1g}}$ ratios. With these observations, it can be stated that the N-doping does not lead to 1H/2H to 1T phase transition in a sample without initial 1T phase. In other words, the compressive strain induced by N doping in 1H-MoS_2 is not enough to convert it to the 1T phase. This agrees with the structural alteration of the Mo-8 sample upon N doping. Hence, it can be assumed that the room temperature low-power N_2 plasma only promotes the 1H to 1T phase transition in the phase boundaries, and no phase transition happens in the absence of the boundaries.

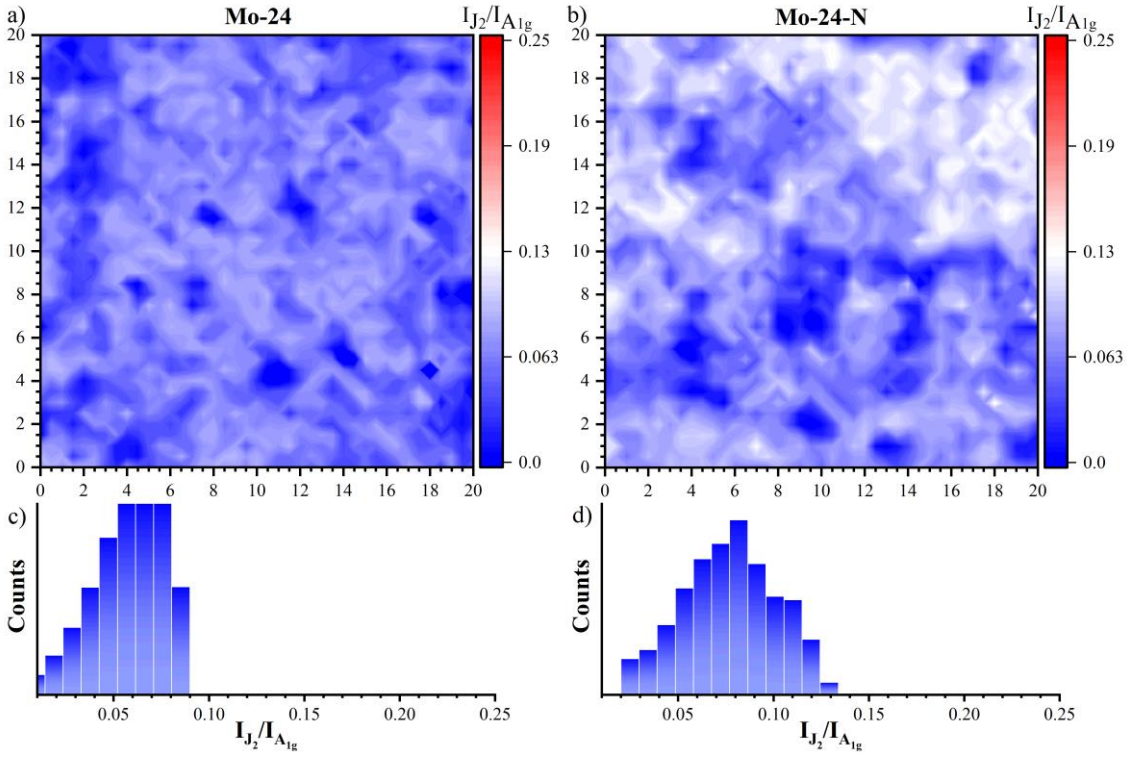

Figure 5-12 Raman maps for the I_{J2}/I_{A1g} ratio of a) Mo-24 and b) Mo-24-N samples and (c-d) their corresponding histograms.

The composition of the samples and the presence of N dopants in the structure were further analyzed by XPS. The presence of 1T-MoS_2 and enhancement in its amount after N doping can be observed from the Mo 3d spectrum of Mo-8-N (Figure 5-13a). Meanwhile, the only difference between Mo-24 and Mo-24-N is the increase in the intensity of the peak at ~235.0 eV (Figure 5-13d). This peak can be assigned to both Mo-O [415] and Mo-N [411] groups. The same trends (i.e., increase in the intensity of 1T-MoS_2 and oxide component related peaks) can be seen by comparing the S 2p spectra of

Mo-8 and Mo-24 before and after N doping. The quantitative analysis has shown a ~13% increase in the 1T-MoS_2 component of Mo-8-N compared to Mo-8. This is in agreement with our finding from the $I_{J_2}/I_{A_{1g}}$ ratio Raman map analysis. The most reliable evidence for the successful doping of N into the MoS_2 structure, is by studying the N 1s spectra which are shown in Figure 5-13c and Figure 5-13f. The blue peak which is appeared at ~395.0 eV is attributed to the Mo $3p_{3/2}$ [416]. The peak at ~399.0 eV can be assigned to Mo-N bonds [417]. All of the peaks related to Mo or S states of Mo-8-N and Mo-24-N have a shift toward higher bonding energy and slight broadening compared to their counterparts in the pristine Mo-8 and Mo-24 samples. This confirms the electron interaction between N, Mo, and S atoms and implies the decrease in electron density on the Mo and S atoms [417]. The creation of N 2p – Mo 3d – S 2p orbital hybridizations and transfer of electrons towards N with higher electronegativity can be the reason for the decrease in the electron density of Mo and S atoms [386].

Finally, the quantitative analysis revealed a similar N content of ~8 at. % in both Mo-8-N and Mo-24-N. In parallel, the S/Mo ratio for both samples decreased upon the introduction of N, suggesting preferential removal of sulfur. So, N doping proceeds with substituting S atoms with N, followed by the creation of N-Mo bonds. This observation has previously been confirmed by first-principles calculations [418]. However, the decrease in S concentration is higher than the amount of N introduced to the structure. Hence, it can be concluded that N_2 plasma has a dual effect of both substituting S with N and creating S vacancies. Also, despite the equal atomic percentage of N dopant in Mo-8-N and Mo-N-24, the S/Mo ratio decrease compared to Mo-8 and Mo-24-N is not the same for the two samples. While Mo-8-N has a S/Mo ratio of ~1.6 (~16% less than Mo-8), this value for Mo-24-N is ~0.86 (~25% less than Mo-24-N). This shows that creating S vacancies by plasma is more efficient on a sample with more edge sites and initial vacancies.

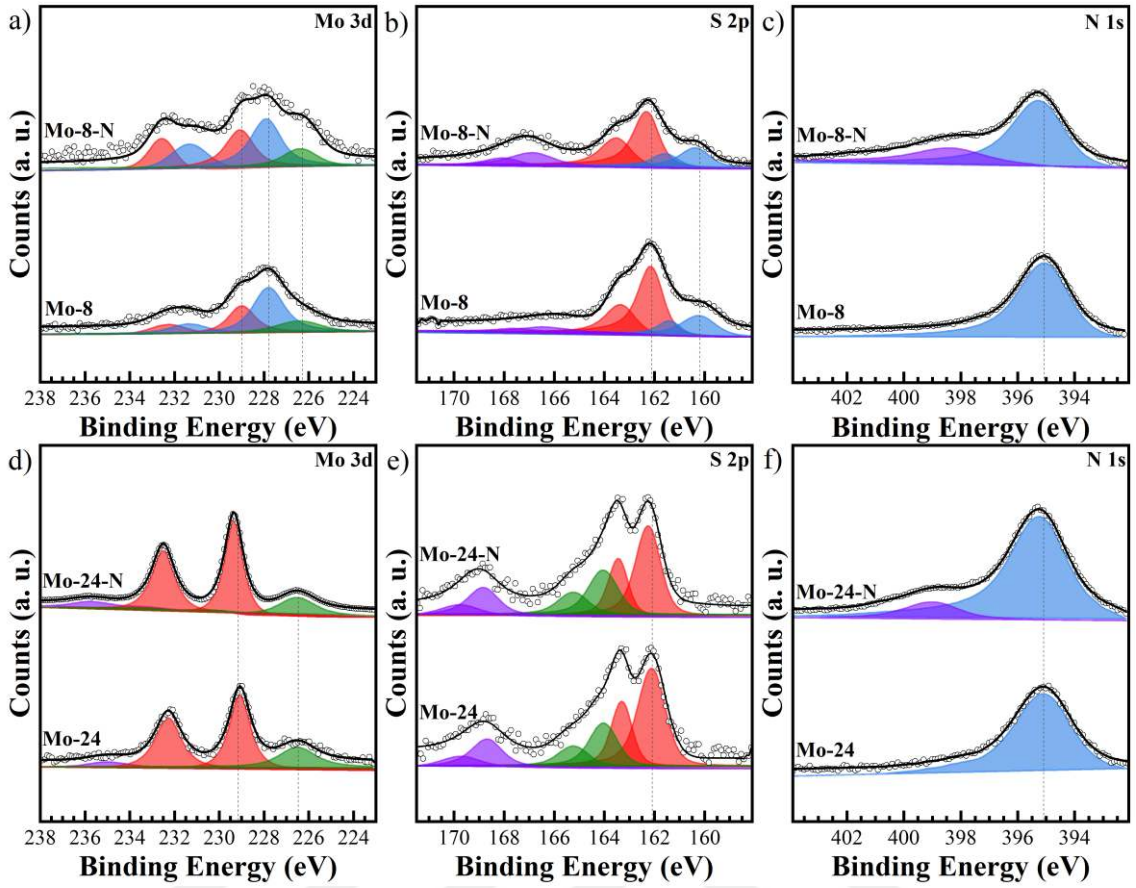

Figure 5-13 Deconvoluted high-resolution XPS spectra of a,d) Mo 3d, b,e) S 2p, and c,f) N 1s regions for Mo-8 and Mo-8-N (upper row) as well as for Mo-24 and Mo-24-N (lower row).

The N doping effect on the HER activity of Mo-8 and Mo-24 was studied by comparing the CV scans of these samples with the results obtained from Mo-8-N and Mo-24-N (Figure 5-14a). Previous studies have shown that N dopants enhance the HER activity of both S-edges and Mo-edges on MoS_2 [386]. This results in an improved onset potential and current density, clearly seen in Figure 5-14a. Figure 5-14b shows that the Tafel slope for both Mo-8 and Mo-24 decreases after doping with N, confirming lower kinetic barriers for Mo-8-N and Mo-24-N. The strong Mo 3d – S 2p – N 2p hybridizations at the Fermi level, which uniformly spread conducting charges over the basal plane and promote rapid charger transfer for the HER process, might be the main reason for this kinetic improvement [386]. Despite significant enhancement in the recorded current density from CV scans upon N doping, the C_{DL} values have decreased for both samples. In comparing ECSA of the samples through their C_{DL} values, the effect of surface roughness on the calculated C_{DL} has to be considered carefully. The formation of vacancies and defects on the basal plane of MoS_2 induced by N_2 plasma changes the morphological surface properties of the films. In addition, due to the single-layer property of the films synthesized in this project, there is a chance to partially remove MoS_2 film and expose

the Au substrate to the electrolyte by applying plasma. All these alterations affect the calculated C_{DL} values [175]. The variation of the η_{10} value versus CV cycles for the Mo-24-N has a similar trend to the Mo-24. However, the Mo-8-N shows a much more rapid increase in the η_{10} value compared to Mo-8 and reaches the same overpotential value after nine cycles. This can imply that the mechanism by which N doping improves the HER activity of the 1T phase is not stable.

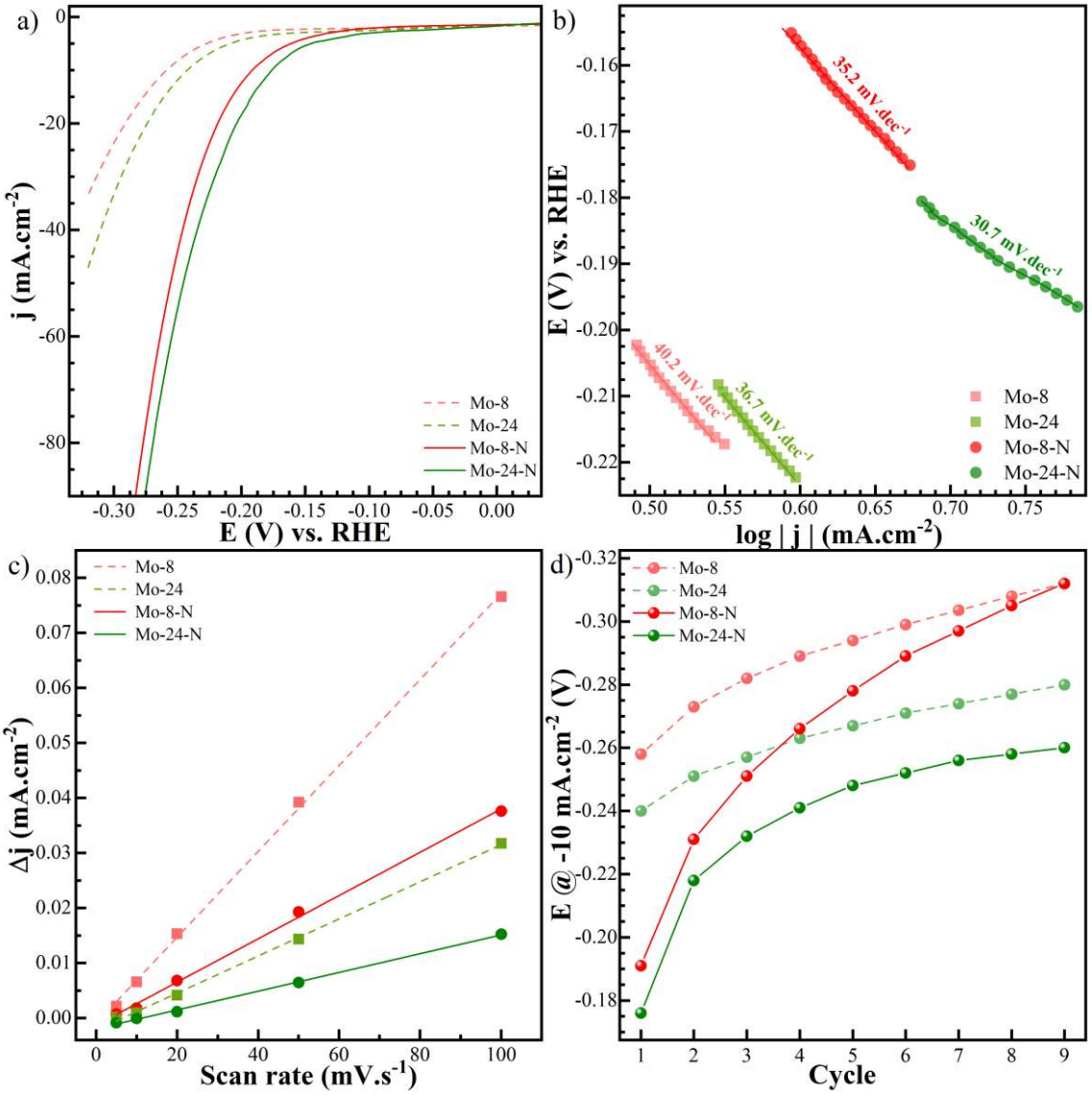

Figure 5-14 a) CV scans, b) Tafel plot and, c) potential scan rate dependent variation of current density in non-faradaic region obtained from Mo-8 and Mo-24 samples before and after N doping. d) The variation in the required overpotential to reach -10 $mA.cm^{-2}$ over CV scan cycles for Mo-8 and Mo-24 samples before and after N doping.

As it was concluded from XPS deconvolutions and quantitative analysis, the exposure of Mo-8 to N_2 plasma had the dual effect of promoting 1T phase coverage and introduction of S vacancies. Raman spectra obtained from the single spot of Mo-8 and Mo-8-N before

and after taking nine cycles of CV scans revealed that the J_2 peak vanishes after CV (Figure 5-15). This can be attributed to the conversion of the 1T phase to 1H during electrochemical measurement. As a result, the trends observed in Figure 5-7c and Figure 5-14d can be explained by this conversion. Consequently, as a result of sliding S atoms of the Mo-8 sample under operando conditions it contains only 1H-MoS_2 phase after nine CV cycles. In the case of Mo-8-N, despite the presence of S vacancies and having a lower S/Mo ratio than Mo-8, following the conversion of 1T phase to 1H, the η_{10} value equals the overpotential of Mo-8. Recent theoretical studies have shown that the presence of S vacancies on 1T'-MoS_2 does not positively affect its HER activity [419].

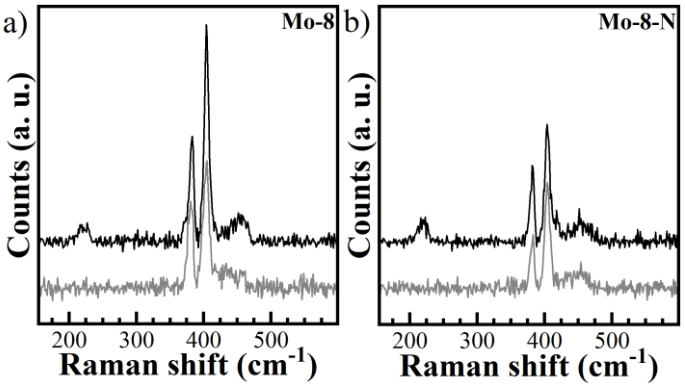

Figure 5-15 Raman spectra of a) Mo-8, and b) Mo-8-N before (black lines) and after (grey lines) obtaining CV

In order to further investigate the phase transition of the Mo-8-N sample during electrochemical measurement, the SEC-Raman experiment was performed on this sample. Raman spectra were taken by 0.05 V intervals, starting from a positive potential region. The selection of this region is based on the results reported in previous SEC-Raman investigations on MoS_2, where it is shown that MoS_2 goes through an "activation" process prior to HER onset potential. During this activation stage, H adsorbs on the electrochemically active S atoms of MoS_2 [420]. This provides a unique chance to study the structural modifications of MoS_2 induced by H adsorption. Figure 5-16a and Figure 5-16b show the data obtained from Mo-8-N for the J_2 peak and the E^1_{2g}/A_{1g} peaks regions, respectively. While there is no significant change in the properties of E^1_{2g} and A_{1g} peaks, the intensity, and position of the J_2 peak show sensitivity to the applied potential. The variation of $I_{J_2}/I_{A_{1g}}$ ratio and J_2 peak position with respect to the applied potential can be seen in Figure 5-16c. Despite slight changes, both variables can be considered constant up to 0.00 V. Immediately after applying negative potential, the $I_{J_2}/I_{A_{1g}}$ ratio starts to drop, which resembles the 1T to 1H phase conversion. Between -0.05 and -0.20 V

potential region, where the rate by which the $I_{J_2}/I_{A_{1g}}$ ratio drops started to decrease, the J_2 peak shows a red shift. This can be attributed to the weakening of the Mo-Mo bond in the remaining 1T-MoS_2 component due to the H adsorption. According to our previous electrochemical measurement results, the onset potential for the Mo-8-N sample is ~-0.215 V. Applying potentials more negative than this potential results in having a further decrease in both $I_{J_2}/I_{A_{1g}}$ ratio and J_2 peak position, confirming further phase conversion and Mo-Mo bond weakening. Due to the generation of a vast amount of H_2 bubbles, hindering the Raman signals, it was not possible to continue the experiment at more negative potential values. Additionally, Raman spectra were collected before and after the experiment, without applying any potential. These spectra are shown with red and dark cyan lines in Figure 5-16a and Figure 5-16b. Also, the $I_{J_2}/I_{A_{1g}}$ ratio for these two Raman spectra are shown with purple circles in Figure 5-16c. Interestingly, both $I_{J_2}/I_{A_{1g}}$ ratio and J_2 peak position recover after stopping the application of potential. However, it is important to consider that this is a partial recovery, and the initial and final values do not match precisely.

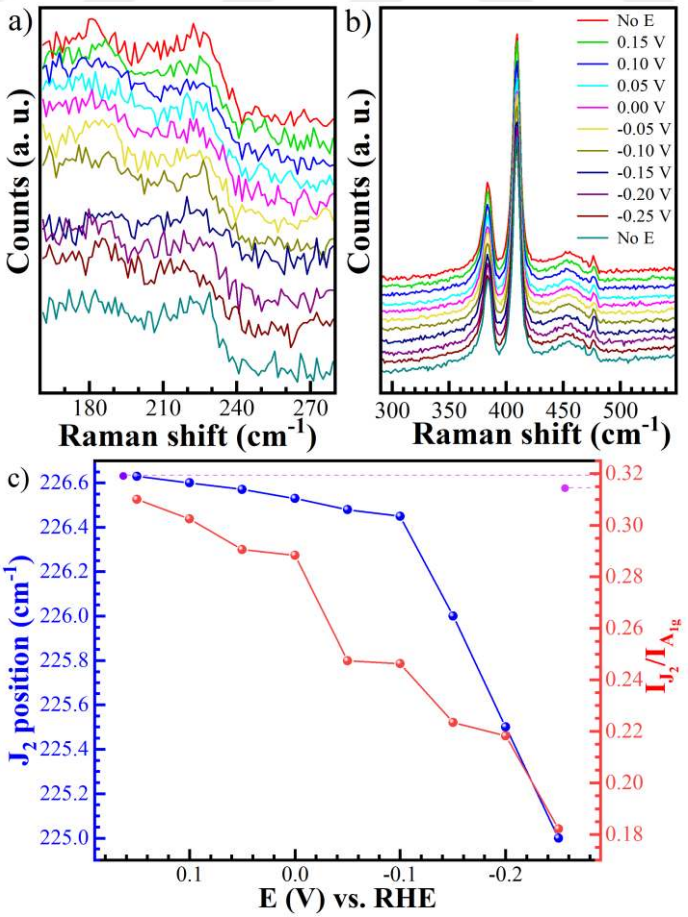

Figure 5-16 SEC-Raman results of Mo-8-N sample in a) J_2 peak and b) E^1_{2g}/A_{1g} peaks regions. c) The

variation in I_{J2}/I_{A1g} and J_2 peak position with respect to the applied potential. The red and dark cyan spectra and the purple circles show the data obtained from the sample without applying any potential.

The partial recovery of the J_2 peak after SEC-Raman measurement looks contradictory with its disappearance after taking nine cycles of CV, shown in Figure 5-16b. Hence, XPS measurements on the Mo-8-N sample after one and nine CV cycles were performed to investigate the compositional change of the samples. Figure 5-17 compares the obtained results with Mo-8 and Mo-8-N in Mo 3d, S 2p, and N 1s XPS regions. The spectra for the sample after one and nine CV cycles are named Mo-8-n_{C1} and Mo-8-N_{C9}, respectively. It is clearly shown in N 1s XPS spectra that N atoms entirely leave the structure after performing one cycle of CV. This is accompanied by the decrease of the 1T-related peaks in the Mo 3d and S 2p spectra. Hence, it can be concluded that the elimination of N groups after the first CV cycle results in the conversion of the 1T component induced by the presence of N back to 1H. The remaining 1T phase can be the origin of the J_2 peak in the Raman spectrum after the SEC-Raman experiment. Upon performing nine consecutive CV cycles, the initial 1T phase also gets converted to 1H. The XPS Spectra of Mo-8-N_{C9} are very similar to the purely 1H covered samples such as Mo-16 and Mo-18 with a small Mo^{6+} peak in the Mo 3d spectrum, attributed to the Mo-O groups. The absence of 1T-related peaks in XPS results for the Mo-8-N_{C9} agrees with the disappearance of the J_2 peak in Figure 5-15b.

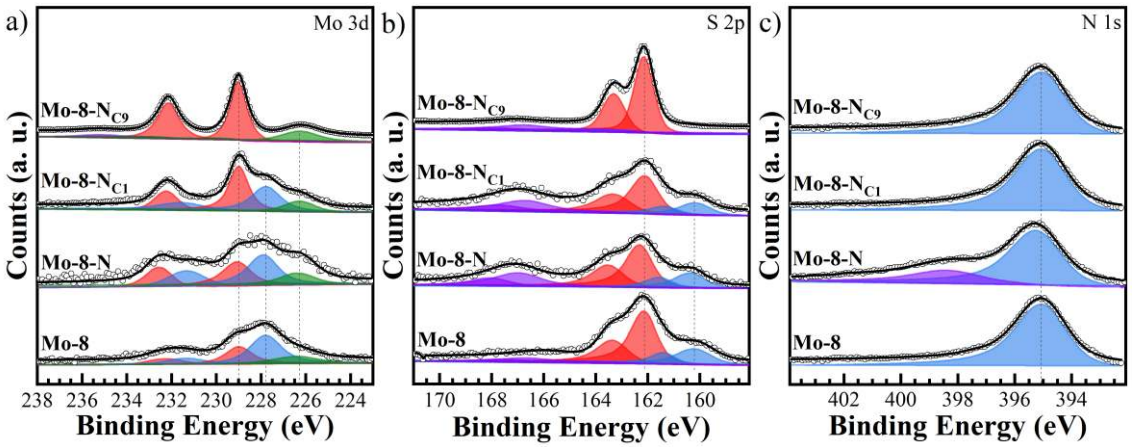

Figure 5-17 Deconvoluted high resolution XPS spectra of a) Mo 3d, b) S 2p, and c) N 1s regions for Mo-8, Mo-8-N, Mo-8-N_{C1} and Mo-8-N_{C9} samples.

5.4 Conclusion

In summary, it has been shown that it is possible to engineer the phase, composition, flake size and defect density of MoS_2 by modifying its synthesis parameters. The best HER

activity was obtained from the samples which had either highest metallic 1T phase or semiconductor phase with small flake size and high number of vacancies. The Volmer-Heyrovsky mechanism with Heyrovsky step and the rate-determining step was suggested as the HER mechanism of these samples. The activity of the samples was further enhanced by introducing ~8 at. % N dopants into the MoS_2 structure using room temperature low power N_2 plasma. While this treatment did not have any effect on the thickness of the samples, it induced compressive strain in the MoS_2 structure by substituting S atoms with N. This strain resulted in the further conversion of 1H phase to 1T. The SEC-Raman and ex-situ XPS measurements revealed that adsorption of H on 1T-MoS_2 causes 1T to 1H phase transformation during HER which results in significant activity loss for this sample after recording consecutive LSV scans.

Chapter 6:
The Effect of Compositional Stability of Nickel Sulfides on their HER Activity

6.1 Introduction

6.1.1 Structure, Properties, and HER Activity of Nickel Sulfides

Nickel-based dichalcogenides, consisting of sulfides, selenides, and tellurides, have been attracted the electrochemical research society due to their promising properties. Among these, nickel sulfides are the most studied form for electrocatalytic hydrogen generation. Ni-S has a relatively complicated phase diagram compared to other TMDs. Ni_yS_x can have different polymorphs such as Ni_3S_2, Ni_7S_6, Ni_9S_8, NiS, Ni_3S_4, and NiS_2 [421]. The insolubility of all these polymorphs in water makes them suitable candidates for neutral, near-neutral, and alkaline water splitting electrocatalysis. However, they dissolve readily in a strong acidic medium [422]. Numerous synthesis methods have been developed for the facile and straightforward synthesis of nickel sulfides. But it is challenging to control chemical composition and morphologies of nickel sulfide in most of these methods.

Recent studies with relatively better compositional controlled synthesis methods have shown a difference in HER activity of various nickel sulfide polymorphs [423]–[429]. Zhu et al. have reported a remarkable HER activity for the NiS microspheres prepared on Ni foam with an overpotential of 158 mV for delivering 20 $mA.cm^{-2}$ in 0.1 M KOH electrolyte [428]. In another study, the Ni_3S_2 electrode on Ni foam showed a higher overpotential (200 mV) [430] than that of the NiS microspheres prepared by Zhu et al. [428]. Tang et al. [431] investigated the HER activity of the pyrite type NiS_2 polymorph. This electrode showed promising activity, demanding 243 mV at 10 $mA.cm^{-2}$. Due to the sensitivity of the overpotential value to the cathode loading amount, chosen substrate, Ni:S stoichiometric ratio, and morphological differences, it is not possible to have a distinct comparison between the HER activity of nickel sulfide polymorphs based on these studies [422], [432]. For instance, pure NiS_2 in different morphologies displays varying activities in alkaline media, with overpotentials between 67 and 220 mV [425].

Recently, Manjunatha et al. [421] synthesized NiS, Ni_3S_4, and NiS_2 hydrothermally and investigated the OER activities of these polymorphs. Their results revealed the lowest onset overpotential for NiS electrodes with cubic morphology. However, this finding can be misleading since the morphology of synthesized polymorphs was not identical.

Even in the case of studies with the same Ni:S stoichiometric ratio or similar morphology, the overpotential value may have been drastically affected by the current normalization method (i.e., whether it has normalized based on ECSA or geometric surface area or specific surface area). To overcome these uncertainties, Jiang et al.[426] performed a case study where a series of nickel sulfide nanoparticles were prepared with varying stoichiometries such as NiS, NiS_2, and Ni_3S_2. It was found that these nickel sulfide nanoparticles exhibited HER activity in the following order: Ni_3S_2 > NiS_2 > NiS. The higher ECSA and electrical conductivity of Ni_3S_2 were introduced as the origin of this superior activity. The results of this study contradict the earlier studies discussed above.

In light of outstanding findings in the electrochemical activity of metal-rich TMDs, numerous studies have been performed on Ni_3S_2 and Ni_9S_8 polymorphs [433], [434]. However, despite the high HER activity of the cubic pyrite-phase NiS_2, there is a lack of comprehensive investigation about their stability and degradation during HER. Operando studies performed by Zhu et al. [435] on CoP_2 revealed the surface composition transformation during electrochemical experiments. According to their findings, the reactive species are metallic cobalt (for HER) and cobalt oxyhydroxide (for OER), not the initial phases. Recently, Karakaya et al. studied the surface composition and structure transformation of mesoporous NiS_2 electrocatalyst during HER in alkaline media by ex-situ characterizations. According to their results, while the presence of S on the surface is critical for the stimulation of HER activity, partially hydroxylated, under-coordinated Ni sites formed upon amorphization along with sulfurous ions leaching out provide the most active surface for the HER [436].

Theoretical calculations have suggested the high electronegativity of S as the origin of elevated activity of nickel sulfides in weak acidic electrolytes [437]. Other studies propose that both S and Ni sites on (001) terminated NiS_2 could be active with the relatively smaller free energy of H adsorption on Ni sites [438]. These findings are similar to the results of investigations on other TMDs, where under coordinated metal sites have been pointed out to have an essential role in determining the electrochemical activity [434], [439].

All these contradictory experimental results, albeit the presence of detailed theoretical studies, show the importance of performing experimental investigation about the details of HER mechanism and electrode evolution under operando conditions. Such a study would be possible only on a pure electrode with stable and reproducible morphology.

6.1.2 Aims of Study

Here we report a facile one-step S treatment and hydrothermal synthesis of nickel sulfide, which result in different phases with 2D and 3D structures. Due to the high number of available active sites of the 2D structures, these samples showed superior electrochemical HER activity. Different dynamic behavior was observed in the HER activity of the samples based on their composition and morphologies. The CA-Raman and CA-XPS experiments revealed the alterations in the composition of the samples during electrochemical measurements and confirmed the importance of the co-existence of hydroxylated and sulfurized Ni groups in enhancing the HER activity.

6.2 Experimental

6.2.1 Synthesis of Nickel Hydroxide

For the synthesis of $Ni(OH)_2$, which was used as the Ni precursor in the nickel sulfide synthesis procedure, two different methods based on the presence of surfactant were used [440], [441]. For the preparation of surfactant-free exfoliated $Ni(OH)_2$ nanosheets (SF-$Ni(OH)_2$), 30 mL of 0.75 M NaOH was added to 50 ml of 0.35 M $Ni(NO_3)_2.6H_2O$ solution dropwise with an addition rate of 0.5 $ml.min^{-1}$. The solution was then centrifuged at 8000 rpm for 5 min, followed by washing with deionized water (DI water) four times. The precipitated green solid part was transferred to a 1000 ml beaker, and 800 ml DI water was added. The mixture was stirred for 20 h with a stirring rate of 300 rpm to exfoliate the flakes mechanically. In the end, a homogeneous green solution was obtained. To eliminate the aggregated nanosheets, the solution was centrifuged at 10000 rpm for 30 min, and the supernatant part was collected as exfoliated $Ni(OH)_2$.

The surfactant-assisted exfoliated nanosheets (S-$Ni(OH)_2$) were synthesized in two steps [442]. First, 1.2 mmol of nickel nitrate hexahydrate ($Ni(NO_3)_2.6H_2O$, Sigma Aldrich, 99.9% purity), 3.0 mmol of sodium dodecyl sulfate (SDS) ($NaC_{12}H_{25}SO_4$, Sigma Aldrich, 99.00% purity), and 7.2 mmol of Hexamethylenetetramine (HMT) ($C_6H_{12}N_4$, Sigma Aldrich, 99.00% purity) were dissolved in DI water, and the volume of the solution was set to 60 ml. The mixed solution was hydrothermally treated at 90 ºC for 24 h inside a sealed Teflon vessel. During the heating process, slow hydrolysis of HMT occurs,

releasing OH^- ions [443]. As a result of the reaction between Ni ions with these anions, octahedral structures with OH^- vertices form. The edge-sharing of these octahedrons creates two-dimensional sheets stacked by hydrogen bonding [443]. The intercalation of dodecyl sulfate between these sheets weakens the hydrogen bonding due to the hydrophobic tail groups [444]. Then, the solution was centrifuged at 10000 rpm for 30 min to collect the green precipitation, which was washed with DI and ethanol in turn for three times with shaking and centrifugation. Finally, the precipitated nanosheets were dried at room temperature overnight. In the second step, 60 mg of the synthesized nanosheets were dispersed in 50 ml of formamide (Sigma Aldrich, 99.5%). The carbonyl functions of the highly polar formamide molecules interact strongly with the OH-groups of intercalated water molecules and $Ni(OH)_2$ [445]. The strong interaction of the positively charge $Ni(OH)_2$ backbone and formamide and swelling hydration shell of formamide, due to its high hydration enthalpy, promote the exfoliation and lamination of the flakes [446]. The solution was stirred at 200 rpm for 4 days to obtain a translucent solution. Then, it was centrifuged at 2000 rpm for 10 min. The exfoliated $Ni(OH)_2$ nanosheets were obtained by collecting the supernatant part of this solution. The schematic representations for the synthesis procedures of SF-$Ni(OH)_2$ and S-$Ni(OH)_2$ are shown in Figure 6-1 upper and bottom panel, respectively.

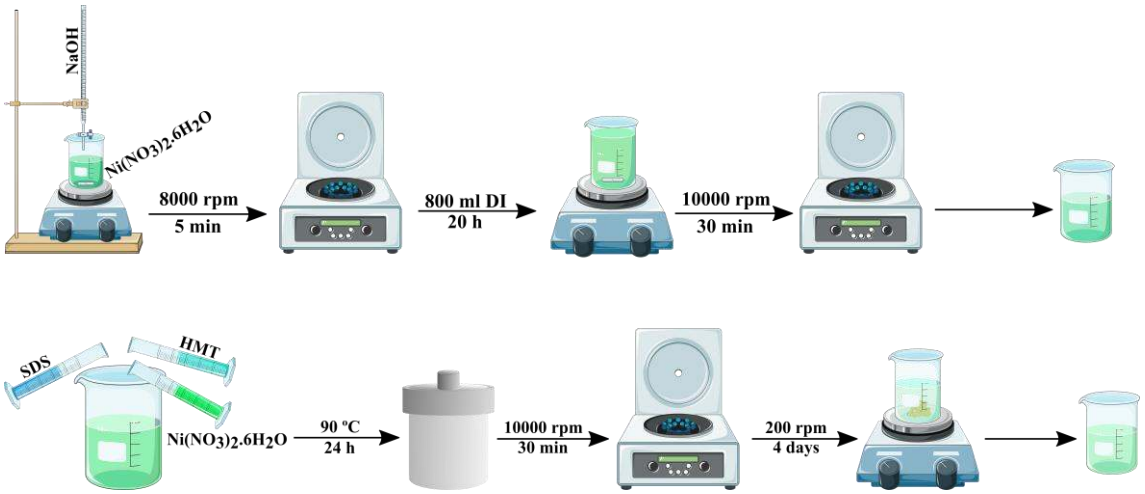

Figure 6-1 Schematic representation for the synthesis procedure of SF-$Ni(OH)_2$ (upper panel), and S-$Ni(OH)_2$ (bottom panel).

6.2.2 Synthesis of Nickel Sulfide

The 2D NiS_2 nanosheets were synthesized inside a multitemperature-zone tubular furnace. The nickel precursors were prepared by two different methods. In the first method, the SiO_2/Si or FTO substrates were dip-coated by diluted (100 times) solutions of SF-$Ni(OH)_2$ and S-$Ni(OH)_2$ nanosheets for 160 times, followed by drying overnight at

room temperature. In the other method, the solution of SF-$Ni(OH)_2$ nanosheets was freeze-dried at -48 ℃ for 24 h to obtain 0.01 g of these nanosheets in powder form. Both forms of nickel precursors were placed on the downstream region of the quartz tube. Meanwhile, the S powder, placed outside the hot zone, was mildly sublimated at ~150 ℃ with heating tape and carried by N_2 gas (100 sccm) to the downstream growth zone. The growth process was initiated by increasing the temperature of the hot zone of the tube to 350 ℃ with a heating rate of ~10 ℃/min under ambient pressure. The growth time was set to 4h. The samples obtained from this method are henceforth mentioned as 2D-S (prepared using S-$Ni(OH)_2$) and 2D-SF (prepared using SF-$Ni(OH)_2$).

Additionally, nickel sulfide nanoparticles were synthesized by the hydrothermal method. The freeze-dried SF-$Ni(OH)_2$ nanosheets were used as nickel precursors and were mixed in a 1:3 mole ratio with thiourea, as the S precursor, in 60 ml DI water. The mixture was then placed inside a sealed Teflon vessel. The synthesis was performed at 210 ℃ for 7h. The black precipitation was then washed with DI water and ethanol in turn for 5 times by centrifuging the solution at 10000 rpm for 10 min. Finally, the black paste was dried at 50 ℃ for 6h to obtain nickel sulfide nanoparticles (3D sample). The different synthesis procedures of nickel sulfide are depicted schematically in Figure 6-2.

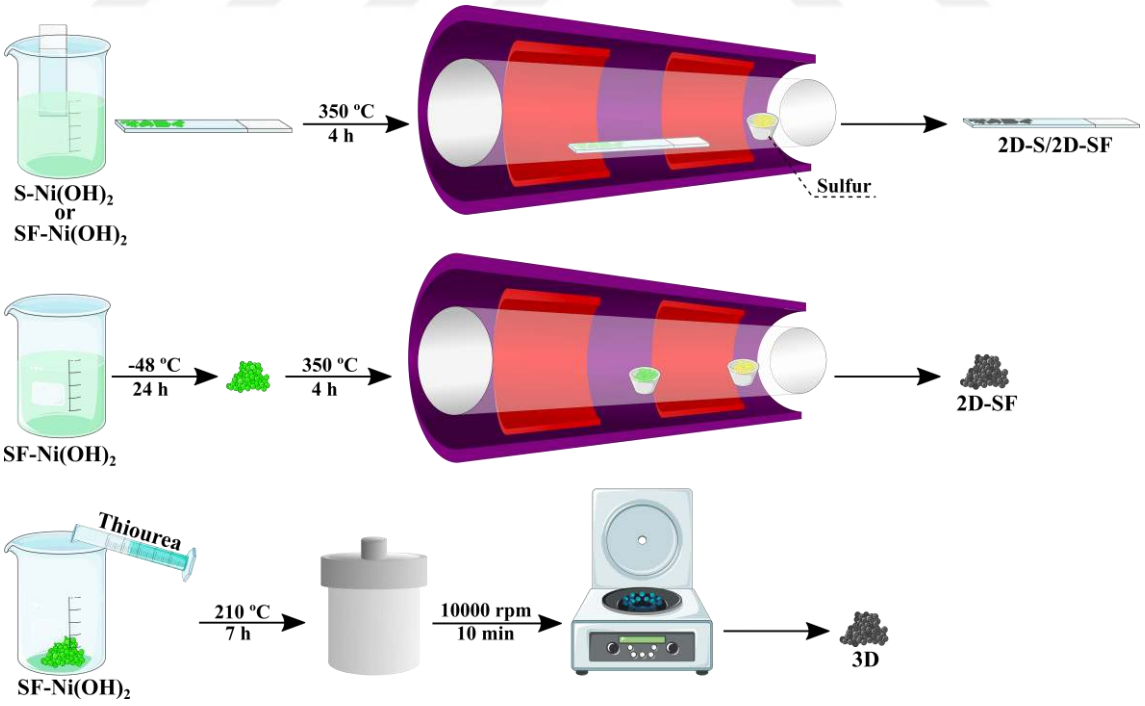

Figure 6-2 Schematic representation of nickel sulfide synthesis.

6.2.3 Physical Characterizations

XRD patterns were obtained by BRUKER D8 advanced X-ray diffractometer for 2θ

values between 10 and 85°. A Thermo K-alpha laboratory XPS system equipped with a monochromatized Al K-alpha X-ray source was used to perform XPS measurements. The XPS binding energies were referenced to the C 1s peak at 284.5 eV. Raman spectroscopy (Renishaw INVIA) investigations were conducted by setting the laser excitation wavelength at 532 nm and the laser power to 20.3 mW. The morphology of the nanosheets was studied by a "Bruker Dimension Icon" AFM system equipped with a "Bruker ScanAssyst-Air" tip.

6.2.4 Electrochemical Characterizations

All electrochemical measurements were carried out using a Biologic SP-200 potentiostat in a standard three-electrode cell at room temperature. The three-electrode cell configuration consisted of a Pt spiral wire as a counter electrode, an Ag/AgCl in 4 M KCl as a reference electrode, and nickel sulfide samples on FTO glass as the working electrode. 0.1 M KOH was chosen as the electrolyte solution. The LSV measurements were performed at room temperature from 0.05 to -0.42 V vs. RHE with a scan rate of 10 mV/s. All potentials reported here are vs. RHE. The double-layer capacitances (C_{DL}) were estimated by plotting anodic and cathodic current density differences (Δj) against the potential scan rate. The slopes of such plots were assumed to be twice C_{DL} and used to represent the ECSA. The EIS measurement was carried out at -0.4 V for frequencies between 0.1 Hz and 100 kHz.

6.3 Compositional Transformation of Nickel Sulfide During HER

Due to the different crystallographic structures of various nickel sulfide forms, they can be distinguished by XRD. The obtained XRD pattern from nickel sulfides synthesized by S treatment of S-$Ni(OH)_2$ and SF-$Ni(OH)_2$ nanosheets on FTO substrate (2D-S and 2D-SF, respectively), reveal identical results. The XRD pattern acquired from 2D-S, which is shown in Figure 6-3a matches the pure NiS_2 pyrite phase (COD 9012538). The extra peaks in the XRD pattern of this sample (labeled with "F") are attributed to the FTO substrate [447]. In order to make sure about the attribution of these extra peaks to FTO and eliminate them, the XRD pattern of 2D-SF synthesized by S treatment of the freeze-dried SF-$Ni(OH)_2$ powder was studied. The pattern consists of only pyrite NiS_2 phase-related peaks (Green pattern in Figure 6-3a) and no additional peak is observed. These results confirm the feasibility of synthesizing pure NiS_2 phase by S treatment of $Ni(OH)_2$ flakes, regardless of the preparation procedure of those flakes. On the other hand, the hydrothermally synthesized nickel sulfide (henceforth 3D) contains different phases. The

presence of NiS_2, Ni_3S_4, and NiS in this sample was confirmed by the XRD pattern shown in blue in Figure 6-3a. Comparing the results of 2D-S, 2D-SF, 3D with the XRD pattern obtained from SF-$Ni(OH)_2$ (grey pattern in Figure 6-3a) confirms the full conversion of $Ni(OH)_2$ to nickel sulfide in all methods. The peak positions and attributed diffraction planes for NiS_2, NiS, Ni_3S_4, and $Ni(OH)_2$ are shown in Table 6-1. According to the Reference Intensity Ratio (RIR) method [165], the compositional percentage of the NiS_2, Ni_3S_4, and NiS phases in 3D are 28.0, 20.3, and 51.7, respectively.

The compositions of all three samples were also studied using Raman spectroscopy. According to group theory analysis, five Raman active modes $A_g + E_g + 3T_g$ are expected for the NiS_2 phase [24]. However, experimentally it is not possible to observe the $T_g(2)$ mode, which is expected to have a peak at ~340 cm^{-1} wavenumber. This absence has often been interpreted as the result of the coupling between the rotational and stretching vibrations of S_2 dimers [449]. The remaining four modes result in a doublet in the lower wavenumber (~280 cm^{-1}) and another in the higher (~470 cm^{-1}) region. These peaks can be seen in the Raman spectra attributed to 2D-S and 2D-SF samples in Figure 6-3b. The in-phase and out-of-phase stretching vibrations of the S-S pairs result in $T_g(1)$ and A_g modes at ~488 cm^{-1} and ~478 cm^{-1} wavenumber, respectively [450]. The low-frequency doublet is attributed to the rotational modes of S_2 dimers and is scribed by E_g (~284 cm^{-1}) and $T_g(3)$ (~274 cm^{-1}) [449]. As was expected from the XRD results, in addition to the NiS_2 related peak, the NiS and Ni_3S_4 related peaks can also be seen in the Raman spectrum of the 3D sample. The NiS phase has eight Raman active modes; however, due to the experimental limitations and the presence of other phases, six of them can be resolved in the spectrum presented in Figure 6-3b. These are $A_1(1)$ (~370 cm^{-1}), E(1) (~351 cm^{-1}), $A_1(2)$ (~301 cm^{-1}), E(2) (~247 cm^{-1}), E(3) (~233 cm^{-1}), and E(4) (~189 cm^{-1}) peaks [449]. There are hexagonal and rhombohedral polymorphs for the NiS. The peak position of the E(1) and E(2) modes, as well as the intensity ratio of E(3) to E(4), can be used to determine these polymorphs [451]. All these quantities confirm the presence of rhombohedral β-NiS. Finally, among five Raman active vibration modes of Ni_3S_4, the A_{1g}, $T_{2g}(1)$, and $T_{2g}(3)$ can be seen at ~386, ~337, and ~205 cm^{-1}, respectively. The absence of the $T_{2g}(2)$ and E_g modes is due to the vibration frequency overlap of these modes with the modes attributed to the NiS and NiS_2 phases.

Due to the 2D nature of S treated samples (2D-S and 2D-SF), it is beneficial to investigate their properties with a surface-sensitive method, such as XPS, and compare them with the

hydrothermally synthesized 3D nanoparticles. Figure 6-3c shows the Ni 2p XPS spectra of the 2D-S, 2D-SF, and 3D samples. The Ni 2p spectra of different nickel sulfide phases are very similar [427], hence, all three samples show Ni $2p_{3/2}$ and Ni $2p_{1/2}$ at the same binding energies and it is not possible to distinguish them. The broad satellite peak visible at ~859.0 eV is also attributed to nickel sulfide. Additionally, the Ni-O related Ni $2p_{3/2}$ and Ni $2p_{1/2}$ peaks can be seen at 586.0 and 587.7 eV, respectively [452], [453]. These peaks can be attributed to either oxidation or hydroxylation of nickel in the ambient conditions. Among the three samples, 2D-SF looks more prone to this oxidation/hydroxylation. For the 2D-SF samples with a high concentration of surface Ni-O species, three additional satellite features are visible at ~861.1, ~864.2, and ~875.2 eV [453]. In order to further investigate the nature of these groups, the O 1s spectra of the samples were analyzed. Unfortunately, since the stock solution of S-$Ni(OH)_2$ is very dilute, the prepared 2D-S sample is very thin and there is a significant contribution of oxide groups attributed to FTO to the O 1s spectrum of this sample. Hence, it was not possible to distinguish the oxidized/hydroxylated Ni groups. The O 1s spectra of 2D-SF and 3D are shown in the inset of Figure 6-3a, and Figure 6-3b, respectively. For both of the samples, the O 1s spectrum was consisted of two peaks; the low binding energy peak (shown with red), which is attributed to O-Ni, and the high binding energy (shown with blue), which is attributed to O-H [454]. This analysis clearly shows that while the peak at 856.0 eV of Ni 2p spectrum for 2D-SF is mainly attributed to the $Ni(OH)_2$, the same peak for 3D samples is due to the presence of surface oxide groups. The S 2p spectra for the samples are shown in Figure 6-3d-f. The main peaks (shown with blue) at ~161.5 162.3 and ~162.7 163.5 eV are attributed to S $2p_{3/2}$ and S $2p_{1/2}$ states of S_2^{2-} dimers. There is also a double at ~168.7 eV (shown with red) which arises due to the surface oxidation in ambient condition. The high binding energy doublet (162.3 and 163.5 eV) which is apparent in the S 2p spectrum of the 3D sample with purple, can be related to S^{2-}.

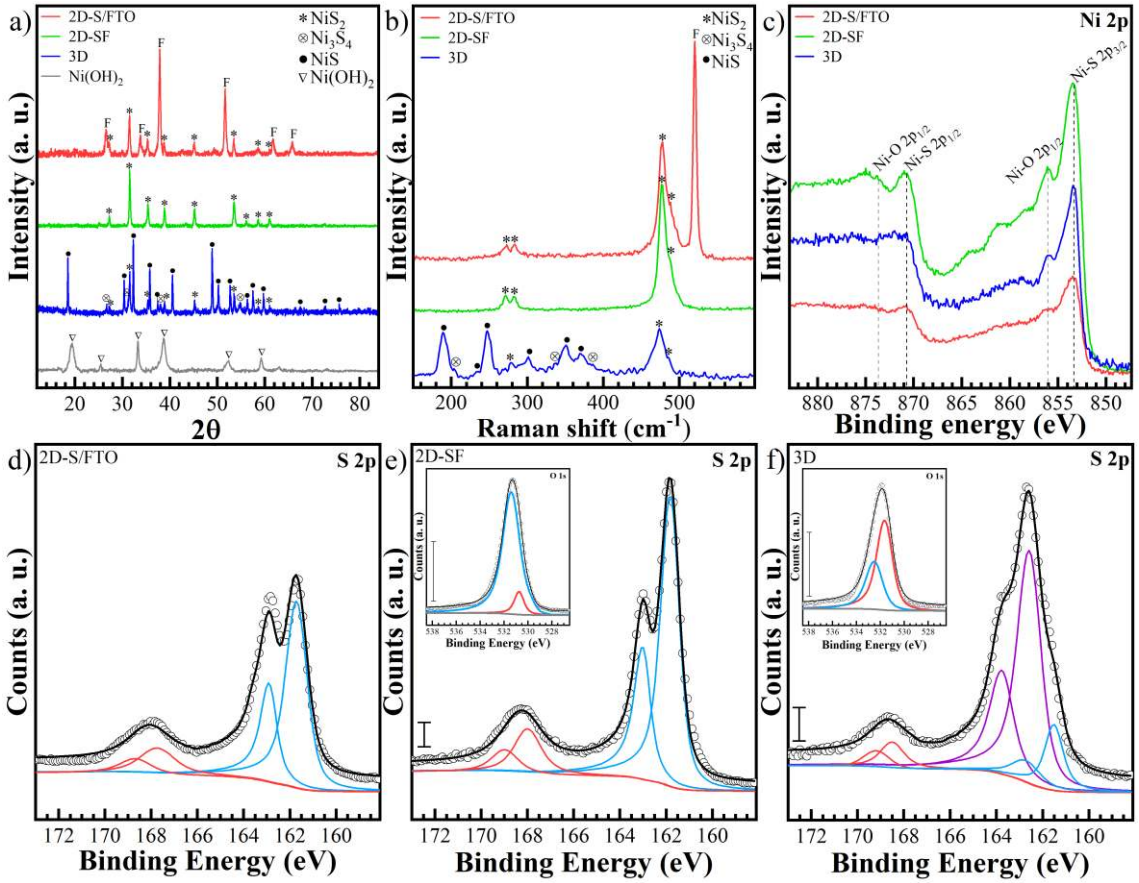

Figure 6-3 a) XRD pattern, b) Raman spectra of 2D-S on FTO (red curves), 2D-SF (green curves), and 3D (blue curves). c) XPS spectra of Ni 2p region, and deconvoluted spectra of S 2p region for d) 2D-S on FTO, e) 2D-SF, and f) 3D samples. The insets in e) and f) show deconvoluted O 1s XPS spectra of 2D-SF and 3D, respectively.

Table 6-1 XRD peak positions and assigned diffraction planes for NiS_2, NiS, Ni_3S_4, and $Ni(OH)_2$

NiS_2									
2θ	27.1	31.4	35.2	38.7	45.0	53.3	55.9	58.4	60.9
Plane	111	002	012	112	022	113	222	023	123

NiS															
2θ	18.4	30.3	32.2	35.7	37.4	40.5	48.8	50.1	52.6	56.3	57.4	59.7	67.4	72.6	75.7
Plane	110	011	030	021	220	121	131	140	041	231	330	012	060	132	341

Ni_3S_4				
2θ	26.6	31.3	38.0	54.9
Plane	022	113	004	044

$Ni(OH)_2$						
2θ	19.2	33.1	38.6	52.0	59.2	62.8
Plane	001	010	011	012	110	111

The morphology of 2D nanosheets of 2D-S and 2D-SF samples were investigated using AFM. Figure 6-4a-b and Figure 6-4g-h show the SF-$Ni(OH)_2$ and S-$Ni(OH)_2$ flakes,

respectively. While line scan profile of both flakes, shown in Figure 6-4e, and Figure 6-4k, reveal a similar thickness of 2-3 nm, the lateral size of the S-$Ni(OH)_2$ sample is ten times larger than the SF-$Ni(OH)_2$ and has a diameter of ~1µm. The AFM images of the same samples after S treatment can be seen in Figure 6-4c-d and Figure 6-4i-j. The bright spots on the flakes and the increased roughness (which can be detected by line scan profiles shown in Figure 6-4f, and Figure 6-4l) are signs of the conversion of the 2D $Ni(OH)_2$ to NiS_2. The smaller diameter of the 2D-SF samples, which results in a higher edge to the basal plane ratio, explains the greater extent of oxidation at ambient conditions reported in Ni 2p XPS spectra (Figure 6-3c).

The morphology of 3D samples was investigated by SEM. The SEM images in Figure 6-4m, and Figure 6-4n, which have been obtained with 8000 and 17000 magnifications, respectively, show the presence of spherical structures with average diameter of 200-250 nm.

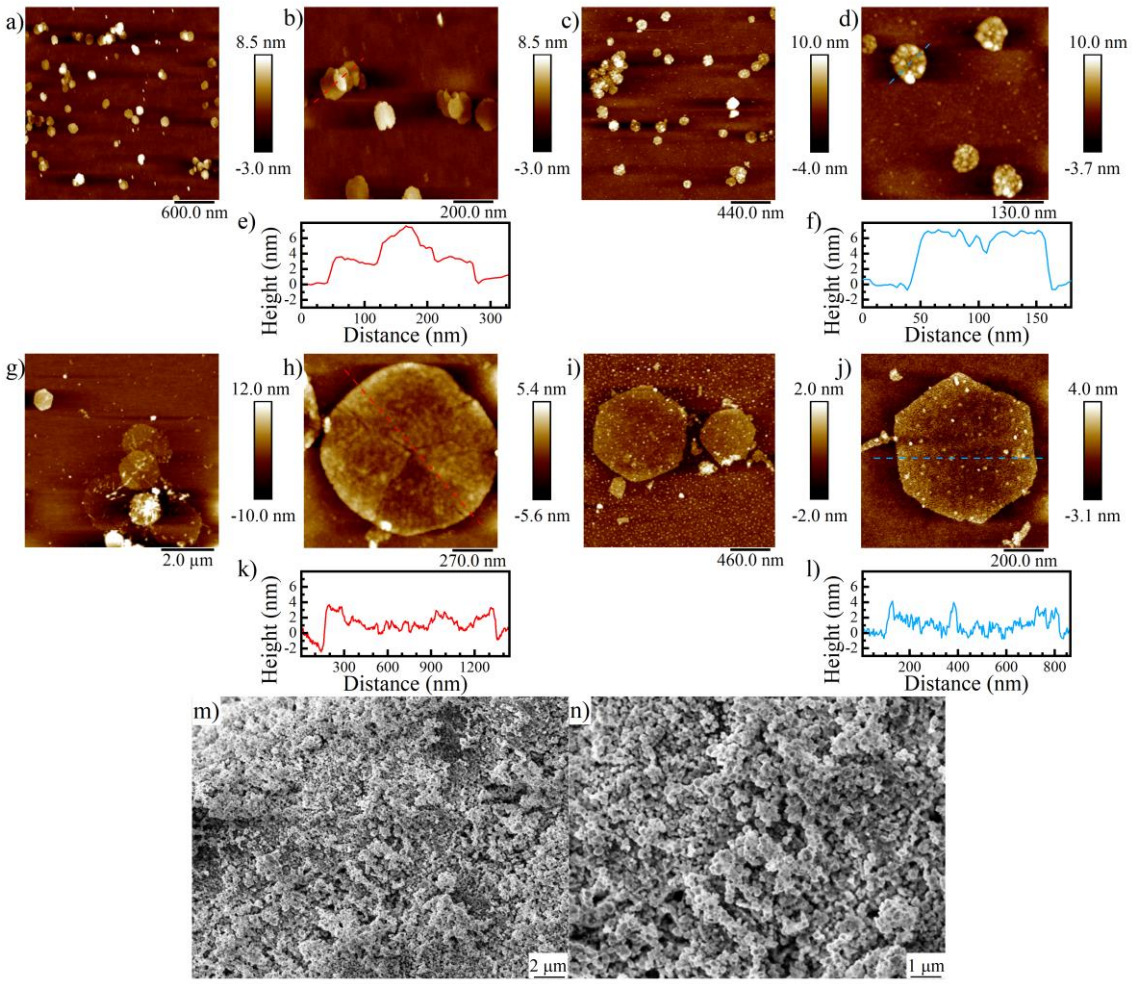

Figure 6-4 AFM images of SF-$Ni(OH)_2$ a-b) before and c-d) after S treatment. The same images for the S-$Ni(OH)_2$ g-h) before and i-j) after S treatment. The line scan profile for (b), (d), (h), and (j) are shown in

(e), (f), (k), and (l), respectively. SEM images taken from 3D samples with m) 8000x, and n) 17000x magnification.

The electrochemical activity of the 2D samples and the hydrothermally synthesized sample towards HER were investigated by taking seven consecutive LSV scans. After recording the last LSV scan, the samples were kept inside the electrolyte for 3 minutes, followed by a new consecutive LSV scan set. The LSV scan number (x) and the number of run (y) to which this scan belongs to, are shown using Rx-Sy coding in Figure 6-5. The HER activities of both 2D-SF and 2D-S samples decline gradually by increasing the LSV scans (Figure 6-5a, and Figure 6-5b). This decline can be clearly seen by studying the onset potential and current densities. However, there is a slight difference between the trends of these two samples. Comparing the required potential to reach -5.0 $mA.cm^{-2}$ (η_5) for these two samples helps to better realize this difference. The plot for the variation of η_5 value over different scans are shown in the insets of Figure 6-5. There is a linear decline in the HER activity for the LSV scans in each run of 2D-SF, and almost identical steps can be seen for the η_5 change between the last LSV of each run with the first LSV scan of the next one. This type of repeatable trend is missing for the 2D-S.

On the contrary, increasing the scan number in the first LSV run results in an improvement in the activity of the 3D sample (Figure 6-5c). The first scan of the second run reveals significant enhancement; however, the trend is similar to the 2D samples for the rest of the scans, and the activity diminishes. Stopping the experiment and running it for the third time causes further enhancement in the recorded LSV scan followed by a similar trend seen in the second LSV run of this sample. Hence, it can be stated that all of the samples experience a dynamic alteration during the electrochemical measurements. However, the effect of this alteration on electrochemical activity and probably its nature for the 3D sample is different than the 2D samples.

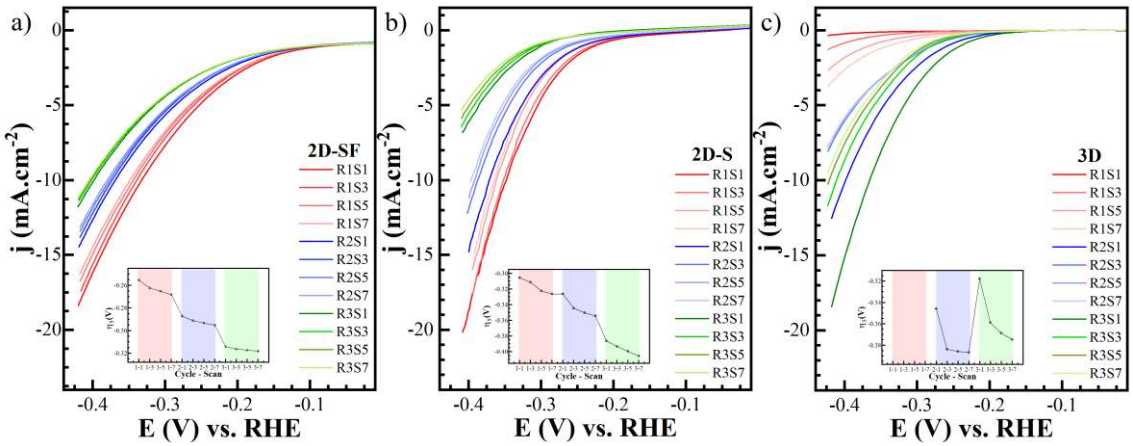

Figure 6-5 Consecutive LSV scans obtained from a) 2D-SF, b) 2D-S, and c) 3D samples.

To evaluate the evolution of dynamic HER activity of the samples over long-time exposure to high negative potentials, the LSV and EIS scans, as well as the C_{DL} value of the fresh samples, were compared to the same results obtained from them after keeping under the constant potential of -0.5 V for 1000 s. Figure 6-6a-c reveals similar results to the general trends observed in Figure 6-5; a decline in the activity of 2D-SF and 2D-S and an increase in the HER performance of 3D. While the onset potential of fresh 2D-SF and 2D-S were recorded as -0.200 and -0.259 V, respectively, these values shifted to -0.226 and -0.272 V after 1000 s of -0.50 V application. The same alteration can be observed for the η_{10} values of these two samples. The η_{10} of 2D-SF and 2D-S, shifted from -0.331 to -0.379 V and from -0.346 to -0.403 V, respectively. Meanwhile, the inferior activity of the 3D sample with an onset potential of -0.365 V improves, and it reaches -0.246 V. The significantly lower current density of 3D compared to 2D-SF and 2D-S can be due to the different loaded catalyst amounts. Also, the 2D nature of the 2D-SF and 2D-S samples provides more available active sites resulting in higher recorded current density. The EIS measurement was performed to study the charge transfer resistance (R_{ct}) variation of the electrodes. Upon applying cathodic potential, there is an increase in the R_{ct} value of 2D-SF and 2D-S (Figure 6-6d, and Figure 6-6e). The same treatment causes a decline in the R_{ct} of the 3D sample (Figure 6-6f). This is congruent with the HER activity enhancement seen in the LSV scans of this sample. Finally, comparing the C_{DL} values of the samples shown in Figure 6-6g, Figure 6-6h, and Figure 6-6i reveals similar results; enhancement for the 3D and diminution for 2D-SF and 2D-S. Both R_{ct} and C_{DL} values of the 3D sample after keeping inside the electrolyte are significantly better than the initial values for the 2D-SF and 2D-S samples. Hence, the above-stated lower current density value of 3D seems to be mainly affected by the amount

of loaded catalyst.

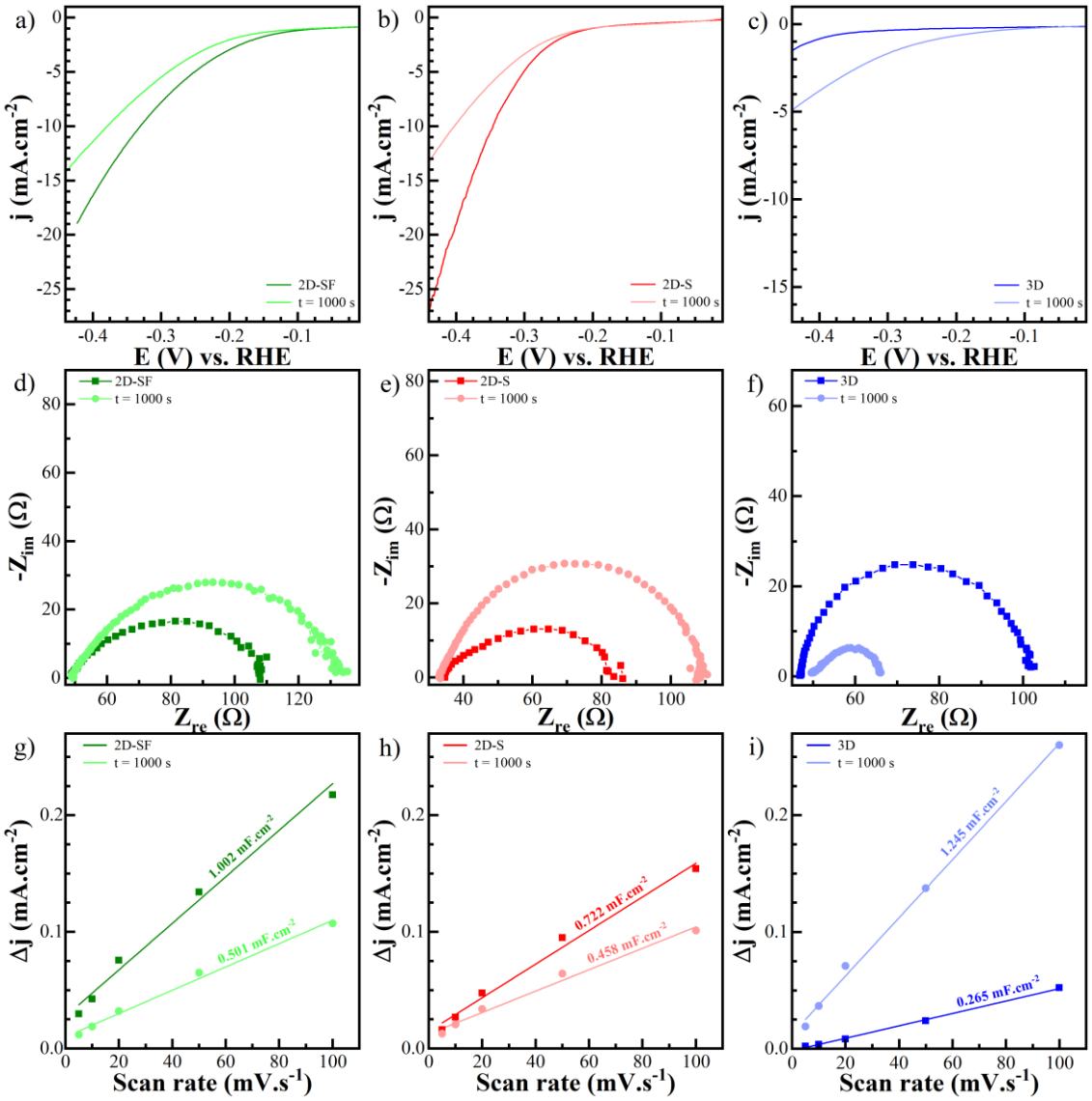

Figure 6-6 a-c) LSV scans, d-f) EIS measurements, and g-i) C_{DL} analysis obtained from 2D-SF, 2D-S, and 3D samples in their fresh forms and after keeping under -0.50 V for 1000 s.

A set of CA-Raman and CA-XPS experiments were designed and performed to better understand the compositional alteration of the samples under operando conditions. The samples were subjected to cathodic voltage for 100 s and then characterized by Raman spectroscopy and XPS. Figure 6-7 shows results obtained for 2D-SF. The Raman, Ni 2p, ,S 2p, and O 1s XPS spectra related to α-$Ni(OH)_2$ are also shown as a reference. Previous studies have introduced four Raman active vibration modes for α-$Ni(OH)_2$. The corresponding peaks for these vibrations can be detected at 460 cm^{-1} (lattice vibrations), 1075 cm^{-1} (second-order lattice transitions), 1620 cm^{-1} (O-H bond bending) and 3647 cm^{-1} (O-H bond stretching) [455], [456]. It is expected to detect nitrate groups vibration related peaks in Raman spectrum of α-$Ni(OH)_2$ synthesized using $Ni(NO_3)_2$ as precursor.

These peaks are ν_1 at 1048 cm^{-1} (A'_1), ν_2 at 831 cm^{-1} (A''_2) ν_3 at 1390 cm^{-1} (E'), and ν_4 at 720 cm^{-1} (E') [457]. Among all nickel hydroxide and nitrate-related peaks, only the ones at 460 cm^{-1}, 3647 cm^{-1} (for nickel hydroxide), 1050 cm^{-1}, and 1390 cm^{-1} (for nitrate groups) are strong enough to be detected in dilute and thin samples. Since the electrodes studied in the CA-Raman experiments were wet and due to the large water background in the wavenumbers higher than ~1250 it was not possible to observe the peaks in this region. Immediately after immersing the 2D-SF electrode inside the electrolyte (t = 0 s), NiS_2 related Raman active modes, which were detected as two doublets at around 280 cm^{-1} ($T_g(3)$ and E_g) and 470 cm^{-1} ($T_g(1)$ and A_g), start to diminish (Figure 6-7a). In parallel with this diminishing, the intercalated nitrate ions vibrations related peak at ~1045 cm^{-1} wavenumber appears. Also, instead of the higher wavenumber Raman doublet of NiS_2 (~480 cm^{-1}) a single peak at ~465 cm^{-1} can be detected. This peak can be attributed to the A_{1g} vibration mode of $Ni(OH)_2$ lattice. Applying a small cathodic potential of -0.05 V results in a further decrease of NiS_2 related peaks and enhancement of the modes attributed to $Ni(OH)_2$. Hence, it can be concluded that 2D NiS_2 gets converted to $Ni(OH)_2$.

This conversion is very fast, and it starts to propagate after inserting the sample inside the electrolyte. This trend can be traced by studying the Ni 2p, and S 2p XPS spectra (Figure 6-7b, and Figure 6-7c). The immersion inside the electrolyte significantly affects the Ni $2p_{3/2}$ and Ni $2p_{1/2}$ peaks and results in the oxidation of a notable portion of the S groups. While minute NiS_2 related peaks can be seen in the Raman spectrum of 2D-SF after applying -0.05 V, there is no S_2^{2-} attributed peak in the S 2p spectrum, and the Ni 2p spectrum matches the reference Ni 2p spectrum of $Ni(OH)_2$. This inconsistency between Raman and XPS spectra indicates that after conversion of NiS_2 at the surface of the electrode, the formed $Ni(OH)_2$ layer on the sample prevents the deeper parts from further conversion.

Considering the consecutive LSV trend for this sample, it can be stated that the conversion of the sample to $Ni(OH)_2$ after immersion inside the electrolyte and the progress of this conversion during LSV measurements is the reason for the weakening of HER activity. The conversion of NiS_2 to $Ni(OH)_2$ progresses more after each LSV scan, and at the third run of consecutive LSV scans, the sample contains only $Ni(OH)_2$. Consequently, the LSV scans started to become constant.

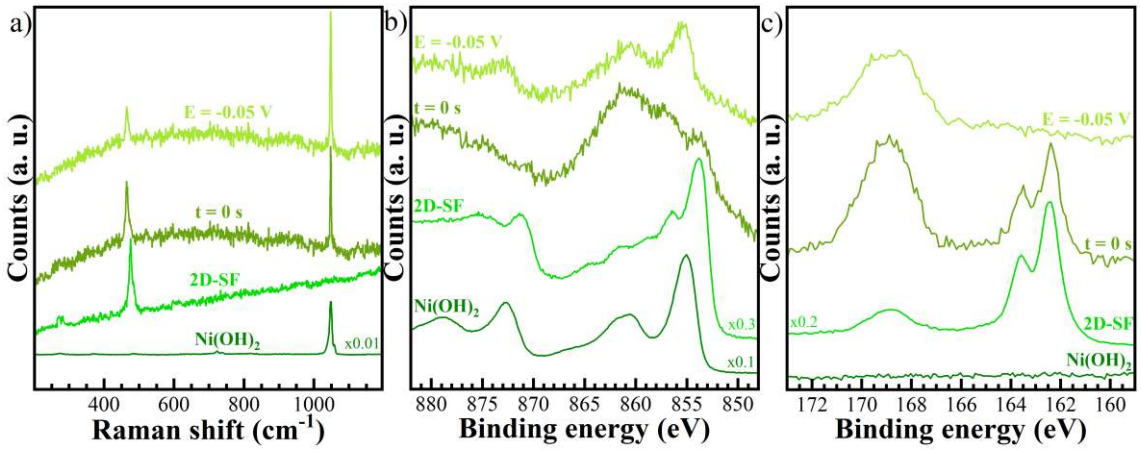

Figure 6-7 a) Raman spectra, b) Ni 2p, and c) S 2p XPS spectra of Fresh 2D-SF, after immersing inside electrolyte and after applying -0.05 V for 100 s. The bottom spectra in each part are obtained from α-$Ni(OH)_2$.

Due to the larger lateral dimensions of the 2D-S sample, the ex-situ Raman investigation was performed on the edges and center of this sample separately. Figure 6-8a, and Figure 6-8b show the Raman spectra obtained from the edge and center of the flakes, respectively. In the Raman spectra obtained from the edge of the flakes, the NiS_2 $T_g(3)$ and E_g vibrations related doublet at ~280 cm^{-1} disappears after performing CA at -0.25 V. simultaneously with this disappearance, the redshift of the peak at ~480 cm^{-1} to ~465 cm^{-1} can be detected. The same changes can be seen on the Raman spectra obtained from the center, but at higher cathodic potential (-0.35 V). The difference in the potential at which the alterations of Raman peaks happen, suggests that the hydroxylation starts from the edges and propagates towards the center of the flakes. The Ni 2p and S 2p spectra obtained from 2D-S after performing CA at -0.25 V confirm partial conversion of the samples to $Ni(OH)_2$. It is noteworthy that according to Figure 6-7c, and Figure 6-8d, a significant amount of sulfate groups are formed on both 2D-S and 2D-SF samples after conversion to the $Ni(OH)_2$. Hence, the final state of 2D-S and 2D-SF consist of a mixture of nickel hydroxide and nickel sulfate rather than pure hydroxide phase.

The gradual NiS_2 to $Ni(OH)_2$ conversion of the 2D-S samples can be the main reason for having an inconsistent trend in the LSV scans of this sample shown in Figure 6-5. There is a high possibility of having a mixture of NiS_2 and $Ni(OH)_2$ throughout the initial LSV scans. The similar trend in the third LSV run of this sample to the LSV runs of 2D-SF can indicate the completion of the NiS_2 to $NiSO_4/Ni(OH)_2$ conversion.

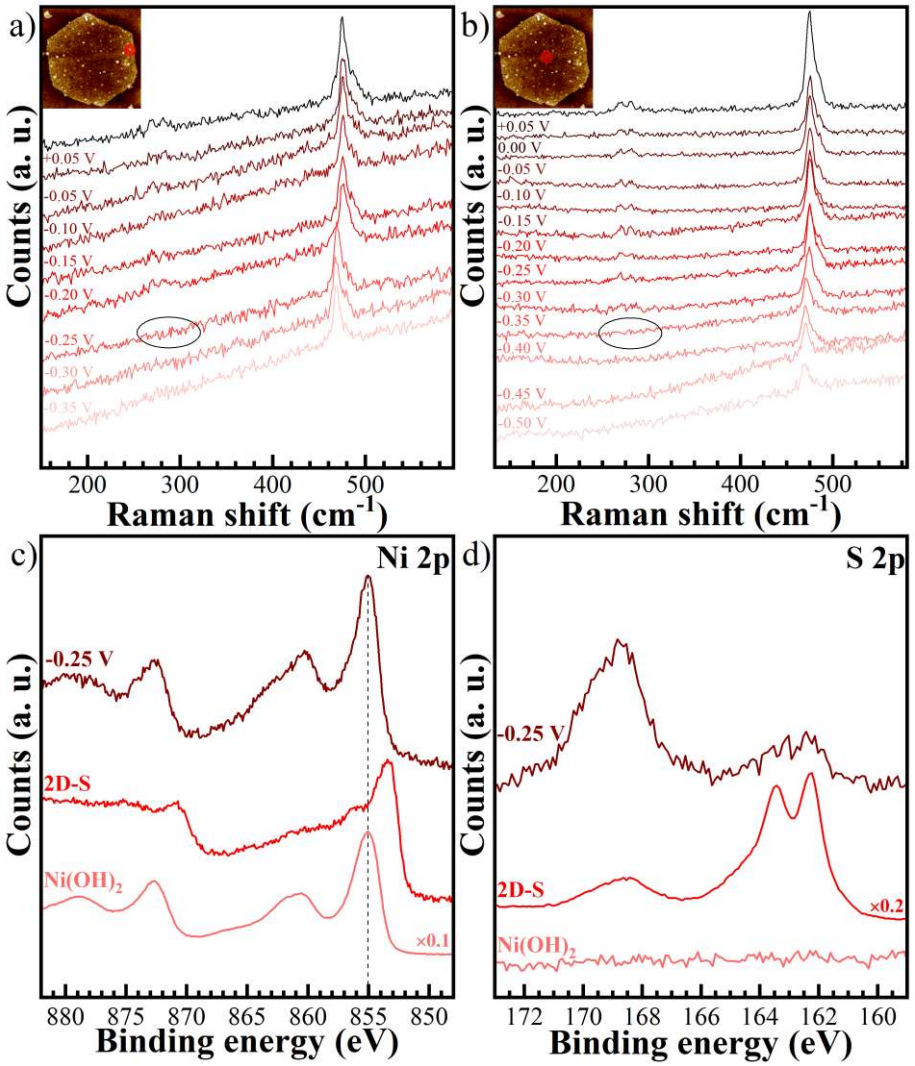

Figure 6-8 Raman spectra from the a) edges and b) center of the 2D-S flakes after applying CA at different potentials. c) Ni 2p, and d) S 2p XPS spectra of α-$Ni(OH)_2$, Fresh 2D-S, and after applying CA at -0.25 V.

Performing ex-situ Raman and XPS analysis on 3D revealed a different trend than 2D-S and 2D-SF. As it was shown in Figure 6-3, the 3D sample was composed of NiS_2, Ni_3S_4 and NiS. Due to the low signal-to-noise ratio of the sample used for the CA-Raman experiment, it is not possible to distinguish all characteristic peaks in Figure 6-9a. However, the E(2) mode of NiS at ~247 cm^{-1} (shown with a blue arrow) and the $T_g(3)$ (~274 cm^{-1}), $T_g(1)$ (~488 cm^{-1}), and A_g (~478 cm^{-1}) modes of NiS_2 (shown with black arrows) can be detected. The peak at ~284 cm^{-1} (shown with green arrow) can be attributed to either E_g vibration mode of NiS_2, $A_1(3)$ vibration mode of NiS, or $T_{2g}(2)$ vibration mode of Ni_3S_4 [449]. After performing CA at -0.25 V, the $Ni(OH)_2$ attributed peak at ~1045 cm^{-1} wavenumber appears, and the peak at ~480 cm^{-1} starts to show a redshift similar to the case of 2D-S. Also, characteristic Raman peaks of NiS become more pronounced and visible. These peaks are shown with blue arrows in Figure 6-9a.

The Raman spectrum obtained after performing CA at -0.45 V contains only $Ni(OH)_2$ and NiS related peaks. The XPS spectra related to this state of the 3D sample confirm the co-presence of nickel sulfide and $Ni(OH)_2$. The small shoulder at ~852.1 eV of the Ni 2p spectrum (Figure 6-9b) and the S^{2-} related peaks in the S 2p spectrum (Figure 6-9c) show that in contrast with the sulfur-rich NiS_2 phase, the NiS phase has better stability and does not convert to $Ni(OH)_2$. The higher stability of the Ni-rich sulfide phases has been previously predicted based on their lower DOS at the Fermi level [449].

These results reveal that the 3D sample is the only sample that contains nickel sulfide during electrochemical measurement. Hence, the different LSV trend observed for this sample is a result of the co-existence of sulfide and nickel hydroxide. Previously, it has been shown that the presence of surface OH groups in a Ni-based sample that contains S groups results in dynamic LSV behavior similar to the one detected for the 3D sample in Figure 6-5c [436].

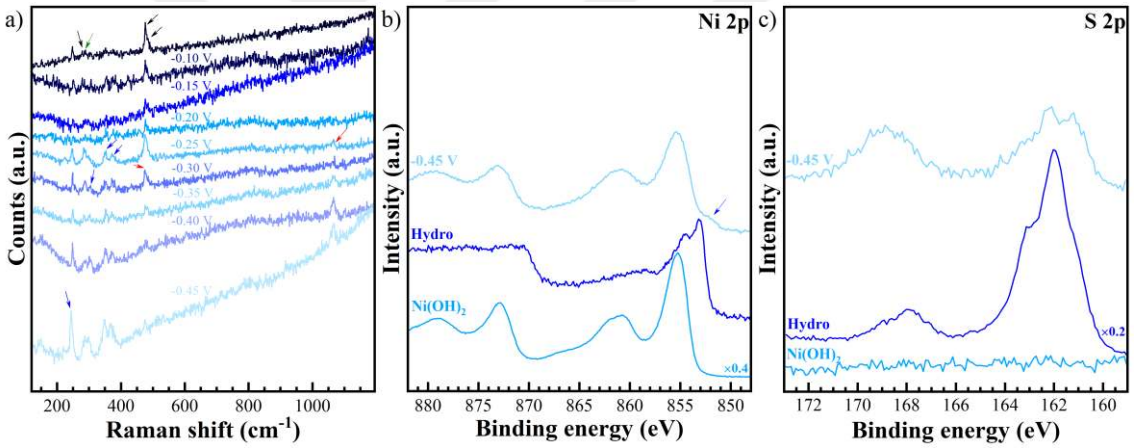

Figure 6-9 a) Raman spectra, b) Ni 2p, and c) S 2p XPS spectra of Fresh 3D and after applying CA at different potentials as well as Ni 2p and S 2p XPS spectra of α-$Ni(OH)_2$.

Due to the partial or complete conversion of 2D-S, 2D-SF, and 3D to $Ni(OH)_2$, observed in CA-Raman experiment, the surface roughness alteration after this conversion should also be considered in interpreting the C_{DL} measurement results reported in Figure 6-6g-i. Normalizing the LSV results reported in Figure 6-5a-c with respect to the C_{DL} values (shown in Figure 6-10a-c) reveals a different trend for the HER activity of the samples. Hence, it can be concluded that both ECSA and roughness have effect in the observed C_{DL} changes. Unfortunately, it is not possible to distinguish the effect of these two, using the characterization methods of this study. However, designing a preparation and characterization method which enables microscopic investigation of the flakes before and after the electrochemical reactions, can elucidate the actual electrochemical surface

changes upon nickel sulfide to nickel hydroxide conversion.

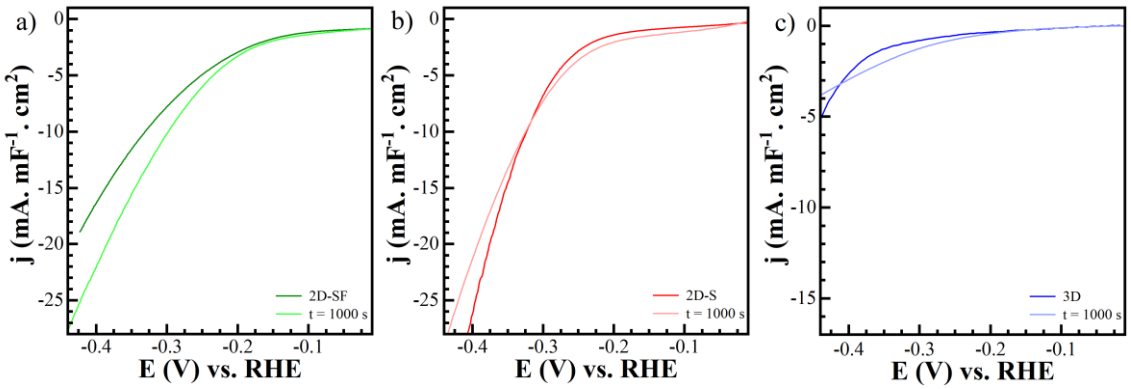

Figure 6-10 LSV scans obtained from a) 2D-SF, b) 2D-S, and c) 3D samples in their fresh forms and after keeping under -0.50 V for 1000 s normalized with respect to the corresponding C_{DL} values.

6.4 Conclusion

In conclusion, it has been shown that CVD synthesis yields pure NiS_2 with a 2D structure. The lateral dimensions of this 2D structure can be controlled by modifying the preparation method of $Ni(OH)_2$. While the unique form of 2D films provides a high number of available sites for better electrochemical performance, the ex-situ CA-Raman and CA-XPS experiments revealed that the NiS_2 phase is not stable and converts to $Ni(OH)_2$. This conversion is the main reason for the diminution of the HER activity of 2D NiS_2 electrodes. In contrast, performing additives and surfactant-free hydrothermal synthesis methods results in multi-phase nickel sulfide. After applying cathodic potential on a hydrothermally synthesized sample, the metal-rich phases show better stability than the NiS_2. The presence of hydroxylated Ni simultaneously with Nickel sulfides promotes the HER activity of the electrode by increasing its ECSA and decreasing the charge transfer resistance.

Chapter 7:
Conclusion and Future Perspectives

The electrochemical activity of 2D materials including graphene, MoS_2 and nickel sulfides was investigated in this thesis. Possible modifications for enhancement of the activity of these materials were suggested. Additionally, some fundamental aspects such as electrochemical reaction mechanisms, the active sites and alterations of the structure and composition of the electrodes under operando conditions were investigated using cross-examined physical/electrochemical characterizations.

The role of N dopant configuration on the electrochemical activity of bilayer N-doped graphene towards the ORR was investigated by modifying content and configuration of N in CVD grown graphene structure via adjusting N_2 plasma exposure time and power. It was shown that N_{pydn}-rich bilayer graphene exhibits electrochemical activities toward ORR superior to N_{grap}-rich graphene with lower onset potential, higher electrochemical current density, and lower Tafel slope. XPS, N and C K-edge XES, and Raman spectroscopy investigations reveal that N_{pydn} and $N_{pydn'}$ enhance the metallicity of N-doped graphene by inducing stronger interlayer interactions via an increased π-π orbital overlap. These modifications results improve the ORR activity by promoting electron transfer kinetics between layers. Moreover, the formation of N_{pydn} and $N_{pydn'}$ leads to a significant increase in the active sites.

The mechanism for ORR activity of single layer N-doped graphene was investigated by performing SEC-Raman measurements. It has been shown that the presence of H/OH groups, which adsorb on the surface of N-doped graphene prior to ORR process has a significant effect on the ORR mechanism and the reaction sites. Different evolution of Raman spectra of N_{pydn} and N_{grap}-doped graphene revealed that there are different ORR sites for these two structures based on the distance of the reaction site with respect to the N dopants. Finally, considering SEC-Raman investigation results, a new 4e- pathway which produces 4 OH^- was proposed as possible mechanism on the N-doped graphene.

2D MoS_2 flakes with controlled phase composition, size and defect density were synthesized by modifying the distance of Mo precursor from the substrates. The HER activity of the samples synthesized at different distances were compared and it has been

shown that the sample with highest metallic 1T phase (the closest to the precursor) and the samples with small flake size and high number of vacancies (the furthest from the precursor) have the best activity. After investigating the HER mechanism and the rate determining step, the activity of the samples was further improved by applying N_2 plasma. It has been shown that the induced compressive strain in the MoS_2 structure by substituting S atoms with N results in further conversion of 1H phase to 1T phase in the sample with initial 1T component. The SEC-Raman and ex-situ XPS measurements revealed that adsorption of H on 1T-MoS_2 causes 1T to 1H phase transformation during HER which results in significant activity loss for this sample after recording consecutive LSV scans.

nickel sulfide samples with 2D and 3D structures and different compositions were synthesized using CVD and hydrothermal methods. The 2D films obtained from CVD were composed of a single phase (NiS_2). The performed physical and electrochemical experiments showed that these structures had a significant initial HER activity owing to the high number of available active sites. However, this remarkable activity diminishes after exposing the samples to the electrolyte and high cathodic potential for long time. It has been proposed that the fully conversion of NiS_2 phase to $Ni(OH)_2$ is the main reason for this negative change in the activity.

In contrast, the 3D structures, which were composed of NiS, Ni_3S_4 and NiS_2 and initially were almost inactive, show better activity after applying cathodic potential. While the NiS_2 compartment of these samples had a similar conversion as the 2D samples, the metal-rich phases showed better stability and was preserved throughout the electrochemical experiment. The presence of hydroxylated Ni simultaneously with nickel sulfides promotes the HER activity of these electrodes by increasing their ECSA and decreasing the charge transfer resistance.

Considering the contradictory results between theoretical and experimental investigations regarding role of N configurations in N-doped graphene, performing SEC-Raman investigation on bilayer N-doped graphene could provide new insights about this issue. Also performing in-situ XPS, XES or XAS measurements could provide more detailed information regarding the active site and ORR mechanisms on single layer and bilayer N-doped graphene. Tracking the structural differences between MoS_2 samples synthesized at different distances and their alterations after electrochemical measurement can be helpful in better understanding the results reported in this thesis.

Bibliography

[1] V. Nicolosi, M. Chhowalla, M. G. Kanatzidis, M. S. Strano, and J. N. Coleman, "Liquid Exfoliation of Layered Materials," *Science*, vol. 340, no. 6139, p. 1226419, Jun. 2013, doi: 10.1126/science.1226419.

[2] K. S. Novoselov *et al.*, "Electric Field Effect in Atomically Thin Carbon Films," *Science*, vol. 306, no. 5696, pp. 666–669, Oct. 2004, doi: 10.1126/science.1102896.

[3] J. R. Dahn, T. Zheng, Y. Liu, and J. S. Xue, "Mechanisms for Lithium Insertion in Carbonaceous Materials," *Science*, vol. 270, no. 5236, pp. 590–593, Oct. 1995, doi: 10.1126/science.270.5236.590.

[4] S. Domínguez-Meister, T. C. Rojas, M. Brizuela, and J. C. Sánchez-López, "Solid lubricant behavior of MoS2 and WSe2-based nanocomposite coatings," *Sci. Technol. Adv. Mater.*, vol. 18, no. 1, pp. 122–133, Dec. 2017, doi: 10.1080/14686996.2016.1275784.

[5] Y. Zhu, L. Peng, Z. Fang, C. Yan, X. Zhang, and G. Yu, "Structural Engineering of 2D Nanomaterials for Energy Storage and Catalysis," *Adv. Mater.*, vol. 30, no. 15, p. 1706347, doi: 10.1002/adma.201706347.

[6] K. Zhang, Y. Feng, F. Wang, Z. Yang, and J. Wang, "Two dimensional hexagonal boron nitride (2D-hBN): synthesis, properties and applications," *J. Mater. Chem. C*, vol. 5, no. 46, pp. 11992–12022, 2017, doi: 10.1039/C7TC04300G.

[7] C. Tan, Z. Lai, and H. Zhang, "Ultrathin Two-Dimensional Multinary Layered Metal Chalcogenide Nanomaterials," *Adv. Mater.*, vol. 29, no. 37, p. 1701392, 2017, doi: 10.1002/adma.201701392.

[8] M. Zeng, Y. Xiao, J. Liu, K. Yang, and L. Fu, "Exploring Two-Dimensional Materials toward the Next-Generation Circuits: From Monomer Design to Assembly Control," *Chem. Rev.*, vol. 118, no. 13, pp. 6236–6296, Jul. 2018, doi: 10.1021/acs.chemrev.7b00633.

[9] P. Avouris, T. F. Heinz, and T. Low, Eds., *2D Materials: Properties and Devices*. Cambridge: Cambridge University Press, 2017. doi: 10.1017/9781316681619.

[10] H. Li, Y. Li, A. Aljarb, Y. Shi, and L.-J. Li, "Epitaxial Growth of Two-Dimensional Layered Transition-Metal Dichalcogenides: Growth Mechanism, Controllability, and Scalability," *Chem. Rev.*, vol. 118, no. 13, pp. 6134–6150, Jul. 2018, doi: 10.1021/acs.chemrev.7b00212.

[11] A. J. Mannix *et al.*, "Synthesis of borophenes: Anisotropic, two-dimensional boron polymorphs," *Science*, vol. 350, no. 6267, pp. 1513–1516, Dec. 2015, doi: 10.1126/science.aad1080.

[12] Q. Fan *et al.*, "High-yield production of few-layer boron nanosheets for efficient electrocatalytic N 2 reduction," *Chem. Commun.*, vol. 55, no. 29, pp. 4246–4249, 2019, doi: 10.1039/C9CC00985J.

[13] T. Hartman and Z. Sofer, "Beyond Graphene: Chemistry of Group 14 Graphene Analogues: Silicene, Germanene, and Stanene," *ACS Nano*, vol. 13, no. 8, pp. 8566–8576, Aug. 2019, doi: 10.1021/acsnano.9b04466.

[14] Y. Zhang *et al.*, "Exfoliation of Stable 2D Black Phosphorus for Device Fabrication," *Chem. Mater.*, vol. 29, no. 15, pp. 6445–6456, Aug. 2017, doi: 10.1021/acs.chemmater.7b01991.

[15] J. Sturala, A. Ambrosi, Z. Sofer, and M. Pumera, "Covalent Functionalization of Exfoliated Arsenic with Chlorocarbene," *Angew. Chem.*, vol. 130, no. 45, pp. 15053–15056, 2018, doi: 10.1002/ange.201809341.

[16] X. Wang *et al.*, "Bandgap-Tunable Preparation of Smooth and Large Two-Dimensional Antimonene," *Angew. Chem.*, vol. 130, no. 28, pp. 8804–8809, 2018, doi: 10.1002/ange.201804886.

[17] F. Reis *et al.*, "Bismuthene on a SiC substrate: A candidate for a high-temperature quantum spin Hall material," *Science*, vol. 357, no. 6348, pp. 287–290, Jul. 2017, doi: 10.1126/science.aai8142.

[18] K. P. Loh, Q. Bao, G. Eda, and M. Chhowalla, "Graphene oxide as a chemically tunable platform for optical applications," *Nat. Chem.*, vol. 2, no. 12, pp. 1015–1024, Dec. 2010, doi: 10.1038/nchem.907.

[19] N. Solati, S. Mobassem, A. Kahraman, H. Ogasawara, and S. Kaya, "A comprehensive study on the characteristic spectroscopic features of nitrogen doped graphene," *Appl. Surf. Sci.*, vol. 495, p. 143518, Nov. 2019, doi: 10.1016/j.apsusc.2019.07.260.

[20] C. Huang *et al.*, "Progress in Research into 2D Graphdiyne-Based Materials," *Chem. Rev.*, vol. 118, no. 16, pp. 7744–7803, Aug. 2018, doi: 10.1021/acs.chemrev.8b00288.

[21] D. C. Elias *et al.*, "Control of Graphene's Properties by Reversible Hydrogenation: Evidence for Graphane," *Science*, vol. 323, no. 5914, pp. 610–613, Jan. 2009, doi: 10.1126/science.1167130.

[22] J. R. Brent, N. Savjani, and P. O'Brien, "Synthetic approaches to two-dimensional transition metal dichalcogenide nanosheets," *Prog. Mater. Sci.*, vol. 89, no. Supplement C, pp. 411–478, Aug. 2017, doi: 10.1016/j.pmatsci.2017.06.002.

[23] Y. Sugita, T. Miyake, and Y. Motome, "Multiple Dirac cones and topological magnetism in honeycomb-monolayer transition metal trichalcogenides," *Phys. Rev. B*, vol. 97, no. 3, 2018, doi: 10.1103/PhysRevB.97.035125.

[24] J. Dai, M. Li, and X. C. Zeng, "Group IVB transition metal trichalcogenides: a new class of 2D layered materials beyond graphene," *WIREs Comput. Mol. Sci.*, vol. 6, no. 2, pp.

211–222, 2016, doi: 10.1002/wcms.1243.

[25] H. Wang and X. Qian, “Two-dimensional multiferroics in monolayer group IV monochalcogenides,” *2D Mater.*, vol. 4, no. 1, p. 015042, Jan. 2017, doi: 10.1088/2053-1583/4/1/015042.

[26] J. Liu, H. Wang, and M. Antonietti, “Graphitic carbon nitride ‘reloaded’: Emerging applications beyond (photo)catalysis,” *Chem. Soc. Rev.*, vol. 45, no. 8, pp. 2308–2326, 2016, doi: 10.1039/c5cs00767d.

[27] Q. Fan *et al.*, “Liquid Exfoliation of Two-Dimensional PbI2 Nanosheets for Ultrafast Photonics,” *ACS Photonics*, vol. 6, no. 4, pp. 1051–1057, Apr. 2019, doi: 10.1021/acsphotonics.9b00122.

[28] M. P. Browne, Z. Sofer, and M. Pumera, “Layered and two dimensional metal oxides for electrochemical energy conversion,” *Energy Environ. Sci.*, vol. 12, no. 1, pp. 41–58, Jan. 2019, doi: 10.1039/C8EE02495B.

[29] M. H. Seo, H. W. Park, D. U. Lee, M. G. Park, and Z. Chen, “Design of Highly Active Perovskite Oxides for Oxygen Evolution Reaction by Combining Experimental and ab Initio Studies,” *ACS Catal.*, vol. 5, no. 7, pp. 4337–4344, Jul. 2015, doi: 10.1021/acscatal.5b00114.

[30] M. Taibi, S. Ammar, N. Jouini, F. Fiévet, P. Molinié, and M. Drillon, “Layered nickel hydroxide salts: synthesis, characterization and magnetic behaviour in relation to the basal spacing,” *J. Mater. Chem.*, vol. 12, no. 11, pp. 3238–3244, Oct. 2002, doi: 10.1039/B204087E.

[31] L. Lv, Z. Yang, K. Chen, C. Wang, and Y. Xiong, “2D Layered Double Hydroxides for Oxygen Evolution Reaction: From Fundamental Design to Application,” *Adv. Energy Mater.*, vol. 9, no. 17, p. 1803358, 2019, doi: 10.1002/aenm.201803358.

[32] M. Naguib, V. N. Mochalin, M. W. Barsoum, and Y. Gogotsi, “25th Anniversary Article: MXenes: A New Family of Two-Dimensional Materials,” *Adv. Mater.*, vol. 26, no. 7, pp. 992–1005, 2014, doi: 10.1002/adma.201304138.

[33] C. S. Diercks and O. M. Yaghi, “The atom, the molecule, and the covalent organic framework,” *Science*, vol. 355, no. 6328, p. eaal1585, Mar. 2017, doi: 10.1126/science.aal1585.

[34] A. J. Clough *et al.*, “Metallic Conductivity in a Two-Dimensional Cobalt Dithiolene Metal–Organic Framework,” *J. Am. Chem. Soc.*, vol. 139, no. 31, pp. 10863–10867, Aug. 2017, doi: 10.1021/jacs.7b05742.

[35] C. Guerrero-Bermea *et al.*, “Two-dimensional and three-dimensional hybrid assemblies based on graphene oxide and other layered structures: A carbon science perspective,” *Carbon*, vol. 125, pp. 437–453, Dec. 2017, doi: 10.1016/j.carbon.2017.09.082.

[36] A. K. Geim and I. V. Grigorieva, “Van der Waals heterostructures,” *Nature*, vol. 499, no.

7459, pp. 419–425, Jul. 2013, doi: 10.1038/nature12385.

[37] Q. Yu *et al.*, "Iron sulfide/carbon hybrid cluster as an anode for potassium-ion storage," *J. Alloys Compd.*, vol. 766, pp. 1086–1091, Oct. 2018, doi: 10.1016/j.jallcom.2018.07.065.

[38] Y. Li *et al.*, "Multifunctional Nanoplatform Based on Black Phosphorus Quantum Dots for Bioimaging and Photodynamic/Photothermal Synergistic Cancer Therapy," *ACS Appl. Mater. Interfaces*, vol. 9, no. 30, pp. 25098–25106, Aug. 2017, doi: 10.1021/acsami.7b05824.

[39] Y. Cao *et al.*, "Engineered Exosome-Mediated Near-Infrared-II Region V2C Quantum Dot Delivery for Nucleus-Target Low-Temperature Photothermal Therapy," *ACS Nano*, vol. 13, no. 2, pp. 1499–1510, Feb. 2019, doi: 10.1021/acsnano.8b07224.

[40] N. Zhu *et al.*, "Surface Modification of Magnetic Iron Oxide Nanoparticles," *Nanomaterials*, vol. 8, no. 10, Art. no. 10, Oct. 2018, doi: 10.3390/nano8100810.

[41] A. Aziz *et al.*, "Self-stacking of exfoliated charged nanosheets of LDHs and graphene as biosensor with real-time tracking of dopamine from live cells," *Anal. Chim. Acta*, vol. 1047, pp. 197–207, Jan. 2019, doi: 10.1016/j.aca.2018.10.008.

[42] T. Uemura, R. Nakanishi, T. Kaseda, N. Uchida, and S. Kitagawa, "Controlled Cyclopolymerization of Difunctional Vinyl Monomers in Coordination Nanochannels," *Macromolecules*, vol. 47, no. 21, pp. 7321–7326, Nov. 2014, doi: 10.1021/ma501232n.

[43] Y. Kong, Y. Huang, C. Meng, and Z. Zhang, "Sodium dodecylsulfate-layered double hydroxide and its use in the adsorption of 17β-estradiol in wastewater," *RSC Adv.*, vol. 8, no. 55, pp. 31440–31454, 2018, doi: 10.1039/C8RA05726E.

[44] B. Manna, S. Singh, A. Karmakar, A. V. Desai, and S. K. Ghosh, "Selective Anion Exchange and Tunable Luminescent Behaviors of Metal–Organic Framework Based Supramolecular Isomers," *Inorg. Chem.*, vol. 54, no. 1, pp. 110–116, Jan. 2015, doi: 10.1021/ic501879w.

[45] E. Lee, A. VahidMohammadi, Y. S. Yoon, M. Beidaghi, and D.-J. Kim, "Two-Dimensional Vanadium Carbide MXene for Gas Sensors with Ultrahigh Sensitivity Toward Nonpolar Gases," *ACS Sens.*, vol. 4, no. 6, pp. 1603–1611, Jun. 2019, doi: 10.1021/acssensors.9b00303.

[46] S.-H. Huang, S.-J. Liu, and J.-Y. Uan, "Controllable luminescence of a Li–Al layered double hydroxide used as a sensor for reversible sensing of carbonate," *J. Mater. Chem. C*, vol. 7, no. 36, pp. 11191–11206, 2019, doi: 10.1039/C9TC00870E.

[47] G. Ma, K. Huang, J.-S. Ma, Z. Ju, Z. Xing, and Q. Zhuang, "Phosphorus and oxygen dual-doped graphene as superior anode material for room-temperature potassium-ion batteries," *J. Mater. Chem. A*, vol. 5, no. 17, pp. 7854–7861, 2017, doi: 10.1039/C7TA01108C.

[48] J. C. Pramudita, D. Sehrawat, D. Goonetilleke, and N. Sharma, "An Initial Review of the Status of Electrode Materials for Potassium-Ion Batteries," *Adv. Energy Mater.*, vol. 7, no.

24, p. 1602911, 2017, doi: 10.1002/aenm.201602911.

[49] B. Jia *et al.*, "Bamboo-Like Hollow Tubes with MoS2/N-Doped-C Interfaces Boost Potassium-Ion Storage," *Adv. Funct. Mater.*, vol. 28, no. 40, p. 1803409, 2018, doi: 10.1002/adfm.201803409.

[50] X. Ren *et al.*, "Few-Layer Black Phosphorus Nanosheets as Electrocatalysts for Highly Efficient Oxygen Evolution Reaction," *Adv. Energy Mater.*, vol. 7, no. 19, p. 1700396, 2017, doi: 10.1002/aenm.201700396.

[51] C. Chowdhury, S. Karmakar, and A. Datta, "Capping Black Phosphorene by h-BN Enhances Performances in Anodes for Li and Na Ion Batteries," *ACS Energy Lett.*, vol. 1, no. 1, pp. 253–259, Jul. 2016, doi: 10.1021/acsenergylett.6b00164.

[52] Q. Wan, S. Li, and J.-B. Liu, "First-Principle Study of Li-Ion Storage of Functionalized Ti2C Monolayer with Vacancies," *ACS Appl. Mater. Interfaces*, vol. 10, no. 7, pp. 6369–6377, Feb. 2018, doi: 10.1021/acsami.7b18369.

[53] M. M.-J. Li *et al.*, "CO2 Hydrogenation to Methanol over Catalysts Derived from Single Cationic Layer CuZnGa LDH Precursors," *ACS Catal.*, vol. 8, no. 5, pp. 4390–4401, May 2018, doi: 10.1021/acscatal.8b00474.

[54] P. J. Jeon, Y. T. Lee, J. Y. Lim, J. S. Kim, D. K. Hwang, and S. Im, "Black Phosphorus–Zinc Oxide Nanomaterial Heterojunction for p–n Diode and Junction Field-Effect Transistor," *Nano Lett.*, vol. 16, no. 2, pp. 1293–1298, Feb. 2016, doi: 10.1021/acs.nanolett.5b04664.

[55] X. Ren *et al.*, "Environmentally Robust Black Phosphorus Nanosheets in Solution: Application for Self-Powered Photodetector," *Adv. Funct. Mater.*, vol. 27, no. 18, p. 1606834, 2017, doi: 10.1002/adfm.201606834.

[56] X. Zhang, L. Hou, A. Ciesielski, and P. Samorì, "2D Materials Beyond Graphene for High-Performance Energy Storage Applications," *Adv. Energy Mater.*, vol. 6, no. 23, p. 1600671, 2016, doi: 10.1002/aenm.201600671.

[57] C. J. Heard, J. Čejka, M. Opanasenko, P. Nachtigall, G. Centi, and S. Perathoner, "2D Oxide Nanomaterials to Address the Energy Transition and Catalysis," *Adv. Mater.*, vol. 31, no. 3, p. 1801712, 2019, doi: 10.1002/adma.201801712.

[58] H. Tang *et al.*, "In Situ Formed Protective Barrier Enabled by Sulfur@Titanium Carbide (MXene) Ink for Achieving High-Capacity, Long Lifetime Li-S Batteries," *Adv. Sci.*, vol. 5, no. 9, p. 1800502, 2018, doi: 10.1002/advs.201800502.

[59] H. Tang *et al.*, "A Robust, Freestanding MXene-Sulfur Conductive Paper for Long-Lifetime Li–S Batteries," *Adv. Funct. Mater.*, vol. 29, no. 30, p. 1901907, 2019, doi: 10.1002/adfm.201901907.

[60] Y. Wei *et al.*, "Layered carbide-derived carbon with hierarchically porous structure for high rate lithium-sulfur batteries," *Electrochimica Acta*, vol. 188, pp. 385–392, Jan. 2016,

doi: 10.1016/j.electacta.2015.12.012.

[61] D. Voiry *et al.*, "Enhanced catalytic activity in strained chemically exfoliated WS2 nanosheets for hydrogen evolution," *Nat. Mater.*, vol. 12, no. 9, pp. 850–855, Sep. 2013, doi: 10.1038/nmat3700.

[62] G. Ye *et al.*, "Defects Engineered Monolayer MoS2 for Improved Hydrogen Evolution Reaction," *Nano Lett.*, vol. 16, no. 2, pp. 1097–1103, Feb. 2016, doi: 10.1021/acs.nanolett.5b04331.

[63] H. Li *et al.*, "Kinetic Study of Hydrogen Evolution Reaction over Strained MoS2 with Sulfur Vacancies Using Scanning Electrochemical Microscopy," *J. Am. Chem. Soc.*, vol. 138, no. 15, pp. 5123–5129, Apr. 2016, doi: 10.1021/jacs.6b01377.

[64] Y. Qu, H. Pan, C. T. Kwok, and Z. Wang, "Effect of Doping on Hydrogen Evolution Reaction of Vanadium Disulfide Monolayer," *Nanoscale Res. Lett.*, vol. 10, no. 1, p. 480, Dec. 2015, doi: 10.1186/s11671-015-1182-y.

[65] Y. Sun, S. Gao, F. Lei, and Y. Xie, "Atomically-thin two-dimensional sheets for understanding active sites in catalysis," *Chem. Soc. Rev.*, vol. 44, no. 3, pp. 623–636, 2015, doi: 10.1039/C4CS00236A.

[66] C. Tan *et al.*, "Recent Advances in Ultrathin Two-Dimensional Nanomaterials," *Chem. Rev.*, vol. 117, no. 9, pp. 6225–6331, May 2017, doi: 10.1021/acs.chemrev.6b00558.

[67] Y. Zhu, L. Peng, D. Chen, and G. Yu, "Intercalation Pseudocapacitance in Ultrathin VOPO4 Nanosheets: Toward High-Rate Alkali-Ion-Based Electrochemical Energy Storage," *Nano Lett.*, vol. 16, no. 1, pp. 742–747, Jan. 2016, doi: 10.1021/acs.nanolett.5b04610.

[68] B. Ni and X. Wang, "Face the Edges: Catalytic Active Sites of Nanomaterials," *Adv. Sci.*, vol. 2, no. 7, p. 1500085, 2015, doi: 10.1002/advs.201500085.

[69] S. M. Oh, S. B. Patil, X. Jin, and S.-J. Hwang, "Recent Applications of 2D Inorganic Nanosheets for Emerging Energy Storage System," *Chem. – Eur. J.*, vol. 24, no. 19, pp. 4757–4773, doi: 10.1002/chem.201704284.

[70] K. Du *et al.*, "Weak Van der Waals Stacking, Wide-Range Band Gap, and Raman Study on Ultrathin Layers of Metal Phosphorus Trichalcogenides," *ACS Nano*, vol. 10, no. 2, pp. 1738–1743, Feb. 2016, doi: 10.1021/acsnano.5b05927.

[71] P. Ares *et al.*, "Mechanical Isolation of Highly Stable Antimonene under Ambient Conditions," *Adv. Mater.*, vol. 28, no. 30, pp. 6332–6336, 2016, doi: 10.1002/adma.201602128.

[72] C. R. Dean *et al.*, "Boron nitride substrates for high-quality graphene electronics," *Nat. Nanotechnol.*, vol. 5, no. 10, pp. 722–726, Oct. 2010, doi: 10.1038/nnano.2010.172.

[73] J. N. Coleman *et al.*, "Two-Dimensional Nanosheets Produced by Liquid Exfoliation of Layered Materials," *Science*, vol. 331, no. 6017, pp. 568–571, Feb. 2011, doi:

10.1126/science.1194975.

[74] J. L. Gunjakar, I. Y. Kim, J. M. Lee, Y. K. Jo, and S.-J. Hwang, "Exploration of Nanostructured Functional Materials Based on Hybridization of Inorganic 2D Nanosheets," *J. Phys. Chem. C*, vol. 118, no. 8, pp. 3847–3863, Feb. 2014, doi: 10.1021/jp410626y.

[75] R. Ma, K. Takada, K. Fukuda, N. Iyi, Y. Bando, and T. Sasaki, "Topochemical Synthesis of Monometallic (Co2+–Co3+) Layered Double Hydroxide and Its Exfoliation into Positively Charged Co(OH)2 Nanosheets," *Angew. Chem.*, vol. 120, no. 1, pp. 92–95, 2008, doi: 10.1002/ange.200703941.

[76] L. Niu, J. N. Coleman, H. Zhang, H. Shin, M. Chhowalla, and Z. Zheng, "Production of Two-Dimensional Nanomaterials via Liquid-Based Direct Exfoliation," *Small*, vol. 12, no. 3, pp. 272–293, 2016, doi: 10.1002/smll.201502207.

[77] C. Tan and H. Zhang, "Wet-chemical synthesis and applications of non-layer structured two-dimensional nanomaterials," *Nat. Commun.*, vol. 6, no. 1, p. 7873, Aug. 2015, doi: 10.1038/ncomms8873.

[78] H. Duan *et al.*, "Ultrathin rhodium nanosheets," *Nat. Commun.*, vol. 5, no. 1, Art. no. 1, Jan. 2014, doi: 10.1038/ncomms4093.

[79] Y. Sun *et al.*, "Fabrication of flexible and freestanding zinc chalcogenide single layers," *Nat. Commun.*, vol. 3, no. 1, p. 1057, Sep. 2012, doi: 10.1038/ncomms2066.

[80] S. Gao *et al.*, "Partially oxidized atomic cobalt layers for carbon dioxide electroreduction to liquid fuel," *Nature*, vol. 529, no. 7584, pp. 68–71, Jan. 2016, doi: 10.1038/nature16455.

[81] J. Yu, J. Li, W. Zhang, and H. Chang, "Synthesis of high quality two-dimensional materials via chemical vapor deposition," *Chem. Sci.*, vol. 6, no. 12, pp. 6705–6716, Nov. 2015, doi: 10.1039/C5SC01941A.

[82] W. Zhang *et al.*, "CVD synthesis of Mo(1−x)WxS2 and MoS2(1−x)Se2x alloy monolayers aimed at tuning the bandgap of molybdenum disulfide," *Nanoscale*, vol. 7, no. 32, pp. 13554–13560, Aug. 2015, doi: 10.1039/C5NR02515J.

[83] K. K. Kim *et al.*, "Synthesis of Monolayer Hexagonal Boron Nitride on Cu Foil Using Chemical Vapor Deposition," *Nano Lett.*, vol. 12, no. 1, pp. 161–166, Jan. 2012, doi: 10.1021/nl203249a.

[84] S. Wang, X. Wang, and J. H. Warner, "All Chemical Vapor Deposition Growth of MoS2:h-BN Vertical van der Waals Heterostructures," *ACS Nano*, vol. 9, no. 5, pp. 5246–5254, May 2015, doi: 10.1021/acsnano.5b00655.

[85] S. Tongay *et al.*, "Tuning Interlayer Coupling in Large-Area Heterostructures with CVD-Grown MoS2 and WS2 Monolayers," *Nano Lett.*, vol. 14, no. 6, pp. 3185–3190, Jun. 2014, doi: 10.1021/nl500515q.

[86] P. K. Shen, C.-Y. Wang, S. P. Jiang, X. Sun, and J. Zhang, Eds., *Electrochemical Energy:*

Advanced Materials and Technologies. Boca Raton: CRC Press, 2017. doi: 10.1201/9781351228756.

[87] M. Wang, Z. Wang, X. Gong, and Z. Guo, "The intensification technologies to water electrolysis for hydrogen production – A review," *Renew. Sustain. Energy Rev.*, vol. 29, pp. 573–588, Jan. 2014, doi: 10.1016/j.rser.2013.08.090.

[88] L. Dai, Y. Xue, L. Qu, H.-J. Choi, and J.-B. Baek, "Metal-Free Catalysts for Oxygen Reduction Reaction," *Chem. Rev.*, vol. 115, no. 11, pp. 4823–4892, Jun. 2015, doi: 10.1021/cr5003563.

[89] V. S. Bagotsky, *Fuel Cells: Problems and Solutions*. John Wiley & Sons, 2012.

[90] S. T. Revankar and P. Majumdar, *Fuel Cells: Principles, Design, and Analysis*. CRC Press, 2014.

[91] Y. Li and H. Dai, "Recent advances in zinc–air batteries," *Chem. Soc. Rev.*, vol. 43, no. 15, pp. 5257–5275, 2014, doi: 10.1039/C4CS00015C.

[92] M. K. Debe, "Electrocatalyst approaches and challenges for automotive fuel cells," *Nature*, vol. 486, no. 7401, pp. 43–51, Jun. 2012, doi: 10.1038/nature11115.

[93] H. Tao *et al.*, "Two-dimensional materials for energy conversion and storage," *Prog. Mater. Sci.*, vol. 111, p. 100637, Jun. 2020, doi: 10.1016/j.pmatsci.2020.100637.

[94] J. K. Nørskov *et al.*, "Origin of the Overpotential for Oxygen Reduction at a Fuel-Cell Cathode," *J. Phys. Chem. B*, vol. 108, no. 46, pp. 17886–17892, Nov. 2004, doi: 10.1021/jp047349j.

[95] D.-W. Wang and D. Su, "Heterogeneous nanocarbon materials for oxygen reduction reaction," *Energy Environ. Sci.*, vol. 7, no. 2, pp. 576–591, Jan. 2014, doi: 10.1039/C3EE43463J.

[96] H. Cheng *et al.*, "Catalytic System Based on Sub-2 nm Pt Particles and Its Extraordinary Activity and Durability for Oxygen Reduction," *Nano Lett.*, vol. 19, no. 8, pp. 4997–5002, Aug. 2019, doi: 10.1021/acs.nanolett.9b01221.

[97] R. Ma *et al.*, "A review of oxygen reduction mechanisms for metal-free carbon-based electrocatalysts," *Npj Comput. Mater.*, vol. 5, no. 1, Art. no. 1, Jul. 2019, doi: 10.1038/s41524-019-0210-3.

[98] F. Cheng and J. Chen, "Metal–air batteries: from oxygen reduction electrochemistry to cathode catalysts," *Chem. Soc. Rev.*, vol. 41, no. 6, pp. 2172–2192, Feb. 2012, doi: 10.1039/C1CS15228A.

[99] Z.-L. Wang, D. Xu, J.-J. Xu, and X.-B. Zhang, "Oxygen electrocatalysts in metal–air batteries: from aqueous to nonaqueous electrolytes," *Chem. Soc. Rev.*, vol. 43, no. 22, pp. 7746–7786, Oct. 2014, doi: 10.1039/C3CS60248F.

[100] A. S. Ryabova *et al.*, "Further insights into the role of carbon in manganese oxide/carbon composites in the oxygen reduction reaction in alkaline media," *Electrochimica Acta*, vol.

246, pp. 643–653, Aug. 2017, doi: 10.1016/j.electacta.2017.06.017.

[101] Y. Tong *et al.*, "A Bifunctional Hybrid Electrocatalyst for Oxygen Reduction and Evolution: Cobalt Oxide Nanoparticles Strongly Coupled to B,N-Decorated Graphene," *Angew. Chem. Int. Ed.*, vol. 56, no. 25, pp. 7121–7125, 2017, doi: 10.1002/anie.201702430.

[102] Y. Li, Q. Li, H. Wang, L. Zhang, D. P. Wilkinson, and J. Zhang, "Recent Progresses in Oxygen Reduction Reaction Electrocatalysts for Electrochemical Energy Applications," *Electrochem. Energy Rev.*, vol. 2, no. 4, pp. 518–538, Dec. 2019, doi: 10.1007/s41918-019-00052-4.

[103] R. Yue *et al.*, "TiN and TiC as stable and promising supports for oxygen reduction reaction: Theoretical and experimental study," *Appl. Surf. Sci.*, vol. 495, p. 143620, Nov. 2019, doi: 10.1016/j.apsusc.2019.143620.

[104] E. Davari and D. G. Ivey, "Synthesis and electrochemical performance of manganese nitride as an oxygen reduction and oxygen evolution catalyst for zinc–air secondary batteries," *J. Appl. Electrochem.*, vol. 47, no. 7, pp. 815–827, Jul. 2017, doi: 10.1007/s10800-017-1084-z.

[105] M. E. Kreider *et al.*, "Nitride or Oxynitride? Elucidating the Composition–Activity Relationships in Molybdenum Nitride Electrocatalysts for the Oxygen Reduction Reaction," *Chem. Mater.*, vol. 32, no. 7, pp. 2946–2960, Apr. 2020, doi: 10.1021/acs.chemmater.9b05212.

[106] J. Zhang, Z. Xia, and L. Dai, "Carbon-based electrocatalysts for advanced energy conversion and storage," *Sci. Adv.*, vol. 1, no. 7, p. e1500564, doi: 10.1126/sciadv.1500564.

[107] K. Gong, F. Du, Z. Xia, M. Durstock, and L. Dai, "Nitrogen-Doped Carbon Nanotube Arrays with High Electrocatalytic Activity for Oxygen Reduction," *Science*, vol. 323, no. 5915, pp. 760–764, Feb. 2009, doi: 10.1126/science.1168049.

[108] L. Yang *et al.*, "Boron-Doped Carbon Nanotubes as Metal-Free Electrocatalysts for the Oxygen Reduction Reaction," *Angew. Chem. Int. Ed.*, vol. 50, no. 31, pp. 7132–7135, 2011, doi: 10.1002/anie.201101287.

[109] Z.-H. Sheng, H.-L. Gao, W.-J. Bao, F.-B. Wang, and X.-H. Xia, "Synthesis of boron doped graphene for oxygen reduction reaction in fuel cells," *J. Mater. Chem.*, vol. 22, no. 2, pp. 390–395, 2012, doi: 10.1039/C1JM14694G.

[110] Z. Yang *et al.*, "Sulfur-Doped Graphene as an Efficient Metal-free Cathode Catalyst for Oxygen Reduction," *ACS Nano*, vol. 6, no. 1, pp. 205–211, Jan. 2012, doi: 10.1021/nn203393d.

[111] Z. Ma, S. Dou, A. Shen, L. Tao, L. Dai, and S. Wang, "Sulfur-Doped Graphene Derived from Cycled Lithium–Sulfur Batteries as a Metal-Free Electrocatalyst for the Oxygen

Reduction Reaction," *Angew. Chem. Int. Ed.*, vol. 54, no. 6, pp. 1888–1892, 2015, doi: 10.1002/anie.201410258.

[112] Z.-W. Liu, F. Peng, H.-J. Wang, H. Yu, W.-X. Zheng, and J. Yang, "Phosphorus-Doped Graphite Layers with High Electrocatalytic Activity for the O2 Reduction in an Alkaline Medium," *Angew. Chem. Int. Ed.*, vol. 50, no. 14, pp. 3257–3261, 2011, doi: 10.1002/anie.201006768.

[113] I.-Y. Jeon *et al.*, "Facile, scalable synthesis of edge-halogenated graphene nanoplatelets as efficient metal-free eletrocatalysts for oxygen reduction reaction," *Sci. Rep.*, vol. 3, no. 1, p. 1810, Jun. 2013, doi: 10.1038/srep01810.

[114] S. Kattel, P. Atanassov, and B. Kiefer, "Density functional theory study of the oxygen reduction reaction mechanism in a BN co-doped graphene electrocatalyst," *J. Mater. Chem. A*, vol. 2, no. 26, pp. 10273–10279, 2014, doi: 10.1039/C4TA01460J.

[115] H. Tabassum, R. Zou, A. Mahmood, Z. Liang, and S. Guo, "A catalyst-free synthesis of B, N co-doped graphene nanostructures with tunable dimensions as highly efficient metal free dual electrocatalysts," *J. Mater. Chem. A*, vol. 4, no. 42, pp. 16469–16475, 2016, doi: 10.1039/C6TA07214C.

[116] R. Sibul *et al.*, "Sulphur and nitrogen co-doped graphene-based electrocatalysts for oxygen reduction reaction in alkaline medium," *Electrochem. Commun.*, vol. 109, p. 106603, Dec. 2019, doi: 10.1016/j.elecom.2019.106603.

[117] G.-L. Chai, K. Qiu, M. Qiao, M.-M. Titirici, C. Shang, and Z. Guo, "Active sites engineering leads to exceptional ORR and OER bifunctionality in P,N Co-doped graphene frameworks," *Energy Environ. Sci.*, vol. 10, no. 5, pp. 1186–1195, 2017, doi: 10.1039/C6EE03446B.

[118] F. Dong, Y. Cai, C. Liu, J. Liu, and J. Qiao, "Heteroatom (B, N and P) doped porous graphene foams for efficient oxygen reduction reaction electrocatalysis," *Int. J. Hydrog. Energy*, vol. 43, no. 28, pp. 12661–12670, Jul. 2018, doi: 10.1016/j.ijhydene.2018.04.118.

[119] S. Yang, L. Zhi, K. Tang, X. Feng, J. Maier, and K. Müllen, "Efficient Synthesis of Heteroatom (N or S)-Doped Graphene Based on Ultrathin Graphene Oxide-Porous Silica Sheets for Oxygen Reduction Reactions," *Adv. Funct. Mater.*, vol. 22, no. 17, pp. 3634–3640, 2012, doi: 10.1002/adfm.201200186.

[120] Y. Jiang *et al.*, "Significant Contribution of Intrinsic Carbon Defects to Oxygen Reduction Activity," *ACS Catal.*, vol. 5, no. 11, pp. 6707–6712, Nov. 2015, doi: 10.1021/acscatal.5b01835.

[121] X. Zou and Y. Zhang, "Noble metal-free hydrogen evolution catalysts for water splitting," *Chem. Soc. Rev.*, vol. 44, no. 15, pp. 5148–5180, 2015, doi: 10.1039/C4CS00448E.

[122] N. Dubouis and A. Grimaud, "The hydrogen evolution reaction: from material to interfacial descriptors," *Chem. Sci.*, vol. 10, no. 40, pp. 9165–9181, 2019, doi:

10.1039/C9SC03831K.

[123] Y. Cao, “Roadmap and Direction toward High-Performance MoS2 Hydrogen Evolution Catalysts,” *ACS Nano*, vol. 15, no. 7, pp. 11014–11039, Jul. 2021, doi: 10.1021/acsnano.1c01879.

[124] A. R. Kucernak and C. Zalitis, “General Models for the Electrochemical Hydrogen Oxidation and Hydrogen Evolution Reactions: Theoretical Derivation and Experimental Results under Near Mass-Transport Free Conditions,” *J. Phys. Chem. C*, vol. 120, no. 20, pp. 10721–10745, May 2016, doi: 10.1021/acs.jpcc.6b00011.

[125] H. Wang and L. Gao, “Recent developments in electrochemical hydrogen evolution reaction,” *Curr. Opin. Electrochem.*, vol. 7, pp. 7–14, Jan. 2018, doi: 10.1016/j.coelec.2017.10.010.

[126] J. Durst, C. Simon, F. Hasché, and H. A. Gasteiger, “Hydrogen Oxidation and Evolution Reaction Kinetics on Carbon Supported Pt, Ir, Rh, and Pd Electrocatalysts in Acidic Media,” *J. Electrochem. Soc.*, vol. 162, no. 1, p. F190, Dec. 2014, doi: 10.1149/2.0981501jes.

[127] S. Trasatti, “Work function, electronegativity, and electrochemical behaviour of metals: III. Electrolytic hydrogen evolution in acid solutions,” *J. Electroanal. Chem. Interfacial Electrochem.*, vol. 39, no. 1, pp. 163–184, Sep. 1972, doi: 10.1016/S0022-0728(72)80485-6.

[128] E. Skúlason *et al.*, “Modeling the Electrochemical Hydrogen Oxidation and Evolution Reactions on the Basis of Density Functional Theory Calculations,” *J. Phys. Chem. C*, vol. 114, no. 42, pp. 18182–18197, Oct. 2010, doi: 10.1021/jp1048887.

[129] A. R. Zeradjanin, A. Vimalanandan, G. Polymeros, A. A. Topalov, K. J. J. Mayrhofer, and M. Rohwerder, “Balanced work function as a driver for facile hydrogen evolution reaction – comprehension and experimental assessment of interfacial catalytic descriptor,” *Phys. Chem. Chem. Phys.*, vol. 19, no. 26, pp. 17019–17027, 2017, doi: 10.1039/C7CP03081A.

[130] M. J. Janik, I. T. McCrum, and M. T. M. Koper, “On the presence of surface bound hydroxyl species on polycrystalline Pt electrodes in the "hydrogen potential region" (0-0.4 V-RHE),” *J. Catal.*, vol. 367, pp. 332–337, Nov. 2018, doi: 10.1016/j.jcat.2018.09.031.

[131] N. M. Marković, B. N. Grgur, and P. N. Ross, “Temperature-Dependent Hydrogen Electrochemistry on Platinum Low-Index Single-Crystal Surfaces in Acid Solutions,” *J. Phys. Chem. B*, vol. 101, no. 27, pp. 5405–5413, Jul. 1997, doi: 10.1021/jp970930d.

[132] W. Sheng, H. A. Gasteiger, and Y. Shao-Horn, “Hydrogen Oxidation and Evolution Reaction Kinetics on Platinum: Acid vs Alkaline Electrolytes,” *J. Electrochem. Soc.*, vol. 157, no. 11, p. B1529, Sep. 2010, doi: 10.1149/1.3483106.

[133] N. Dubouis, C. Yang, R. Beer, L. Ries, D. Voiry, and A. Grimaud, “Interfacial Interactions

as an Electrochemical Tool To Understand Mo-Based Catalysts for the Hydrogen Evolution Reaction," *ACS Catal.*, vol. 8, no. 2, pp. 828–836, Feb. 2018, doi: 10.1021/acscatal.7b03684.

[134] Y. Zheng, Y. Jiao, A. Vasileff, and S.-Z. Qiao, "The Hydrogen Evolution Reaction in Alkaline Solution: From Theory, Single Crystal Models, to Practical Electrocatalysts," *Angew. Chem. Int. Ed.*, vol. 57, no. 26, pp. 7568–7579, 2018, doi: 10.1002/anie.201710556.

[135] T. Shinagawa, A. T. Garcia-Esparza, and K. Takanabe, "Insight on Tafel slopes from a microkinetic analysis of aqueous electrocatalysis for energy conversion," *Sci. Rep.*, vol. 5, no. 1, p. 13801, Sep. 2015, doi: 10.1038/srep13801.

[136] W. Sheng, M. Myint, J. G. Chen, and Y. Yan, "Correlating the hydrogen evolution reaction activity in alkaline electrolytes with the hydrogen binding energy on monometallic surfaces," *Energy Environ. Sci.*, vol. 6, no. 5, pp. 1509–1512, 2013, doi: 10.1039/C3EE00045A.

[137] J. Zheng, W. Sheng, Z. Zhuang, B. Xu, and Y. Yan, "Universal dependence of hydrogen oxidation and evolution reaction activity of platinum-group metals on pH and hydrogen binding energy," *Sci. Adv.*, Mar. 2016, doi: 10.1126/sciadv.1501602.

[138] R. Subbaraman *et al.*, "Enhancing Hydrogen Evolution Activity in Water Splitting by Tailoring Li+-Ni(OH)2-Pt Interfaces," *Science*, Dec. 2011, doi: 10.1126/science.1211934.

[139] V. Grozovski, S. Vesztergom, G. G. Láng, and P. Broekmann, "Electrochemical Hydrogen Evolution: H+ or H2O Reduction? A Rotating Disk Electrode Study," *J. Electrochem. Soc.*, vol. 164, no. 11, p. E3171, May 2017, doi: 10.1149/2.0191711jes.

[140] B. You, Y. Zhang, Y. Jiao, K. Davey, and S. Z. Qiao, "Negative Charging of Transition-Metal Phosphides via Strong Electronic Coupling for Destabilization of Alkaline Water," *Angew. Chem.*, vol. 131, no. 34, pp. 11922–11926, 2019, doi: 10.1002/ange.201906683.

[141] I. T. McCrum and M. J. Janik, "pH and Alkali Cation Effects on the Pt Cyclic Voltammogram Explained Using Density Functional Theory," *J. Phys. Chem. C*, vol. 120, no. 1, pp. 457–471, Jan. 2016, doi: 10.1021/acs.jpcc.5b10979.

[142] X. Chen, I. T. McCrum, K. A. Schwarz, M. J. Janik, and M. T. M. Koper, "Co-adsorption of Cations as the Cause of the Apparent pH Dependence of Hydrogen Adsorption on a Stepped Platinum Single-Crystal Electrode," *Angew. Chem. Int. Ed.*, vol. 56, no. 47, pp. 15025–15029, 2017, doi: 10.1002/anie.201709455.

[143] M. Favaro *et al.*, "Unravelling the electrochemical double layer by direct probing of the solid/liquid interface," *Nat. Commun.*, vol. 7, no. 1, p. 12695, Aug. 2016, doi: 10.1038/ncomms12695.

[144] L. Lin, B. Deng, J. Sun, H. Peng, and Z. Liu, "Bridging the Gap between Reality and Ideal in Chemical Vapor Deposition Growth of Graphene," *Chem. Rev.*, vol. 118, no. 18, pp.

9281–9343, Sep. 2018, doi: 10.1021/acs.chemrev.8b00325.

[145] H. Pedersen and S. D. Elliott, "Studying Chemical Vapor Deposition Processes with Theoretical Chemistry," *Theor. Chem. Acc.*, pp. 1–10, 2014, doi: 10.1007/s00214-014-1476-7.

[146] A. Grill, *Cold plasma in materials fabrication*, vol. 151. IEEE Press, New York, 1994.

[147] D. A. Gurnett and A. Bhattacharjee, "Introduction to Plasma Physiscs; With Space and Laboratory Applications," 2005. doi: 10.1017/CBO9781107415324.004.

[148] H. Conards and Schmidt M, "Plasma generation and plasma sources," *IOP Sci.*, vol. 9, pp. 441–454, 2000.

[149] K. Iwaszczuk, M. Zalkovskij, A. C. Strikwerda, and P. U. Jepsen, "Nitrogen plasma formation through terahertz-induced ultrafast electron field emission," *Optica*, vol. 2, no. 2, p. 116, 2015, doi: 10.1364/OPTICA.2.000116.

[150] S. Mazouffre *et al.*, "Density and temperature of N atoms in the afterglow of a microwave discharge measured by a two-photon laser-induced fluorescence technique," *Plasma Sources Sci Technol*, vol. 10, pp. 168–175, 2001, doi: 10.1088/0963-0252/10/2/306.

[151] Y. Kubota, R. Ichiki, T. Hara, N. Yamaguchi, and Y. Takemura, "Spectroscopic analysis of nitrogen atmospheric plasma jet," *J Plasma Fusion Res*, vol. 8, pp. 740–743, 2009.

[152] P. Vandenabeele, *Practical Raman Spectroscopy: An Introduction*. John Wiley & Sons, 2013.

[153] E. Smith and G. Dent, *Modern Raman Spectroscopy: A Practical Approach*. John Wiley & Sons, 2019.

[154] C. S. S. R. Kumar, Ed., *Raman Spectroscopy for Nanomaterials Characterization*. Berlin, Heidelberg: Springer Berlin Heidelberg, 2012. doi: 10.1007/978-3-642-20620-7.

[155] P. Van Der Heide, *X-ray Photoelectron Spectroscopy: An introduction to Principles and Practices*, vol. 2011. 2011. doi: 10.1002/9781118162897.ch1.

[156] G. A. Somorjai, *Chemistry in two dimensions: surfaces*. Cornell University Press, 1981.

[157] C. S. Schnohr and M. C. Ridgway, "Introduction to X-Ray Absorption Spectroscopy," in *X-Ray Absorption Spectroscopy of Semiconductors*, C. S. Schnohr and M. C. Ridgway, Eds. Berlin, Heidelberg: Springer, 2015, pp. 1–26. doi: 10.1007/978-3-662-44362-0_1.

[158] S. Calvin, *XAFS for Everyone*. CRC Press, 2013.

[159] M. Wang, L. Árnadóttir, Z. J. Xu, and Z. Feng, "In Situ X-ray Absorption Spectroscopy Studies of Nanoscale Electrocatalysts," *Nano-Micro Lett.*, vol. 11, no. 1, p. 47, Jun. 2019, doi: 10.1007/s40820-019-0277-x.

[160] G. Bunker, *Introduction to XAFS: A Practical Guide to X-ray Absorption Fine Structure Spectroscopy*. Cambridge University Press, 2010.

[161] F. Boscherini, "9 - X-ray absorption fine structure in the study of semiconductor heterostructures and nanostructures," in *Characterization of Semiconductor*

Heterostructures and Nanostructures, C. Lamberti, Ed. Amsterdam: Elsevier, 2008, pp. 289–330. doi: 10.1016/B978-0-444-53099-8.00009-9.

[162] J. A. van Bokhoven and C. Lamberti, *X-Ray Absorption and X-Ray Emission Spectroscopy: Theory and Applications*. John Wiley & Sons, 2016.

[163] P. Willmott, *An Introduction to Synchrotron Radiation: Techniques and Applications*. Wiley, 2011.

[164] C. Hammond, *The Basics of Crystallography and Diffraction*, 4th ed. Oxford: Oxford University Press, 2015. doi: 10.1093/acprof:oso/9780198738671.001.0001.

[165] C. R. Hubbard and R. L. Snyder, "RIR - Measurement and Use in Quantitative XRD," *Powder Diffr.*, vol. 3, no. 2, pp. 74–77, Jun. 1988, doi: 10.1017/S0885715600013257.

[166] G. Binnig and C. F. Quate, "Atomic Force Microscope," *Phys. Rev. Lett.*, vol. 56, no. 9, 1986.

[167] G. Binnig and H. Rohrer, "Scanning tunneling microscopy," *Surf. Sci.*, vol. 126, no. 1–3, pp. 236–244, 1983.

[168] G. Haugstad, *Atomic Force Microscopy: Understanding Basic Modes and Advanced Applications*. Wiley, 2012.

[169] K. C. A. Smith and D. McMullan, "1.1 Charles Oatley: Father of Modern Scanning Electron Microscopy," in *Advances in Imaging and Electron Physics*, vol. 133, Elsevier, 2004, pp. 3–6. doi: 10.1016/S1076-5670(04)33001-6.

[170] J. I. Goldstein *et al.*, "Introduction," in *Scanning Electron Microscopy and X-ray Microanalysis: Third Edition*, J. I. Goldstein, D. E. Newbury, P. Echlin, D. C. Joy, C. E. Lyman, E. Lifshin, L. Sawyer, and J. R. Michael, Eds. Boston, MA: Springer US, 2003, pp. 1–20. doi: 10.1007/978-1-4615-0215-9_1.

[171] A. J. Bard and L. R. Faulkner, *Electrochemical Methods: Fundamentals and Applications, 2nd Edition*. John Wiley & Sons, Incorporated, 2000.

[172] X. Min, Y. Chen, and M. W. Kanan, "Alkaline O2 reduction on oxide-derived Au: high activity and 4e− selectivity without (100) facets," *Phys. Chem. Chem. Phys.*, vol. 16, no. 27, pp. 13601–13604, Jun. 2014, doi: 10.1039/C4CP01337A.

[173] S. Trasatti and O. A. Petrii, "Real surface area measurements in electrochemistry," *Pure Appl. Chem.*, vol. 63, no. 5, pp. 711–734, Jan. 1991, doi: 10.1351/pac199163050711.

[174] J. P. Barton and D. G. Infield, "Energy storage and its use with intermittent renewable energy," *IEEE Trans. Energy Convers.*, vol. 19, no. 2, pp. 441–448, Jun. 2004, doi: 10.1109/TEC.2003.822305.

[175] C. C. L. McCrory, S. Jung, J. C. Peters, and T. F. Jaramillo, "Benchmarking Heterogeneous Electrocatalysts for the Oxygen Evolution Reaction," *J. Am. Chem. Soc.*, vol. 135, no. 45, pp. 16977–16987, Nov. 2013, doi: 10.1021/ja407115p.

[176] P. Connor, J. Schuch, B. Kaiser, and W. Jaegermann, "The Determination of

Electrochemical Active Surface Area and Specific Capacity Revisited for the System MnOx as an Oxygen Evolution Catalyst," *Z. Für Phys. Chem.*, vol. 234, no. 5, pp. 979–994, May 2020, doi: 10.1515/zpch-2019-1514.

[177] Y. Zhai, Z. Zhu, S. Zhou, C. Zhu, and S. Dong, "Recent advances in spectroelectrochemistry," *Nanoscale*, vol. 10, no. 7, pp. 3089–3111, Feb. 2018, doi: 10.1039/C7NR07803J.

[178] Y. J. Tong, "In situ electrochemical nuclear magnetic resonance spectroscopy for electrocatalysis: Challenges and prospects," *Curr. Opin. Electrochem.*, vol. 4, no. 1, pp. 60–68, Aug. 2017, doi: 10.1016/j.coelec.2017.09.017.

[179] L. León and J. D. Mozo, "Designing spectroelectrochemical cells: A review," *TrAC Trends Anal. Chem.*, vol. 102, pp. 147–169, May 2018, doi: 10.1016/j.trac.2018.02.002.

[180] J. Garoz-Ruiz, J. V. Perales-Rondon, A. Heras, and A. Colina, "Spectroelectrochemical Sensing: Current Trends and Challenges," *Electroanalysis*, vol. 31, no. 7, pp. 1254–1278, 2019, doi: 10.1002/elan.201900075.

[181] L. Dunsch, "Recent Advances in in situ multi-spectroelectrochemistry," *J. Solid State Electrochem.*, vol. 15, no. 7, pp. 1631–1646, Jul. 2011, doi: 10.1007/s10008-011-1453-1.

[182] H. Oberacher, F. Pitterl, R. Erb, and S. Plattner, "Mass spectrometric methods for monitoring redox processes in electrochemical cells," *Mass Spectrom. Rev.*, vol. 34, no. 1, pp. 64–92, Feb. 2015, doi: 10.1002/mas.21409.

[183] A. J. Wain and M. A. O'Connell, "Advances in surface-enhanced vibrational spectroscopy at electrochemical interfaces," *Adv. Phys. X*, vol. 2, no. 1, pp. 188–209, Jan. 2017, doi: 10.1080/23746149.2016.1268931.

[184] J. M. Yoo, H. Shin, S. Park, and Y.-E. Sung, "Recent progress in in situ/operando analysis tools for oxygen electrocatalysis," *J. Phys. D: Appl. Phys.*, vol. 54, no. 17, p. 173001, Feb. 2021, doi: 10.1088/1361-6463/abd9a4.

[185] J. J. A. Lozeman, P. Führer, W. Olthuis, and M. Odijk, "Spectroelectrochemistry, the future of visualizing electrode processes by hyphenating electrochemistry with spectroscopic techniques," *Analyst*, vol. 145, no. 7, pp. 2482–2509, Mar. 2020, doi: 10.1039/C9AN02105A.

[186] T. Kuwana, R. K. Darlington, and D. W. Leedy, "Electrochemical Studies Using Conducting Glass Indicator Electrodes.," *ACS Publications*, May 01, 2002. https://pubs.acs.org/doi/pdf/10.1021/ac60216a003 (accessed Nov. 14, 2021).

[187] J. Tarábek, L. Kavan, L. Dunsch, and M. Kalbac, "Chemical States of Electrochemically Doped Single Wall Carbon Nanotubes As Probed by Raman Spectroelectrochemistry and ex Situ X-ray Photoelectron Spectroscopy," *J. Phys. Chem. C*, vol. 112, no. 36, pp. 13856–13861, Sep. 2008, doi: 10.1021/jp803514h.

[188] O. Frank, M. S. Dresselhaus, and M. Kalbac, "Raman Spectroscopy and in Situ Raman

Spectroelectrochemistry of Isotopically Engineered Graphene Systems," Jan. 08, 2015. https://pubs.acs.org/doi/abs/10.1021/ar500384p (accessed Sep. 03, 2018).

[189] W. T. E. van den Beld *et al.*, "In-situ Raman spectroscopy to elucidate the influence of adsorption in graphene electrochemistry," *Sci. Rep.*, vol. 7, no. 1, Art. no. 1, Mar. 2017, doi: 10.1038/srep45080.

[190] R. Mažeikienė, G. Niaura, and A. Malinauskas, "In situ time-resolved Raman spectroelectrochemical study of aniline polymerization at platinum and gold electrodes," *Chemija*, vol. 29, no. 2, Art. no. 2, Jun. 2018, doi: 10.6001/chemija.v29i2.3710.

[191] P. Song, X. Guo, Y. Pan, Y. Wen, Z. Zhang, and H. Yang, "SERS and in situ SERS spectroelectrochemical investigations of serotonin monolayers at a silver electrode," *J. Electroanal. Chem.*, vol. 688, pp. 384–391, Jan. 2013, doi: 10.1016/j.jelechem.2012.09.008.

[192] R. A. Karaballi, S. Merchant, S. R. Power, and C. L. Brosseau, "Electrochemical surface-enhanced Raman spectroscopy (EC-SERS) study of the interaction between protein aggregates and biomimetic membranes," *Phys. Chem. Chem. Phys.*, vol. 20, no. 6, pp. 4513–4526, Feb. 2018, doi: 10.1039/C7CP06838G.

[193] J.-C. Dong *et al.*, "Direct In Situ Raman Spectroscopic Evidence of Oxygen Reduction Reaction Intermediates at High-Index Pt(hkl) Surfaces," *J. Am. Chem. Soc.*, vol. 142, no. 2, pp. 715–719, Jan. 2020, doi: 10.1021/jacs.9b12803.

[194] P.-H. Tan, Ed., *Raman Spectroscopy of Two-Dimensional Materials*, vol. 276. Singapore: Springer Singapore, 2019. doi: 10.1007/978-981-13-1828-3.

[195] C. Lee, X. Wei, J. W. Kysar, and J. Hone, "Measurement of the Elastic Properties and Intrinsic Strength of Monolayer Graphene," *Science*, vol. 321, no. 5887, pp. 385–388, Jul. 2008, doi: 10.1126/science.1157996.

[196] K. I. Bolotin *et al.*, "Ultrahigh electron mobility in suspended graphene," *Solid State Commun.*, vol. 146, no. 9, pp. 351–355, Jun. 2008, doi: 10.1016/j.ssc.2008.02.024.

[197] J. H. Seol *et al.*, "Two-Dimensional Phonon Transport in Supported Graphene," *Science*, vol. 328, no. 5975, pp. 213–216, Apr. 2010, doi: 10.1126/science.1184014.

[198] R. R. Nair *et al.*, "Fine Structure Constant Defines Visual Transparency of Graphene," *Science*, vol. 320, no. 5881, pp. 1308–1308, Jun. 2008, doi: 10.1126/science.1156965.

[199] R. S. Edwards and K. S. Coleman, "Graphene synthesis: relationship to applications," *Nanoscale*, vol. 5, no. 1, pp. 38–51, Dec. 2012, doi: 10.1039/C2NR32629A.

[200] J. Zhang, H. Yang, G. Shen, P. Cheng, J. Zhang, and S. Guo, "Reduction of graphene oxide viaL-ascorbic acid," *Chem. Commun.*, vol. 46, no. 7, pp. 1112–1114, Feb. 2010, doi: 10.1039/B917705A.

[201] H. Zhu, X. Gan, A. McCreary, R. Lv, Z. Lin, and M. Terrones, "Heteroatom doping of two-dimensional materials: From graphene to chalcogenides," *Nano Today*, vol. 30, p.

100829, Feb. 2020, doi: 10.1016/j.nantod.2019.100829.

[202] J. E. Johns and M. C. Hersam, "Atomic Covalent Functionalization of Graphene," *Acc. Chem. Res.*, vol. 46, no. 1, pp. 77–86, Jan. 2013, doi: 10.1021/ar300143e.

[203] Q. Li *et al.*, "Locally Induced Spin States on Graphene by Chemical Attachment of Boron Atoms," *Nano Lett.*, vol. 18, no. 9, pp. 5482–5487, Sep. 2018, doi: 10.1021/acs.nanolett.8b01798.

[204] H. Xu, L. Ma, and Z. Jin, "Nitrogen-doped graphene: Synthesis, characterizations and energy applications," *J. Energy Chem.*, vol. 27, no. 1, pp. 146–160, Jan. 2018, doi: 10.1016/j.jechem.2017.12.006.

[205] L. Zhang and Z. Xia, "Mechanisms of Oxygen Reduction Reaction on Nitrogen-Doped Graphene for Fuel Cells," *J. Phys. Chem. C*, vol. 115, no. 22, pp. 11170–11176, Jun. 2011, doi: 10.1021/jp201991j.

[206] Y. Shao *et al.*, "Nitrogen-doped graphene and its electrochemical applications," *J. Mater. Chem.*, vol. 20, no. 35, pp. 7491–7496, 2010.

[207] B. Sensale-Rodriguez *et al.*, "Broadband graphene terahertz modulators enabled by intraband transitions," *Nat. Commun.*, vol. 3, p. 780, Apr. 2012, doi: 10.1038/ncomms1787.

[208] S. Feng *et al.*, "Ultrasensitive molecular sensor using N-doped graphene through enhanced Raman scattering," *Sci. Adv.*, vol. 2, no. 7, p. e1600322, Jul. 2016, doi: 10.1126/sciadv.1600322.

[209] L. Lai *et al.*, "Exploration of the active center structure of nitrogen-doped graphene-based catalysts for oxygen reduction reaction," *Energy Environ. Sci.*, vol. 5, no. 7, pp. 7936–7942, 2012, doi: 10.1039/C2EE21802J.

[210] L. Qu, Y. Liu, J.-B. Baek, and L. Dai, "Nitrogen-Doped Graphene as Efficient Metal-Free Electrocatalyst for Oxygen Reduction in Fuel Cells," *ACS Nano*, vol. 4, no. 3, pp. 1321–1326, Mar. 2010, doi: 10.1021/nn901850u.

[211] K. R. Lee, K. U. Lee, J. W. Lee, B. T. Ahn, and S. I. Woo, "Electrochemical oxygen reduction on nitrogen doped graphene sheets in acid media," *Electrochem. Commun.*, vol. 12, no. 8, pp. 1052–1055, Aug. 2010, doi: 10.1016/j.elecom.2010.05.023.

[212] H. M. Jeong *et al.*, "Nitrogen-Doped Graphene for High-Performance Ultracapacitors and the Importance of Nitrogen-Doped Sites at Basal Planes," *Nano Lett.*, vol. 11, pp. 2472–2477, 2011.

[213] L. Zhao *et al.*, "Visualizing Individual Nitrogen Dopants in Monolayer Graphene," *Science*, vol. 333, no. 6045, pp. 999–1003, Aug. 2011, doi: 10.1126/science.1208759.

[214] R. Jasinski, "A New Fuel Cell Cathode Catalyst," *Nature*, vol. 201, no. 4925, pp. 1212–1213, Mar. 1964, doi: 10.1038/2011212a0.

[215] M. Winter and R. J. Brodd, "What Are Batteries, Fuel Cells, and Supercapacitors? (Chem.

Rev. 2003, 104, 4245−4269. Published on the Web 09/28/2004.)," *Chem. Rev.*, vol. 105, no. 3, pp. 1021–1021, Mar. 2005, doi: 10.1021/cr040110e.

[216] L. Zhang, J. Zhang, D. P. Wilkinson, and H. Wang, "Progress in preparation of non-noble electrocatalysts for PEM fuel cell reactions," *J. Power Sources*, vol. 156, no. 2, pp. 171–182, Jun. 2006, doi: 10.1016/j.jpowsour.2005.05.069.

[217] S. Maldonado and K. J. Stevenson, "Influence of Nitrogen Doping on Oxygen Reduction Electrocatalysis at Carbon Nanofiber Electrodes," *J. Phys. Chem. B*, vol. 109, no. 10, pp. 4707–4716, Mar. 2005, doi: 10.1021/jp044442z.

[218] V. Nallathambi, J.-W. Lee, S. P. Kumaraguru, G. Wu, and B. N. Popov, "Development of high performance carbon composite catalyst for oxygen reduction reaction in PEM Proton Exchange Membrane fuel cells," *J. Power Sources*, vol. 183, no. 1, pp. 34–42, Aug. 2008, doi: 10.1016/j.jpowsour.2008.05.020.

[219] T. Chen *et al.*, "Nitrogen-Doped Carbon Nanotube Composite Fiber with a Core–Sheath Structure for Novel Electrodes," *Adv. Mater.*, vol. 23, no. 40, pp. 4620–4625, 2011, doi: 10.1002/adma.201102200.

[220] X. Zhou, Z. Yang, H. Nie, Z. Yao, L. Zhang, and S. Huang, "Catalyst-free growth of large scale nitrogen-doped carbon spheres as efficient electrocatalysts for oxygen reduction in alkaline medium," *J. Power Sources*, vol. 196, no. 23, pp. 9970–9974, Dec. 2011, doi: 10.1016/j.jpowsour.2011.08.029.

[221] H. Niwa *et al.*, "X-ray absorption analysis of nitrogen contribution to oxygen reduction reaction in carbon alloy cathode catalysts for polymer electrolyte fuel cells," *J. Power Sources*, vol. 187, no. 1, pp. 93–97, Feb. 2009, doi: 10.1016/j.jpowsour.2008.10.064.

[222] D. Geng *et al.*, "High oxygen-reduction activity and durability of nitrogen-doped graphene," *Energy Environ. Sci.*, vol. 4, no. 3, pp. 760–764, Mar. 2011, doi: 10.1039/C0EE00326C.

[223] W. Ouyang *et al.*, "Exploring the active sites of nitrogen-doped graphene as catalysts for the oxygen reduction reaction," *Int. J. Hydrog. Energy*, vol. 39, no. 28, pp. 15996–16005, Sep. 2014, doi: 10.1016/j.ijhydene.2014.01.045.

[224] T. Ikeda, M. Boero, S.-F. Huang, K. Terakura, M. Oshima, and J. Ozaki, "Carbon Alloy Catalysts: Active Sites for Oxygen Reduction Reaction," *J. Phys. Chem. C*, vol. 112, no. 38, pp. 14706–14709, Sep. 2008, doi: 10.1021/jp806084d.

[225] H. Kim, K. Lee, S. I. Woo, and Y. Jung, "On the mechanism of enhanced oxygen reduction reaction in nitrogen-doped graphene nanoribbons," *Phys. Chem. Chem. Phys.*, vol. 13, no. 39, pp. 17505–17510, Sep. 2011, doi: 10.1039/C1CP21665A.

[226] S.-F. Huang *et al.*, "First-principles calculation of the electronic properties of graphene clusters doped with nitrogen and boron: Analysis of catalytic activity for the oxygen reduction reaction," *Phys. Rev. B*, vol. 80, no. 23, p. 235410, Dec. 2009, doi:

10.1103/PhysRevB.80.235410.

[227] Z.-H. Sheng, L. Shao, J.-J. Chen, W.-J. Bao, F.-B. Wang, and X.-H. Xia, "Catalyst-Free Synthesis of Nitrogen-Doped Graphene via Thermal Annealing Graphite Oxide with Melamine and Its Excellent Electrocatalysis," *ACS Nano*, vol. 5, no. 6, pp. 4350–4358, Jun. 2011, doi: 10.1021/nn103584t.

[228] Z. Chen, D. Higgins, H. Tao, R. S. Hsu, and Z. Chen, "Highly Active Nitrogen-Doped Carbon Nanotubes for Oxygen Reduction Reaction in Fuel Cell Applications," *J. Phys. Chem. C*, vol. 113, no. 49, pp. 21008–21013, Dec. 2009, doi: 10.1021/jp908067v.

[229] C. V. Rao, C. R. Cabrera, and Y. Ishikawa, "In Search of the Active Site in Nitrogen-Doped Carbon Nanotube Electrodes for the Oxygen Reduction Reaction," *J. Phys. Chem. Lett.*, vol. 1, no. 18, pp. 2622–2627, Sep. 2010, doi: 10.1021/jz100971v.

[230] R. Ma *et al.*, "Novel synthesis of N-doped graphene as an efficient electrocatalyst towards oxygen reduction," *Nano Res.*, vol. 9, no. 3, pp. 808–819, Mar. 2016, doi: 10.1007/s12274-015-0960-2.

[231] L. Zhang and Z. Xia, "Mechanisms of Oxygen Reduction Reaction on Nitrogen-Doped Graphene for Fuel Cells," *J. Phys. Chem. C*, vol. 115, no. 22, pp. 11170–11176, Jun. 2011, doi: 10.1021/jp201991j.

[232] S. Yasuda, L. Yu, J. Kim, and K. Murakoshi, "Selective nitrogen doping in graphene for oxygen reduction reactions," *Chem. Commun.*, vol. 49, no. 83, pp. 9627–9629, 2013, doi: 10.1039/C3CC45641B.

[233] J. Wu *et al.*, "Nitrogen-Doped Graphene with Pyridinic Dominance as a Highly Active and Stable Electrocatalyst for Oxygen Reduction," *ACS Appl. Mater. Interfaces*, vol. 7, no. 27, pp. 14763–14769, Jul. 2015, doi: 10.1021/acsami.5b02902.

[234] T. Xing *et al.*, "Observation of Active Sites for Oxygen Reduction Reaction on Nitrogen-Doped Multilayer Graphene," *ACS Nano*, vol. 8, no. 7, pp. 6856–6862, Jul. 2014, doi: 10.1021/nn501506p.

[235] C. Zhang, R. Hao, H. Liao, and Y. Hou, "Synthesis of amino-functionalized graphene as metal-free catalyst and exploration of the roles of various nitrogen states in oxygen reduction reaction," *Nano Energy*, vol. 2, no. 1, pp. 88–97, Jan. 2013, doi: 10.1016/j.nanoen.2012.07.021.

[236] Z. Hou, X. Wang, T. Ikeda, K. Terakura, M. Oshima, and M. Kakimoto, "Electronic structure of N-doped graphene with native point defects," *Phys. Rev. B*, vol. 87, no. 16, p. 165401, Apr. 2013, doi: 10.1103/PhysRevB.87.165401.

[237] Y. Fujimoto and S. Saito, "Formation, stabilities, and electronic properties of nitrogen defects in graphene," *Phys. Rev. B*, vol. 84, no. 24, p. 245446, Dec. 2011, doi: 10.1103/PhysRevB.84.245446.

[238] D. Guo, R. Shibuya, C. Akiba, S. Saji, T. Kondo, and J. Nakamura, "Active sites of

nitrogen-doped carbon materials for oxygen reduction reaction clarified using model catalysts," *Science*, vol. 351, no. 6271, pp. 361–365, Jan. 2016, doi: 10.1126/science.aad0832.

[239] X. Ge *et al.*, "Oxygen Reduction in Alkaline Media: From Mechanisms to Recent Advances of Catalysts," *ACS Catal.*, vol. 5, no. 8, pp. 4643–4667, Aug. 2015, doi: 10.1021/acscatal.5b00524.

[240] C. Hu and L. Dai, "Doping of Carbon Materials for Metal-Free Electrocatalysis," *Adv. Mater.*, vol. 31, no. 7, p. 1804672, 2019, doi: 10.1002/adma.201804672.

[241] F. de Groot and A. Kotani, *Core Level Spectroscopy of Solids*. Boca Raton: CRC Press, 2008. doi: 10.1201/9781420008425.

[242] S. Rajasekaran, F. Abild-Pedersen, H. Ogasawara, A. Nilsson, and S. Kaya, "Interlayer Carbon Bond Formation Induced by Hydrogen Adsorption in Few-Layer Supported Graphene," *Phys. Rev. Lett.*, vol. 111, no. 8, p. 085503, Aug. 2013, doi: 10.1103/PhysRevLett.111.085503.

[243] T. Schiros *et al.*, "Connecting Dopant Bond Type with Electronic Structure in N-Doped Graphene," *Nano Lett.*, vol. 12, no. 8, pp. 4025–4031, Aug. 2012, doi: 10.1021/nl301409h.

[244] X. Liang *et al.*, "Toward clean and crackless transfer of graphene," *ACS Nano*, vol. 5, no. 11, pp. 9144–9153, 2011.

[245] J. N. Ullom and D. A. Bennett, "Review of superconducting transition-edge sensors for x-ray and gamma-ray spectroscopy," *Supercond. Sci. Technol.*, vol. 28, no. 8, p. 084003, Jul. 2015, doi: 10.1088/0953-2048/28/8/084003.

[246] S.-J. Lee *et al.*, "Soft X-ray spectroscopy with transition-edge sensors at Stanford Synchrotron Radiation Lightsource beamline 10-1," *Rev. Sci. Instrum.*, vol. 90, no. 11, p. 113101, Nov. 2019, doi: 10.1063/1.5119155.

[247] G. Kresse and J. Furthmüller, "Efficient iterative schemes for ab initio total-energy calculations using a plane-wave basis set," *Phys. Rev. B*, vol. 54, no. 16, pp. 11169–11186, Oct. 1996, doi: 10.1103/PhysRevB.54.11169.

[248] G. Kresse and J. Furthmüller, "Efficiency of ab-initio total energy calculations for metals and semiconductors using a plane-wave basis set," *Comput. Mater. Sci.*, vol. 6, no. 1, pp. 15–50, Jul. 1996, doi: 10.1016/0927-0256(96)00008-0.

[249] G. Kresse and D. Joubert, "From ultrasoft pseudopotentials to the projector augmented-wave method," *Phys. Rev. B*, vol. 59, no. 3, pp. 1758–1775, Jan. 1999, doi: 10.1103/PhysRevB.59.1758.

[250] J. P. Perdew, K. Burke, and M. Ernzerhof, "Generalized Gradient Approximation Made Simple," *Phys. Rev. Lett.*, vol. 77, no. 18, pp. 3865–3868, Oct. 1996, doi: 10.1103/PhysRevLett.77.3865.

[251] S. Grimme, J. Antony, S. Ehrlich, and H. Krieg, "A consistent and accurate ab initio

parametrization of density functional dispersion correction (DFT-D) for the 94 elements H-Pu," *J. Chem. Phys.*, vol. 132, no. 15, p. 154104, Apr. 2010, doi: 10.1063/1.3382344.

[252] C. R. S. V. Boas *et al.*, "Characterization of nitrogen doped graphene bilayers synthesized by fast, low temperature microwave plasma-enhanced chemical vapour deposition," *Sci. Rep.*, vol. 9, no. 1, Art. no. 1, Sep. 2019, doi: 10.1038/s41598-019-49900-9.

[253] R. P. Hardikar, A. Samanta, A. Manjanath, and A. K. Singh, "Vacancy mediated clipping of multi-layered graphene: A precursor for 1, 2 and 3D carbon structures," *Carbon*, vol. 94, pp. 67–72, Nov. 2015, doi: 10.1016/j.carbon.2015.06.040.

[254] M. Nakayama, K. Komine, and D. Inohara, "Nitrogen-Doped Carbon Cloth for Supercapacitors Prepared via a Hydrothermal Process," *J. Electrochem. Soc.*, vol. 163, no. 10, p. A2428, Sep. 2016, doi: 10.1149/2.0091613jes.

[255] C. Ma *et al.*, "Tuning the Doping Types in Graphene Sheets by N Monoelement," *Nano Lett.*, vol. 18, no. 1, pp. 386–394, Jan. 2018, doi: 10.1021/acs.nanolett.7b04249.

[256] N. Hellgren *et al.*, "Electronic structure of carbon nitride thin films studied by X-ray spectroscopy techniques," *Thin Solid Films*, vol. 471, no. 1, pp. 19–34, Jan. 2005, doi: 10.1016/j.tsf.2004.03.027.

[257] S. Sakulsermsuk, P. Singjai, and C. Chaiwong, "Influence of plasma process on the nitrogen configuration in graphene," *Diam. Relat. Mater.*, vol. 70, pp. 211–218, Nov. 2016, doi: 10.1016/j.diamond.2016.11.001.

[258] R. Saito, M. Hofmann, G. Dresselhaus, A. Jorio, and M. S. Dresselhaus, "Raman spectroscopy of graphene and carbon nanotubes," *Adv. Phys.*, vol. 60, no. 3, pp. 413–550, Jun. 2011, doi: 10.1080/00018732.2011.582251.

[259] A. Eckmann, A. Felten, I. Verzhbitskiy, R. Davey, and C. Casiraghi, "Raman study on defective graphene: Effect of the excitation energy, type, and amount of defects," *Phys. Rev. B*, vol. 88, no. 3, p. 035426, Jul. 2013, doi: 10.1103/PhysRevB.88.035426.

[260] A. Nilsson *et al.*, "Probing chemical bonding in adsorbates using X-ray emission spectroscopy," *J. Electron Spectrosc. Relat. Phenom.*, vol. 110–111, pp. 15–39, Oct. 2000, doi: 10.1016/S0368-2048(00)00155-9.

[261] D. Usachov *et al.*, "Nitrogen-Doped Graphene: Efficient Growth, Structure, and Electronic Properties," *Nano Lett.*, vol. 11, no. 12, pp. 5401–5407, Dec. 2011, doi: 10.1021/nl2031037.

[262] J. Zhong *et al.*, "Probing solid state N-doping in graphene by X-ray absorption near-edge structure spectroscopy," *Carbon*, vol. 50, no. 1, pp. 335–338, Jan. 2012, doi: 10.1016/j.carbon.2011.08.046.

[263] H. Zhang *et al.*, "Comprehensive electronic structure characterization of pristine and nitrogen/phosphorus doped carbon nanocages," *Carbon*, vol. 103, pp. 480–487, Jul. 2016, doi: 10.1016/j.carbon.2016.03.042.

[264] X. Li, W. Hua, J. Guo, and Y. Luo, “Electronic Structure of Nitrogen-Doped Graphene in the Ground and Core-Excited States from First-Principles Simulations,” *J. Phys. Chem. C*, vol. 119, no. 29, pp. 16660–16666, Jul. 2015, doi: 10.1021/acs.jpcc.5b03981.

[265] R. F. W. Bader, *Atoms in Molecules: A Quantum Theory*. Oxford, New York: Oxford University Press, 1994.

[266] T. Balkan, H. Küçükkeçeci, H. Zarenezhad, S. Kaya, and Ö. Metin, “One-pot synthesis of monodisperse copper–silver alloy nanoparticles and their composition-dependent electrocatalytic activity for oxygen reduction reaction,” *J. Alloys Compd.*, vol. 831, p. 154787, Aug. 2020, doi: 10.1016/j.jallcom.2020.154787.

[267] Y. Liu *et al.*, “Exploring the nitrogen species of nitrogen doped graphene as electrocatalysts for oxygen reduction reaction in Al–air batteries,” *Int. J. Hydrog. Energy*, vol. 41, no. 24, pp. 10354–10365, Jun. 2016, doi: 10.1016/j.ijhydene.2015.10.109.

[268] J. Tsurumi, Y. Saito, and P. Verma, “Evaluation of the interlayer interactions of few layers of graphene,” *Chem. Phys. Lett.*, vol. 557, pp. 114–117, Feb. 2013, doi: 10.1016/j.cplett.2012.12.015.

[269] Y. Hao *et al.*, “Probing Layer Number and Stacking Order of Few-Layer Graphene by Raman Spectroscopy,” *Small*, vol. 6, no. 2, pp. 195–200, 2010, doi: 10.1002/smll.200901173.

[270] M. Okano, R. Matsunaga, K. Matsuda, S. Masubuchi, T. Machida, and Y. Kanemitsu, “Raman study on the interlayer interactions and the band structure of bilayer graphene synthesized by alcohol chemical vapor deposition,” *Appl. Phys. Lett.*, vol. 99, no. 15, p. 151916, Oct. 2011, doi: 10.1063/1.3651325.

[271] A. C. Ferrari and D. M. Basko, “Raman spectroscopy as a versatile tool for studying the properties of graphene,” *Nat. Nanotechnol.*, vol. 8, no. 4, pp. 235–246, Apr. 2013, doi: 10.1038/nnano.2013.46.

[272] Y.-H. Tian, J. Huang, X. Sheng, B. G. Sumpter, M. Yoon, and M. Kertesz, “Nitrogen Doping Enables Covalent-Like π–π Bonding between Graphenes,” *Nano Lett.*, vol. 15, no. 8, pp. 5482–5491, Aug. 2015, doi: 10.1021/acs.nanolett.5b01940.

[273] A. G. Güell, N. Ebejer, M. E. Snowden, J. V. Macpherson, and P. R. Unwin, “Structural Correlations in Heterogeneous Electron Transfer at Monolayer and Multilayer Graphene Electrodes,” *J. Am. Chem. Soc.*, vol. 134, no. 17, pp. 7258–7261, May 2012, doi: 10.1021/ja3014902.

[274] N. B. Schorr, A. G. Jiang, and J. Rodríguez-López, “Probing Graphene Interfacial Reactivity via Simultaneous and Colocalized Raman–Scanning Electrochemical Microscopy Imaging and Interrogation,” *Anal. Chem.*, vol. 90, no. 13, pp. 7848–7854, Jul. 2018, doi: 10.1021/acs.analchem.8b00730.

[275] J. M. B. Lopes dos Santos, N. M. R. Peres, and A. H. Castro Neto, “Graphene Bilayer with

a Twist: Electronic Structure," *Phys. Rev. Lett.*, vol. 99, no. 25, p. 256802, Dec. 2007, doi: 10.1103/PhysRevLett.99.256802.

[276] S. Latil, V. Meunier, and L. Henrard, "Massless fermions in multilayer graphitic systems with misoriented layers: Ab initio calculations and experimental fingerprints," *Phys. Rev. B*, vol. 76, no. 20, p. 201402, Nov. 2007, doi: 10.1103/PhysRevB.76.201402.

[277] J. Hass *et al.*, "Why multilayer graphene on 4H-SiC(0001[over]) behaves like a single sheet of graphene," *Phys. Rev. Lett.*, vol. 100, no. 12, p. 125504, Mar. 2008, doi: 10.1103/PhysRevLett.100.125504.

[278] C.-T. Hung *et al.*, "Highly nitrogen-doped mesoscopic carbons as efficient metal-free electrocatalysts for oxygen reduction reactions," *J. Mater. Chem. A*, vol. 2, no. 47, pp. 20030–20037, Nov. 2014, doi: 10.1039/C4TA04403G.

[279] H. W. Kim *et al.*, "Mechanisms of Two-Electron and Four-Electron Electrochemical Oxygen Reduction Reactions at Nitrogen-Doped Reduced Graphene Oxide," *ACS Catal.*, vol. 10, no. 1, pp. 852–863, Jan. 2020, doi: 10.1021/acscatal.9b04106.

[280] G.-S. Kang, S. Lee, D. C. Lee, C. W. Yoon, and H.-I. Joh, "Edge-enriched graphene with boron and nitrogen co-doping for enhanced oxygen reduction reaction," *Curr. Appl. Phys.*, vol. 20, no. 3, pp. 456–461, Mar. 2020, doi: 10.1016/j.cap.2020.01.008.

[281] G. Lemes, D. Sebastián, E. Pastor, and M. J. Lázaro, "N-doped graphene catalysts with high nitrogen concentration for the oxygen reduction reaction," *J. Power Sources*, vol. 438, p. 227036, Oct. 2019, doi: 10.1016/j.jpowsour.2019.227036.

[282] M. Li, L. Zhang, Q. Xu, J. Niu, and Z. Xia, "N-doped graphene as catalysts for oxygen reduction and oxygen evolution reactions: Theoretical considerations," *J. Catal.*, vol. 314, pp. 66–72, May 2014, doi: 10.1016/j.jcat.2014.03.011.

[283] J. Rossmeisl, A. Logadottir, and J. K. Nørskov, "Electrolysis of water on (oxidized) metal surfaces," *Chem. Phys.*, vol. 319, no. 1, pp. 178–184, Dec. 2005, doi: 10.1016/j.chemphys.2005.05.038.

[284] A. Ferre-Vilaplana and E. Herrero, "Understanding the chemisorption-based activation mechanism of the oxygen reduction reaction on nitrogen-doped graphitic materials," *Electrochimica Acta*, vol. 204, pp. 245–254, Jun. 2016, doi: 10.1016/j.electacta.2016.04.039.

[285] Y. She *et al.*, "Oxygen Reduction Reaction Mechanism of Nitrogen-Doped Graphene Derived from Ionic Liquid," *Energy Procedia*, vol. 142, pp. 1319–1326, Dec. 2017, doi: 10.1016/j.egypro.2017.12.508.

[286] Y. Uchida, S. Gomi, H. Matsuyama, A. Akaishi, and J. Nakamura, "Mechanism of stabilization and magnetization of impurity-doped zigzag graphene nanoribbons," *J. Appl. Phys.*, vol. 120, no. 21, p. 214301, Dec. 2016, doi: 10.1063/1.4971175.

[287] L. Tao *et al.*, "Edge-rich and dopant-free graphene as a highly efficient metal-free

electrocatalyst for the oxygen reduction reaction," *Chem. Commun.*, vol. 52, no. 13, pp. 2764–2767, 2016, doi: 10.1039/C5CC09173J.

[288] H. W. Kim *et al.*, "Mechanisms of Two-Electron and Four-Electron Electrochemical Oxygen Reduction Reactions at Nitrogen-Doped Reduced Graphene Oxide," *ACS Catal.*, vol. 10, no. 1, pp. 852–863, Jan. 2020, doi: 10.1021/acscatal.9b04106.

[289] J. C. Chacón-Torres, L. Wirtz, and T. Pichler, "Manifestation of Charged and Strained Graphene Layers in the Raman Response of Graphite Intercalation Compounds," *ACS Nano*, vol. 7, no. 10, pp. 9249–9259, Oct. 2013, doi: 10.1021/nn403885k.

[290] K. N. Kudin, B. Ozbas, H. C. Schniepp, R. K. Prud'homme, I. A. Aksay, and R. Car, "Raman Spectra of Graphite Oxide and Functionalized Graphene Sheets," *Nano Lett.*, vol. 8, no. 1, pp. 36–41, Jan. 2008, doi: 10.1021/nl071822y.

[291] D. Yoon *et al.*, "Interference effect on Raman spectrum of graphene on SiO2Si," *Phys. Rev. B*, vol. 80, no. 12, p. 125422, Sep. 2009, doi: 10.1103/PhysRevB.80.125422.

[292] A. Eckmann *et al.*, "Probing the Nature of Defects in Graphene by Raman Spectroscopy," *Nano Lett.*, vol. 12, no. 8, pp. 3925–3930, Aug. 2012, doi: 10.1021/nl300901a.

[293] Q. H. Wang, C.-J. Shih, G. L. C. Paulus, and M. S. Strano, "Evolution of Physical and Electronic Structures of Bilayer Graphene upon Chemical Functionalization," *J. Am. Chem. Soc.*, vol. 135, no. 50, pp. 18866–18875, Dec. 2013, doi: 10.1021/ja4083914.

[294] A. C. Ferrari *et al.*, "Raman Spectrum of Graphene and Graphene Layers," *Phys. Rev. Lett.*, vol. 97, no. 18, p. 187401, Oct. 2006, doi: 10.1103/PhysRevLett.97.187401.

[295] H. W. Kim *et al.*, "Efficient hydrogen peroxide generation using reduced graphene oxide-based oxygen reduction electrocatalysts," *Nat. Catal.*, vol. 1, no. 4, pp. 282–290, Apr. 2018, doi: 10.1038/s41929-018-0044-2.

[296] A. C. Ferrari and J. Robertson, "Interpretation of Raman spectra of disordered and amorphous carbon," *Phys. Rev. B*, vol. 61, no. 20, pp. 14095–14107, May 2000, doi: 10.1103/PhysRevB.61.14095.

[297] C. Thomsen and S. Reich, "Double Resonant Raman Scattering in Graphite," *Phys. Rev. Lett.*, vol. 85, no. 24, pp. 5214–5217, Dec. 2000, doi: 10.1103/PhysRevLett.85.5214.

[298] A. C. Ferrari, "Raman spectroscopy of graphene and graphite: Disorder, electron-phonon coupling, doping and nonadiabatic effects," *Solid State Commun.*, vol. 143, no. 1–2, pp. 47–57, 2007, doi: 10.1016/j.ssc.2007.03.052.

[299] P. Lazar, R. Mach, and M. Otyepka, "Spectroscopic Fingerprints of Graphitic, Pyrrolic, Pyridinic, and Chemisorbed Nitrogen in N-Doped Graphene," *J. Phys. Chem. C*, vol. 123, no. 16, pp. 10695–10702, Apr. 2019, doi: 10.1021/acs.jpcc.9b02163.

[300] P. Vecera *et al.*, "Precise determination of graphene functionalization by in situ Raman spectroscopy," *Nat. Commun.*, vol. 8, no. 1, Art. no. 1, May 2017, doi: 10.1038/ncomms15192.

[301] L. G. Cançado *et al.*, "Measuring the degree of stacking order in graphite by Raman spectroscopy," *Carbon*, vol. 46, no. 2, pp. 272–275, Feb. 2008, doi: 10.1016/j.carbon.2007.11.015.

[302] D. Yoon, Y.-W. Son, and H. Cheong, "Strain-Dependent Splitting of the Double-Resonance Raman Scattering Band in Graphene," *Phys. Rev. Lett.*, vol. 106, no. 15, p. 155502, Apr. 2011, doi: 10.1103/PhysRevLett.106.155502.

[303] K. Vijayarangamuthu, S. Ahn, H. Seo, S.-H. Yoon, C.-M. Park, and K.-J. Jeon, "Temporospatial Control of Graphene Wettability," *Adv. Mater.*, vol. 28, no. 4, pp. 661–667, 2016, doi: 10.1002/adma.201503444.

[304] D. C. Tranca, F. Rodríguez-Hernández, G. Seifert, and X. Zhuang, "Theoretical models for hydrogen evolution reaction at combined Mo2C and N – doped graphene," *J. Catal.*, vol. 381, pp. 234–247, Jan. 2020, doi: 10.1016/j.jcat.2019.10.028.

[305] R. Muhammad, Y. Shuai, and H.-P. Tan, "First-principles study on hydrogen adsorption on nitrogen doped graphene," *Phys. E Low-Dimens. Syst. Nanostructures*, vol. 88, pp. 115–124, Apr. 2017, doi: 10.1016/j.physe.2016.12.012.

[306] D. Deng *et al.*, "Size effect of graphene on electrocatalytic activation of oxygen," *Chem. Commun.*, vol. 47, no. 36, pp. 10016–10018, Aug. 2011, doi: 10.1039/C1CC13033A.

[307] N. Ramaswamy and S. Mukerjee, "Fundamental Mechanistic Understanding of Electrocatalysis of Oxygen Reduction on Pt and Non-Pt Surfaces: Acid versus Alkaline Media," *Advances in Physical Chemistry*, 2012. https://www.hindawi.com/journals/apc/2012/491604/ (accessed Mar. 05, 2020).

[308] M. Kalbac, A. Reina-Cecco, H. Farhat, J. Kong, L. Kavan, and M. S. Dresselhaus, "The Influence of Strong Electron and Hole Doping on the Raman Intensity of Chemical Vapor-Deposition Graphene," *ACS Nano*, vol. 4, no. 10, pp. 6055–6063, Oct. 2010, doi: 10.1021/nn1010914.

[309] S. Piscanec, M. Lazzeri, F. Mauri, A. C. Ferrari, and J. Robertson, "Kohn Anomalies and Electron-Phonon Interactions in Graphite," *Phys. Rev. Lett.*, vol. 93, no. 18, p. 185503, Oct. 2004, doi: 10.1103/PhysRevLett.93.185503.

[310] J. Vazquez-Arenas, A. Galano, D. U. Lee, D. Higgins, A. Guevara-García, and Z. Chen, "Theoretical and experimental studies of highly active graphene nanosheets to determine catalytic nitrogen sites responsible for the oxygen reduction reaction in alkaline media," *J. Mater. Chem. A*, vol. 4, no. 3, pp. 976–990, Jan. 2016, doi: 10.1039/C5TA06653K.

[311] R. Kappera *et al.*, "Phase-engineered low-resistance contacts for ultrathin MoS2 transistors," *Nat. Mater.*, vol. 13, no. 12, pp. 1128–1134, Dec. 2014, doi: 10.1038/nmat4080.

[312] M. Acerce, D. Voiry, and M. Chhowalla, "Metallic 1T phase MoS2 nanosheets as supercapacitor electrode materials," *Nat. Nanotechnol.*, vol. 10, no. 4, pp. 313–318, Apr.

2015, doi: 10.1038/nnano.2015.40.

[313] Q. H. Wang, K. Kalantar-Zadeh, A. Kis, J. N. Coleman, and M. S. Strano, "Electronics and optoelectronics of two-dimensional transition metal dichalcogenides," *Nat. Nanotechnol.*, vol. 7, no. 11, pp. 699–712, Nov. 2012, doi: 10.1038/nnano.2012.193.

[314] K.-K. Liu *et al.*, "Growth of Large-Area and Highly Crystalline MoS2 Thin Layers on Insulating Substrates," *Nano Lett.*, vol. 12, no. 3, pp. 1538–1544, Mar. 2012, doi: 10.1021/nl2043612.

[315] S. Balendhran *et al.*, "Atomically thin layers of MoS 2via a two step thermal evaporation-exfoliation method," *Nanoscale*, vol. 4, no. 2, pp. 461–466, 2012, doi: 10.1039/c1nr10803d.

[316] Y. Shi *et al.*, "van der Waals Epitaxy of MoS2 Layers Using Graphene As Growth Templates," *Nano Lett.*, vol. 12, no. 6, pp. 2784–2791, Jun. 2012, doi: 10.1021/nl204562j.

[317] M. A. Lukowski, A. S. Daniel, F. Meng, A. Forticaux, L. Li, and S. Jin, "Enhanced Hydrogen Evolution Catalysis from Chemically Exfoliated Metallic MoS2 Nanosheets," *J. Am. Chem. Soc.*, vol. 135, no. 28, pp. 10274–10277, Jul. 2013, doi: 10.1021/ja404523s.

[318] S. Jiménez Sandoval, D. Yang, R. F. Frindt, and J. C. Irwin, "Raman study and lattice dynamics of single molecular layers of MoS2," *Phys. Rev. B*, vol. 44, no. 8, pp. 3955–3962, Aug. 1991, doi: 10.1103/PhysRevB.44.3955.

[319] R. Lv *et al.*, "Transition Metal Dichalcogenides and Beyond: Synthesis, Properties, and Applications of Single- and Few-Layer Nanosheets," *Acc. Chem. Res.*, vol. 48, no. 1, pp. 56–64, Jan. 2015, doi: 10.1021/ar5002846.

[320] D. Voiry *et al.*, "Covalent functionalization of monolayered transition metal dichalcogenides by phase engineering," *Nat. Chem.*, vol. 7, no. 1, pp. 45–49, Jan. 2015, doi: 10.1038/nchem.2108.

[321] K. F. Mak, C. Lee, J. Hone, J. Shan, and T. F. Heinz, "Atomically Thin MoS2: A New Direct-Gap Semiconductor," *Phys. Rev. Lett.*, vol. 105, no. 13, p. 136805, Sep. 2010, doi: 10.1103/PhysRevLett.105.136805.

[322] D. Braga, I. Gutiérrez Lezama, H. Berger, and A. F. Morpurgo, "Quantitative Determination of the Band Gap of WS2 with Ambipolar Ionic Liquid-Gated Transistors," *Nano Lett.*, vol. 12, no. 10, pp. 5218–5223, Oct. 2012, doi: 10.1021/nl302389d.

[323] R. R. Chianelli *et al.*, "Catalytic Properties of Single Layers of Transition Metal Sulfide Catalytic Materials," *Catal. Rev.*, vol. 48, no. 1, pp. 1–41, Jan. 2006, doi: 10.1080/01614940500439776.

[324] W. Zhou *et al.*, "Synthesis of Few-Layer MoS2 Nanosheet-Coated TiO2 Nanobelt Heterostructures for Enhanced Photocatalytic Activities," *Small*, vol. 9, no. 1, pp. 140–147, 2013, doi: 10.1002/smll.201201161.

[325] B. Radisavljevic, A. Radenovic, J. Brivio, V. Giacometti, and A. Kis, "Single-layer MoS2

transistors," *Nat. Nanotechnol.*, vol. 6, no. 3, pp. 147–150, Mar. 2011, doi: 10.1038/nnano.2010.279.

[326] Z. Yin *et al.*, "Single-Layer MoS2 Phototransistors," *ACS Nano*, vol. 6, no. 1, pp. 74–80, Jan. 2012, doi: 10.1021/nn2024557.

[327] T. Onodera *et al.*, "A Computational Chemistry Study on Friction of h-MoS2. Part I. Mechanism of Single Sheet Lubrication," *J. Phys. Chem. B*, vol. 113, no. 52, pp. 16526–16536, Dec. 2009, doi: 10.1021/jp9069866.

[328] S. Zhang, B. V. R. Chowdari, Z. Wen, J. Jin, and J. Yang, "Constructing Highly Oriented Configuration by Few-Layer MoS2: Toward High-Performance Lithium-Ion Batteries and Hydrogen Evolution Reactions," *ACS Nano*, vol. 9, no. 12, pp. 12464–12472, Dec. 2015, doi: 10.1021/acsnano.5b05891.

[329] K.-J. Huang, Y.-J. Liu, H.-B. Wang, Y.-Y. Wang, and Y.-M. Liu, "Sub-femtomolar DNA detection based on layered molybdenum disulfide/multi-walled carbon nanotube composites, Au nanoparticle and enzyme multiple signal amplification," *Biosens. Bioelectron.*, vol. 55, pp. 195–202, May 2014, doi: 10.1016/j.bios.2013.11.061.

[330] T. Liu *et al.*, "Drug Delivery with PEGylated MoS2 Nano-sheets for Combined Photothermal and Chemotherapy of Cancer," *Adv. Mater.*, vol. 26, no. 21, pp. 3433–3440, 2014, doi: 10.1002/adma.201305256.

[331] Z. He and W. Que, "Molybdenum disulfide nanomaterials: Structures, properties, synthesis and recent progress on hydrogen evolution reaction," *Appl. Mater. Today*, vol. 3, pp. 23–56, Jun. 2016, doi: 10.1016/j.apmt.2016.02.001.

[332] W. Zhao *et al.*, "Metastable MoS2: Crystal Structure, Electronic Band Structure, Synthetic Approach and Intriguing Physical Properties," *Chem. – Eur. J.*, vol. 24, no. 60, pp. 15942–15954, 2018, doi: 10.1002/chem.201801018.

[333] H. Li *et al.*, "Optical Identification of Single- and Few-Layer MoS2 Sheets," *Small*, vol. 8, no. 5, pp. 682–686, 2012, doi: 10.1002/smll.201101958.

[334] H. Li *et al.*, "Fabrication of Single- and Multilayer MoS2 Film-Based Field-Effect Transistors for Sensing NO at Room Temperature," *Small*, vol. 8, no. 1, pp. 63–67, 2012, doi: 10.1002/smll.201101016.

[335] G. Zhang, H. Liu, J. Qu, and J. Li, "Two-dimensional layered MoS 2 : rational design, properties and electrochemical applications," *Energy Environ. Sci.*, vol. 9, no. 4, pp. 1190–1209, 2016, doi: 10.1039/C5EE03761A.

[336] Z. Zeng *et al.*, "An Effective Method for the Fabrication of Few-Layer-Thick Inorganic Nanosheets," *Angew. Chem. Int. Ed.*, vol. 51, no. 36, pp. 9052–9056, 2012, doi: 10.1002/anie.201204208.

[337] K.-G. Zhou, N.-N. Mao, H.-X. Wang, Y. Peng, and H.-L. Zhang, "A Mixed-Solvent Strategy for Efficient Exfoliation of Inorganic Graphene Analogues," *Angew. Chem. Int.*

Ed., vol. 50, no. 46, pp. 10839–10842, 2011, doi: 10.1002/anie.201105364.

[338] A. O'Neill, U. Khan, and J. N. Coleman, "Preparation of High Concentration Dispersions of Exfoliated MoS2 with Increased Flake Size," *Chem. Mater.*, vol. 24, no. 12, pp. 2414–2421, Jun. 2012, doi: 10.1021/cm301515z.

[339] Z. Zeng *et al.*, "Single-Layer Semiconducting Nanosheets: High-Yield Preparation and Device Fabrication," *Angew. Chem.*, vol. 123, no. 47, pp. 11289–11293, 2011, doi: 10.1002/ange.201106004.

[340] Y. Yan, B. Xia, X. Ge, Z. Liu, J.-Y. Wang, and X. Wang, "Ultrathin MoS2 Nanoplates with Rich Active Sites as Highly Efficient Catalyst for Hydrogen Evolution," *ACS Appl. Mater. Interfaces*, vol. 5, no. 24, pp. 12794–12798, Dec. 2013, doi: 10.1021/am404843b.

[341] J. Xie *et al.*, "Defect-Rich MoS2 Ultrathin Nanosheets with Additional Active Edge Sites for Enhanced Electrocatalytic Hydrogen Evolution," *Adv. Mater.*, vol. 25, no. 40, pp. 5807–5813, 2013, doi: 10.1002/adma.201302685.

[342] L. Cai *et al.*, "Vacancy-Induced Ferromagnetism of MoS2 Nanosheets," *J. Am. Chem. Soc.*, vol. 137, no. 7, pp. 2622–2627, Feb. 2015, doi: 10.1021/ja5120908.

[343] M.-R. Gao *et al.*, "An efficient molybdenum disulfide/cobalt diselenide hybrid catalyst for electrochemical hydrogen generation," *Nat. Commun.*, vol. 6, no. 1, p. 5982, Jan. 2015, doi: 10.1038/ncomms6982.

[344] Q. Ji *et al.*, "Epitaxial Monolayer MoS2 on Mica with Novel Photoluminescence," *Nano Lett.*, vol. 13, no. 8, pp. 3870–3877, Aug. 2013, doi: 10.1021/nl401938t.

[345] S. Najmaei *et al.*, "Vapour phase growth and grain boundary structure of molybdenum disulphide atomic layers," *Nat. Mater.*, vol. 12, no. 8, pp. 754–759, Aug. 2013, doi: 10.1038/nmat3673.

[346] J. Shi *et al.*, "Controllable Growth and Transfer of Monolayer MoS2 on Au Foils and Its Potential Application in Hydrogen Evolution Reaction," *ACS Nano*, vol. 8, no. 10, pp. 10196–10204, Oct. 2014, doi: 10.1021/nn503211t.

[347] Y.-H. Lee *et al.*, "Synthesis of Large-Area MoS2 Atomic Layers with Chemical Vapor Deposition," *Adv. Mater.*, vol. 24, no. 17, pp. 2320–2325, May 2012, doi: 10.1002/adma.201104798.

[348] Y.-H. Lee *et al.*, "Synthesis and Transfer of Single-Layer Transition Metal Disulfides on Diverse Surfaces," *Nano Lett.*, vol. 13, no. 4, pp. 1852–1857, Apr. 2013, doi: 10.1021/nl400687n.

[349] S. Najmaei, J. Yuan, J. Zhang, P. Ajayan, and J. Lou, "Synthesis and Defect Investigation of Two-Dimensional Molybdenum Disulfide Atomic Layers," *Acc. Chem. Res.*, vol. 48, no. 1, pp. 31–40, Jan. 2015, doi: 10.1021/ar500291j.

[350] X. Wang, H. Feng, Y. Wu, and L. Jiao, "Controlled Synthesis of Highly Crystalline MoS2 Flakes by Chemical Vapor Deposition," *J. Am. Chem. Soc.*, vol. 135, no. 14, pp. 5304–

5307, Apr. 2013, doi: 10.1021/ja4013485.

[351] Y. Zhan, Z. Liu, S. Najmaei, P. M. Ajayan, and J. Lou, "Large-Area Vapor-Phase Growth and Characterization of MoS2 Atomic Layers on a SiO2 Substrate," *Small*, vol. 8, no. 7, pp. 966–971, Apr. 2012, doi: 10.1002/smll.201102654.

[352] Y. Gao *et al.*, "Large-area synthesis of high-quality and uniform monolayer WS 2 on reusable Au foils," *Nat. Commun.*, vol. 6, no. 1, p. 8569, Oct. 2015, doi: 10.1038/ncomms9569.

[353] A. L. Elías *et al.*, "Controlled Synthesis and Transfer of Large-Area WS2 Sheets: From Single Layer to Few Layers," *ACS Nano*, vol. 7, no. 6, pp. 5235–5242, Jun. 2013, doi: 10.1021/nn400971k.

[354] Y.-C. Lin, D. O. Dumcenco, Y.-S. Huang, and K. Suenaga, "Atomic mechanism of the semiconducting-to-metallic phase transition in single-layered MoS2," *Nat. Nanotechnol.*, vol. 9, no. 5, pp. 391–396, May 2014, doi: 10.1038/nnano.2014.64.

[355] H. Tributsch and J. C. Bennett, "Electrochemistry and photochemistry of MoS2 layer crystals. I," *J. Electroanal. Chem. Interfacial Electrochem.*, vol. 81, no. 1, pp. 97–111, Aug. 1977, doi: 10.1016/S0022-0728(77)80363-X.

[356] B. Hinnemann *et al.*, "Biomimetic Hydrogen Evolution: MoS2 Nanoparticles as Catalyst for Hydrogen Evolution," *J. Am. Chem. Soc.*, vol. 127, no. 15, pp. 5308–5309, Apr. 2005, doi: 10.1021/ja0504690.

[357] N. Zhang, S. Gan, T. Wu, W. Ma, D. Han, and L. Niu, "Growth Control of MoS2 Nanosheets on Carbon Cloth for Maximum Active Edges Exposed: An Excellent Hydrogen Evolution 3D Cathode," *ACS Appl. Mater. Interfaces*, vol. 7, no. 22, pp. 12193–12202, Jun. 2015, doi: 10.1021/acsami.5b02586.

[358] Y. Guo, X. Zhang, X. Zhang, and T. You, "Defect- and S-rich ultrathin MoS2 nanosheet embedded N-doped carbon nanofibers for efficient hydrogen evolution," *J. Mater. Chem. A*, vol. 3, no. 31, pp. 15927–15934, Jul. 2015, doi: 10.1039/C5TA03766B.

[359] H. Huang *et al.*, "Strongly coupled MoS2 nanoflake–carbon nanotube nanocomposite as an excellent electrocatalyst for hydrogen evolution reaction," *J. Mater. Chem. A*, vol. 5, no. 4, pp. 1558–1566, Jan. 2017, doi: 10.1039/C6TA09612C.

[360] A. Behranginia *et al.*, "Highly Efficient Hydrogen Evolution Reaction Using Crystalline Layered Three-Dimensional Molybdenum Disulfides Grown on Graphene Film," *Chem. Mater.*, vol. 28, no. 2, pp. 549–555, Jan. 2016, doi: 10.1021/acs.chemmater.5b03997.

[361] D. Voiry *et al.*, "The role of electronic coupling between substrate and 2D MoS2 nanosheets in electrocatalytic production of hydrogen," *Nat. Mater.*, vol. 15, no. 9, pp. 1003–1009, Sep. 2016, doi: 10.1038/nmat4660.

[362] G. Li *et al.*, "Engineering Substrate Interaction To Improve Hydrogen Evolution Catalysis of Monolayer MoS2 Films beyond Pt," *ACS Nano*, vol. 14, no. 2, pp. 1707–1714, Feb.

2020, doi: 10.1021/acsnano.9b07324.

[363] D. Kong *et al.*, "Synthesis of MoS2 and MoSe2 Films with Vertically Aligned Layers," *Nano Lett.*, vol. 13, no. 3, pp. 1341–1347, Mar. 2013, doi: 10.1021/nl400258t.

[364] T. F. Jaramillo, K. P. Jørgensen, J. Bonde, J. H. Nielsen, S. Horch, and I. Chorkendorff, "Identification of Active Edge Sites for Electrochemical H2 Evolution from MoS2 Nanocatalysts," *Science*, vol. 317, no. 5834, pp. 100–102, Jul. 2007, doi: 10.1126/science.1141483.

[365] Y. Li, H. Wang, L. Xie, Y. Liang, G. Hong, and H. Dai, "MoS2 Nanoparticles Grown on Graphene: An Advanced Catalyst for the Hydrogen Evolution Reaction," *J. Am. Chem. Soc.*, vol. 133, no. 19, pp. 7296–7299, May 2011, doi: 10.1021/ja201269b.

[366] C. Tsai *et al.*, "Electrochemical generation of sulfur vacancies in the basal plane of MoS2 for hydrogen evolution," *Nat. Commun.*, vol. 8, no. 1, p. 15113, Apr. 2017, doi: 10.1038/ncomms15113.

[367] Z. Wang *et al.*, "Controllable etching of MoS2 basal planes for enhanced hydrogen evolution through the formation of active edge sites," *Nano Energy*, vol. 49, pp. 634–643, Jul. 2018, doi: 10.1016/j.nanoen.2018.04.067.

[368] J. Yang *et al.*, "Single Atomic Vacancy Catalysis," *ACS Nano*, vol. 13, no. 9, pp. 9958–9964, Sep. 2019, doi: 10.1021/acsnano.9b05226.

[369] C. Meng, M.-C. Lin, X.-W. Du, and Y. Zhou, "Molybdenum Disulfide Modified by Laser Irradiation for Catalyzing Hydrogen Evolution," *ACS Sustain. Chem. Eng.*, vol. 7, no. 7, pp. 6999–7003, Apr. 2019, doi: 10.1021/acssuschemeng.8b06717.

[370] S. Kang *et al.*, "Defect-engineered MoS2 with extended photoluminescence lifetime for high-performance hydrogen evolution," *J. Mater. Chem. C*, vol. 7, no. 33, pp. 10173–10178, Aug. 2019, doi: 10.1039/C9TC02256B.

[371] L. Li *et al.*, "Role of Sulfur Vacancies and Undercoordinated Mo Regions in MoS2 Nanosheets toward the Evolution of Hydrogen," *ACS Nano*, vol. 13, no. 6, pp. 6824–6834, Jun. 2019, doi: 10.1021/acsnano.9b01583.

[372] Q. Tang and D. Jiang, "Stabilization and Band-Gap Tuning of the 1T-MoS2 Monolayer by Covalent Functionalization," *Chem. Mater.*, vol. 27, no. 10, pp. 3743–3748, May 2015, doi: 10.1021/acs.chemmater.5b00986.

[373] H. Wang, Z. Lu, D. Kong, J. Sun, T. M. Hymel, and Y. Cui, "Electrochemical Tuning of MoS2 Nanoparticles on Three-Dimensional Substrate for Efficient Hydrogen Evolution," *ACS Nano*, vol. 8, no. 5, pp. 4940–4947, May 2014, doi: 10.1021/nn500959v.

[374] B. Shang *et al.*, "Lattice -Mismatch-Induced Ultrastable 1T-Phase MoS2–Pd/Au for Plasmon-Enhanced Hydrogen Evolution," *Nano Lett.*, vol. 19, no. 5, pp. 2758–2764, May 2019, doi: 10.1021/acs.nanolett.8b04104.

[375] S.-Z. Yang *et al.*, "Rhenium-Doped and Stabilized MoS2 Atomic Layers with Basal-Plane

Catalytic Activity," *Adv. Mater.*, vol. 30, no. 51, p. 1803477, 2018, doi: 10.1002/adma.201803477.

[376] S. Wei *et al.*, "Iridium-Triggered Phase Transition of MoS2 Nanosheets Boosts Overall Water Splitting in Alkaline Media," *ACS Energy Lett.*, vol. 4, no. 1, pp. 368–374, Jan. 2019, doi: 10.1021/acsenergylett.8b01840.

[377] W. Ding *et al.*, "Highly Ambient-Stable 1T-MoS2 and 1T-WS2 by Hydrothermal Synthesis under High Magnetic Fields," *ACS Nano*, vol. 13, no. 2, pp. 1694–1702, Feb. 2019, doi: 10.1021/acsnano.8b07744.

[378] L. Wang *et al.*, "Self-Optimization of the Active Site of Molybdenum Disulfide by an Irreversible Phase Transition during Photocatalytic Hydrogen Evolution," *Angew. Chem. Int. Ed.*, vol. 56, no. 26, pp. 7610–7614, 2017, doi: 10.1002/anie.201703066.

[379] Q. Tang and D. Jiang, "Mechanism of Hydrogen Evolution Reaction on 1T-MoS2 from First Principles," *ACS Catal.*, vol. 6, no. 8, pp. 4953–4961, Aug. 2016, doi: 10.1021/acscatal.6b01211.

[380] J. Zhu *et al.*, "Boundary activated hydrogen evolution reaction on monolayer MoS2," *Nat. Commun.*, vol. 10, no. 1, p. 1348, Mar. 2019, doi: 10.1038/s41467-019-09269-9.

[381] T. Zhang *et al.*, "Theoretical investigation on the hydrogen evolution reaction mechanism at MoS2 heterostructures: the essential role of the 1T/2H phase interface," *Catal. Sci. Technol.*, vol. 10, no. 2, pp. 458–465, Jan. 2020, doi: 10.1039/C9CY01901D.

[382] N. Zhao, L. Wang, Z. Zhang, and Y. Li, "Activating the MoS2 Basal Planes for Electrocatalytic Hydrogen Evolution by 2H/1T′ Structural Interfaces," *ACS Appl. Mater. Interfaces*, vol. 11, no. 45, pp. 42014–42020, Nov. 2019, doi: 10.1021/acsami.9b11708.

[383] A. N. Enyashin *et al.*, "New Route for Stabilization of 1T-WS2 and MoS2 Phases," *J. Phys. Chem. C*, vol. 115, no. 50, pp. 24586–24591, Dec. 2011, doi: 10.1021/jp2076325.

[384] Y. Shi *et al.*, "Energy Level Engineering of MoS2 by Transition-Metal Doping for Accelerating Hydrogen Evolution Reaction," *J. Am. Chem. Soc.*, vol. 139, no. 43, pp. 15479–15485, Nov. 2017, doi: 10.1021/jacs.7b08881.

[385] L. Yang *et al.*, "Large-area synthesis of monolayered MoS 2(1−x) Se 2x with a tunable band gap and its enhanced electrochemical catalytic activity," *Nanoscale*, vol. 7, no. 23, pp. 10490–10497, 2015, doi: 10.1039/C5NR02652K.

[386] W. Xiao *et al.*, "Dual-Functional N Dopants in Edges and Basal Plane of MoS2 Nanosheets Toward Efficient and Durable Hydrogen Evolution," *Adv. Energy Mater.*, vol. 7, no. 7, p. 1602086, 2017, doi: 10.1002/aenm.201602086.

[387] X. Huang *et al.*, "Activating Basal Planes and S-Terminated Edges of MoS2 toward More Efficient Hydrogen Evolution," *Adv. Funct. Mater.*, vol. 27, no. 6, p. 1604943, 2017, doi: 10.1002/adfm.201604943.

[388] Y. Tan *et al.*, "Monolayer MoS2 Films Supported by 3D Nanoporous Metals for High-

Efficiency Electrocatalytic Hydrogen Production," *Adv. Mater.*, vol. 26, no. 47, pp. 8023–8028, 2014, doi: 10.1002/adma.201403808.

[389] H. Li *et al.*, "Activating and optimizing MoS2 basal planes for hydrogen evolution through the formation of strained sulphur vacancies," *Nat. Mater.*, vol. 15, no. 1, pp. 48–53, Jan. 2016, doi: 10.1038/nmat4465.

[390] S. Guo *et al.*, "Monitoring Hydrogen Evolution Reaction Intermediates of Transition Metal Dichalcogenides via Operando Raman Spectroscopy," *Adv. Funct. Mater.*, vol. 30, no. 35, p. 2003035, 2020, doi: 10.1002/adfm.202003035.

[391] Y. Deng, L. R. L. Ting, P. H. L. Neo, Y.-J. Zhang, A. A. Peterson, and B. S. Yeo, "Operando Raman Spectroscopy of Amorphous Molybdenum Sulfide (MoSx) during the Electrochemical Hydrogen Evolution Reaction: Identification of Sulfur Atoms as Catalytically Active Sites for H+ Reduction," *ACS Catal.*, vol. 6, no. 11, pp. 7790–7798, Nov. 2016, doi: 10.1021/acscatal.6b01848.

[392] B. Lassalle-Kaiser *et al.*, "Evidence from in Situ X-ray Absorption Spectroscopy for the Involvement of Terminal Disulfide in the Reduction of Protons by an Amorphous Molybdenum Sulfide Electrocatalyst," *J. Am. Chem. Soc.*, vol. 137, no. 1, pp. 314–321, Jan. 2015, doi: 10.1021/ja510328m.

[393] S. C. Lee *et al.*, "Chemical and Phase Evolution of Amorphous Molybdenum Sulfide Catalysts for Electrochemical Hydrogen Production," *ACS Nano*, vol. 10, no. 1, pp. 624–632, Jan. 2016, doi: 10.1021/acsnano.5b05652.

[394] H. Li *et al.*, "From Bulk to Monolayer MoS2: Evolution of Raman Scattering," *Adv. Funct. Mater.*, vol. 22, no. 7, pp. 1385–1390, 2012, doi: 10.1002/adfm.201102111.

[395] J. L. Verble and T. J. Wieting, "Lattice Mode Degeneracy in MoS2 and Other Layer Compounds," *Phys. Rev. Lett.*, vol. 25, no. 6, pp. 362–365, Aug. 1970, doi: 10.1103/PhysRevLett.25.362.

[396] C. Lee, H. Yan, L. E. Brus, T. F. Heinz, J. Hone, and S. Ryu, "Anomalous Lattice Vibrations of Single- and Few-Layer MoS2," *ACS Nano*, vol. 4, no. 5, pp. 2695–2700, May 2010, doi: 10.1021/nn1003937.

[397] X. Zhang *et al.*, "Raman spectroscopy of shear and layer breathing modes in multilayer MoS2," *Phys. Rev. B*, vol. 87, no. 11, p. 115413, Mar. 2013, doi: 10.1103/PhysRevB.87.115413.

[398] M. O'Brien, N. Scheuschner, J. Maultzsch, G. S. Duesberg, and N. McEvoy, "Raman Spectroscopy of Suspended MoS2," *Phys. Status Solidi B*, vol. 254, no. 11, p. 1700218, 2017, doi: 10.1002/pssb.201700218.

[399] J. Huang *et al.*, "In situ monitoring of the electrochemically induced phase transition of thermodynamically metastable 1T-MoS2 at nanoscale," *Nanoscale*, vol. 12, no. 16, pp. 9246–9254, Apr. 2020, doi: 10.1039/D0NR02161J.

[400] M. Calandra, "Chemically exfoliated single-layer MoS2: Stability, lattice dynamics, and catalytic adsorption from first principles," *Phys. Rev. B*, vol. 88, no. 24, p. 245428, Dec. 2013, doi: 10.1103/PhysRevB.88.245428.

[401] É. Blanco, P. Afanasiev, G. Berhault, D. Uzio, and S. Loridant, "Resonance Raman spectroscopy as a probe of the crystallite size of MoS2 nanoparticles," *Comptes Rendus Chim.*, vol. 19, no. 10, pp. 1310–1314, Oct. 2016, doi: 10.1016/j.crci.2015.08.014.

[402] A. Kumar and P. K. Ahluwalia, "A first principle Comparative study of electronic and optical properties of 1H – MoS2 and 2H – MoS2," *Mater. Chem. Phys.*, vol. 135, no. 2, pp. 755–761, Aug. 2012, doi: 10.1016/j.matchemphys.2012.05.055.

[403] F. J. Crowne *et al.*, "Blueshift of the A-exciton peak in folded monolayer 1H-MoS2," *Phys. Rev. B*, vol. 88, no. 23, p. 235302, Dec. 2013, doi: 10.1103/PhysRevB.88.235302.

[404] Y. Zhao *et al.*, "Interlayer Breathing and Shear Modes in Few-Trilayer MoS2 and WSe2," *Nano Lett.*, vol. 13, no. 3, pp. 1007–1015, Mar. 2013, doi: 10.1021/nl304169w.

[405] X. Wang *et al.*, "Single-Atom Vacancy Defect to Trigger High-Efficiency Hydrogen Evolution of MoS2," *J. Am. Chem. Soc.*, vol. 142, no. 9, pp. 4298–4308, Mar. 2020, doi: 10.1021/jacs.9b12113.

[406] W. Xun *et al.*, "Activating the MoS2 Basal Plane toward Enhanced Solar Hydrogen Generation via in Situ Photoelectrochemical Control," *ACS Energy Lett.*, vol. 6, no. 1, pp. 267–276, Jan. 2021, doi: 10.1021/acsenergylett.0c02320.

[407] G. Eda, H. Yamaguchi, D. Voiry, T. Fujita, M. Chen, and M. Chhowalla, "Photoluminescence from Chemically Exfoliated MoS2," *Nano Lett.*, vol. 11, no. 12, pp. 5111–5116, Dec. 2011, doi: 10.1021/nl201874w.

[408] M. J. Lacey, A. Yalamanchili, J. Maibach, C. Tengstedt, K. Edström, and D. Brandell, "The Li–S battery: an investigation of redox shuttle and self-discharge behaviour with LiNO3-containing electrolytes," *RSC Adv.*, vol. 6, no. 5, pp. 3632–3641, Jan. 2016, doi: 10.1039/C5RA23635E.

[409] T. Tian, L. Huang, L. Ai, and J. Jiang, "Surface anion-rich NiS2 hollow microspheres derived from metal–organic frameworks as a robust electrocatalyst for the hydrogen evolution reaction," *J. Mater. Chem. A*, vol. 5, no. 39, pp. 20985–20992, Oct. 2017, doi: 10.1039/C7TA06671F.

[410] B. E. Conway and B. V. Tilak, "Interfacial processes involving electrocatalytic evolution and oxidation of H2, and the role of chemisorbed H," *Electrochimica Acta*, vol. 47, no. 22, pp. 3571–3594, Aug. 2002, doi: 10.1016/S0013-4686(02)00329-8.

[411] A. Azcatl *et al.*, "Covalent Nitrogen Doping and Compressive Strain in MoS2 by Remote N2 Plasma Exposure," *Nano Lett.*, vol. 16, no. 9, pp. 5437–5443, Sep. 2016, doi: 10.1021/acs.nanolett.6b01853.

[412] Y. Y. Hui *et al.*, "Exceptional Tunability of Band Energy in a Compressively Strained

Trilayer MoS2 Sheet," *ACS Nano*, vol. 7, no. 8, pp. 7126–7131, Aug. 2013, doi: 10.1021/nn4024834.

[413] B. Chakraborty, A. Bera, D. V. S. Muthu, S. Bhowmick, U. V. Waghmare, and A. K. Sood, "Symmetry-dependent phonon renormalization in monolayer MoS2 transistor," *Phys. Rev. B*, vol. 85, no. 16, p. 161403, Apr. 2012, doi: 10.1103/PhysRevB.85.161403.

[414] K. Le *et al.*, "Controllably Doping Nitrogen into 1T/2H MoS2 Heterostructure Nanosheets for Enhanced Supercapacitive and Electrocatalytic Performance by Low-Power N2 Plasma," *ACS Appl. Mater. Interfaces*, vol. 13, no. 37, pp. 44427–44439, Sep. 2021, doi: 10.1021/acsami.1c12973.

[415] X. Fan *et al.*, "Efficacious nitrogen introduction into MoS2 as bifunctional electrocatalysts for long-life Li-O2 batteries," *Electrochimica Acta*, vol. 369, p. 137653, Feb. 2021, doi: 10.1016/j.electacta.2020.137653.

[416] R. Wu *et al.*, "N dopants triggered new active sites and fast charge transfer in MoS2 nanosheets for full Response-Recovery NO2 detection at room temperature," *Appl. Surf. Sci.*, vol. 571, p. 151162, Jan. 2022, doi: 10.1016/j.apsusc.2021.151162.

[417] Q. Yang *et al.*, "Activating MoS2 with Super-High Nitrogen-Doping Concentration as Efficient Catalyst for Hydrogen Evolution Reaction," *J. Phys. Chem. C*, vol. 123, no. 17, pp. 10917–10925, May 2019, doi: 10.1021/acs.jpcc.9b00059.

[418] K. Dolui, I. Rungger, C. Das Pemmaraju, and S. Sanvito, "Possible doping strategies for MoS2 monolayers: An ab initio study," *Phys. Rev. B*, vol. 88, no. 7, p. 075420, Aug. 2013, doi: 10.1103/PhysRevB.88.075420.

[419] J. Zhou, J. Chen, S. Chen, Y. Wu, J. Cao, and Y. Zhang, "Mechanism of sulfur vacancies and doping in 1 T'-MoS2 toward the evolution of hydrogen," *Chem. Phys. Lett.*, vol. 787, p. 139231, 2021, doi: 10.1016/j.cplett.2021.139231.

[420] Y. Li and R. Nakamura, "Structural change of molybdenum sulfide facilitates the electrocatalytic hydrogen evolution reaction at neutral pH as revealed by in situ Raman spectroscopy," *Chin. J. Catal.*, vol. 39, no. 3, pp. 401–406, Mar. 2018, doi: 10.1016/S1872-2067(17)62945-0.

[421] C. Manjunatha, N. Srinivasa, S. K. Chaitra, M. Sudeep, R. Chandra Kumar, and S. Ashoka, "Controlled synthesis of nickel sulfide polymorphs: studies on the effect of morphology and crystal structure on OER performance," *Mater. Today Energy*, vol. 16, p. 100414, Jun. 2020, doi: 10.1016/j.mtener.2020.100414.

[422] S. Anantharaj, S. Kundu, and S. Noda, "Progress in nickel chalcogenide electrocatalyzed hydrogen evolution reaction," *J. Mater. Chem. A*, vol. 8, no. 8, pp. 4174–4192, Feb. 2020, doi: 10.1039/C9TA14037A.

[423] S. Surendran and R. K. Selvan, "Growth and Characterization of 3D Flower-Like β-NiS on Carbon Cloth: A Dexterous and Flexible Multifunctional Electrode for Supercapattery

and Water-Splitting Applications," *Adv. Mater. Interfaces*, vol. 5, no. 4, p. 1701056, 2018, doi: 10.1002/admi.201701056.

[424] J. Mohammed-Ibrahim and X. Sun, "Recent progress on earth abundant electrocatalysts for hydrogen evolution reaction (HER) in alkaline medium to achieve efficient water splitting – A review," *J. Energy Chem.*, vol. 34, pp. 111–160, Jul. 2019, doi: 10.1016/j.jechem.2018.09.016.

[425] Q. Ma *et al.*, "Identifying the electrocatalytic sites of nickel disulfide in alkaline hydrogen evolution reaction," *Nano Energy*, vol. 41, pp. 148–153, Nov. 2017, doi: 10.1016/j.nanoen.2017.09.036.

[426] N. Jiang, Q. Tang, M. Sheng, B. You, D. Jiang, and Y. Sun, "Nickel sulfides for electrocatalytic hydrogen evolution under alkaline conditions: a case study of crystalline NiS, NiS 2 , and Ni 3 S 2 nanoparticles," *Catal. Sci. Technol.*, vol. 6, no. 4, pp. 1077–1084, 2016, doi: 10.1039/C5CY01111F.

[427] P. Luo *et al.*, "Targeted Synthesis of Unique Nickel Sulfide (NiS, NiS2) Microarchitectures and the Applications for the Enhanced Water Splitting System," *ACS Appl. Mater. Interfaces*, vol. 9, no. 3, pp. 2500–2508, Jan. 2017, doi: 10.1021/acsami.6b13984.

[428] W. Zhu *et al.*, "Nickel sulfide microsphere film on Ni foam as an efficient bifunctional electrocatalyst for overall water splitting," *Chem. Commun.*, vol. 52, no. 7, pp. 1486–1489, Jan. 2016, doi: 10.1039/C5CC08064A.

[429] L.-L. Feng *et al.*, "High-Index Faceted Ni3S2 Nanosheet Arrays as Highly Active and Ultrastable Electrocatalysts for Water Splitting," *J. Am. Chem. Soc.*, vol. 137, no. 44, pp. 14023–14026, Nov. 2015, doi: 10.1021/jacs.5b08186.

[430] C. Ouyang *et al.*, "Hierarchically Porous Ni3S2 Nanorod Array Foam as Highly Efficient Electrocatalyst for Hydrogen Evolution Reaction and Oxygen Evolution Reaction," *Electrochimica Acta*, vol. 174, pp. 297–301, Aug. 2015, doi: 10.1016/j.electacta.2015.05.186.

[431] C. Tang, Z. Pu, Q. Liu, A. M. Asiri, and X. Sun, "NiS2 nanosheets array grown on carbon cloth as an efficient 3D hydrogen evolution cathode," *Electrochimica Acta*, vol. 153, pp. 508–514, Jan. 2015, doi: 10.1016/j.electacta.2014.12.043.

[432] Y. Pan, Y. Chen, X. Li, Y. Liu, and C. Liu, "Nanostructured nickel sulfides: phase evolution, characterization and electrocatalytic properties for the hydrogen evolution reaction," *RSC Adv.*, vol. 5, no. 127, pp. 104740–104749, Dec. 2015, doi: 10.1039/C5RA18737K.

[433] D. Siegmund, N. Blanc, M. Smialkowski, K. Tschulik, and U.-P. Apfel, "Metal-Rich Chalcogenides for Electrocatalytic Hydrogen Evolution: Activity of Electrodes and Bulk Materials," *ChemElectroChem*, vol. 7, no. 7, pp. 1514–1527, 2020, doi:

10.1002/celc.201902125.

[434] I. Zegkinoglou *et al.*, "Operando Phonon Studies of the Protonation Mechanism in Highly Active Hydrogen Evolution Reaction Pentlandite Catalysts," *J. Am. Chem. Soc.*, vol. 139, no. 41, pp. 14360–14363, Oct. 2017, doi: 10.1021/jacs.7b07902.

[435] Y. Zhu *et al.*, "Operando Unraveling of the Structural and Chemical Stability of P-Substituted CoSe2 Electrocatalysts toward Hydrogen and Oxygen Evolution Reactions in Alkaline Electrolyte," *ACS Energy Lett.*, vol. 4, no. 4, pp. 987–994, Apr. 2019, doi: 10.1021/acsenergylett.9b00382.

[436] C. Karakaya *et al.*, "Mesoporous Thin-Film NiS2 as an Idealized Pre-Electrocatalyst for a Hydrogen Evolution Reaction," *ACS Catal.*, vol. 10, no. 24, pp. 15114–15122, Dec. 2020, doi: 10.1021/acscatal.0c03094.

[437] B. Yan, D. Krishnamurthy, C. H. Hendon, S. Deshpande, Y. Surendranath, and V. Viswanathan, "Surface Restructuring of Nickel Sulfide Generates Optimally Coordinated Active Sites for Oxygen Reduction Catalysis," *Joule*, vol. 1, no. 3, pp. 600–612, Nov. 2017, doi: 10.1016/j.joule.2017.08.020.

[438] Y. Ge *et al.*, "Insight into the hydrogen evolution reaction of nickel dichalcogenide nanosheets: activities related to non-metal ligands," *Nanoscale*, vol. 9, no. 17, pp. 5538–5544, May 2017, doi: 10.1039/C6NR09977G.

[439] J. Staszak-Jirkovský *et al.*, "Design of active and stable Co–Mo–Sx chalcogels as pH-universal catalysts for the hydrogen evolution reaction," *Nat. Mater.*, vol. 15, no. 2, Art. no. 2, Feb. 2016, doi: 10.1038/nmat4481.

[440] F. E. Sarac Oztuna and U. Unal, "Charge storage characteristics of layer-by-layer assembled nickel hydroxide and graphene oxide nanosheets," *J. Solid State Electrochem.*, vol. 23, no. 5, pp. 1409–1417, May 2019, doi: 10.1007/s10008-019-04230-8.

[441] B. Schneiderová *et al.*, "Nickel hydroxide ultrathin nanosheets as building blocks for electrochemically active layers," *J. Mater. Chem. A*, vol. 1, no. 37, pp. 11429–11437, 2013, doi: 10.1039/C3TA12129A.

[442] D. Wang, W. Yan, and G. G. Botte, "Exfoliated nickel hydroxide nanosheets for urea electrolysis," *Electrochem. Commun.*, vol. 13, no. 10, pp. 1135–1138, Oct. 2011, doi: 10.1016/j.elecom.2011.07.016.

[443] J. W. Lee, J. M. Ko, and J.-D. Kim, "Hierarchical Microspheres Based on α-Ni(OH)2 Nanosheets Intercalated with Different Anions: Synthesis, Anion Exchange, and Effect of Intercalated Anions on Electrochemical Capacitance," Sep. 08, 2011. https://pubs.acs.org/doi/abs/10.1021/jp206379h (accessed Aug. 02, 2018).

[444] S. Ida, D. Shiga, M. Koinuma, and Y. Matsumoto, "Synthesis of Hexagonal Nickel Hydroxide Nanosheets by Exfoliation of Layered Nickel Hydroxide Intercalated with Dodecyl Sulfate Ions," Oct. 04, 2008. https://pubs.acs.org/doi/abs/10.1021/ja804397n

(accessed Aug. 02, 2018).

[445] J. Karthikeyan, H. Fjellvåg, S. Bundli, and A. O. Sjåstad, "Efficient Exfoliation of Layered Double Hydroxides; Effect of Cationic Ratio, Hydration State, Anions and Their Orientations," *Materials*, vol. 14, no. 2, Art. no. 2, Jan. 2021, doi: 10.3390/ma14020346.

[446] G. V. Manohara, D. A. Kunz, P. V. Kamath, W. Milius, and J. Breu, "Homogeneous Precipitation by Formamide Hydrolysis: Synthesis, Reversible Hydration, and Aqueous Exfoliation of the Layered Double Hydroxide (LDH) of Ni and Al," *Langmuir*, vol. 26, no. 19, pp. 15586–15591, Oct. 2010, doi: 10.1021/la103108f.

[447] Y. Kong *et al.*, "Enhanced photoelectrochemical performance of tungsten oxide film by bifunctional Au nanoparticles," *RSC Adv.*, vol. 7, no. 25, pp. 15201–15210, Mar. 2017, doi: 10.1039/C7RA01426K.

[448] C. Marini *et al.*, "Combined Raman and infrared investigation of the insulator-to-metal transition in NiS2-xSex compounds," *Phys. Rev. B*, vol. 84, no. 23, p. 235134, Dec. 2011, doi: 10.1103/PhysRevB.84.235134.

[449] J.-H. Wang, Z. Cheng, J.-L. Brédas, and M. Liu, "Electronic and vibrational properties of nickel sulfides from first principles," *J. Chem. Phys.*, vol. 127, no. 21, p. 214705, Dec. 2007, doi: 10.1063/1.2801985.

[450] V. Lemos, G. M. Gualberto, J. B. Salzberg, and F. Cerdeira, "First-Order Raman Scattering in NiS2—xSex," *Phys. Status Solidi B*, vol. 100, no. 2, pp. 755–762, 1980, doi: 10.1002/pssb.2221000245.

[451] D. W. Bishop, P. S. Thomas, and A. S. Ray, "Raman spectra of nickel(II) sulfide," *Mater. Res. Bull.*, vol. 33, no. 9, pp. 1303–1306, Sep. 1998, doi: 10.1016/S0025-5408(98)00121-4.

[452] A. Galtayries and J. Grimblot, "Formation and electronic properties of oxide and sulphide films of Co, Ni and Mo studied by XPS," *J. Electron Spectrosc. Relat. Phenom.*, vol. 98–99, pp. 267–275, Jan. 1999, doi: 10.1016/S0368-2048(98)00292-8.

[453] L. Sangaletti, F. Parmigiani, T. Thio, and J. W. Bennett, "Electronic-correlation effects in the x-ray-photoemission spectra of NiS2," *Phys. Rev. B*, vol. 55, no. 15, pp. 9514–9519, Apr. 1997, doi: 10.1103/PhysRevB.55.9514.

[454] D. Xiong, W. Li, and L. Liu, "Vertically Aligned Porous Nickel(II) Hydroxide Nanosheets Supported on Carbon Paper with Long-Term Oxygen Evolution Performance," *Chem. – Asian J.*, vol. 12, no. 5, pp. 543–551, 2017, doi: 10.1002/asia.201601590.

[455] D. S. Hall, D. J. Lockwood, S. Poirier, C. Bock, and B. R. MacDougall, "Applications of in Situ Raman Spectroscopy for Identifying Nickel Hydroxide Materials and Surface Layers during Chemical Aging," *ACS Appl. Mater. Interfaces*, vol. 6, no. 5, pp. 3141–3149, Mar. 2014, doi: 10.1021/am405419k.

[456] Hall David S., Lockwood David J., Bock Christina, and MacDougall Barry R., "Nickel

hydroxides and related materials: a review of their structures, synthesis and properties," *Proc. R. Soc. Math. Phys. Eng. Sci.*, vol. 471, no. 2174, p. 20140792, Feb. 2015, doi: 10.1098/rspa.2014.0792.

[457] D. S. Hall, D. J. Lockwood, S. Poirier, C. Bock, and B. R. MacDougall, "Raman and Infrared Spectroscopy of α and β Phases of Thin Nickel Hydroxide Films Electrochemically Formed on Nickel," *J. Phys. Chem. A*, vol. 116, no. 25, pp. 6771–6784, Jun. 2012, doi: 10.1021/jp303546r.